



## ATLAS Note

ANA-TOPQ-2020-03-INT1

27th April 2020



Draft version 0.13

# Measurements of inclusive and differential cross-sections of $t\bar{t}\gamma$ production in $e\mu$ final states at 13 TeV with the ATLAS detector

Carmen Diez Pardos<sup>a</sup>, Ivor Fleck<sup>a</sup>, Steffen Korn<sup>b</sup>, Yichen Li<sup>c</sup>, John Meshreki<sup>a</sup>, Thomas Peiffer<sup>b</sup>, Arnulf Quadt<sup>b</sup>, Amartya Rej<sup>a</sup>, Elizaveta Shabalina<sup>b</sup>, Knut Zoch<sup>b</sup>

<sup>a</sup>*University of Siegen*

<sup>b</sup>*University of Göttingen*

<sup>c</sup>*DESY*

Inclusive and differential cross-sections for the production of a top-quark pair in association with a photon are measured with the full LHC Run2 proton-proton collision data corresponding to an integrated luminosity of  $139 \text{ fb}^{-1}$ . The data were collected by the ATLAS detector at the LHC, between 2015 and 2018 at a centre-of-mass energy of 13 TeV. The measurements are performed in the  $e\mu$  final states in a fiducial volume. Events with exactly one photon, one electron and one muon of opposite sign, and at least two jets, out of which at least one is  $b$ -tagged, are selected. The fiducial cross-section is measured to be  $39.6^{+2.7}_{-2.3} \text{ fb}$ . Differential cross-sections as a function of several observables are unfolded to parton level and compared to state-of-the-art Monte-Carlo simulations and NLO calculations. These include cross-sections as a function of the photon transverse momentum, the photon absolute pseudorapidity, and the azimuthal opening angle between the electron and the muon. All measurements are in agreement with the theoretical predictions.

© 2020 CERN for the benefit of the ATLAS Collaboration.

Reproduction of this article or parts of it is allowed as specified in the CC-BY-4.0 license.

## 25 **Contents**

26	<b>1 Introduction</b>	11
27	<b>2 The ATLAS detector</b>	14
28	<b>3 Simulation of signal and background</b>	15
29	3.1 Used dedicated samples	15
30	3.2 Used inclusive samples	17
31	3.3 Sample-overlap removal procedure	17
32	3.4 Categorisation of photons	19
33	3.5 Contribution of pile-up photons	20
34	<b>4 Event selection</b>	21
35	4.1 Definition of objects	21
36	4.2 Event pre-selection	23
37	4.3 Definition of the signal region	23
38	<b>5 Cross-section definition and fit strategy</b>	30
39	5.1 Object and phase space definitions at parton level	30
40	5.2 Fit strategy for the inclusive cross-section	31
41	5.3 Unfolding method for the differential cross-section	32
42	<b>6 Systematic uncertainties</b>	38
43	6.1 Theoretical Uncertainties	40
44	6.2 Experimental Uncertainties	54
45	<b>7 Pre-fit distributions and Asimov tests</b>	60
46	<b>8 Unfolding studies</b>	71
47	8.1 Binning optimisation	71
48	8.2 Pseudo-data	71
49	8.3 Number of iterations	77
50	8.4 Closure test	78
51	8.5 Pull test	79
52	8.6 Stress test	80
53	<b>9 Results</b>	83
54	9.1 Inclusive fiducial cross-section	83
55	9.2 Differential cross-section	91
56	<b>10 Conclusion</b>	104
57	<b>A <math>Wt+PS</math> versus <math>tW\gamma</math></b>	110
58	A.1 Summary of the comparison studies	110
59	A.2 Reweighting studies of $tW\gamma$ production mode	110
60	<b>B <math>tW\gamma</math> contribution to fiducial region</b>	115

---

61	<b>C Lists of Monte-Carlo samples</b>	<b>116</b>
62	<b>D Hadron-fake estimates</b>	<b>121</b>
63	<b>E <math>t\bar{t}\gamma</math>-only fit scenario</b>	<b>139</b>
64	<b>F <math>t\bar{t}\gamma</math>-only scenario for differential measurement</b>	<b>144</b>
65	<b>G Fit benchmarks</b>	<b>153</b>
66	<b>H Pruning optimisation</b>	<b>162</b>
67	<b>I Fit results with correlated rate/shape modelling variations</b>	<b>170</b>

---

## 68 List of contributions

---

Carmen Diez Pardos	Analysis coordination, communication with theorists, supervision of J. Meshreki, A. Rej.
Ivor Fleck	Supervision of J. Meshreki, A. Rej.
Steffen Korn	Data-driven h-fake estimation.
Yichen Li	General advisory role, parton level definitions, background studies.
John Meshreki	INT note editor, unfolding, differential cross-section.
Thomas Peiffer	Analysis coordination, supervision of S. Korn and K. Zoch.
Arnulf Quadt	Supervision of S. Korn and K. Zoch.
Amartya Rej	MC samples, $t\bar{t}\gamma$ parton history.
Elizaveta Shabalina	Supervision of S. Korn and K. Zoch.
Knut Zoch	INT note editor, ntuple production, cut optimisation, systematics, inclusive cross-section measurement.

---

70

Not reviewed, for internal circulation only

## 71 List of changes

### 72 Changes in v0.13 (1 April 2020)

73 Upon request by the top group conveners, the strongly pulled nuisance parameters for the  $t\bar{t}\gamma$  PYTHIA8 *var3c*  
 74 and PS model variations were decorrelated in rate and shape. This relaxes the constraints and the pulls of  
 75 the shape-only components are less strong; the rate components remain unpulled and not constrained. This  
 76 increases the overall uncertainties on the final result from  $+5.8\%$  to  $+6.8\%$ , and it increases the impact of  
 77 the signal modelling uncertainties on the final result from 1.9% to 3.8%. The central value of the result  
 78 remains (almost) unchanged. For comparison, a fit scenario with rate/shape correlated for both modelling  
 79 variations is summarised in the newly added Appendix I, which explicitly points out differences in pulls,  
 80 constraints, ranking and correlations.

### 81 Changes in v0.12 (27 March 2020)

- 82 • Major change in the treatment of signal modelling uncertainties: the templates used in the fit are now  
 83 reweighted to match the fiducial cross-section of the nominal MC prediction. This reduces differences  
 84 between these templates and the nominal prediction to effects from efficiency and migration – and  
 85 the resulting rate differences now correspond to the pre-fit relative uncertainties on  $C$ , as quoted in  
 86 Table 7. This also means that evaluating them on  $C$  is now redundant and *no* uncertainties on  $C$  need  
 87 to be considered anymore. The only remaining uncertainty on the fiducial cross-section is the  $tW\gamma$   
 88 parton-matching uncertainty, which gets added to the post-fit uncertainties of the fit in quadrature to  
 89 obtain the final result.
- 90 • A bug was found and fixed with evaluating systematic templates against AFII and applying them  
 91 to a FS nominal simulation. Instead of the desired behaviour, they were compared against the FS  
 92 simulation directly, which increased rate/shape effects in some cases.
- 93 • Information about strong nuisance-parameter constraints was added to the Asimov fit results in  
 94 Section 7, and information about strong constraints and pulls to the data fit results in Section 9.

### 95 Changes in v0.11 (26 February 2020)

- 96 • For comparison, a  $t\bar{t}\gamma$ -only differential measurement is newly added in Appendix F.
- 97 • To be consistent with top-group-internal conventions, we switched to using  $tW\gamma$  instead of  $Wt\gamma$  for  
 98 single-top production in association with a  $W$ -boson and a photon throughout the text.
- 99 • To avoid confusion, the acceptance-related uncertainties on the correction factor  $C$  were removed  
 100 from the fit framework. Thus, they do not show up in correlation matrices, NP pulls or ranking plots  
 101 anymore. As a consequence, the uncertainty on the signal strength is now quoted without these  
 102 uncertainties included. They only get added once the extrapolation to the fiducial phase space is  
 103 done for the inclusive cross-section, for which the uncertainties remain the same.
- 104 • Yield tables now rounded to integers, not according to ATLAS rounding convention, because this  
 105 caused confusion in the scaling of the signal prediction to data.

<sup>106</sup> **Changes in v0.10 (20 January 2020)**

<sup>107</sup> This constitutes the first INT note version after the CONF note was made public:

- <sup>108</sup> • Updated  $tW\gamma$  simulation, now includes both  $tW\gamma$  with photon from production and from decay. The previously used reweighting of  $tW\gamma$  is dropped. Descriptions updated in Section 3, event yields and control plots updated with and without systematic uncertainties (Sections 4 and 7).
- <sup>111</sup> •  $t\bar{t}\gamma$  and  $tW\gamma$  are now measured simultaneously as a combined signal to be consistent with the fixed-order NLO theory calculation in Ref. [1]. For that,  $tW\gamma$  is now split in two distinct categories,  $tW\gamma$  *ep* and *Other tW $\gamma$* . Tables, plots and text in Section 4 updated accordingly .
- <sup>114</sup> • For consistency with the NLO calculation, Frixione isolation criteria for photons were added to the definition of the parton-level fiducial phase space and its description is added to Section 5.1. This reduces the number of selected events on parton level and affects matching efficiencies between parton-level and reco-level events.
- <sup>118</sup> • Efficiencies, outside migration fraction and acceptance correction factors were recalculated with the combined  $t\bar{t}\gamma + tW\gamma$  signal and the added Frixione isolation criteria. The corresponding Table 7 on page 33 was extended and its values updated. Also updated plots of correction efficiencies and acceptances and migration matrcies in Section 5.3 with the combined scenario and final binning.
- <sup>122</sup> • Updated prescriptions for systematics (Section 6):
  - <sup>123</sup> – Bugfix for jet uncertainties: effective NPs for jet energy resolution were not included correctly. This slightly increases the overall uncertainties on the result.
  - <sup>125</sup> – An additional uncertainty,  $tW\gamma$  *parton match*, on the correction factor was added to reflect the uncertainties in the fiducial phase-space selection for  $tW\gamma$  samples.
  - <sup>127</sup> – Removed *one-sided* symmetrisation technique, introduce a *maximum* symmetrisation instead. This is used for modelling uncertainties with large statistical fluctuations where a conservative symmetrisation approach is needed (e.g. *hdamp* variation, PS model uncertainty).
  - <sup>130</sup> – Modelling uncertainties: updated as requested during CONF note approval. Scales are now evaluated separately, smoothing and symmetrisation are only performed if the systematic variations are *not* obtained through reweighting.  $t\bar{t}$  *radiation* uncertainties now split into *var3c*, scales (separately) and *hdamp* variation.  $t\bar{t}$  matrix-element variation dropped entirely.
  - <sup>134</sup> –  $t\bar{t}\gamma$  NNPDF uncertainties now directly enter the fit for the inclusive measurement.
  - <sup>135</sup> – All red/blue plots updated due to new event yields and systematic prescriptions.
- <sup>136</sup> • All fits for the inclusive measurement redone (on Asimov in Section 7 and on data in Section 9) due to new measurement strategy, updated acceptance correction factors and systematic uncertainty prescriptions:
  - <sup>139</sup> – All tables and plots related to Asimov and data fit results updated.
  - <sup>140</sup> – Asimov fit with new expected uncertainty  $^{+7.1\%}_{-6.3\%}$ , compared to previous  $\pm 6.2\%$ . Constraints on pulls and ranking of systematics basically unchanged.

- 142     – Data fit with similar uncertainties. Reduced fiducial cross-section due to the added Frixione  
 143       isolation at parton level. New value for the combined  $t\bar{t}\gamma + tW\gamma$  signal is  $39.7^{+2.6}_{-2.3}$  fb compared  
 144       to the previous value of  $44.2 \pm 2.6$  fb for  $t\bar{t}\gamma$  only. Only minor changes in pulls and ranking.  
 145       Acceptance uncertainty from  $t\bar{t}\gamma$  PS modelling remains the dominant uncertainty of the  
 146       measurement.
- 147     – For comparison, a  $t\bar{t}\gamma$ -only measurement scenario is summarised in the newly added Appendix E.  
 148       The  $t\bar{t}\gamma$ -only measurement shows larger uncertainties than the combined due to extra freedom  
 149       given to the  $tW\gamma$  normalisation.
- 150     • Unfolding and differential cross-section measurement (Sections 8 and 9):
  - 151       – Added control plots with the same binning as used in unfolding, see Figure 32 on page 64.
  - 152       – Binning is re-optimised to have less up/down fluctuations (Top Conf comment).
  - 153       – Added one more stress test using (data-MC/data).
  - 154       – Updated all unfolding tests with the combined scenario and final binning.
  - 155       – Updated all differential cross-section results (plots, tables, etc) in Section 9 with the signal  
 156       combined scenario of  $t\bar{t}\gamma + tW\gamma$  and with the final binning.
- 157     • Updated citations and bibliography (based on comments received on CONF note).

## 158 Changes in v0.9 (20 September 2019)

- 159     • Inconsistencies in the naming of variables fixed (e.g.  $|\Delta\eta(\ell, \ell)|$ ,  $\Delta\phi(\ell, \ell)$  and  $\Delta R_{\min}(\gamma, \ell)$  were not  
 160       typeset consistently throughout the document)
- 161     • Fixed digit alignment in tables
- 162     • Some typo/spelling corrections (e.g. consistently spell as ‘cross-section’)
- 163     • Pre-fit and post-fit plots updated with latest plotting style (from CONF note draft)

## 164 Changes in v0.8 (17 September 2019)

- 165     • Plot updates requested during circulation (both pre-fit/post-fit and differential measurements)
- 166     • Harmonisation of plotting styles (label sizes etc.)
- 167     • Ranking plot for fit on data added
- 168     • Table with pre-fit yields with all stat+syst. uncertainties added (split in years)
- 169     • Updated uncertainties on  $C$ , now evaluating ISR/FSR and scale relative to the  $C$  value obtained in  
 170       the nominal  $t\bar{t}\gamma$  AFII (this reduced the uncertainties)
- 171     • Updated systematic breakdown table: now luminosity is listed as separate category

## 172 Changes in v0.7 (7 September 2019)

- 173 • Added MadGraph+HERWIG7 to the unfolded normalised cross-section plots and added a 2nd ratio to  
174 compare shape difference between MC and theory (comment during Top-approval).
- 175 • Zoomed in decomposed systematics plots (comment during Top-approval).
- 176 • Merged last 2 bins of  $\Delta R(\text{lepton}, \gamma)$  (comment during Top-approval).
- 177 • Added cross-section tables for absolute (including the sum over all bins) and normalized unfolded  
178 data (comment during Top-approval).
- 179 • Added Chi2 test between unfolded data and theory NLO and between unfolded data and MC  
180 (comment during Top-approval).
- 181 • Added Chi2 test for the closure study (comment during Top-approval).

## 182 Changes in v0.6 (28 August 2019)

- 183 • Pre-fit plots, yield tables, Asimov and data fit results updated with latest processing of ntuples
- 184 • Fixed asymmetries in  $t\bar{t}$  uncertainties
- 185 • Acceptance effects of all  $t\bar{t}\gamma$  uncertainties now estimated from correction factor  $C$ . This now goes  
186 into the inclusive measurement as a separate uncertainty, shape component is treated as before.
- 187 • Consistent symmetrisation applied to scale uncertainties
- 188 • Results for inclusive cross-section updated: now includes value for fiducial cross-section including  
189 breakdown of systematics, and post-fit distribution of  $S_T$
- 190 • Changed fiducial phase space definition: follow recommendation from M. Worek and define fiducial  
191 phase space on parton level as LO ME+PS to be compared to NLO ME theory.
- 192 • Chapter 5 (xsec definition): updated purity distributions, and correction efficiency and acceptance  
193 plots with the changed fiducial phase space definition.
- 194 • Chapter 8 (unfolding): updated all studies with the changed fiducial phase space defintion.
- 195 • Updated results with the changed fiducial phase space defintion.
- 196 • Comparison with NLO theory prediction (comment during pre-approval).
- 197 • Added PDF variations of signal added to diff. xsec results.

198 **Changes in v0.5 (22 August 2019)**

199 **General changes:**

- 200 • Ntuples updated to v7.0, which fixes a bug with the photon isolation efficiency scale factors. The  
201 new version also updates to AnalysisTop 21.2.85, which fixes several bugs in the b-tagging scale  
202 factors (MC/MC scale factors and c-tagging scale factors).
- 203 • Pre-fit plots, yield tables, Asimov and data fit results updated accordingly.
- 204 • Description of dedicated  $tW\gamma$  sample added in Chapter 2. Studies were done to compare this against  
205 the inclusive Wt+PS samples, as documented in Appendix B. For  $tW\gamma$ , we also apply a reweighting  
206 procedure documented in the same appendix.
- 207 • Calculations of efficiency, outside migration and correction factor  $C$  added, including systematic  
208 uncertainties originating from scale and PDF variations.
- 209 • All orange to-do boxes resolved.
- 210 • Evaluation of the  $t\bar{t}\gamma$  PDF shape systematics added. The variations were checked in individual fit  
211 scenarios, and their overall impact on the  $t\bar{t}\gamma$  signal strength was measured. The effect turned out to  
212 be negligible as expected.

213 **Chapter 5: Cross-section definition and fit strategy**

- 214 • Changed b-quark definition at parton level, which were selected as post-FSR and not before FSR as  
215 written in the INT (bug fixed), leptons and photons are before-FSR. Updated accordingly normalized  
216 bin-by-bin migration matrices, and correction efficiency and acceptance plots. Bin-by-bin migration  
217 matrices are also reweighted with the usual scale factor, pile-up, etc. weights before being normalized.

218 **Chapter 8: Unfolding studies**

- 219 • Updated all plots so that parton definitions are consistent.
- 220 • Use two iterations instead of one as the regularization parameter for all the tests (comment during  
221 pre-app).
- 222 • Added missing stress test for  $|\Delta\eta(\ell, \ell)|$ .

223 **Chapter 9: Results (Section 9.2)**

- 224 • Updated results with the definition at parton level.
- 225 • Use 2 iterations for unfolding results (comment during pre-app).
- 226 • Added results for  $\Delta\eta(1,1)$ .
- 227 • *Other  $t\bar{t}\gamma$*  background subtracted by applying a signal fraction factor to the (Data-Bkg) where the  
228 factor is the ratio of  $t\bar{t}\gamma$   $e\mu$  to all  $t\bar{t}\gamma$ . Thus, the results are insensitive to the normalisation  $t\bar{t}\gamma$ .
- 229 •  $tW\gamma$  is considered as background and hence subtracted from data while the migration matrix used  
230 for the unfolding is built only using  $t\bar{t}\gamma$ .
- 231 • Added  $tW\gamma$  modeling following the same treatment as in the inclusive measurement, added all signal  
232 modeling, i.e.,  $t\bar{t}\gamma$  modeling (except PDFs).

**233 Changes in v0.4 (11 July 2019)**

**234 General change:** update of ntuples from version 3.1 to 5.0 with many technical changes and updates:

- 235** • AnalysisTop version updated from 21.2.60 to 21.2.77
- 236** • Updated photon isolation efficiency
- 237** • Updated small-R JER uncertainties
- 238** • Updated categorisation of photons into prompt/fake
- 239** • New muon isolation working point: FCTight\_FixedRad (before was Gradient)

**240 Chapter 2 (Simulation):** as requested, we tried to add a plot with the photon pT spectrum on truth level.  
**241** Currently only added as placeholder, because that plot would require changes in the implementation of the  
**242** truth level in the ntuples, and a reprocessing.

**243 Chapter 4: Event selection**

- 244** • Clarified statements about inclusion of fake scale factors
- 245** •  $t\bar{t}\gamma$  now split into  $t\bar{t}\gamma e\mu$  and Other  $t\bar{t}\gamma$  based on the W decays on truth level. This was done to be in sync with the theory paper which only predicts the cross-section for the  $e\mu$  final state.
- 247** • Yield tables and stat-only controlplots updated accordingly

**248 Chapter 6: Systematics**

- 249** •  $t\bar{t}\gamma$  radiation systematics added (Pythia's var3c tune)
- 250** • Revised treatment of ttbar modelling systematics: use them as shape only, because both categories  
**251** (h-fake and prompt y) already have a global uncertainty of 50% assigned. Amplify this shape by a  
**252** factor 3 to overcome statistical limitations of the variations. This is supported by additional studies.
- 253** • Less rigid pruning thresholds chosen to keep approximately 50% of systematics both for shape and  
**254** normalisation effects. The pruning thresholds are chosen based on additional studies presented in  
**255** Appendix E.
- 256** • Table added for smoothing and symmetrisation applied to the systematics.
- 257** • Revised and optimised smoothing thresholds for modelling systematics.
- 258** • All red/blue systematics plots updated with latest ntuples

**259 Chapter 7 (Pre-fit and Asimov):** all plots updated with latest ntuples and changes in systematics

**260 Chapter 8 (Unfolding):**

- 261** • Binning optimisation for all variables.
- 262** • Stress tests included.

**263 Chapter 9 (Results):**

- 264** • All plots for the fiducial measurement updated with latest ntuples and changes in systematics.
- 265** • Systematic uncertainties for differential measurement: experimental and background included

- 266 • Absolute and normalized differential cross-sections reported.

[Not reviewed, for internal circulation only]

## 267 1 Introduction

268 The study of the top quark is one of the major fields in modern particle physics. Due to its heavy mass and  
 269 short life time, the top quark plays an important role in the Standard Model, and is a good candidate to  
 270 interact with new physics in many Beyond Standard Model theories. Precise measurements of its properties  
 271 are therefore pivotal, and have been subject of many analyses, as for example summarised in Ref. [2]. In  
 272 particular, the electroweak coupling of the top quark with the photon,  $t\bar{t}\gamma$ , can be affected through anomalous  
 273 dipole moments [3–8]. One of the processes to give access to the top quark-photon coupling is top-quark  
 274 pair production in association with a photon, or  $t\bar{t}\gamma$  production.

275 First evidence of  $t\bar{t}\gamma$  production was seen by the CDF collaboration at the Tevatron [9], and since then,  
 276 several  $t\bar{t}\gamma$  cross-section measurements have been performed at the LHC. A summary of previous results is  
 277 given in Table 1.

278 The  $t\bar{t}\gamma$  final state is similar to that of top-quark pair production, but contains an additional prompt photon.  
 279 The photon in this final state, however, can have various origins. First, it can be the result of initial-state  
 280 radiation (ISR), that is, it is radiated by an initial parton. ISR photons do not occur when the top-quark pair  
 281 is produced via gluon-gluon fusion, but only through production via quark-antiquark annihilation. Second,  
 282 it can radiate by one of the two top quarks directly, which is the relevant contribution for studying the  
 283 top-photon coupling. Third, it can be produced through final-state radiation (FSR), that is, it is radiated by  
 284 one of the decay products of the top quark: the  $W$ -boson, the  $b$ -quark or the subsequent decay products of  
 285 the  $W$ -boson.

286 Theoretical NLO cross-section calculations have been performed considering the unstable-top-quark  
 287 hypothesis, therefore including the latter case [16]. Some representative Feynman diagrams for the photon  
 288 radiated during top production and during top decay are shown in Figure 1 and Figure 2, respectively. For  
 289 this analysis, top-quark pair production with an additional photons from any of the three sources described

Table 1: Previous measurements of the  $t\bar{t}\gamma$  cross-section. If not splitted, the uncertainties is the combined uncertainties. Otherwise, the keywords *sy*, *st*, *lu*, *sc* and *pdf* stands for, respectively, the uncertainty due to systematical uncertainties, statistical uncertainties, luminosity, scale and PDF. The last-but-one column is the relative combined uncertainty of the observed result.

$\mathcal{L}$ [fb $^{-1}$ ]	Measurement	$p_T^{\min}$ [GeV]	Theory [fb]	Observed result [fb]	Unc. [%]	Ref.
Tevatron ( $p\bar{p}$ ), CDF, 1.96 TeV						
6.0	inclusive	10	$170 \pm 30$	$180 \pm 70(\text{st}) \pm 40(\text{sy}) \pm 10(\text{lu})$	45	[9]
LHC ( $p\bar{p}$ ), ATLAS, 7 TeV						
1.04	inclusive non-all-hadronic	8	$2100 \pm 400$	$2000 \pm 500(\text{st}) \pm 700(\text{sy})$	43.0	[10]
4.59	fiducial $\ell$ +jets	20	$48000 \pm 10000$	$63000 \pm 8000(\text{st})^{+17000}_{-13000}(\text{sy})$	27.0	[11]
LHC ( $p\bar{p}$ ), CMS, 8 TeV						
19.7	inclusive $\mu$ +jets	20	$1800 \pm 500$	$2400 \pm 200(\text{st}) \pm 600(\text{sy})$	26.3	[12]
19.7	inclusive $\ell$ +jets	25	$591 \pm 71(\text{sc}) \pm 30(\text{pdf})$	$515 \pm 108$	21.0	[13]
19.7	fiducial $\ell$ +jets	25	-	$127 \pm 27$	21.2	[13]
LHC ( $p\bar{p}$ ), ATLAS, 8 TeV						
20.2	fiducial $\ell$ +jets	15	$151 \pm 24$	$139 \pm 7(\text{st}) \pm 17(\text{sy})$	13.2	[14]
20.2	differential $\ell$ +jets	15	-	-	-	[14]
LHC ( $p\bar{p}$ ), ATLAS, 13 TeV						
36.1	fiducial $\ell$ +jets	20	$495 \pm 99$	$521 \pm 9(\text{st}) \pm 41(\text{sy})$	8.0	[15]
36.1	fiducial dilepton	20	$63 \pm 9$	$69 \pm 3(\text{st}) \pm 4(\text{sy})$	7.2	[15]
36.1	differential $\ell$ +jets, dilepton	20	-	-	-	[15]

above is considered signal. However, selections are applied to reduce contributions by photons from top decays, and to enhance contributions which include the top-photon coupling.

The strategy is to select a final state of  $t\bar{t}$ , and request the presence of a photon. The full data set collected during the Run 2 data-taking period between 2015 and 2018 is employed to perform the measurements, corresponding to an integrated luminosity of  $139 \text{ fb}^{-1}$ .

The final state considered is the  $e\mu$  channel, excluding electrons and muons from possible leptonic decays of  $\tau$ -leptons. These are not considered as part of the signal to compare to the latest NLO  $t\bar{t}\gamma$  calculation in Ref. [1] which only considers the decay of  $W$  bosons to electrons and muons as final state. The calculation constitutes the first full computation for top quark pair production with a final state photon in hadronic collisions at NLO in QCD and includes all resonant and non-resonant diagrams, interferences, and off-shell effects of the top quarks and the  $W$  bosons. To be in accordance with the theory prediction, leading-order simulations in QCD of  $t\bar{t}\gamma$  and  $tW\gamma$  are combined and measured simultaneously as these two processes overlap at next-to-leading or higher orders in QCD. The inclusive and differential cross-sections are extracted. The differential cross-sections are presented as a function of the photon transverse momentum, the photon pseudo-rapidity, as well as angular variables related to the photon and the leptons and b-jets in the event. An unfolding procedure is performed, and the results are compared with the theoretical prediction.

Compared to the previous  $t\bar{t}\gamma$  ATLAS analysis with 13 TeV data no multivariate analysis techniques to separate signal and background processes are applied owing to the clean final state in the  $e\mu$  channel. Additionally, the differential cross-section are measured at parton level instead of at particle level to compare to the theory calculation in Ref. [1].

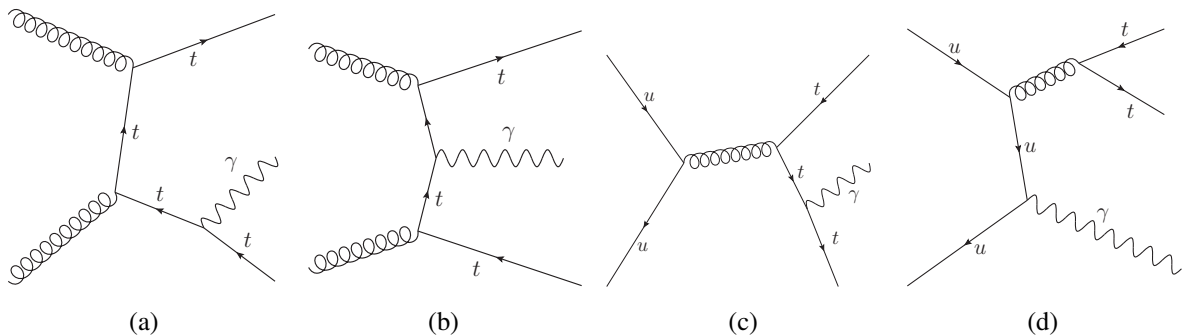


Figure 1: Feynman diagrams of  $t\bar{t}\gamma$  production where the photon is radiated during production (a, b, c) and radiated from initial partons (d).

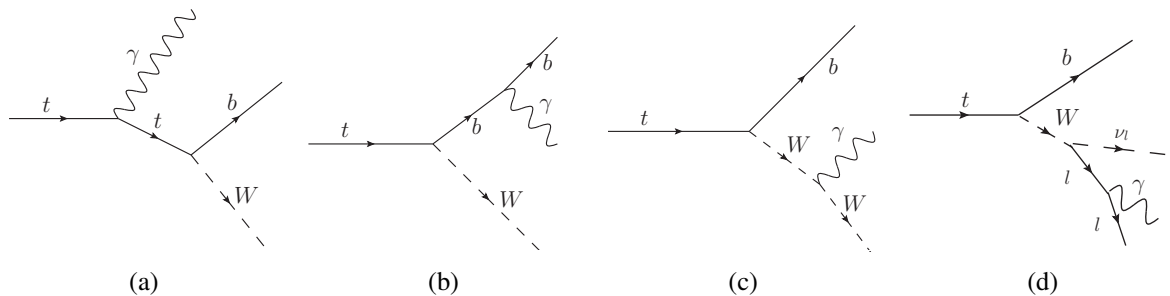


Figure 2: Feynman diagrams of  $t\bar{t}\gamma$  production where the photon is radiated during top-quark decay.

311 The note is organised as follows. Section 2 provides a brief introduction to the ATLAS detector. Section 3  
312 contains the description of the simulated samples used for the analysis. This also includes explanations  
313 of sample-overlap removal procedures and categorisation of photons in events. Section 4 details the  
314 used ATLAS data, describes the definition of physics objects and the definition of the  $e\mu$  signal region.  
315 Section 5 describes the definition and the procedure to obtain the inclusive and the differential cross-section  
316 measurement. The systematic uncertainties are presented in Section 6. Section 7 presents the pre-fit  
317 distributions and the Asimov tests performed for the inclusive cross-sections and Section 8 describes the  
318 unfolding procedure and the tests carried out. Finally, Section 9 summarises the results of the analysis.  
319 The conclusions are presented in Section 10.

320 Background studies and additional information are documented in various appendices. Appendix A  
321 summarises studies where  $Wt+PS$  versus  $tW\gamma$  simulations were compared. These comparisons were  
322 done to decide which of the two simulations yields the more accurate description of  $tW\gamma$ . Studies how  
323 largely  $tW\gamma$  contributes to the fiducial phase space are summarised in Appendix B. A list of all used  
324 Monte-Carlo samples is given in Appendix C. Appendix D documents background studies performed to  
325 estimate the contribution of hadron fakes. As a cross-check, a  $t\bar{t}\gamma$ -only measurement was performed where  
326  $tW\gamma$  processes are treated as background. These additional measurements are summarised in Appendix E.  
327 To find the optimal setup, fit benchmarks were performed, documented in detail in Appendix G. In addition,  
328 various pruning thresholds for systematic uncertainties were tested, as shown in Appendix H.

## 329 2 The ATLAS detector

330 ATLAS [17–19] is a multipurpose detector with a forward–backward symmetric cylindrical geometry with  
 331 respect to the LHC beam axis.<sup>1</sup> The innermost layers consist of tracking detectors in the pseudorapidity  
 332 range  $|\eta| < 2.5$ . The high-granularity silicon pixel detector covers the vertex region and typically provides  
 333 four measurements per track, the first hit being normally in the insertable B-layer (IBL) installed before  
 334 Run 2 [18, 19]. This inner detector (ID) is surrounded by a thin superconducting solenoid that provides a  
 335 2 T axial magnetic field. It is enclosed by the electromagnetic and hadronic calorimeters, which cover  
 336  $|\eta| < 4.9$ . The outermost layers of ATLAS consist of an external muon spectrometer (MS) within  $|\eta| < 2.7$ ,  
 337 incorporating three large toroidal magnetic assemblies with eight coils each. The field integral of the  
 338 toroids ranges between 2.0 and 6.0 Tm for most of the acceptance. The MS includes precision tracking  
 339 chambers and fast detectors for triggering. A two-level trigger system [20] reduces the recorded event rate  
 340 to an average of 1 kHz.

---

<sup>1</sup> ATLAS uses a right-handed coordinate system with its origin at the nominal interaction point (IP) in the centre of the detector and the  $z$ -axis along the beam pipe. The  $x$ -axis points from the IP to the centre of the LHC ring, and the  $y$ -axis points upwards. Cylindrical coordinates  $(r, \phi)$  are used in the transverse plane,  $\phi$  being the azimuthal angle around the  $z$ -axis. The pseudorapidity is defined in terms of the polar angle  $\theta$  as  $\eta = -\ln \tan(\theta/2)$ . Angular distance is measured in units of  $\Delta R \equiv \sqrt{(\Delta\eta)^2 + (\Delta\phi)^2}$ .

### 341 3 Simulation of signal and background

342 Monte-Carlo-generated simulated data is used to estimate contributions from the signal and various  
 343 background processes. After event generation, the response of the ATLAS detector to these Monte-Carlo  
 344 samples is simulated [21] with the GEANT4 tool [22]. As a full simulation of the detector response  
 345 is computationally expensive, for some of the estimates of modelling uncertainties, the fast-simulation  
 346 package ATLFAST-II is used, which parametrises hadronic showers in the electromagnetic and hadronic  
 347 calorimeter to speed up simulation.

348 To account for additional  $pp$  interactions from the same bunch crossing, minimum-bias interactions  
 349 generated with PYTHIA 8 [23, 24] using the set of tuned parameters called A2 [25] and the Mstw2008LO  
 350 PDF set [26] are superimposed on the hard-scattering events. The Monte-Carlo-generated events are  
 351 then reweighted to match the pile-up conditions observed in data. For that, three different Monte-Carlo  
 352 subcampaigns, *mc16a*, *mc16d* and *mc16e*, are defined to reflect the data-taking conditions in 2015+16,  
 353 2017 and 2018, respectively. Events in the subcampaigns are produced with different generator seeds and  
 354 can, thus, be combined statistically to give a total prediction for the Run 2 data-taking period between 2015  
 355 and 2018.

356 This analysis uses both *dedicated* samples, where photons are included in the matrix-element-level  
 357 generation step, and *inclusive* samples, in which processes are generated on matrix-element level without  
 358 explicitly including a photon in the final state. Dedicated samples with a photon in the matrix element were  
 359 generated for the  $t\bar{t}\gamma$  final state, the  $tW\gamma$  final state and for  $V\gamma$  processes with additional jets. They are  
 360 described in more detail in Section 3.1. The used inclusive samples, as listed in Section 3.2, might, however,  
 361 still contain photons in the simulation as additional photon emission (irrespective of the generated process  
 362 in the matrix element) originating from the showering algorithms. The full list of all samples used in this  
 363 analysis is also given in Appendix C. To avoid possible double-counting of events, an overlap-removal  
 364 procedure is applied between dedicated and inclusive samples as detailed in Section 3.3.

365 To distinguish *prompt* photons from the hard scattering and non-prompt photons and other objects faking  
 366 photon signatures in the detector, truth information is used to identify the true source of all reconstructed  
 367 photons. The categorisation of reconstructed photons based on their truth information is described in  
 368 Section 3.4.

#### 369 3.1 Used dedicated samples

$t\bar{t}$  production in association with a photon on matrix-element level is simulated in a dedicated sample  
 using the MADGRAPH5\_aMC@NLO generator (v2.33) [27] and the NNPDF2.3LO PDF set [28] at leading  
 order in QCD. The matrix-element generation uses a filter to only produce events with at least one lepton.  
 The events are generated at LO accuracy as an inclusive, doubly-resonant  $2 \rightarrow 7$  process, that is, as e.g.  
 $pp \rightarrow q\bar{q}blvby$ , and, thus, include diagrams where the photon is radiated from the intermediate top quarks,  
 the  $b$ -quarks, the intermediate  $W$  bosons as well as the decay products of the  $W$  bosons. Although not  
 the dominant production mode, the final state can also be generated through quark-antiquark annihilation.  
 In that case, the  $2 \rightarrow 7$  process also includes photons radiated from the initial state (ISR). The event  
 generation is interfaced to PYTHIA8 (v8.212) using the A14 tune [29] and the NNPDF2.3LO PDF set to  
 model parton shower, hadronisation, fragmentation and underlying event. EvtGEN [30] is used to simulate

heavy-flavour decays, such as those of  $B$  and  $D$  hadrons. The renormalisation and factorisation scales are dynamic and correspond to half of the sum over all ‘transverse masses’ of all final-state particles:

$$\mu_R = \mu_F = \frac{1}{2} \sum_f \sqrt{m_f^2 + p_{T,f}^2}, \quad (1)$$

where  $f$  runs over all final-state particles, and  $m_f$  and  $p_{T,f}$  are the rest mass and the transverse momentum of particle  $f$ , respectively. To avoid infrared and collinear singularities due to the photon radiation, kinematic cuts are applied on matrix-element level. Photons and leptons are required to have minimal transverse momenta of 15 GeV, and their pseudo-rapidities must fulfil  $|\eta| < 5.0$ . In addition, the generated photons must not be in the vicinity of any other charged particles of the final state and at least be separated with  $\Delta R > 0.2$ .

Associated  $Wt$  production with an additional photon on matrix-element level is simulated in dedicated samples using **MADGRAPH5\_aMC@NLO** and the **NNPDF2.3LO** PDF set at leading order in QCD. One set of events is generated as a  $2 \rightarrow 3$  process in the five-flavour scheme and assumes a stable top quark. Hence, only diagrams where the photon is radiated from the initial state and radiative  $Wt$  production are considered. A second set of events is generated as a  $2 \rightarrow 6$  process in the five-flavour scheme, where the top quark and  $W$  boson are decayed and the photon is radiated during or after those decays. Hence, only diagrams are considered where the photon originates from the decaying top quark, the decaying  $W$  boson or from any of the charged decay products. The two sets of events are complementary and, once combined, provide a full simulation of the  $tW\gamma$  process. In both cases, the matrix-element generator is interfaced to **PYTHIA8** (v8.212), which uses the **A14** tune and the **NNPDF2.3LO** PDF set. **EVTGEN** is used to simulate heavy-flavour decays. During the matrix-element generation step, the photons are required to have minimal transverse momenta of 15 GeV, and their pseudo-rapidities must fulfil  $|\eta| < 5.0$ . At NLO, the  $tW\gamma$  process interferes with the  $t\bar{t}\gamma$  signal process when including the spectator  $b$ -quark and contributes to the off-shell part of the signal. To be in accordance with the fixed-order NLO theory calculation in Ref. [1], the leading-order  $t\bar{t}\gamma$  and  $tW\gamma$  simulations are combined and treated as a single signal process. However, since the used  $tW\gamma$  simulation is generated in the five-flavour scheme and at leading order without the spectator  $b$ -quark, the interference effects cannot be calculated. This means that acceptance, efficiency and migration cannot be estimated accurately with the available  $tW\gamma$  simulation. For this reason, a second fit scenario with a  $t\bar{t}\gamma$ -only signal is documented in detail in Appendix E. In that measurement scenario,  $tW\gamma$  is treated as a background contribution, although a small part of what is defined as signal in the theoretical cross-section calculation for the  $pp \rightarrow bWbW\gamma$  process from Ref. [1] is missing. Additional studies of the  $tW\gamma$  contribution to the fiducial region are also summarised in Appendix B.

Events with  $W\gamma$  and  $Z\gamma$  final states (with additional jets) are simulated in dedicated samples.  $W\gamma$  processes are simulated with **SHERPA 2.2.2** [31, 32] at next-to-leading order in QCD using the **NNPDF3.0NNLO** PDF set, whereas  $Z\gamma$  events are generated with **SHERPA 2.2.4** at leading order in QCD. The samples are normalised to the cross-sections given by the corresponding Monte Carlo simulation. The simulation includes all steps of the event generation, from the hard process to the observable particles. All samples are matched and merged to the **SHERPA**-internal parton showering based on Catani-Seymour dipoles [33, 34] using the **MEPS@NLO** prescription [35–37]. Virtual corrections for the next-to-leading order accuracy in QCD in the matrix element are provided by the **OpenLoops** library [38, 39].

### 406 3.2 Used inclusive samples

407 Inclusive  $t\bar{t}$  production processes are simulated on matrix-element level at next-to-leading order in QCD  
 408 using PowHEG-Box-v2 [40–42]. The matrix-element generator is interfaced to PYTHIA8 (v8.230) to  
 409 simulate parton shower, hadronisation, fragmentation and the underlying event. Heavy-flavour decays are  
 410 modelled with EvtGEN. The matrix-element calculation uses the NNPDF3.0NLO PDF set [43], with  
 411 the top-quark mass fixed to 172.5 GeV. The internal parameter  $h_{\text{damp}}$  to control the probability for gluon  
 412 emission is set to 1.5 times the top-quark mass following ATLAS standards. The showering in PYTHIA  
 413 uses the A14 tune in conjunction with the NNPDF2.3LO PDF set. By applying a  $k$ -factor, the events are  
 414 normalised to a cross-section value calculated with the Top++2.0 programme at next-to-next-to-leading  
 415 order in perturbative QCD, including soft-gluon resummation to next-to-next-to-leading-log order (see [44]  
 416 and references therein), again assuming a top-quark mass of 172.5 GeV. The resulting cross-section for  $t\bar{t}$   
 417 production at  $\sqrt{s} = 13$  TeV amounts to  $\sigma_{t\bar{t}} = 831.76$  pb with remaining theoretical scale uncertainties of  
 418 approximately 3%.

419 Single-top-quark processes are modelled separately for three possible production modes, namely  $s$ -channel,  
 420  $t$ -channel and  $Wt$  production, each of which are generated separately for top-quark and anti-top-quark  
 421 production. The three production modes are simulated on matrix-element level at next-to-leading order in  
 422 QCD with PowHEG-Box and the NNPDF2.3LO PDF set. The matrix-element generator is interfaced to  
 423 PYTHIA8 (v8.???) with the A14 tune as before. Again, heavy-flavour decays are modelled with EvtGEN.  
 424 The sample cross-sections are normalised to next-to-next-to-leading-order precision using  $k$ -factors [45–47].  
 425 For the  $Wt$  production samples, the *diagram removal scheme* is implemented to remove higher-order  
 426 interference effects between  $t\bar{t}$  and  $Wt$  production.

427 Events with  $W$  and  $Z$  bosons in association with additional jets are simulated with SHERPA 2.2.1 at  
 428 next-to-leading order in QCD. The simulation includes the hard-scattering event as well as hadronisation.  
 429 The NNPDF3.0NLO PDF set is used in conjunction with a dedicated tune provided by the SHERPA authors.  
 430 The samples are normalised to the next-to-next-to-leading-order cross-section in QCD [48].

431 Events with two vector bosons, that is  $WW$ ,  $WZ$  and  $ZZ$ , are generated with SHERPA versions 2.2.2 (purely  
 432 leptonic decays) and 2.2.1 (all others) at leading order in QCD. The NNPDF3.0NNLO PDF set is used  
 433 in conjunction with a dedicated tune provided by the SHERPA authors. The samples are normalised to  
 434 next-to-leading order cross-sections in QCD [49].

435 Events with a  $t\bar{t}$  pair and an associated  $W$  or  $Z$  boson ( $t\bar{t}V$ ) are simulated at next-to-leading order in  
 436 QCD on matrix-element level with MADGRAPH5\_aMC@NLO using the NNPDF3.0NLO PDF set. The  
 437 matrix-element generator is interfaced to PYTHIA8 (v8.210), for which the A14 tune is used in conjunction  
 438 with the NNPDF2.3LO PDF set. The samples are normalised to next-to-leading order in both QCD and  
 439 electroweak theory [50].

### 440 3.3 Sample-overlap removal procedure

441 Because events with photons outside the kinematic requirements of the dedicated  $X\gamma$  samples are not  
 442 simulated in these samples, they are to be taken from the inclusive  $X$  samples. Although no photons are  
 443 generated on matrix-element level in the inclusive samples, radiation of extra photons is still accounted  
 444 for by the showering algorithm. This includes simulation of photon radiation from both initial-state and  
 445 final-state objects. For example, if inclusive  $t\bar{t}$  production is generated in the matrix element including  
 446 decays of the top quarks and  $W$  bosons, the simulation of the parton shower includes radiative photons

from any of the charged final-state products, such as leptons from the  $W$  boson decay. If that particular  $t\bar{t}$  event was simulated through quark-antiquark annihilation, radiative photons may also arise from the quarks in the initial state. Hence, events in inclusive samples, where a photon was generated by the showering algorithm, pose a danger of double-counting if a dedicated sample is used simultaneously.

As a consequence, a sample-overlap removal procedure is performed between inclusive  $X$  and dedicated  $X\gamma$  samples. In particular, the removal procedure is applied for simulations of  $t\bar{t}$  and  $t\bar{t}\gamma$  events, for  $W+jets$  and  $W\gamma$  events, and for  $Z+jets$  and  $Z\gamma$  events. The recipe for the removal is (1) to accept all events from the  $X\gamma$  samples, since the photon radiation simulated on matrix-element level comes with higher accuracy than the radiation accounted for in the showering algorithm. In addition, the generated number of events for phase-space areas covered by both inclusive and dedicated samples is by far larger for the latter. And (2) to remove events from the  $X$  samples if they overlap with the  $X\gamma$  simulation. However, removing *all* events with radiative photons from the  $X$  samples would be too strict as the  $X\gamma$  samples apply cuts on the kinematics of the matrix-element photon.

The sample-overlap removal procedure is implemented with the central algorithm *VGammaORTTool*<sup>2</sup>. The algorithm is initialised with a definition of the overlap region, which corresponds to the set of cuts applied to the  $X\gamma$  samples on matrix-element level. For all three overlapping sample types, these cuts are:

- 463 1.  $p_T(\gamma) > 15 \text{ GeV}$  and
- 464 2.  $\Delta R(\ell, \gamma) > 0.2$ .

465 where  $\Delta R := \sqrt{\Delta\phi^2 + \Delta\eta^2}$  in the ATLAS coordinate system. To check whether an event falls into the  
466 overlap region defined by the above cuts, the algorithm first compiles candidate lists to find all photons and  
467 leptons generated on matrix-element level. Photons get added to the candidate list if they fulfil all of the  
468 following criteria:

- 469 1. PDG ID = 22, i.e. the particle truly is a photon.
- 470 2. Status = 1 to only consider stable final-state particles.
- 471 3.  $p_T > 3 \text{ GeV}$ .
- 472 4. Barcode < 100 000 to only consider primary particles from the generator and not from the detector  
473 simulation.
- 474 5. *MCTruthClassifier*::origin  $\notin [23, 35]$ , that is, no photons originating from baryons or mesons, and  
475 neither 9 (photons from  $\tau$ -leptons) nor 42 (photons from  $\pi^0$ ).

476 In particular the last two criteria ensure that the photon does not originate from interaction with the detector  
477 and/or hadronic activity. For the last point *MCTruthClassifier* information provided by the central ATLAS  
478 software is used<sup>3</sup>. Leptons get added to the candidate list if they fulfil all of the following criteria:

- 479 1. PDG ID =  $\pm 11$  (electron),  $\pm 13$  (muon),  $\pm 15$  ( $\tau$ -lepton).
- 480 2. barcode < 100 000.
- 481 3. If  $\tau$ -lepton, none of the children must be a  $\tau$ -lepton. This ensures to only consider  $\tau$ -leptons before  
482 decays.
- 483 4. If electron or muon, its parent particle must not be a  $\tau$ -lepton. In addition, require status = 1.

<sup>2</sup> <https://twiki.cern.ch/twiki/bin/viewauth/AtlasProtected/VGammaORTTool>

<sup>3</sup> <https://twiki.cern.ch/twiki/bin/view/AtlasProtected/MCTruthClassifier>

484     5. `MCTruthClassifier::origin`  $\notin [23, 42]$ , that is, no photons from a hadron or any kind of radiated  
 485       photon, and  $\notin [5, 9]$  (from photon conversion or  $\tau$ -lepton) and not 3 (single photon).

486     After the lists are compiled, all photon candidates are checked against the above  $p_T(\gamma) > 15 \text{ GeV}$  criterion.  
 487     For the remaining photon candidates,  $\Delta R(\ell, \gamma) > 0.2$  is tested with all electron candidates, and the photon  
 488       candidate is discarded as soon as it overlaps with one electron candidate. If any of the photon candidates of  
 489       the event pass both  $p_T$  and  $\Delta R$  requirement, the event is considered to *fall into the overlap region*. Events  
 490       from inclusive  $X$  samples, that is,  $t\bar{t}$ ,  $W+\text{jets}$  and  $Z+\text{jets}$ , are *vetoed* if they fall into the overlap region.

### 491     3.4 Categorisation of photons

492     The main interest of this analysis are  $t\bar{t}$  events where an additional photon is generated in the hard-scattering  
 493       event, also called a *prompt* photon. However, photons can occur at many other stages of what is being  
 494       recorded as an ‘event’ with the ATLAS detector. In addition, other particles and activities in the detector may  
 495       fake photon signatures and be identified as such. Among the photon candidates detected and reconstructed  
 496       with the ATLAS detector, this analysis distinguishes three classes:

- 497       1. Prompt photons originating from the hard-scattering event.
- 498       2. Electron-fake photons, in the following denoted as *e-fake photons*, which are electrons faking a  
     499        photon signature in the calorimeter.
- 500       3. Hadron-fake photons, in the following denoted as *h-fake photons*, which are non-prompt photons  
     501        originating from hadrons, for example from  $\pi^0 \rightarrow \gamma\gamma$  decays. This category *also* includes photon  
     502        signatures faked by hadronic energy depositions in the calorimeter.

503     To assess and estimate contributions to these three classes in simulation, *MCTruthClassifier* information  
 504       is used to identify the origin of a reconstructed photon candidate. For this, the `xAOD::TruthHelpers`  
 505       class is used to retrieve the truth object  $\gamma_{\text{truth}}^{\text{cand}}$  associated to the photon candidate. Then, according to the  
 506       *MCTruthClassifier::origin* and *MCTruthClassifier::truth* values of that truth object, the photon candidate  
 507       is classified into one of the three categories above. To classify a candidate as e-fake photon, *any* of the  
 508       following criteria must be fulfilled:

- 509       • PDG ID =  $\pm 11$  (electron)
- 510       •  $\Delta R(\gamma_{\text{truth}}^{\text{cand}}, e_{\text{truth}}) < 0.1$ , where  $e$  denotes a truth electron. Similar to Section 3.3, a list of truth  
     511        electrons is compiled and  $\gamma_{\text{truth}}^{\text{cand}}$  must not overlap with any of them. The truth-electron criteria are:

- 512       1. PDG ID =  $\pm 11$
- 513       2.  $p_T > 10 \text{ GeV}$
- 514       3.  $|\eta| < 3.0$
- 515       4. barcode < 100 000

516     To avoid any possible double-classification, all photon candidates that match either of the two above e-fake  
 517       photon criteria, are categorised as such and *not examined further*. For all remaining candidates, if  $\gamma_{\text{truth}}^{\text{cand}}$   
 518       meets any of the following criteria, the candidate is classified as h-fake photon:

- 519       • `MCTruthClassifier::type` = 16 and `MCTruthClassifier::origin`  $\in [23, 35]$ . These are photons of type  
     520        *background photon* originating from baryons or mesons.

- 521     • MCTruthClassifier::type = 16 and MCTruthClassifier::origin = 42. These are photons of type  
 522     *background photon* originating from  $\pi^0 \rightarrow \gamma\gamma$  decays.
- 523     • MCTruthClassifier::type = 17, corresponding to hadronic energy deposition.
- 524     If the photon candidate classifies as neither e-fake photon nor h-fake photon, it is treated as prompt.

525     **3.5 Contribution of pile-up photons**

526     It can happen that a hard  $t\bar{t}$  event occurs together with a pile-up event that radiates a hard photon, which  
 527     should be treated as background. Unlike single  $pp$  interaction events, in these pile-up events, the correlation  
 528     between the  $z$  coordinates of the primary vertex and of the pile-up photon is lost. Thus the significance of  
 529     the  $z$  difference between the primary vertex and the photon, which is defined as  $(z_\gamma - z_{PV})/\delta z_\gamma$ , will be  
 530     broader for these events than in single  $pp$  events. Figure 3 shows the shape comparison of this significance  
 531     between the  $t\bar{t}\gamma$  MC and data. There is no visible difference between the two (whether the photon is  
 532     converted or not). Thus, we conclude that pile-up photon contribution is either negligible or well simulated  
 533     by MC.

Not reviewed, for internal circulation only

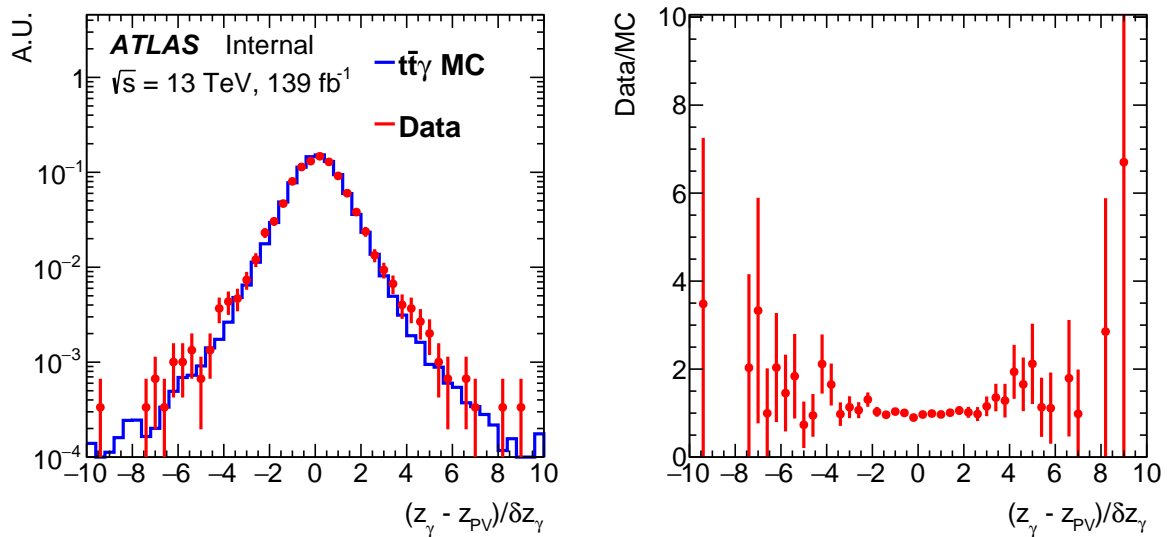


Figure 3: The shape comparison of the  $z$  difference between the primary vertex and the photon for the  $t\bar{t}\gamma$  MC and data.

## 534 4 Event selection

535 The data used in this analysis was recorded during Run 2 of the LHC with the ATLAS detector between  
 536 2015 and 2018 at a centre-of-mass energy of 13 TeV. The dataset corresponds to an integrated luminosity  
 537 of  $138.97 \text{ fb}^{-1}$  for the full Run 2 period, with individual integrated luminosity values as listed in Table 2.  
 538 The uncertainty in the combined 2015–2018 integrated luminosity is  $\pm 1.7\%$  [51], obtained using the  
 539 LUCID-2 detector [52] for the primary luminosity measurements. Only data-taking periods, where the  
 540 ATLAS detector was fully operational and the recorded data satisfies quality criteria, were considered. These  
 541 data-taking periods are defined in *good-run lists*, also listed in Table 2.

542 Both data and Monte-Carlo simulation samples are processed with the top analysis group software  
 543 AnalysisTop<sup>4</sup> in its versions 21.2.85 and 21.2.87. The data is stored in flattened ntuples with a dedicated  
 544  $t\bar{t}\gamma$  ntuple production package<sup>5</sup> in its version 7.2.

### 545 4.1 Definition of objects

546 The main physics objects considered in this analysis are electrons, muons, jets,  $b$ -jets, missing transverse  
 547 energy and photons. The reconstruction of those objects follows the standard methods in ATLAS.  
 548 Recommended corrections and calibrations are applied, using AnalysisTop in the version mentioned above.  
 549 The object definitions of leptons, jets,  $b$ -jets and missing transverse momentum are chosen to be as close  
 550 as possible to the ones of the usual  $t\bar{t}$  analyses like the dilepton cross-section measurement in Ref. [53].  
 551 Identification criteria for leptons and  $b$ -jets are chosen to be slightly looser to enhance signal statistics. The  
 552 photon reconstruction, identification and selection criteria follow the definition of photons optimised in the  
 553 previous ATLAS analysis at 13 TeV (cf. Ref. [15]).

554 The electrons are reconstructed from energy deposits in the central region of the electromagnetic calorimeters  
 555 associated with reconstructed tracks from the ID system, and are required to satisfy the *TightLH* identification  
 556 criteria [54] and the *Gradient* isolation criteria. Scale factors based on comparison between data and  
 557 MC are used to correct the simulation. Electrons are calibrated with the method described in Ref. [55].  
 558 Only electrons with calibrated  $p_T > 25 \text{ GeV}$  and  $|\eta_{\text{clus}}| < 2.47$ , excluding the calorimeter crack region  
 559  $1.37 < |\eta_{\text{clus}}| < 1.52$ , are considered.<sup>6</sup> The recommended requirements on the impact parameter variables  
 560 are also applied: the transverse impact parameter with respect to the beam line  $|d_0|/\sigma(d_0)$  is required to  
 561 be lower than 5 and the difference in the  $z$ -axis between the track origin and the primary vertex when  
 562 expressed at the beam line  $|\Delta z_0 \sin(\theta)|$  is required to be below 0.5 mm.

<sup>4</sup> <https://twiki.cern.ch/twiki/bin/viewauth/AtlasProtected/AnalysisTop21>

<sup>5</sup> <https://gitlab.cern.ch/TopProperties/TtGammaFullRun2/ttgamma-ntuple-production>

<sup>6</sup>  $\eta_{\text{clus}}$  denotes the pseudo-rapidity of the calorimeter cluster associated with the electron.

Table 2: Good-run lists used to define data taking period where the ATLAS detector was fully operational and the recorded data satisfies all quality criteria. The corresponding integrated luminosity values are listed as well.

Year	Good-run list	$\mathcal{L}_{\text{int}} [\text{fb}^{-1}]$
2015	data15_13TeV.periodAllYear_DetStatus-v89-pro21-02_[...].xml	3.22
2016	data16_13TeV.periodAllYear_DetStatus-v89-pro21-01_[...].xml	32.99
2017	data17_13TeV.periodAllYear_DetStatus-v99-pro22-01_[...].Triggerno17e33prim.xml	44.31
2018	data18_13TeV.periodAllYear_DetStatus-v102-pro22-04_[...].Triggerno17e33prim.xml	58.45

563 Muons are reconstructed with a combined algorithm, using the track segments in the various layers of the  
 564 muon spectrometer and the tracks in the ID system. They are required to have the *Medium* identification  
 565 quality criteria and the *FCTight\_FixedRad* isolation criteria. Scale factors based on comparison between  
 566 data and MC are used to correct the simulation. Only muons with calibrated  $p_T > 25 \text{ GeV}$  and  $|\eta| < 2.5$   
 567 are considered. The recommended requirements on the impact parameter variables are also applied:  
 568 the transverse impact parameter with respect to the beam line  $|d_0|/\sigma(d_0)$  is required to be lower than 3  
 569 and the difference in the  $z$ -axis between the track origin and the primary vertex when expressed at the  
 570 beam line  $|\Delta z_0 \sin(\theta)|$  is required to be below 0.5 mm. The reconstruction, identification, calibrations and  
 571 scale-factor-extraction methods are described in [56].

572 Photons are reconstructed from energy deposits in the central region of the electromagnetic calorimeters. If  
 573 the cluster is considered not matched to any reconstructed tracks in the ID system, an unconverted photon  
 574 candidate is reconstructed. If the cluster is matched with reconstructed tracks that are consistent with  
 575 originating from a photon conversion and if in addition a conversion vertex is reconstructed, a converted  
 576 photon candidate is reconstructed. Both kinds of photons are considered in this analysis. The photons are  
 577 required to satisfy the *Tight* identification criteria [57]. They are also required to be isolated, using the  
 578 *FixedCutTight* working point [57] defined as  $E_T^{\text{iso}}|_{\Delta R < 0.4} < 0.022 \cdot E_T(\gamma) + 2.45 \text{ GeV}$  in conjunction with  
 579  $p_T^{\text{iso}}|_{\Delta R < 0.2} < 0.05 \cdot E_T(\gamma)$ . In this case,  $E_T^{\text{iso}}$  refers to the calorimeter isolation within a cone of radius  
 580  $\Delta R < 0.4$  in the direction of the photon candidate, whereas  $p_T^{\text{iso}}$  is the track isolation within  $\Delta R < 0.2$ .  
 581 Photon energies are calibrated with the method described in Ref. [55]. Scale factors based on comparison  
 582 between data and MC are used to correct the simulation. Only photons with calibrated  $E_T > 20 \text{ GeV}$  and  
 583  $|\eta_{\text{clus}}| < 2.37$ , excluding the calorimeter crack region  $1.37 < |\eta_{\text{clus}}| < 1.52$ , are considered.

584 The jets are reconstructed using the anti- $k_t$  algorithm [58] in the FASTJET implementation [59] with a  
 585 distance parameter  $R = 0.4$  (in the  $\eta-\phi$  plane). Their reconstruction is done from topological calorimeter  
 586 clusters [60]. The jet-energy scale and jet-energy resolution are calibrated following Ref. [61]. The jets  
 587 are required to have  $p_T > 25 \text{ GeV}$  and  $|\eta| < 2.5$ . In order to reject jets from pile-up or other primary  
 588 vertices, jets are required to have a *Jet Vertex Tagger* (JVT) discriminant [62] larger than 0.59 for jets with  
 589  $p_T < 60 \text{ GeV}$  and  $|\eta| < 2.4$ . The JVT efficiency is corrected by a scale factor extracted from a comparison  
 590 of data and simulation.

591 The  $b$ -tagging algorithm to identify jets from  $b$ -quark hadronisation is the *MV2c10* algorithm [63], which is  
 592 based on a boosted decision tree (BDT) using the output weights of the *JetFitter*, *IP3D* and *SV1* algorithms  
 593 as input. In the event selection, the 85% working point is used. The flavour-tagging efficiencies of  $b$ -jets as  
 594 well as of  $c$ -jets and light jets are calibrated as described in Ref. [64], with rejection factors of about 2 and  
 595 30 for  $c$ -jets and light jets, respectively<sup>7</sup>.

596 The reconstructed missing transverse momentum  $E_T^{\text{miss}}$  [65] is computed as the negative vector sum over  
 597 all reconstructed, fully calibrated physics objects including photons and remaining unclustered energy, also  
 598 called *soft terms*. These soft terms are estimated from low- $p_T$  tracks associated with the primary vertex not  
 599 being assigned to any reconstructed object.

600 An overlap removal procedure is applied to avoid the same calorimeter energy deposit or the same track  
 601 being reconstructed as two different objects. Electrons sharing their track with a muon candidate are  
 602 removed. Jets within a  $\Delta R = 0.2$  cone of an electron are removed. After that, electrons within a  $\Delta R = 0.4$   
 603 cone of a remaining jet are removed. When a muon and a jet are close, the jet is removed if it has no more  
 604 than two associated tracks and is within  $\Delta R < 0.2$  of the muon, otherwise the muon is removed if it is

<sup>7</sup> Calibration file: `xAODTaggingEfficiency/13TeV/2017-21-13TeV-MC16-CDI-2018-10-19_v1.root`

605 within  $\Delta R < 0.4$  of the jet and the jet has more than two associated tracks. Photons within a  $\Delta R = 0.4$   
 606 cone of a remaining electron or muon are removed. Finally, the jets within a  $\Delta R = 0.4$  cone of a remaining  
 607 photon are removed.

## 608 4.2 Event pre-selection

609 Each event is required to have at least one reconstructed primary vertex with at least two associated  
 610 reconstructed tracks. Furthermore, only events where at least one of the single-lepton triggers listed in  
 611 Table 3 was fired. With increasing instantaneous luminosity values between 2015 and 2018, different sets  
 612 of triggers were in use for different data-taking periods. All selections require at least one electron or muon,  
 613 which is matched to the fired single-lepton trigger. In addition, the trigger-matched lepton must pass the  $p_T$   
 614 thresholds listed in Table 3.

## 615 4.3 Definition of the signal region

616 To select  $t\bar{t}\gamma$  events in the  $e\mu$  final state, an  $e\mu$  signal region is defined by a set of selection cuts on top of  
 617 the pre-selection described in Section 4.2. Events are selected with exactly one electron and exactly one  
 618 muon, each of which must carry  $p_T > 25$  GeV (note that one of the two leptons must nonetheless fulfil the  
 619 trigger-match requirements of the pre-selection). Electron and muon must be of opposite sign. The event is  
 620 required to have at least two jets with  $p_T > 25$  GeV each. At least one of the jets must be  $b$ -tagged. The  
 621 event must contain exactly one photon with  $p_T > 20$  GeV and *Tight ID* and *FixedCutTight* isolation, as  
 622 detailed in Section 4.1. No minimal  $E_T^{\text{miss}}$  is required because of the low background contamination in the  
 623  $e\mu$  signal region. The selection cuts are also summarised in Table 4.

624 To allow separate treatments of the  $t\bar{t}\gamma$  and  $tW\gamma$  contributions to the combined signal, the numbers of  
 625 predicted events for both processes are counted in two distinct categories. The background processes are  
 626 sorted in three categories, the choice of which is based on the origin of the reconstructed photon required  
 627 in the event selection. The three categories are:

Table 3: List of single-lepton triggers used for the event pre-selection. Events need to have either one of the single-electron or single-muon triggers fired. Then, a lepton must be selected above the listed  $p_T$  thresholds and matched to that trigger.

Period	Single-electron	Single-muon	Lepton $p_T$
2015	HLT_e24_lhmedium_L1EM20VH	HLT_mu20_iloose_L1MU15	
	HLT_e60_lhmedium	HLT_mu50	> 25 GeV
	HLT_e120_lhloose		
2016	HLT_e26_lhtight_nod0_ivarloose	HLT_mu26_ivarmedium	
	HLT_e60_lhmedium_nod0	HLT_mu50	> 27 GeV
	HLT_e140_lhloose_nod0		
2017	HLT_e26_lhtight_nod0_ivarloose	HLT_mu26_ivarmedium	
	HLT_e60_lhmedium_nod0	HLT_mu50	> 28 GeV
	HLT_e140_lhloose_nod0		
2018	HLT_e26_lhtight_nod0_ivarloose	HLT_mu26_ivarmedium	
	HLT_e60_lhmedium_nod0	HLT_mu50	> 28 GeV
	HLT_e140_lhloose_nod0		

Table 4: Selection cuts for the  $e\mu$  signal region.

Primary vertex
$\geq 1$ electron or muon, trigger-matched
= 1 electron, $p_T > 25$ GeV
= 1 muon, $p_T > 25$ GeV
opposite-sign requirement
$\geq 2$ jets, $p_T > 25$ GeV
$\geq 1$ b-jet (85% working-point)
= 1 photon, $p_T > 20$ GeV

Not reviewed, for internal circulation only

- 628 1. The *h-fake* category which contains any type of h-fake photons that pass the photon criteria. The  
 629 processes falling into this category include  $t\bar{t}$ ,  $W$ +jets,  $Z$ +jets, diboson and  $t\bar{t}V$  production with an  
 630 additional h-fake photon. But it also includes processes with a prompt photon in the simulation,  
 631 where the prompt photon is not reconstructed in the detector and/or does not pass the selection  
 632 requirements, but an additional h-fake photon does.

633 The contribution of h-fake photons is estimated based on Monte-Carlo simulation only. However,  
 634 studies have been performed with data-driven techniques to improve this Monte-Carlo-based estimate,  
 635 documented in detail in Appendix D. With very few expected events in the  $e\mu$  signal region (the  
 636 overall predicted contribution amounts to about 2.5%, as listed in Table 5), the studies show that  
 637 possible data-driven h-fake scale factors have a negligible effect on the shape of relevant observables  
 638 (e.g.  $S_T$ ). To cover possible rate differences that h-fake scale factors would correct for, a global  
 639 normalisation uncertainty is assigned to the h-fake category, as described in Section 6.

- 640 2. The *e-fake* category which contains any type of e-fake photons. Again, this not only includes  
 641 contributions from processes with an e-fake photon and no prompt photon, but also processes with a  
 642 prompt photon in the simulation but an e-fake photon in the reconstruction.

643 Data-driven e-fake scale factors were derived with the partial 2015/16 dataset and were found  
 644 to be largely compatible with one within statistical uncertainties. More details on this study are  
 645 documented in the internal note in Ref. [66]. Given these previous results and the minor impact  
 646 of e-fake photons in the  $e\mu$  channel – the overall predicted contribution is below 1%, as listed in  
 647 Table 5 – no data-driven estimate for the e-fake category is performed in this analysis. Instead,  
 648 a global normalisation uncertainty is assigned to e-fake photons, as described in detail in Section 6.

- 649 3. The *prompt  $\gamma$*  category which contains any type of background process with a prompt photon.

650 Events where one or both  $W$  bosons decay into  $\tau$ -leptons, which then subsequently decay into  $e$  and/or  $\mu$ ,  
 651 also fall in the definition of the signal region. However, these events are filtered based on truth information  
 652 and categorised as *Other  $t\bar{\gamma}$*  and *Other  $tW\gamma$* , not as  $t\bar{\gamma} e\mu$  or  $tW\gamma e\mu$  signal, respectively, to match the  
 653 theory calculation in Ref. [1]. The analysis implicitly also counts single-lepton events, where a second  
 654 lepton is faked by hadronic energy depositions. In studies performed on 2015/16 data, these were found  
 655 to have negligible contributions to the  $e\mu$  final state and, as a consequence, will only be estimated from  
 656 Monte-Carlo simulation [66]. These migrated single-lepton  $t\bar{\gamma}\gamma$  events are also placed in the categories  
 657 *Other  $t\bar{\gamma}\gamma$*  and *Other  $tW\gamma$* . Based on the Monte-Carlo-based estimate, their yields are below 0.5% of those  
 658 of the  $t\bar{\gamma}\gamma e\mu$  signal. Thus, the *Other  $t\bar{\gamma}\gamma$*  are dominated by di-lepton  $t\bar{\gamma}\gamma$  events with  $\tau$ -leptons. The same  
 659 applies to the *Other  $tW\gamma$*  category.

660 The expected and observed event yields after selection are listed in Table 5. The table also includes  
 661 expected and observed values for the different data-taking periods 2015/16, 2017 and 2018 and Monte-Carlo  
 662 subcampaigns *mc16a*, *mc16d* and *mc16e*. The predictions were scaled to the integrated luminosity values  
 663 of the data-taking period as listed in Table 2. In addition, the combination of all  $t\bar{t}\gamma$  and  $tW\gamma$  categories was  
 664 scaled to match the event yields in data for each data-taking period. The scaling factors are 1.358, 1.445,  
 665 1.414 and 1.408 for 2015/16, 2017, 2018 and the entire 2015–2018 data-taking period, respectively. The  
 666 quoted uncertainty values are the Monte-Carlo statistical uncertainties on the predicted number of events  
 667 only, that is, no systematic uncertainties detailed in Section 6 are included. Table 6 lists the predicted event  
 668 yields for signal and background categories split into individual contributions from Monte-Carlo samples.  
 669 The same scaling factors as in Table 5 are applied to this table. The samples marked with an asterisk were  
 670 found to have negligible contributions and are therefore *not* considered in further steps of the analysis.

671 Data/MC control plots of various event variables are shown in Figures 4 to 6. Again, the shaded error  
 672 bands for the prediction include Monte-Carlo statistical uncertainties only. For simplicity, the *Other  $t\bar{t}\gamma$*   
 673 and the *Other  $tW\gamma$*  categories are not displayed separately. While the primary kinematic variables shown in  
 674 Figure 4 show good agreement between data and prediction, some discrepancies are observed for more  
 675 complex observables, in particular angular variables, such as  $\Delta R_{\min}(\gamma, \ell)$ , the  $\Delta R$  distance between photon  
 676 and closest lepton. Most of these discrepancies are covered by the systematic uncertainties, introduced in  
 677 Section 6. The identical observables of Figures 4 to 6 including pre-fit systematics uncertainty bands are  
 678 shown in Figures 29 to 31 in Section 7. The systematics that cover the observed discrepancies include  
 679 modelling variations of the  $t\bar{t}\gamma$  signal and of the background processes. In addition, the  $t\bar{t}\gamma$  signal sample  
 680 is generated at leading order in QCD and with the narrow-width approximation for the top quark, as  
 681 introduced in Section 3, and it does neither include higher-order corrections nor off-shell effects. However,  
 682 Bevilacqua et al. [1] have shown that these play a significant role, in particular in angular variables. This  
 683 could be a possible reason why slight discrepancies are observed in these observables.

Table 5: Event yields in the  $e\mu$  signal region. All categories are estimated based on Monte-Carlo simulation only. The listed uncertainties correspond to the Monte-Carlo statistical uncertainties. Note that the combination of all  $t\bar{t}\gamma$  and  $tW\gamma$  categories is scaled to match the event yields in data. The scaling factors are 1.358, 1.445, 1.414 and 1.408 for each column, respectively.

	2015/16	2017	2018	full dataset
$t\bar{t}\gamma e\mu$	$643 \pm 5$	$760 \pm 6$	$989 \pm 7$	$2391 \pm 11$
$tW\gamma e\mu$	$42.9 \pm 1.0$	$49.9 \pm 1.1$	$62.9 \pm 1.3$	$155.7 \pm 2.0$
Other $t\bar{t}\gamma$	$70.6 \pm 1.8$	$82.1 \pm 2.0$	$107.6 \pm 2.3$	$260.4 \pm 3.5$
Other $tW\gamma$	$5.0 \pm 0.3$	$6.1 \pm 0.4$	$7.5 \pm 0.4$	$18.6 \pm 0.7$
h-fake	$22.9 \pm 1.0$	$23.1 \pm 1.0$	$31.4 \pm 1.1$	$77.5 \pm 1.8$
e-fake	$5.6 \pm 0.3$	$7.0 \pm 0.4$	$10.3 \pm 0.5$	$23.0 \pm 0.7$
Prompt $\gamma$ bkg.	$19.3 \pm 1.0$	$30.2 \pm 1.2$	$38.0 \pm 1.4$	$87.5 \pm 2.1$
Total	$809 \pm 6$	$958 \pm 7$	$1247 \pm 8$	$3014 \pm 12$
Data	809	958	1247	3014

Table 6: Expected number of events in the  $e\mu$  signal region for signal and background simulations. The values are as shown in Table 5, but the individual processes are listed that contribute to a process category. All event yields are estimated based on Monte-Carlo simulation only. Note that the combination of all  $t\bar{t}\gamma$  and  $tW\gamma$  categories is scaled to match the event yields in data. Processes marked with an asterisk are found to have negligible contributions to any of the categories and are therefore not considered in further steps of the analysis.

	2015/16	2017	2018	full dataset
$t\bar{t}\gamma e\mu$	643	760	989	2391
$tW\gamma e\mu$	42.9	49.9	62.9	155.7
Other $t\bar{t}\gamma$	70.6	82.1	107.6	260.4
Other $tW\gamma$	5.0	6.1	7.5	18.6
h-fake (from $t\bar{t}\gamma$ )	0.2	0.3	0.4	0.9
h-fake (from $t\bar{t}$ )	21.1	21.5	29.9	72.5
h-fake (from $tW\gamma$ )	1.4	0.8	0.6	2.8
h-fake (from $W\gamma$ )	<0.1	<0.1	<0.1	<0.1
h-fake (from $W+jets$ )*	<0.1	<0.1	<0.1	<0.1
h-fake (from $Z\gamma$ )	<0.1	<0.1	<0.1	<0.1
h-fake (from $Z+jets$ )*	<0.1	<0.1	<0.1	<0.1
h-fake (from diboson)	<0.1	0.2	0.1	0.4
h-fake (from $t\bar{t}V$ )	0.3	0.2	0.5	1.0
h-fake complete	22.9	23.1	31.4	77.5
e-fake (from $t\bar{t}\gamma$ )	0.5	1.1	1.6	3.2
e-fake (from $t\bar{t}$ )	1.4	1.7	3.0	6.0
e-fake (from $tW\gamma$ )	0.1	<0.1	<0.1	0.1
e-fake (from $W\gamma$ )	<0.1	<0.1	<0.1	<0.1
e-fake (from $W+jets$ )*	<0.1	<0.1	<0.1	<0.1
e-fake (from $Z\gamma$ )	<0.1	<0.1	<0.1	<0.1
e-fake (from $Z+jets$ )*	<0.1	<0.1	<0.1	<0.1
e-fake (from diboson)	1.9	2.1	2.7	6.6
e-fake (from $t\bar{t}V$ )	1.8	2.2	3.0	7.0
e-fake complete	5.6	7.0	10.3	23.0
Prompt $\gamma$ (from $t\bar{t}$ )	11.9	21.6	25.8	59.3
Prompt $\gamma$ (from $W\gamma$ )	1.0	<0.1	0.1	1.1
Prompt $\gamma$ (from $W+jets$ )*	<0.1	<0.1	<0.1	<0.1
Prompt $\gamma$ (from $Z\gamma$ )	0.6	2.0	3.4	6.0
Prompt $\gamma$ (from $Z+jets$ )*	<0.1	<0.1	<0.1	<0.1
Prompt $\gamma$ (from diboson)	1.2	1.3	1.6	4.1
Prompt $\gamma$ (from $t\bar{t}V$ )	4.6	5.3	7.1	17.0
Prompt $\gamma$ complete	19.3	30.2	38.0	87.5
Total	809	958	1247	3014

Not reviewed, for internal circulation only

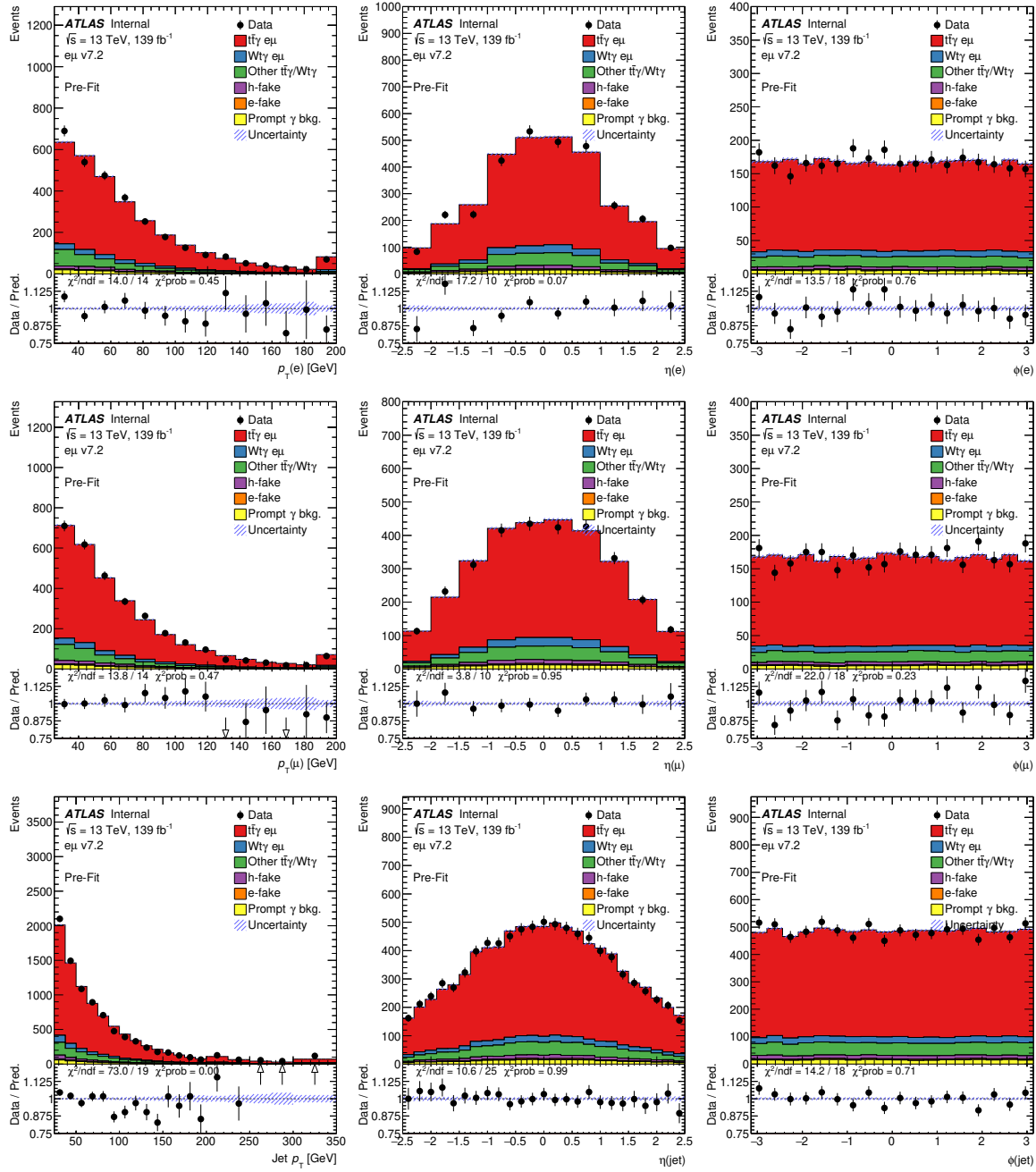


Figure 4: Data/MC control plots of the  $e\mu$  signal region, with statistical uncertainties only. The shown variables are: transverse momentum, pseudo-rapidity and  $\phi$  of the electron, and transverse momentum, pseudo-rapidity and  $\phi$  of the muon, and transverse momenta, pseudo-rapidities and  $\phi$  of all jets in the event.

Not reviewed, for internal circulation only

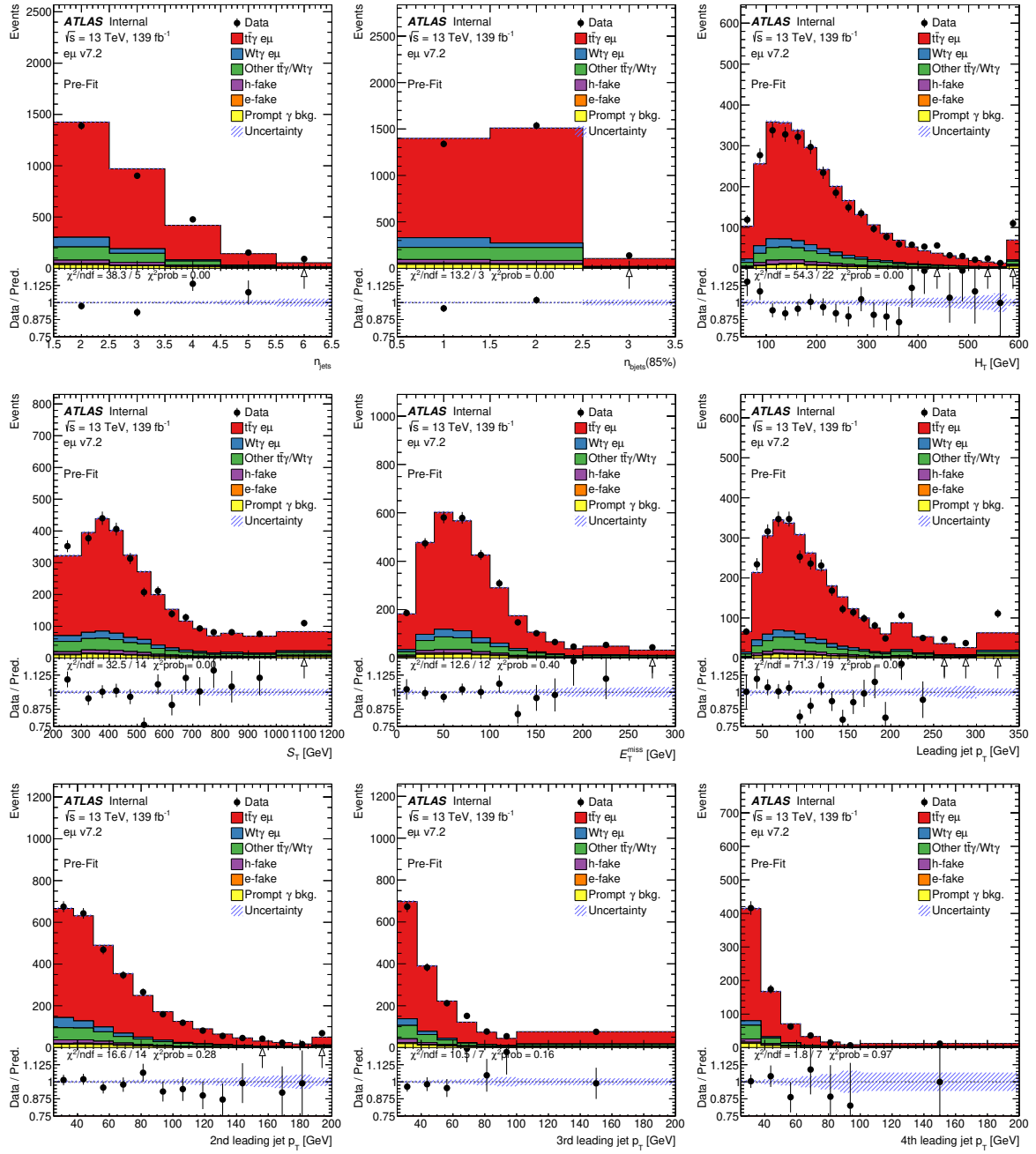


Figure 5: Data/MC control plots of the  $e\mu$  signal region, with statistical uncertainties only. The shown variables are: jet multiplicity,  $b$ -jet multiplicity, total hadronic transverse energy, total transverse energy (includes electrons, muons, jets, photons and  $E_T^{\text{miss}}$ ),  $E_T^{\text{miss}}$ , and the transverse momenta of the four leading jets when ordered in transverse momenta.

Not reviewed, for internal circulation only

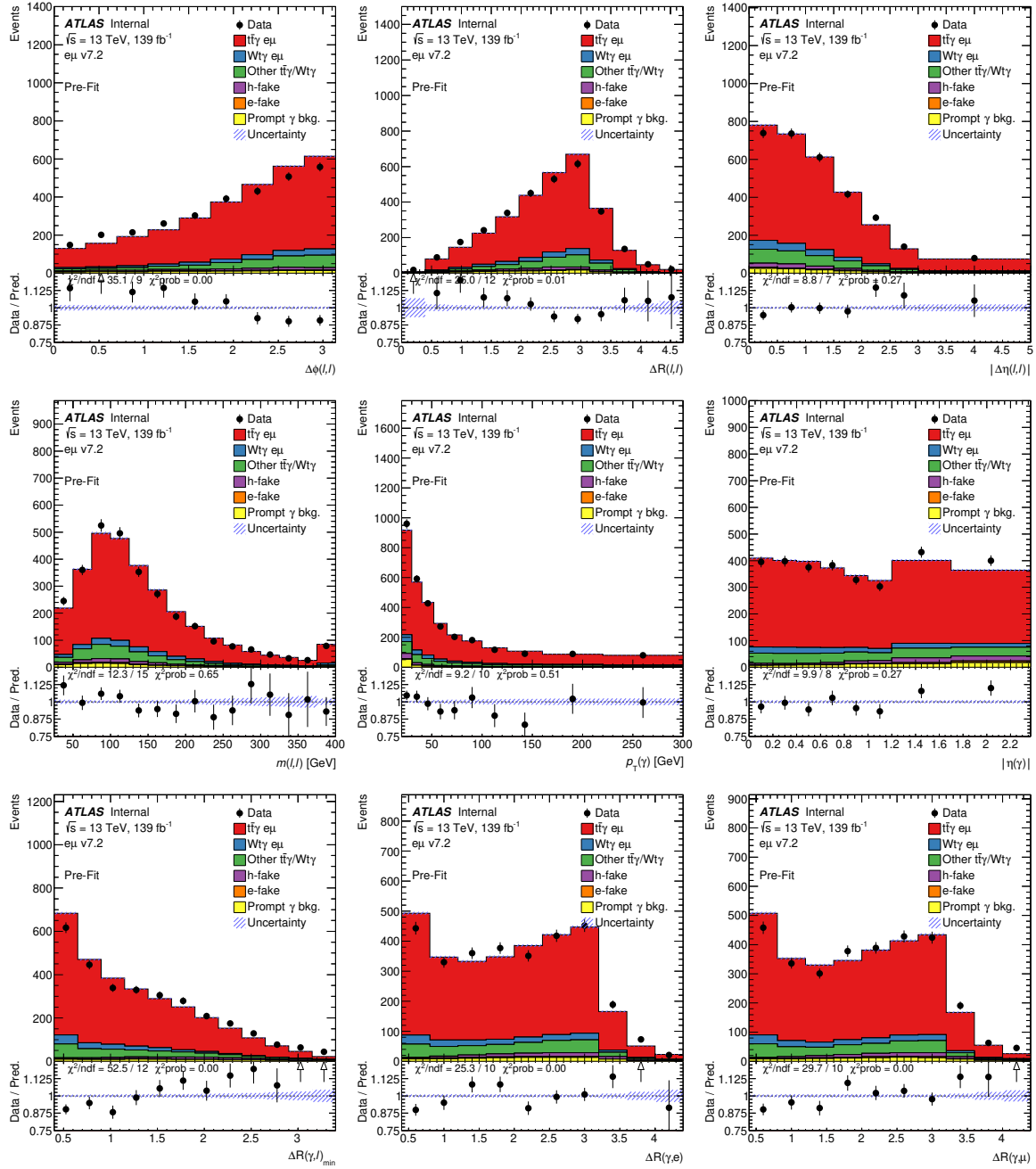


Figure 6: Data/MC control plots of the  $e\mu$  signal region, with statistical uncertainties only. The shown variables are:  $\Delta\phi$ ,  $\Delta R$ ,  $|\Delta\eta|$  and invariant mass of the electron-muon pair, transverse momentum and pseudo-rapidity of the photon,  $\Delta R$  between the photon and the closest lepton,  $\Delta R$  between photon and electron, and  $\Delta R$  between photon and muon.

## 684 5 Cross-section definition and fit strategy

685 The fiducial region definition, in which the inclusive and differential cross-sections is measured, is  
 686 introduced in Section 5.1. The fit strategy is described in Section 5.2. Afterwards, the measurement  
 687 of differential cross-section using the unfolding procedure is discussed in Section 5.3. As previously  
 688 described, this analysis measures the combined signal predicted by  $t\bar{t}\gamma$  and  $tW\gamma$  simulations. Separate  
 689 tests, where only  $t\bar{t}\gamma$  is considered signal and  $tW\gamma$  is treated as a background process, are documented in  
 690 detail in Appendix E.

### 691 5.1 Object and phase space definitions at parton level

692 The fiducial region at parton level is defined to be as close as possible to the signal region at reconstruction  
 693 level, described in Section 4.3, and to be the same as the theory calculation in Ref. [1]. The following  
 694 requirements are looser compared to those of the reference and have been discussed and agreed on with the  
 695 theorist in order to open the phase space and reduce the statistical uncertainties on the measurement.

696 The objects at parton level are defined for matrix-element-plus-parton-shower (ME+PS) level, that is, after  
 697 radiation:

- 698 • **Leptons:** Leptons are dressed with close-by photons within a cone of radius of  $R = 0.1$  around them  
 699 and are required to have  $p_T > 25$  GeV and  $|\eta| < 2.5$ .
- 700 •  **$b$ -quarks:** The  $b$ -jets at parton level in the calculation [1] are jets clustered with the anti- $k_t$  algorithm  
 701 with a radius of  $R = 0.4$  around the  $b$ -quark. Since the events are not showered, the jets correspond  
 702 to the  $b$ -quarks from the top quark decay (with an additional gluon in case the NLO radiation is close  
 703 to one of the  $b$ -quarks). In this analysis, parton level  $b$ -jets are considered. They are clustered with  
 704 the anti- $k_t$  algorithm with a distance parameter of  $R = 0.4$  on all partons that are radiated from the  
 705 two  $b$ -quarks (including the  $b$ -quarks themselves) and from the two initial partons. These jets are  
 706 required to include a  $b$ -quark from the decay of a top quark and have  $p_T > 25$  GeV and  $|\eta| < 2.5$ .
- 707 • **Photons:** Photons are required to have  $E_T > 20$  GeV and  $|\eta| < 2.37$ .

708 The usage of this LO ME+PS definition is recommended by the authors of Ref. [1] for the comparison to  
 709 their QCD NLO prediction. The events are then required to fulfil the following requirements:

- 710 • **Leptons:** Exactly one electron and one muon are required. Events with leptons originating from an  
 711 intermediate  $\tau$ -lepton in the top decay chain are not considered.
- 712 •  **$b$ -quarks:** The presence of the  $b$ -quark and  $\bar{b}$ -quark from the top quark decay are required.
- 713 • **Photon:** Exactly one photon is required. The event is dropped if the photon has a  $\Delta R(l, \gamma) < 0.4$   
 714 with any lepton.
- 715 • **Event variables:**  $\Delta R(l, l) > 0.4$ ,  $\Delta R(b, b) > 0.4$ ,  $\Delta R(l, b) > 0.4$ . These selection cuts are chosen  
 716 as in the theory paper and are meant to mimic isolation requirements at detector level.

717 The authors of Ref. [1] have applied Frixone isolation for the hard photon from matrix element. The same  
 718 isolation selection is also applied in this analysis:

- **Between photon and QCD parton:** The sum of transverse energy of QCD partons within  $\Delta R$  of the photon should not exceed a certain limit. Different  $\Delta R$  values, ranging from 0 to 0.4, will be tried and for each  $\Delta R$  value, the limit will be varied according to  $E_T^{\gamma}(\frac{1-\cos\Delta R}{1-\cos 0.4})$ .
- **Between photon and jet:** The  $\Delta R$  between the photon and both the  $b$ -quark jet and  $\bar{b}$ -quark jet shall be larger than 0.4.

## 724 5.2 Fit strategy for the inclusive cross-section

- 725 The events selected in the signal region, as described in Section 4, subtracting the estimated number of  
 726 background events are the observed signal events. In this analysis, the observed signal events are used to:
- 727 • extract the fiducial cross-section, after correcting for the signal efficiency loss and migration from  
 728 outside the fiducial region using Monte-Carlo simulation.
  - 729 • be compared with the number of predicted signal events in simulation. Their ratio, denoted as  
 730  $\mu$  and called *signal strength*, can be used to quantify the agreement between observation and  
 731 Standard-Model prediction at reconstruction level.
  - 732 • with the background subtraction done differentially, perform measurements of differential cross-  
 733 sections. The strategy for this will be detailed in Section 5.3.

The fiducial cross-section is extracted using a profile likelihood fit to the  $S_T$  distribution, where  $S_T$  is the sum over all transverse momenta the event, including leptons, photons and  $E_T^{\text{miss}}$ . The parameter of interest, the fiducial cross-section  $\sigma_{\text{fid}}$ , is related to the number of signal events in bin  $i$  of the  $S_T$  distribution as

$$N_i^s = L \times \sigma_{\text{fid}} \times C \times f_i^{S_T},$$

where  $L$  is the integrated luminosity,  $f_i^{S_T}$  is the fraction of signal events falling into bin  $i$  of the  $S_T$  distribution, and  $C$  is the correction factor for the signal efficiency  $\epsilon$  and for migration into the fiducial region  $f_{\text{out}}$ , defined as follows:

$$f_{\text{out}} = \frac{N_{\text{reco}}^{\text{non-fid}}}{N_{\text{reco}}}, \quad \epsilon = \frac{N_{\text{reco}}^{\text{fid}}}{N_{\text{MC}}^{\text{fid}}} \quad \Rightarrow C = \frac{\epsilon}{1 - f_{\text{out}}} = \frac{N_{\text{reco}}}{N_{\text{MC}}^{\text{fid}}},$$

- 734 where  $N_{\text{reco}}$  is the simulated number of signal events passing the event selection described in Section 4, and  
 735  $N_{\text{MC}}^{\text{fid}}$  is the corresponding number of signal events generated in the fiducial region defined in Section 5.1.  
 736 Values for efficiency, outside migration and the correction factor were obtained, summarised in Table 7.  
 737 The events were reweighted internally to alternative choices for the scales ( $\mu_R$  and  $\mu_F$ ) to evaluate scale  
 738 uncertainties, separately for  $t\bar{t}\gamma$  and  $tW\gamma$  simulation. Alternative showering with HERWIG7 was performed  
 739 to evaluate the uncertainty on the parton-shower model. For the  $t\bar{t}\gamma$  simulation, PYTHIA var3c eigentune  
 740 variations were evaluated to estimate uncertainties from alternative radiation scenarios. In a last step, the  $t\bar{t}\gamma$   
 741 and  $tW\gamma$  simulated events were reweighted to 100 sampled NNPDF distributions to evaluate uncertainties  
 742 on the PDF choice. For them, the mean values and standard deviations are quoted, as prescribed by  
 743 the NNPDF collaboration. All systematics are described in more detail in Section 6. For reference, the  
 744 obtained relative pre-fit uncertainties on  $C$  from these modelling variations are quoted in the table, too.  
 745 In the profile likelihood fit, the templates of all modelling variations are reweighted to match  $N_{\text{MC}}^{\text{fid}}$  of the  
 746 nominal prediction. Therefore, the quoted relative uncertainties are identical to the rate differences between  
 747 these modelling templates and the nominal prediction.

As described in Section 3, the used  $tW\gamma$  simulation is generated in the five-flavour scheme at leading order in QCD and the spectator  $b$ -quark is not included in the matrix-element generation step. Although it should in principle be produced in the initial state through the PDFs, it was discovered that this spectator  $b$ -quark is not always found at parton level in the MC simulation. Whether this is due to compromises in the MC generation step or due to truth-particle skimming in the ATLAS simulation infrastructure is not clear. The fractions of generated  $tW\gamma$  events without spectator  $b$ -quark were found to be between 30% and 50% depending on the MC sample. Therefore, an additional uncertainty associated to this possibly lost  $b$ -quark is assigned: with respect to the nominal  $tW\gamma$  simulation, the parton-level event yields are doubled, with the fractions of events matched/unmatched to reconstructed events held constant. In addition, the reconstruction efficiency  $\epsilon$  is expected to be unchanged. Therefore, the total number of reconstructed events is held constant, but to match the increased parton-level yields, the fraction of matched reconstructed events is doubled as well. As a result, this additional uncertainty only varies the outside-migration fraction and the correction factor  $C$ . The resulting values are also listed in Table 7. The total value of the correction factor including all uncertainties amounts to  $C = 0.462^{+0.016}_{-0.020}$ .

A likelihood function is defined from the product over all bins of the  $S_T$  distribution:

$$\mathcal{L} = \prod_i P(N_i^{\text{obs}} | N_i^s(\vec{\theta}) + \sum_b N_i^b(\vec{\theta})) \times \prod_t G(0 | \theta_t, 1),$$

where  $N_i^{\text{obs}}$ ,  $N_i^s$ , and  $N_i^b$  are the observed number of events in data, the predicted number of signal events, and the estimated number of background events in bin  $i$  of the  $S_T$  distribution, respectively. Combined, they form a Poisson term  $P$  in that bin. Nuisance parameter  $\theta_t$  is to parameterise a systematic uncertainty  $t$ , which is constrained by a Gaussian  $G(0|\theta_t, 1)$  in such a way, that when it changes from zero to  $\pm 1$ , the quantities affected by this variation in the likelihood change by  $\pm 1$  standard deviation. The collection of all systematic uncertainties is denoted as  $\vec{\theta}$ . For systematic uncertainties related to the finite number of Monte-Carlo events, the Gaussian terms in the likelihood are replaced by Poisson terms. Each systematic uncertainty affects  $N_i^s$  and  $N_i^b$  in each bin of the  $S_T$  distribution. The cross-section is measured by profiling the nuisance parameters and maximising this likelihood.

The signal strength  $\mu$  is defined as the ratio of observed and expected number of signal events and enters the likelihood for each bin according to:

$$N_i^s = \mu \times N_{\text{MC}}^{\text{s,sel.}} \times f_i^{S_T}, \quad (2)$$

where again  $N_{\text{MC}}^{\text{s,sel.}}$  is the simulated number of signal events passing the event selection.

### 5.3 Unfolding method for the differential cross-section

The procedure of retrieving the truth spectrum of an observable from the measured spectrum is called unfolding [67], where the measured spectrum is unfolded to parton level. The unfolding is performed in order to correct for detector effects due to limited resolution and acceptance of the detector. This enables the measured distributions to be compared to theoretical predictions. Unfolding also allows the comparison with other experiments which could have different migration matrices, efficiencies etc.

In the fiducial region, the cross-section can be measured as a function of an observable, meaning it is a differential cross-section measurement. The list of observables to be unfolded in this measurement is:

- photon  $p_T$

Table 7: Obtained values for efficiency, outside migration and the correction factor  $C$  for the nominal signal prediction and its systematic variations. These include variations of the renormalisation and factorisation scales  $\mu_R$  and  $\mu_F$ , alternative modelling of the parton shower with HERWIG7, and variations of the PYTHIA eigentune (the latter for the  $t\bar{t}\gamma$  prediction only). For the  $t\bar{t}\gamma$  scale variations, relative uncertainties on  $C$  with respect to the nominal  $t\bar{t}\gamma$  FS +  $tW\gamma$  simulation are quoted. For the other three  $t\bar{t}\gamma$  variations, relative uncertainties with respect to the nominal  $t\bar{t}\gamma$  AFII +  $tW\gamma$  simulation are given as those Monte Carlo samples use fast simulation. Relative uncertainties for all  $tW\gamma$  variations are quoted with respect to the nominal  $t\bar{t}\gamma$  FS +  $tW\gamma$  simulation. Uncertainties marked with  $\parallel$  are symmetrised.

In addition, uncertainties originating from the choice of the PDF set are evaluated for both  $t\bar{t}\gamma$  and  $tW\gamma$  using 100 sampled NNPDF variations. For them, the mean values and standard deviations are quoted as well as the resulting relative uncertainties. More details for the evaluation of the NNPDF uncertainties are given in Section 6.

All quoted relative uncertainties are for reference only – the correction factor  $C$  is evaluated as a constant and not associated with uncertainties when calculating the fiducial cross-section. But since all modelling templates in the fit are reweighted to  $N_{MC}^{\text{fid}}$  of the nominal prediction, the quoted values are identical to the rate differences between these templates and the nominal prediction.

Evaluated model	$\epsilon$	$f_{\text{out}}$	$C$	rel. uncertainty [%]
Nominal ( $t\bar{t}\gamma$ FS + $tW\gamma$ )	0.2973	0.3567	0.4622	–
Nominal ( $t\bar{t}\gamma$ AFII + $tW\gamma$ )	0.2908	0.3584	0.4533	–
$t\bar{t}\gamma \mu_R \times 2.0$	0.2977	0.3562	0.4623	0.031
$t\bar{t}\gamma \mu_R \times 0.5$	0.2967	0.3575	0.4618	-0.072
$t\bar{t}\gamma \mu_F \times 2.0$	0.2971	0.3563	0.4615	-0.142
$t\bar{t}\gamma \mu_F \times 0.5$	0.2977	0.3570	0.4630	0.180
$t\bar{t}\gamma$ PS model (Herwig7) $\parallel$	0.2915	0.3352	0.4384	-3.278
$t\bar{t}\gamma$ Pythia8 var3c up	0.2908	0.3658	0.4585	1.152
$t\bar{t}\gamma$ Pythia8 var3c down	0.2940	0.3504	0.4526	-0.150
$tW\gamma \mu_R \times 2.0$	0.2973	0.3567	0.4622	0.006
$tW\gamma \mu_R \times 0.5$	0.2973	0.3566	0.4621	-0.008
$tW\gamma \mu_F \times 2.0$	0.2973	0.3566	0.4621	-0.023
$tW\gamma \mu_F \times 0.5$	0.2974	0.3568	0.4623	0.031
$tW\gamma$ PS model (Herwig7) $\parallel$	0.2975	0.3569	0.4626	0.094
$tW\gamma$ parton matching	0.2973	0.3383	0.4495	-2.750
$t\bar{t}\gamma$ NNPDF variations $\parallel$	0.2973(3)	0.3567(9)	0.4622(7)	0.141
$tW\gamma$ NNPDF variations $\parallel$	0.2973(1)	0.3567(1)	0.4622(1)	0.014
Combined up			0.4783	3.484
Combined down			0.4424	-4.288

- 783 • photon  $\eta$
- 784 •  $\Delta R_{\min}(\gamma, \ell)$
- 785 •  $|\Delta\eta(\ell, \ell)|$
- 786 •  $\Delta\phi(\ell, \ell)$

787 The kinematic properties of the photon are sensitive to the  $t\gamma$  coupling, while the dilepton  $|\Delta\eta(\ell, \ell)|$  and  
788  $\Delta\phi(\ell, \ell)$  are sensitive to the  $t\bar{t}$  spin correlation.

789 For this goal, first, the signal spectrum at reconstruction level of an observable  $N_{\text{reco},j}$  is measured from the  
790 data spectrum by subtracting the background spectrum:

$$N_{\text{reco},j} = N_{\text{data},j} - N_{\text{bkgs},j}, \quad (3)$$

791 where  $j$  is the binning index of the observable at reconstruction level. Then, the differential cross-section  
792  $\sigma_k^{\text{diff}}$  can be related to the signal spectrum through:

$$N_{\text{reco},j} = \frac{1}{1 - f_{\text{out},j}} \times \sum_k (L \times \sigma_k^{\text{diff}} \times \epsilon_k \times M_{kj}), \quad (4)$$

- 793 • where  $k$  is the binning index of the observable at truth level (i.e. parton level), which is not necessarily  
794 binned in the same way as at reconstruction level,
- 795 •  $L$  is the integrated luminosity,
- 796 •  $f_{\text{out},j}$  is the fraction of signal events migrated from outside the fiducial region ('non-fiducial') into  
797 the bin  $j$  of the reconstructed distribution:

$$f_{\text{out},j} = \frac{N_{\text{reco},j}^{\text{non-fid}}}{N_{\text{reco},j}}, \quad (5)$$

798 •  $\epsilon_k$  is the efficiency of signal events generated in bin  $k$  on parton level to be reconstructed and selected  
799 on reconstruction level:

$$\epsilon_k = \frac{N_{\text{reco},j=k}^{\text{fid}}}{N_{\text{part},k}^{\text{fid}}}, \quad (6)$$

800 •  $M_{kj}$  is the migration matrix, representing the probability of a signal event generated in bin  $k$  at  
801 parton level to be observed in bin  $j$  of the reconstructed distribution. The events used to calculate  
802 this probability have to pass both the fiducial-region selection and the reconstruction event selection,  
803 and the relevant objects have to match as described above.

804 The correction efficiency  $\epsilon_k$  and acceptance  $(1 - f_{\text{out},j})$  for the observables photon  $p_T$ , photon  $\eta$ ,  $\Delta R_{\min}(\gamma, \ell)$ ,  
805  $\Delta\phi(\ell, \ell)$ , and  $|\Delta\eta(\ell, \ell)|$  are shown in Figure 7. The bin-by-bin migration matrices (normalised to 100 w.r.t  
806 one bin on reconstruction level) for the same observables are shown in Figure 8.

807 Solving Equation (4), the differential cross-section can be expressed as:

$$\sigma_k^{\text{diff}} = \frac{1}{L} \times \frac{1}{\epsilon_k} \times \sum_j M_{jk}^{-1} \times (N_{\text{data},j} - N_{\text{bkgs},j}) \times (1 - f_{\text{out},j}), \quad (7)$$

Not reviewed, for internal circulation only

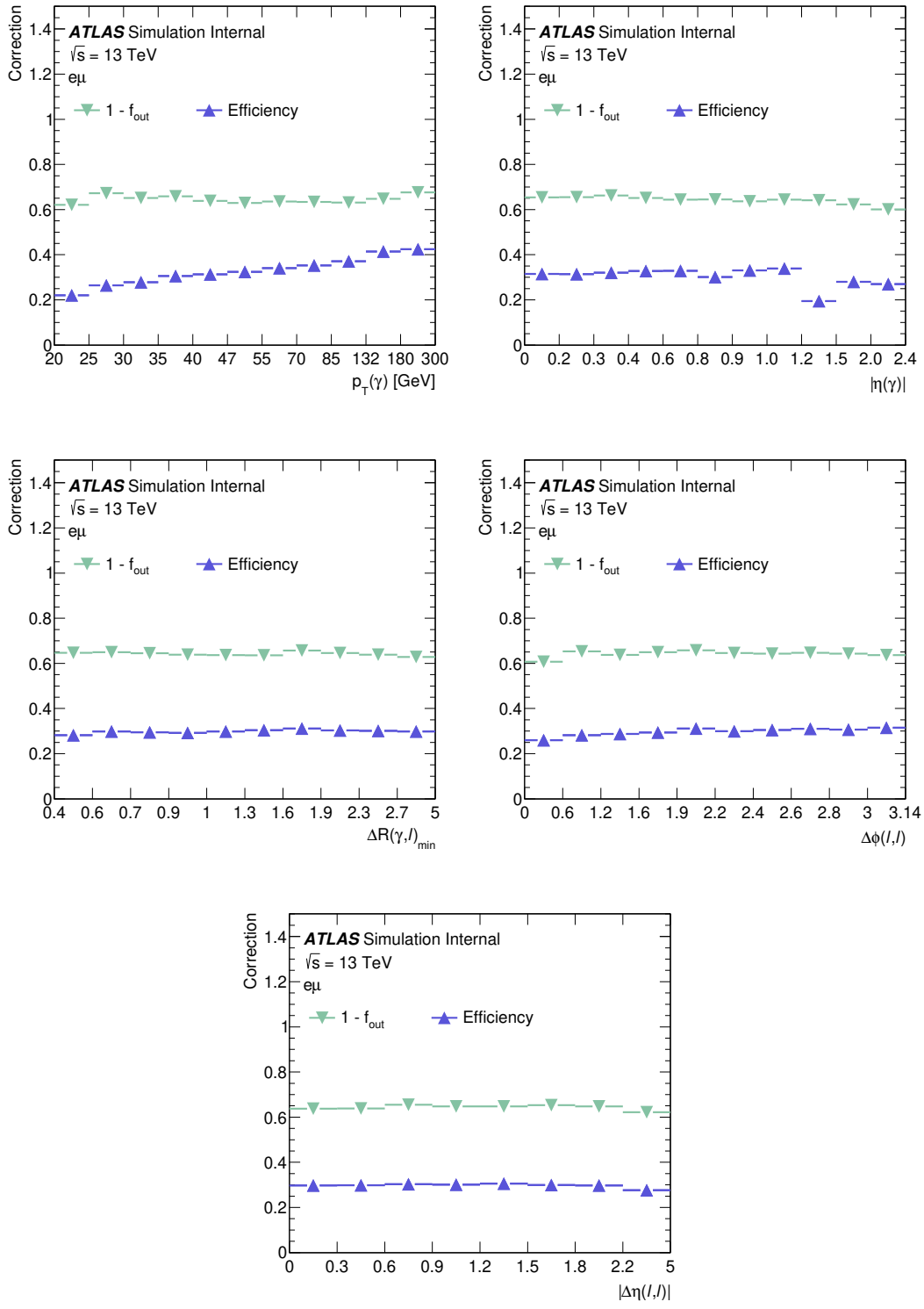


Figure 7: The correction efficiencies  $\epsilon_k$  and acceptances ( $1 - f_{\text{out},j}$ ) for the observables photon  $p_T$ , photon  $\eta$ ,  $\Delta R_{\text{min}}(\gamma, \ell)$ ,  $\Delta \phi(\ell, \ell)$  and  $|\Delta \eta(\ell, \ell)|$ .

Not reviewed, for internal circulation only

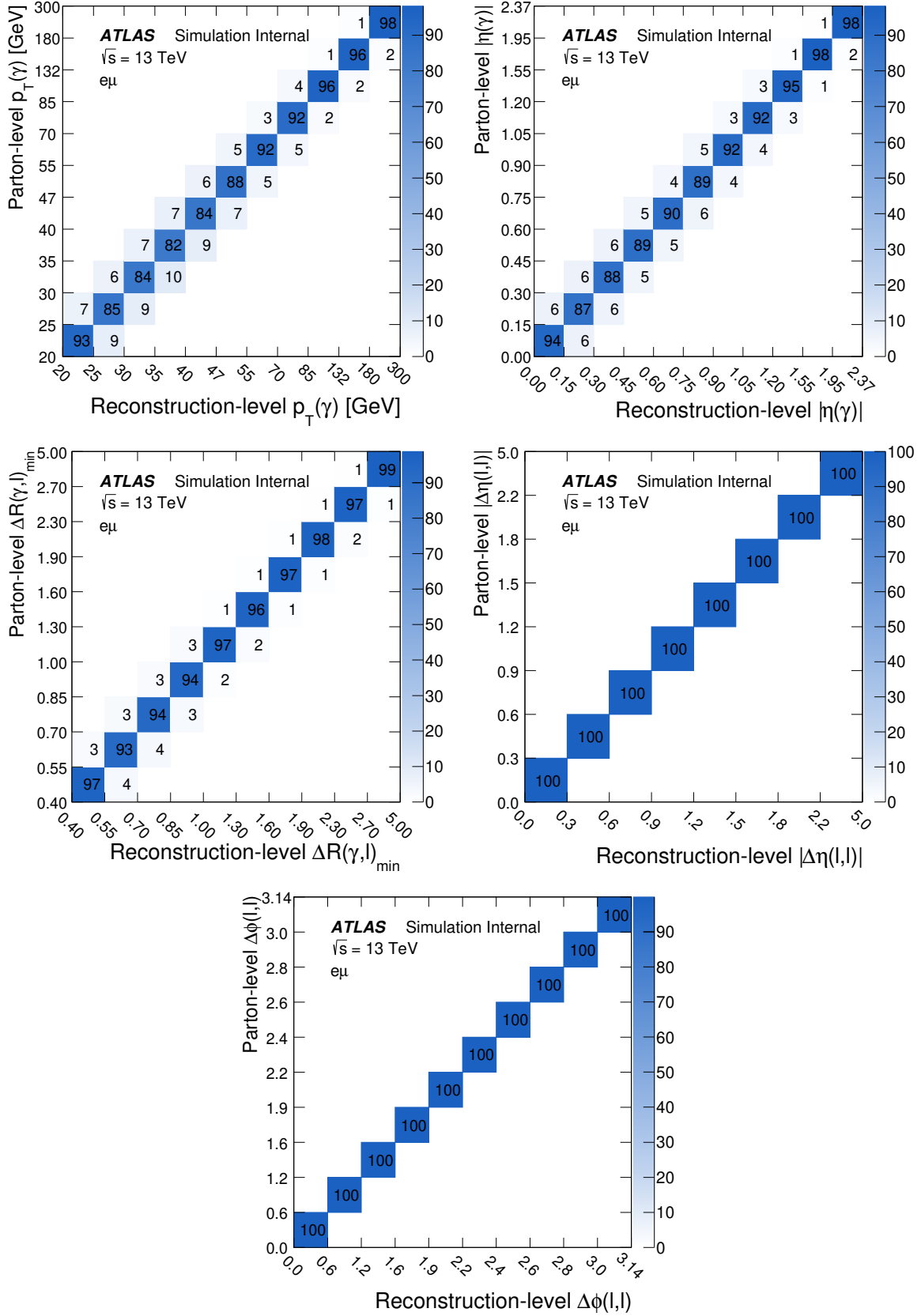


Figure 8: Bin-by-bin migration matrices (normalized to 100 w.r.t one bin on reconstruction level) for the observables photon  $p_T$ , photon  $\eta$ ,  $\Delta R_{\min}(\gamma, \ell)$ ,  $|\Delta\eta(\ell, \ell)|$  and  $\Delta\phi(\ell, \ell)$ .

808 where  $M_{jk}^{-1}$  is the inversion of the bin-by-bin migration matrix. From Equation (7), it is clear that in order  
 809 to measure  $\sigma_k^{\text{diff}}$ , the bin-by-bin matrix has to be inverted, and for that purpose unfolding is used. The main  
 810 task of unfolding is the inversion of the migration matrix. To derive the inverse, various methods have been  
 811 developed. The method in use, for this analysis, is the iterative Bayesian method (IBS) [68].

812 In terms of probability, the migration matrix can be represented as the probability  $P(N_{\text{reco},j}|N_{\text{part},k})$  of  
 813 generated events at parton level in bin  $k$  to be reconstructed in bin  $j$ . This means these probabilities are  
 814 calculated from events that pass both the fiducial-region selection and event selection on reconstruction  
 815 level. According to the Bayesian theorem, the inverse of the migration matrix ( $M_{jk}^{-1}$ ) or in terms of  
 816 probabilities  $P(N_{\text{part},k}|N_{\text{reco},j})$  can be written as:

$$P(N_{\text{part},k}|N_{\text{reco},j}) = \frac{P(N_{\text{reco},j}|N_{\text{part},k}) \cdot P_0(N_{\text{part},k})}{\sum_l P(N_{\text{reco},j}|N_{\text{part},l}) \cdot P_0(N_{\text{part},l})}, \quad (8)$$

817 where the prior truth distribution  $P_0(N_{\text{part}})$  is taken from the MC sample.  $M_{jk}^{-1}$  is used to unfold the  
 818 observed signal distribution resulting in an estimator (unfolded distribution) in the first iteration. This  
 819 unfolded distribution is then used as a prior for the next iteration. The iteration process is repeated until a  
 820 good closure between the unfolded distribution and the prior used for such iteration is reached.

## 821 6 Systematic uncertainties

822 Various sources of systematic uncertainties need to be considered in this measurement. Signal and  
 823 background simulation are subject to modelling uncertainties, detailed in Section 6.1. The experimental  
 824 uncertainties, which are common to both signal and backgrounds, are explained in Section 6.2. Table 11 at  
 825 the end of the chapter details all systematics considered for this analysis in the pre-pruning stage.

826 To avoid high sensitivity to statistical fluctuations in systematic variations, *smoothing* techniques are applied  
 827 to some of the systematics. These algorithms average statistics across bins to prevent large statistical spikes  
 828 in the distributions. In particular, smoothing is applied to some of the modelling variations in Section 6.1  
 829 when they are simulated with a separate event seed and are thus prone to large statistical fluctuations  
 830 with respect to the nominal prediction. This analysis uses smoothing as implemented in the TRExFITTER  
 831 framework, the configuration of which is based on two parameters: the *tolerance* and the threshold for  
 832 the number of slope variations in the systematic histogram. The first step for the algorithm is to ensure  
 833 that the statistical uncertainty for a group of bins is less than an 8% tolerance. If this is not the case, the  
 834 histogram is re-binned. Then, the number of slope variations of the histogram is checked. If the number  
 835 of variations is less than or equal to the provided threshold of four bins, this new histogram is kept. If  
 836 this is not the case, the statistical tolerance is halved, the histogram re-binned, and the slope variation  
 837 checked once again. This procedure is repeated until the slope variations are four or fewer. This process  
 838 only affects the shape of the systematic histogram with the overall normalisation fixed to that of the original  
 839 histogram. In all cases, a second algorithm referred to as *pre-smoothing* is applied, which makes use of  
 840 ROOT’s TH1::Smooth method<sup>8</sup>. Based on the integral of the histogram and neighbouring bin information,  
 841 bin contents are averaged. The TH1 smoothing algorithm does not smooth sign changes in the derivative  
 842 of the variations as rigidly. Therefore, using TH1 smoothing in conjunction with the TRExFitter-internal  
 843 smoothing algorithm, better preserves shape variations.

Another technique applied to some of the systematics is *symmetrisation* to center the variation around a mean value. *Two-sided* symmetrisation may be performed when an up and a down variation is provided for a given systematic. In this procedure, the difference between the two variations is divided by the mean of the variations. The positive and negative of this expression are then taken as new up and down variations, respectively:

$$\text{new variations up/down} = \pm \left| \frac{\text{up} - \text{down}}{(\text{up} + \text{down})/2} \right|$$

844 Thus, after two-sided symmetrisation the  $\pm 1\sigma$  variations are centered around their arithmetic mean. It is  
 845 important to note that this procedure has no effect if the up/down variations are symmetric by construction.  
 846 As an alternative, *maximum* symmetrisation takes the larger of the two variations bin by bin and mirrors  
 847 their values around the nominal prediction. This very conservative symmetrisation technique preserves the  
 848 amplitude and direction of the larger variation, while providing a symmetric output at the same time. Even  
 849 in those cases, where both variations would go to the same direction in a bin, e.g. due to large statistical  
 850 fluctuations, *maximum* symmetrisation provides a symmetric three-point uncertainty based on the largest  
 851 deviation from the nominal prediction. In those cases, it is superior to the *two-sided* symmetrisation, which  
 852 would potentially underestimate the variation in those bins. *Maximum* symmetrisation is used for variations  
 853 with large statistical fluctuations, in particular modelling uncertainties. *One-sided* symmetrisation can be  
 854 used when only *one* variation is provided. In this case, the variation is mirrored around the nominal to

<sup>8</sup> <https://root.cern.ch/doc/master/classTH1.html>.

reflect the supplementary variation. An overview of the smoothing and symmetrisation techniques applied to the different systematic variations is given in Table 8. The variations are explained in more detail in the following sections.

To verify that the symmetrisation of two-point uncertainties does not have any significant impact on the results, additional studies were performed. All systematic variations marked as *two-sided* in Table 8 were turned off in these tests, and the expected uncertainty on the  $t\bar{t}\gamma$  signal strength was calculated in an Asimov fit scenario and compared with the uncertainty obtained with two-sided symmetrisation.<sup>9</sup> The resulting expected uncertainties on the signal strength are shown in Table 9. The expected uncertainties on the  $t\bar{t}\gamma$  signal strength are identical within significant digits, hence, using two-sided symmetrisation in the fit is considered to have negligible impact on the results of the measurement.

In a final step for the measurement of the inclusive cross-section, a *pruning* procedure removes systematics from the final fit if their impact is negligible. This increases the speed of the fit significantly, and also helps to groom plots and tables to make them more human-readable. The pruning is controlled with two separate thresholds for normalisation and shape effects. To find the optimal pruning thresholds for normalisation and shape, tests with different pruning scenarios were performed, documented in detail in Appendix H. The objective was to use pruning thresholds as low as necessary to not alter the sensitivity of the result, while reducing the number of nuisance parameters in the fit as much as possible. Following the studies, pruning

<sup>9</sup> The procedure to perform these Asimov fits is described in more detail in the following Section 7. The tests described here were performed with the ntuples v5.0 and all systematic uncertainties available at that time.

Table 8: Smoothing and symmetrisation applied to the various systematic uncertainties of the measurement. Systematic variations with both up and down variation are usually symmetrised via two-sided symmetrisation, or via maximum symmetrisation in the case of modelling uncertainties. Single systematic variations are symmetrised with one-sided symmetrisation to create a three-point uncertainty.

Systematic	Smoothing	Symmetrisation
$t\bar{t}\gamma \mu_R$	—	—
$t\bar{t}\gamma \mu_F$	—	—
$t\bar{t}\gamma$ PS model	✓	one-sided
$t\bar{t}\gamma$ PYTHIA8 var3c	✓	maximum
$t\bar{t}\gamma$ NNPDF variations	—	one-sided
$tW\gamma \mu_R$	—	—
$tW\gamma \mu_F$	—	—
$tW\gamma$ PS model	✓	one-sided
$t\bar{t}$ $\mu_R$ (shape)	—	—
$t\bar{t}$ $\mu_F$ (shape)	—	—
$t\bar{t}$ PS model (shape)	✓	one-sided
$t\bar{t}$ var3c (shape)	—	—
$t\bar{t}$ hdamp (shape)	✓	one-sided
all experimental, except:	—	two-sided
– CatRed JER data vs. MC	—	one-sided
– MET soft-track reso. par.	—	one-sided
– MET soft-track reso. perp.	—	one-sided

Table 9: Expected uncertainty of the  $t\bar{t}\gamma$  signal strength in percent for the nominal Asimov fit scenario with two-sided symmetrisation turned on as described in Table 8, and for an Asimov fit scenario with two-sided symmetrisation turned off. The tests were performed with ntuples v5.0 and all systematic uncertainties available at that time.

Model	Expected uncertainty
nominal fit (with symmetrisation)	6.257%
two-sided symmetrisation turned off	6.260%

872 thresholds of 0.05% for normalisation and 0.2% for shape were chosen, which each preserve approximately  
 873 40% of the systematics.

874 In the case of the differential cross-section the same sources of systematic uncertainty described below are  
 875 considered. The prefit systematic variations are used for the study since the measurement is still dominated  
 876 by statistical uncertainties. The systematic uncertainties are propagated to the measurement following the  
 877 approach of the previous measurement [15]: In the case of the systematic uncertainty sources related only to  
 878 the non- $t\bar{t}\gamma$ /non- $tW\gamma$  background prediction(ttbar, hfake, efake, prompt photon), the nominal histogram for  
 879 the corresponding background source is shifted by the uncertainty associated to the particular background  
 880 source. The unfolded distributions and compared with the nominal ones. In the case of the experimental  
 881 sources of systematic uncertainty, the nominal histogram is varied with the corresponding shift which  
 882 typically affect both shape and normalization on both the signal and backgrounds, then the resulting  
 883 histogram is unfolded and compared with the nominal unfolded distribution. The difference per bin  
 884 represents the uncertainty associated to that source. In the above cases, the unfolding core, which includes  
 885 the migration matrix, efficiency and migration, are kept to be nominal. For the sources of systematic  
 886 uncertainty related to  $t\bar{t}\gamma/tW\gamma$  modelling, the unfolding procedure is repeated using the alternative signal  
 887 sample (e.g. the parton shower and hadronisation uncertainty) or the nominal one with varied weights (e.g.  
 888 renormalisation and factorisation scales). This alternative prediction replaces the signal sample in all steps  
 889 of the analysis, this is, it used to perform the unfolding and to estimate the migrations out of the fiducial  
 890 phase space and efficiency. The unfolded result is compared to the reference result and the difference is  
 891 assigned to be the uncertainty (bin by bin).

892 The total uncertainty is calculated as the sum in quadrature of all these variations, for each bin of the  
 893 unfolded distribution.

## 894 6.1 Theoretical Uncertainties

895 For the main contributing processes to the analysis, namely  $t\bar{t}\gamma$ ,  $t\bar{t}$  and  $tW\gamma$ , alternative generator scenarios  
 896 are tested for the simulation. These alternative scenarios are then used as systematic variations. In addition,  
 897 overall normalisation uncertainties are assigned to the background categories. Almost all modelling  
 898 uncertainties use smoothing including the pre-smoothing step. The following subsections will give an  
 899 overview of the assigned systematics.

### 900 $t\bar{t}\gamma$ modelling

901 All modelling uncertainties for the  $t\bar{t}\gamma$  signal are normalised to the fiducial cross-section as predicted by  
 902 the nominal prediction to avoid dependencies on the MC-generated phase space. However, differences

Not reviewed, for internal circulation only

in rate and shape might still occur through differences in reconstruction efficiency and migration effects. Therefore, templates are created for all variations of the  $t\bar{t}\gamma$  simulation with both normalisation and shape components. The resulting rate differences are identical to the relative uncertainties on  $C$ , as quoted in Table 7 in Section 5.

The effect of the choices of the renormalisation ( $\mu_R$ ) and factorisation ( $\mu_F$ ) scales are estimated by varying  $\mu_R$  and  $\mu_F$  separately up and down by a factor of 2 with respect to the nominal sample value, thus resulting in two three-point uncertainties. The variations are done by altering event weights to reduce the effect of statistical fluctuations. No smoothing and symmetrisation methods are applied to the variations. The resulting distributions are shown in Figures 9 and 10.

The uncertainty on the parton shower and hadronisation model ( $t\bar{t}\gamma$  PS model) is estimated by comparing the  $t\bar{t}\gamma$  nominal samples, produced with MG5 + PYTHIA8, with showering by HERWIG7. The same MG5 events are used in the shower. One-sided symmetrisation and smoothing including pre-smoothing are applied, the resulting variations are shown in Figure 11.

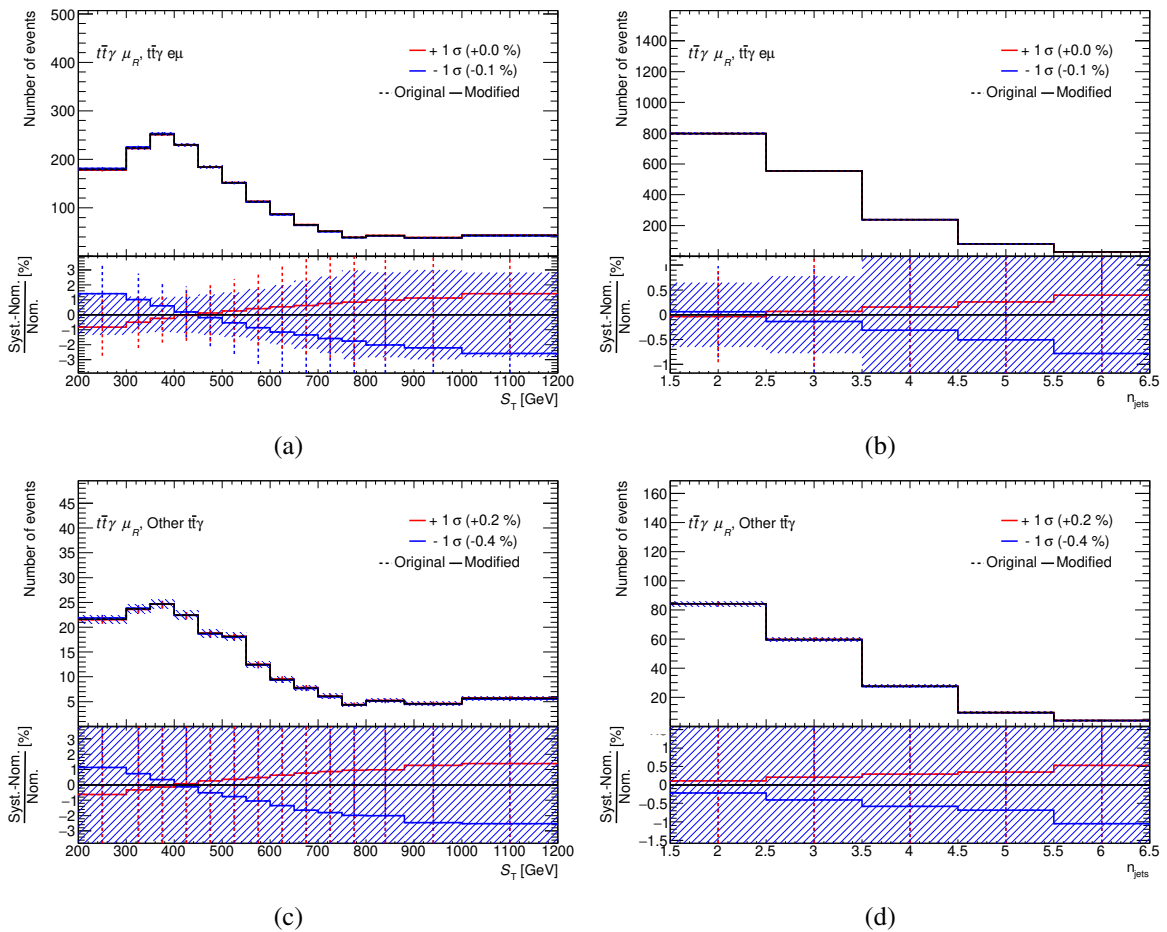


Figure 9: Systematic variations to describe the  $t\bar{t}\gamma$  variation of the  $\mu_R$  scale. The red and blue lines represent the up/down variations with respect to the nominal distribution in black. Shown are the variations for (a) + (b) the  $t\bar{t}\gamma$   $e\mu$  category, and (c) + (d) the *Other  $t\bar{t}\gamma$*  category, both for the total transverse energy of the event  $S_T$  on the left-hand side, and the jet multiplicity on the right-hand side.

Not reviewed, for internal circulation only

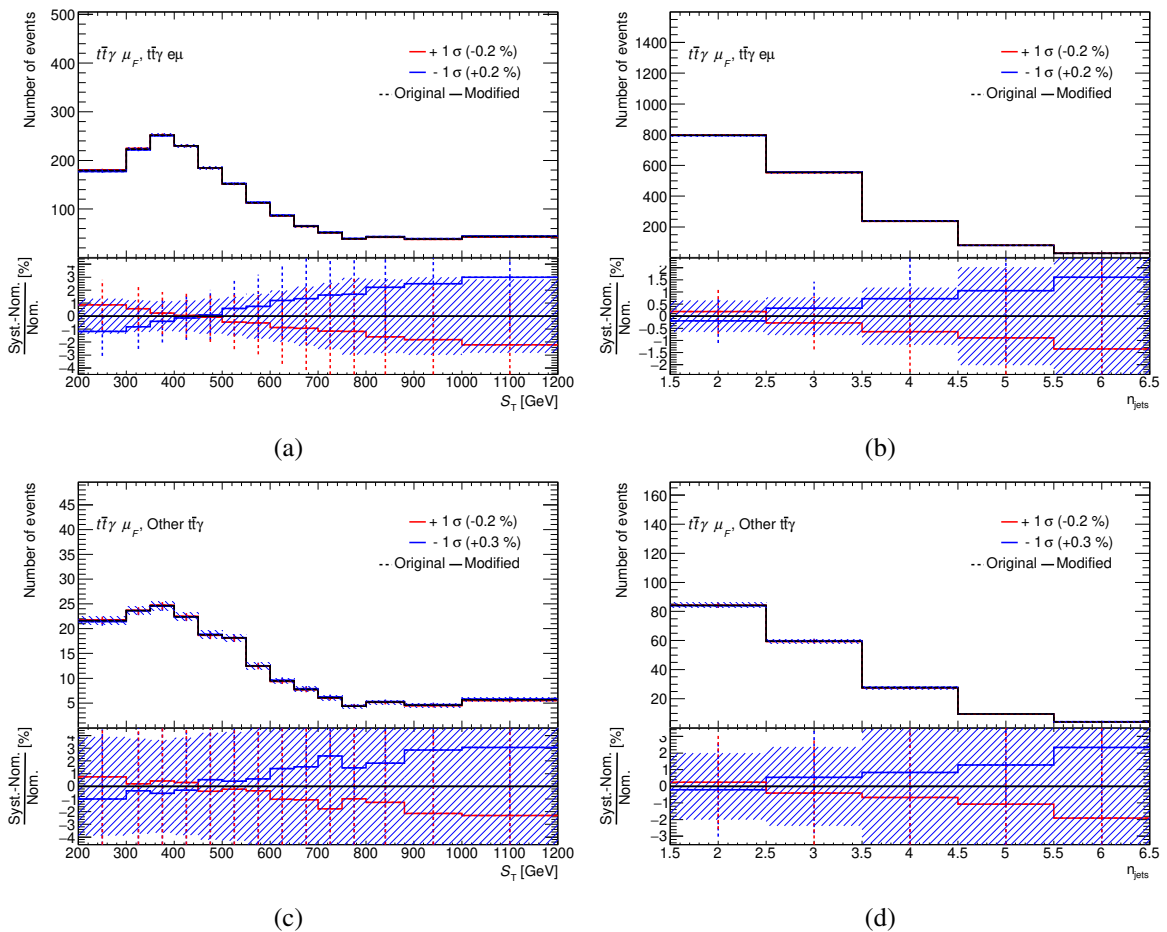


Figure 10: Systematic variations to describe the  $t\bar{\gamma}$  variation of the  $\mu_F$  scale. The red and blue lines represent the up/down variations with respect to the nominal distribution in black. Shown are the variations for (a) + (b) the  $t\bar{\gamma} \mu_F$ ,  $t\bar{\gamma} e\mu$  category, and (c) + (d) the *Other  $t\bar{\gamma}$*  category, both for the the total transverse energy of the event  $S_T$  on the left-hand side, and the jet multiplicity on the right-hand side.

916 The uncertainty on ISR and FSR is estimated through dedicated  $t\bar{\gamma}\gamma$  samples produced with MG5 +  
 917 PYTHIA8, where the *A14 var3c* eigentune of PYTHIA for low and high radiation scenarios is implemented  
 918 ( $t\bar{\gamma}\gamma$  *var3c*). These events are compared against the nominal MG5 + PYTHIA8 production with the standard  
 919 *A14* tune as detailed in Section 3. As the variations are prone to large statistical fluctuations, the *maximum*  
 920 symmetrisation method is chosen. Then smoothing including pre-smoothing is applied. The resulting  
 921 variations are shown in Figure 12.

922 The simulation of the  $t\bar{\gamma}\gamma$  signal uses the NNPDF2.3LO PDF set, and uncertainties on this choice are  
 923 considered as well. The signal simulation comes with 100 sampled variations of the PDF set, which are  
 924 stored as additional weights in the used samples. Their effect is calculated by constructing an Asimov dataset  
 925 for each of these sampled variations, and then performing 100 individual fits with the nominal prediction  
 926 against each of them. The resulting fitted distributions of  $S_T$  are accumulated and the standard deviation  
 927 of the ensemble with respect to the nominal fitted distribution is calculated bin by bin. This resulting  
 928 distribution of bin-by-bin standard deviations enters the fit after applying one-sided symmetrisation. The  
 929 distributions are shown in Figure 13. As they enter the fit as a standard nuisance parameter, their bin-by-bin

Not reviewed, for internal circulation only

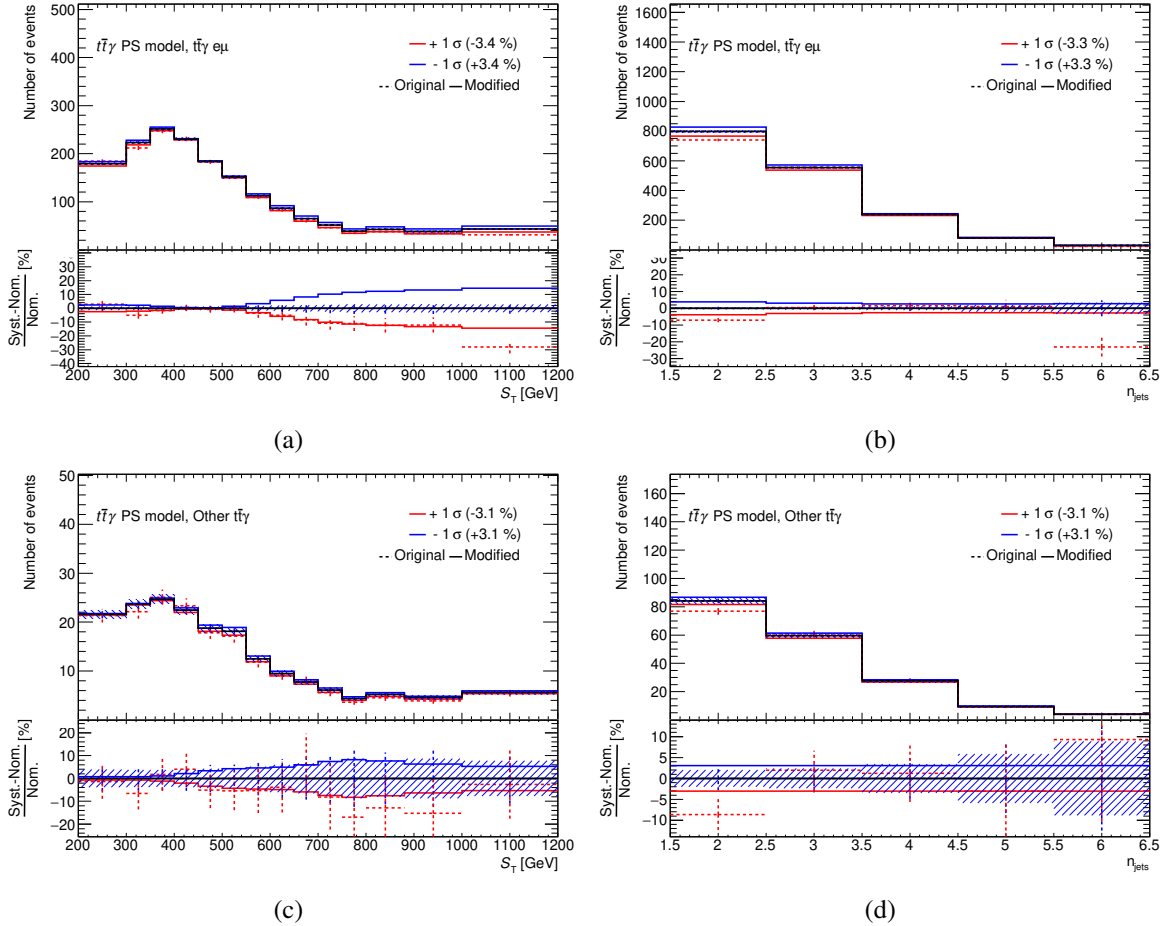


Figure 11: Systematic uncertainties on the choice of the PS model for  $t\bar{t}\gamma$ . The dotted points show the systematic variations with respect to the nominal distribution in black. The red and blue lines represent the resulting up/down variations after symmetrisation and smoothing including pre-smoothing. Shown are the variations for (a) + (b) the  $t\bar{t}\gamma$  e $\mu$  category, and (c) + (d) the Other  $t\bar{t}\gamma$  category, both for the the total transverse energy of the event  $S_T$  on the left-hand side, and the jet multiplicity on the right-hand side.

Not reviewed, for internal circulation only

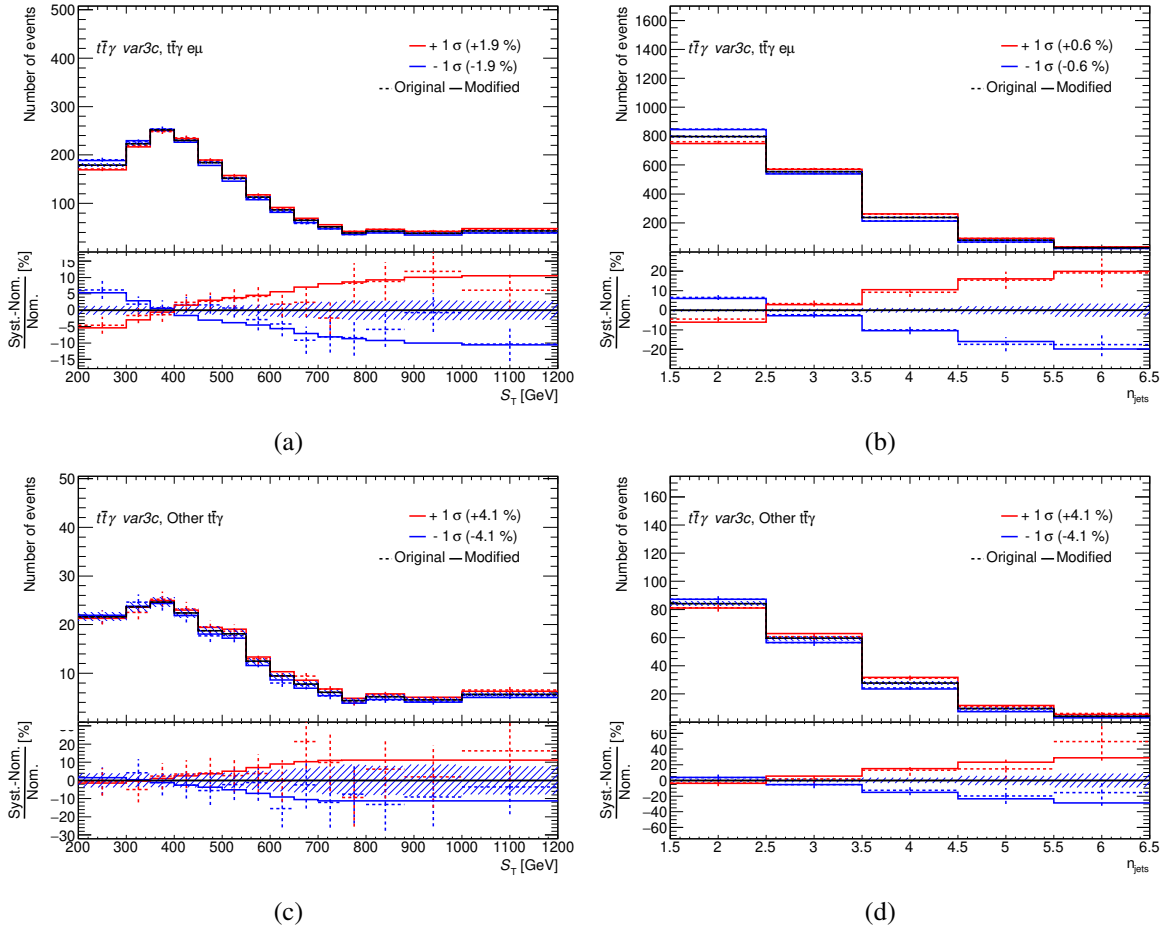


Figure 12: Systematic uncertainties on ISR and FSR in  $t\bar{\gamma}$  ( $t\bar{\gamma} \text{ var3c}$ ). The dotted points show the systematic variations with respect to the nominal distribution in black. The red and blue lines represent the resulting up/down variations after *maximum symmetrisation* and smoothing. Shown are the variations for (a) + (b) the  $t\bar{\gamma} e\mu$  category, and (c) + (d) the *Other  $t\bar{\gamma}$*  category, both for the total transverse energy of the event  $S_T$  on the left-hand side, and the jet multiplicity on the right-hand side.

Not reviewed, for internal circulation only

variations are assumed to be fully correlated. In an alternative scenario, the bins were decorrelated, effectively assigning a Gaussian prior the size of the calculated bin-by-bin uncertainties shown in Figure 13 to all bins. The expected uncertainty on the  $t\bar{t}\gamma$  signal strength was calculated for this scenario and compared to that with correlated bins. Differences in the expected uncertainties were found only in the fifth significant digit, hence, the correlation/decorrelation of bins is considered to have a negligible impact on the result.

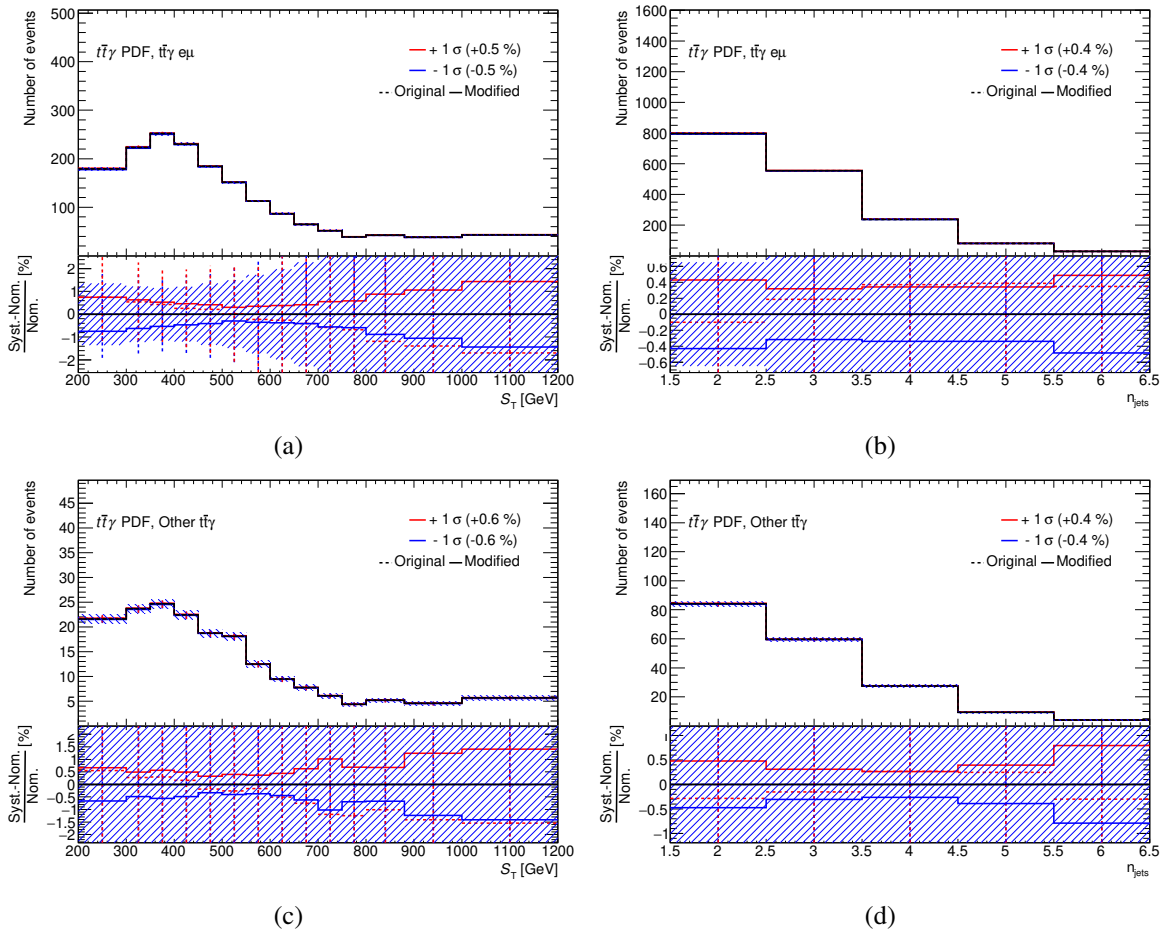


Figure 13: Systematic uncertainties on the PDF choice for  $t\bar{t}\gamma$ . The red and blue lines show the systematic variations with respect to the nominal distribution in black. Shown are the variations for (a) + (b) the  $t\bar{t}\gamma$   $e\mu$  category, and (c) + (d) the *Other  $t\bar{t}\gamma$*  category, both for the total transverse energy of the event  $S_T$  on the left-hand side, and the jet multiplicity on the right-hand side.

### 936 $tW\gamma$ modelling

937 As done for  $t\bar{t}\gamma$ , all modelling uncertainties for  $tW\gamma$  are normalised to the fiducial cross-section as predicted  
 938 by the nominal prediction to avoid dependencies on the MC-generated phase space. However, differences  
 939 in rate and shape might still occur through differences in reconstruction efficiency and migration effects.  
 940 Therefore, templates are created for all variations of the  $tW\gamma$  simulation with both normalisation and shape  
 941 components. The resulting rate differences are identical to the relative uncertainties on  $C$ , as quoted in  
 942 Table 7 in Section 5.

943 Uncertainties on the scale choices are estimated by varying  $\mu_R$  and  $\mu_F$  separately up and down by a factor  
 944 of 2 with respect to the nominal sample value, thus resulting in two three-point uncertainties. The variations  
 945 are done by altering event weights to reduce the effect of statistical fluctuations. No smoothing and  
 946 symmetrisation methods are applied to the variations. The resulting distributions are shown in Figures 14  
 947 and 15.

948 The uncertainties on the parton shower and hadronisation model ( $tW\gamma$  PS model) are estimated by comparing  
 949 the nominal  $tW\gamma$  samples with alternative showering by HERWIG7. The same MADGRAPH5\_aMC@NLO  
 950 events are used in the shower. One-sided symmetrisation and smoothing including pre-smoothing are  
 951 applied, the resulting variations are shown in Figure 16.

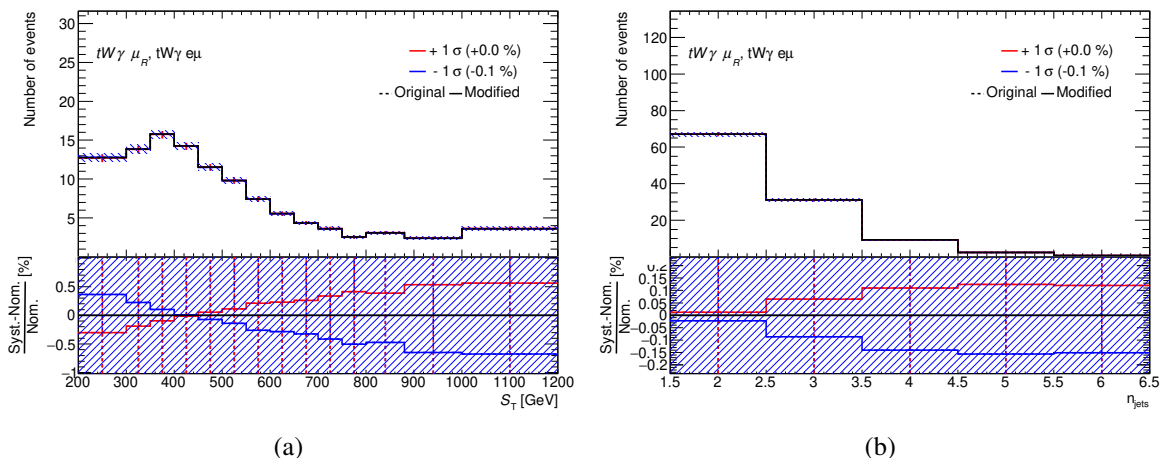


Figure 14: Systematic variations to describe the  $tW\gamma$  variation of the  $\mu_R$  scale. The red and blue lines represent the up/down variations with respect to the nominal distribution in black. Shown are the variations for (a) the total transverse energy of the event  $S_T$ , and (b) the jet multiplicity.

Not reviewed, for internal circulation only

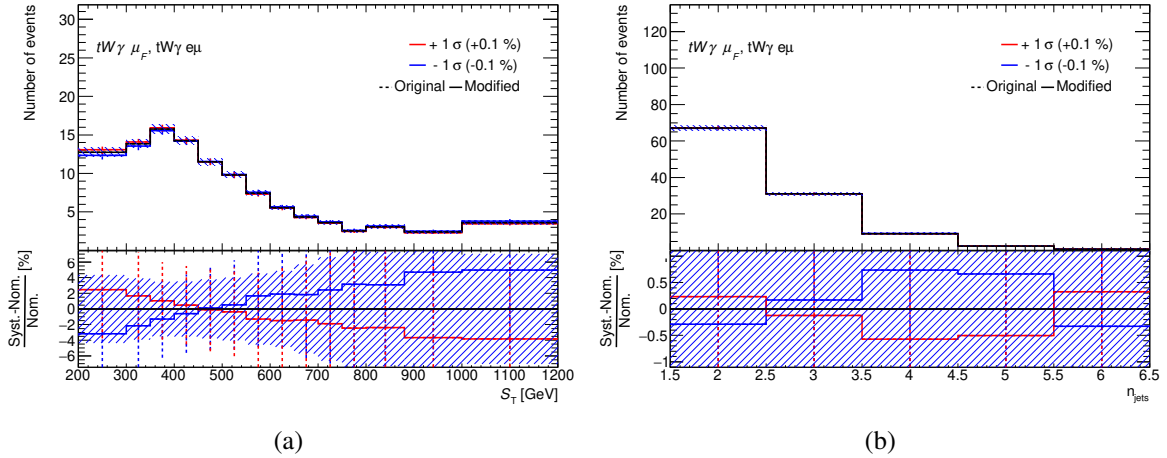


Figure 15: Systematic variations to describe the  $tW\gamma$  variation of the  $\mu_F$  scale. The red and blue lines represent the up/down variations with respect to the nominal distribution in black. Shown are the variations for (a) the total transverse energy of the event  $S_T$ , and (b) the jet multiplicity.

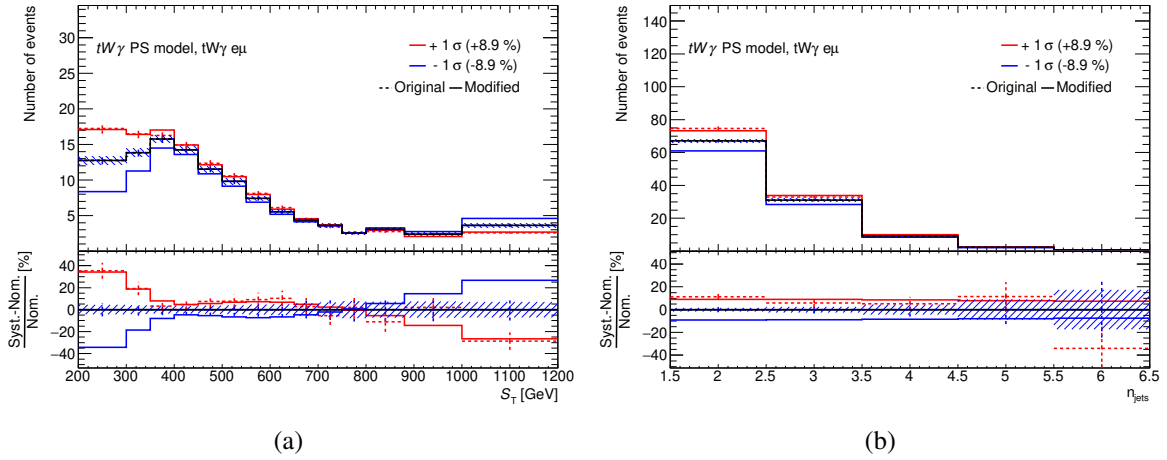


Figure 16: Systematic uncertainties on the choice of the PS model for  $tW\gamma$ . The dotted points show the systematic variations with respect to the nominal distribution in black. The red and blue lines represent the resulting up/down variations after symmetrisation and smoothing including pre-smoothing. Shown are the variations for (a) the total transverse energy of the event  $S_T$ , and (b) the jet multiplicity.

## 952 $t\bar{t}$ modelling

953 Various systematic variations are considered for the modelling of  $t\bar{t}$  processes. As this process contributes  
 954 significantly to both h-fake photons and the prompt  $\gamma$  category, all systematics are evaluated on both of  
 955 these categories simultaneously (correlated through one common nuisance parameter). The variations  
 956 for  $t\bar{t}$  have negligible impact on e-fake photons considering the small number of expected events in that  
 957 category, and the large statistical uncertainties.

958 Both the h-fake and prompt  $\gamma$  categories have a global normalisation uncertainty assigned already. To  
 959 ensure little correlation between these and the  $t\bar{t}$  modelling variations, the  $t\bar{t}$  modelling variations are  
 960 considered as *shape only* (i.e. the normalisation component is dropped). In addition, the  $t\bar{t}$  systematics  
 961 not obtained through reweighting have low event numbers and suffer from large statistical fluctuations.  
 962 Therefore, their shape effect is amplified by a factor 3 to account for possible shape uncertainties hidden by  
 963 the lack of statistics. However, this amplification possibly causes an overestimation of the  $t\bar{t}$  shape effects.  
 964 To verify that this approach does not have any significant impact on the result, Asimov fit scenarios were  
 965 created with various  $t\bar{t}$  shape models: (1) with the 3x-amplified shape effects described above, (2) with  
 966 the nominal shape effects (no amplification), (3) without  $t\bar{t}$  systematics.<sup>10</sup> To evaluate the impact on the  
 967 fit result, the expected uncertainty on the  $t\bar{t}\gamma$  signal strength was evaluated for all three fit scenarios, the  
 968 results of which are shown in Table 10. Compared to the scenario without  $t\bar{t}$  systematics, the expected  
 969 uncertainty increases slightly in the amplified scenario, but not significantly. Hence, the amplified shape  
 970 scenario is chosen for the measurement to cover possible  $t\bar{t}$  shape effects in a conservative manner.

971 The effect of the choices of the renormalisation ( $\mu_R$ ) and factorisation ( $\mu_F$ ) scales are estimated by varying  
 972  $\mu_R$  and  $\mu_F$  separately up and down by a factor of 2 with respect to the nominal sample value, thus resulting  
 973 in two three-point uncertainties. The variations are done by altering event weights to reduce the effect  
 974 of statistical fluctuations. No smoothing and symmetrisation methods are applied to the variations. The  
 975 resulting distributions for the shape-only variations are shown in Figures 17 and 18.

976 The uncertainties on the parton shower and hadronisation model ( $t\bar{t}$  PS model) are estimated by comparing  
 977 the nominal  $t\bar{t}$  samples with alternative showering by HERWIG7. The same POWHEG events are used in  
 978 the shower. One-sided symmetrisation and smoothing including pre-smoothing are applied, the resulting  
 979 variations are shown in Figure 19.

980 Uncertainties on ISR and FSR are estimated by comparing the nominal POWHEG + PYTHIA8 sample against  
 981 two sets of event weights produced with higher and lower radiation scenarios with the PYTHIA A14 var3c

<sup>10</sup> The procedure to perform these Asimov fits is described in more detail in the following Section 7. The tests in *this* section were performed with the ntuples v5.0 and all systematic uncertainties available at that time.

Table 10: Expected uncertainty of the  $t\bar{t}\gamma$  signal strength in percent for different  $t\bar{t}$  systematics scenarios. In the first two models, the  $t\bar{t}$  systematics are considered as *shape only*, once with a 3x amplification of the shape effects, once without. The last scenario shows the expected uncertainty if a fit is performed without  $t\bar{t}$  systematics.

Model	Expected uncertainty
shape only (3x)	6.257%
shape only (1x)	6.208%
no $t\bar{t}$ systematics	6.203%

Not reviewed, for internal circulation only

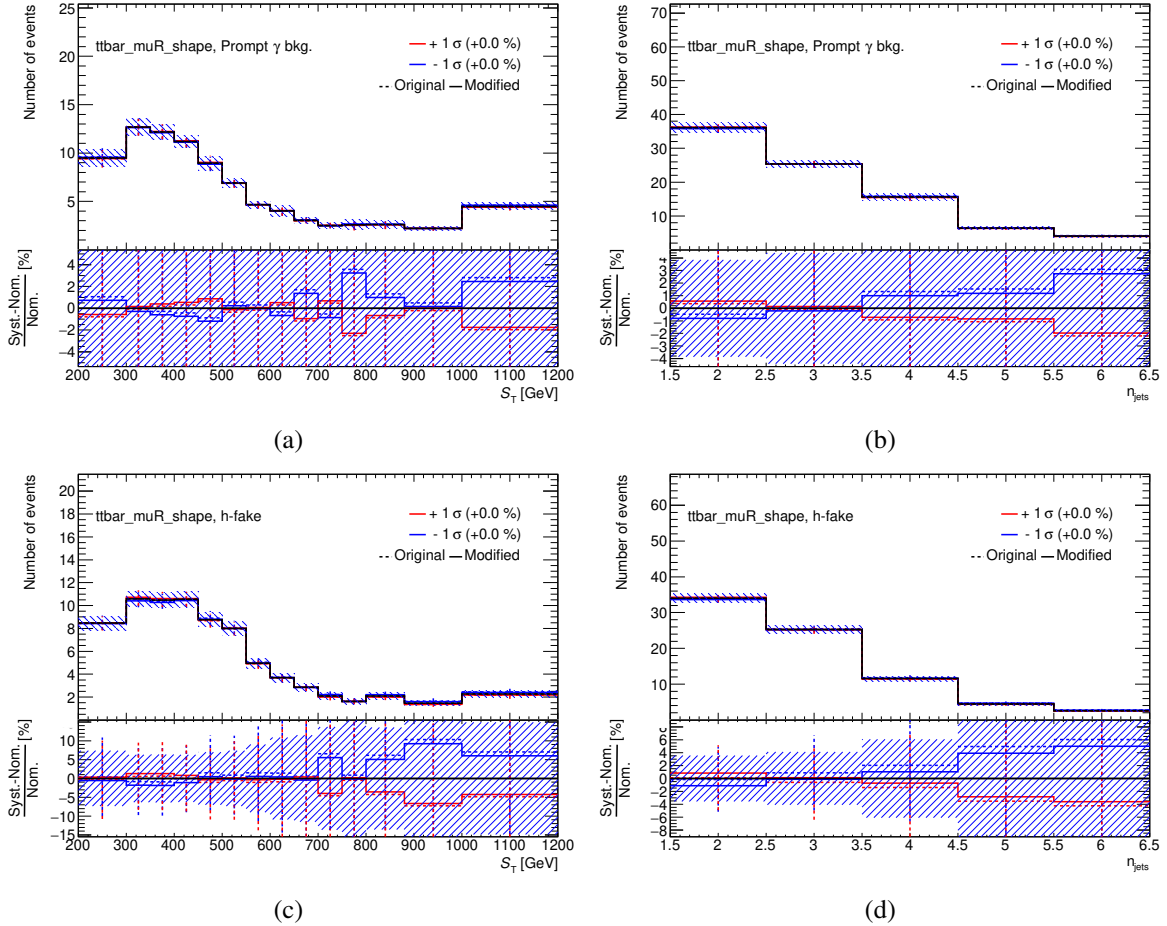


Figure 17: Systematic variations to describe the  $t\bar{t}$  variation of the  $\mu_R$  scale. The dotted points show the systematic variations with respect to the nominal distribution in black. The red and blue lines represent the up/down variations after their normalisation components are dropped. Shown are the variations for (a) + (b) the prompt  $\gamma$  category, and (c) + (d) h-fake photons, both for the total transverse energy of the event  $S_T$  on the left-hand side, and the jet multiplicity on the right-hand side.

Not reviewed, for internal circulation only

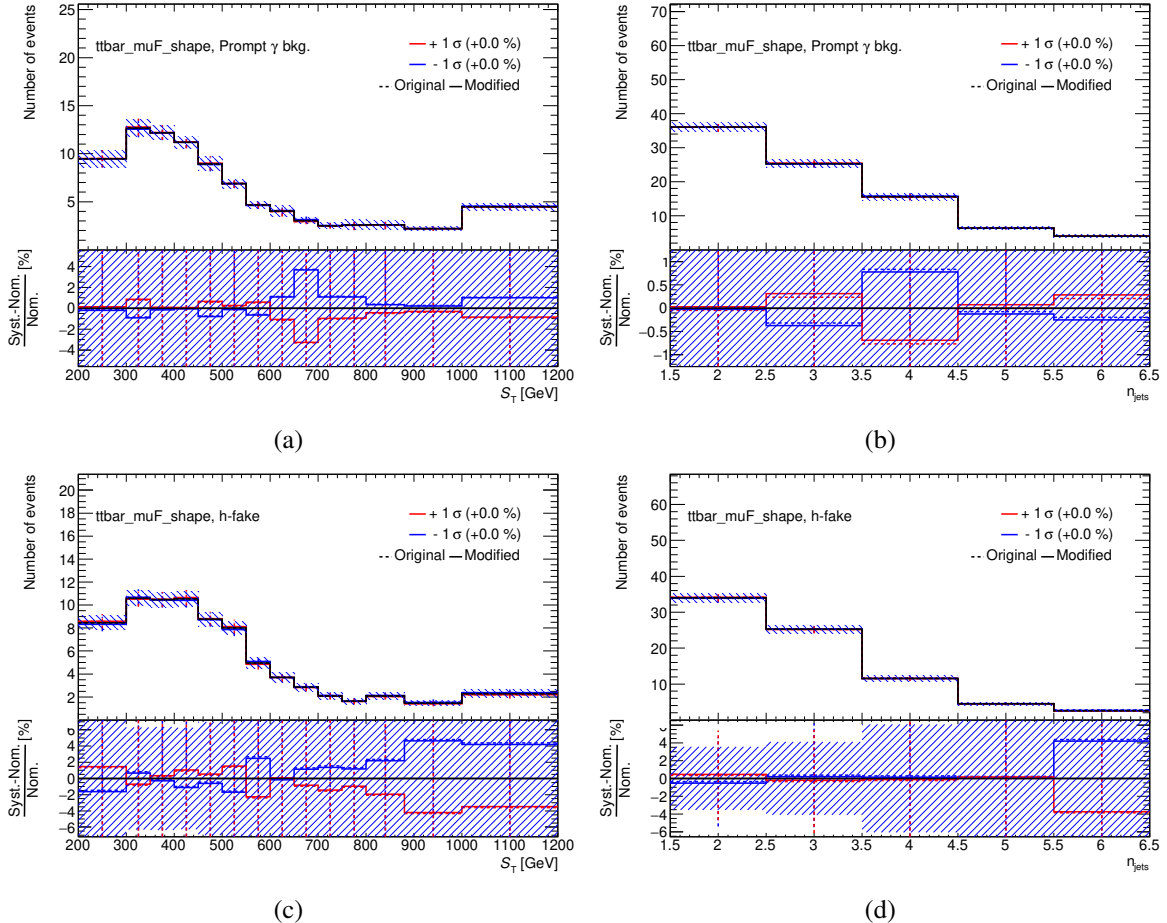


Figure 18: Systematic variations to describe the  $t\bar{t}$  variation of the  $\mu_F$  scale. The dotted points show the systematic variations with respect to the nominal distribution in black. The red and blue lines represent the up/down variations after their normalisation components are dropped. Shown are the variations for (a) + (b) the prompt  $\gamma$  category, and (c) + (d) h-fake photons, both for the total transverse energy of the event  $S_T$  on the left-hand side, and the jet multiplicity on the right-hand side.

Not reviewed, for internal circulation only

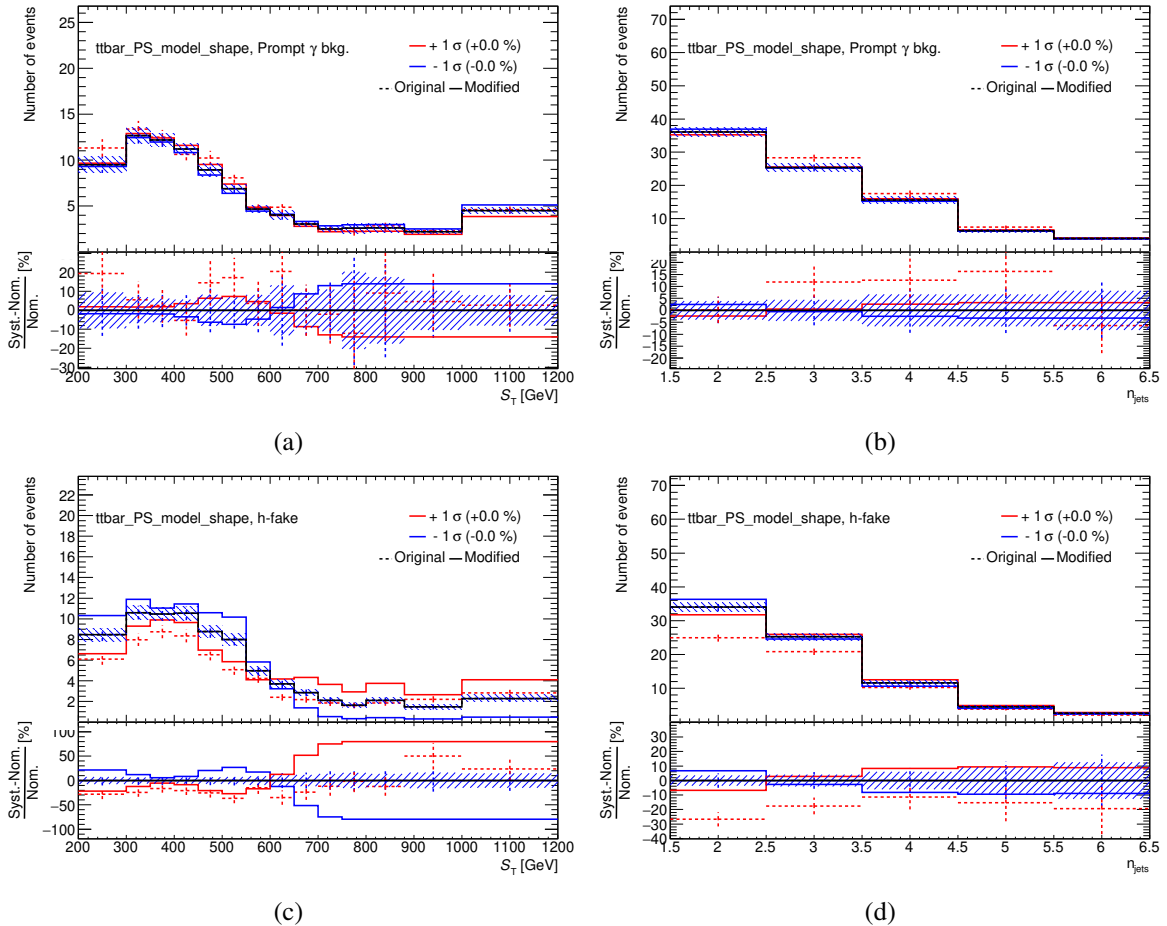


Figure 19: Systematic uncertainties on the PS model choice for  $t\bar{t}$ , as an alternative performed with HERWIG7. The dotted points show the systematic variations with respect to the nominal distribution in black. The red and blue lines represent the resulting up/down variations after symmetrisation and smoothing including pre-smoothing. Note that only the shape is considered for  $t\bar{t}$  variations, and that the shape effect is amplified by a factor 3. Shown are the variations for (a) + (b) the prompt  $\gamma$  category, and (c) + (d) h-fake photons, both for the total transverse energy of the event  $S_T$  on the left-hand side, and the jet multiplicity on the right-hand side.

982 eigentune ( $t\bar{t}$  var3c). No symmetrisation or smoothing methods are applied. The resulting variations are  
 983 shown in Figure 20.

984 An additional uncertainty is considered for  $t\bar{t}$ , where the *hdamp* parameter of PowHEG to control the  
 985 first emission is varied. An alternative set of events is generated with PowHEG + PYTHIA8 with the  
 986 parameter set to twice its nominal value, which is then compared against the nominal prediction. One-sided  
 987 symmetrisation and smoothing including pre-smoothing are applied, the resulting variations are shown in  
 988 Figure 21.

Not reviewed, for internal circulation only

## 989 Other theoretical uncertainties

990 In addition to the process-specific modelling uncertainties described above, global normalisation uncertainties  
 991 are assigned to the three background categories: h-fake photons, e-fake photons and prompt  $\gamma$ . The  
 992 assumed normalisation uncertainty for each category is  $\pm 50\%$  with a Gaussian prior.

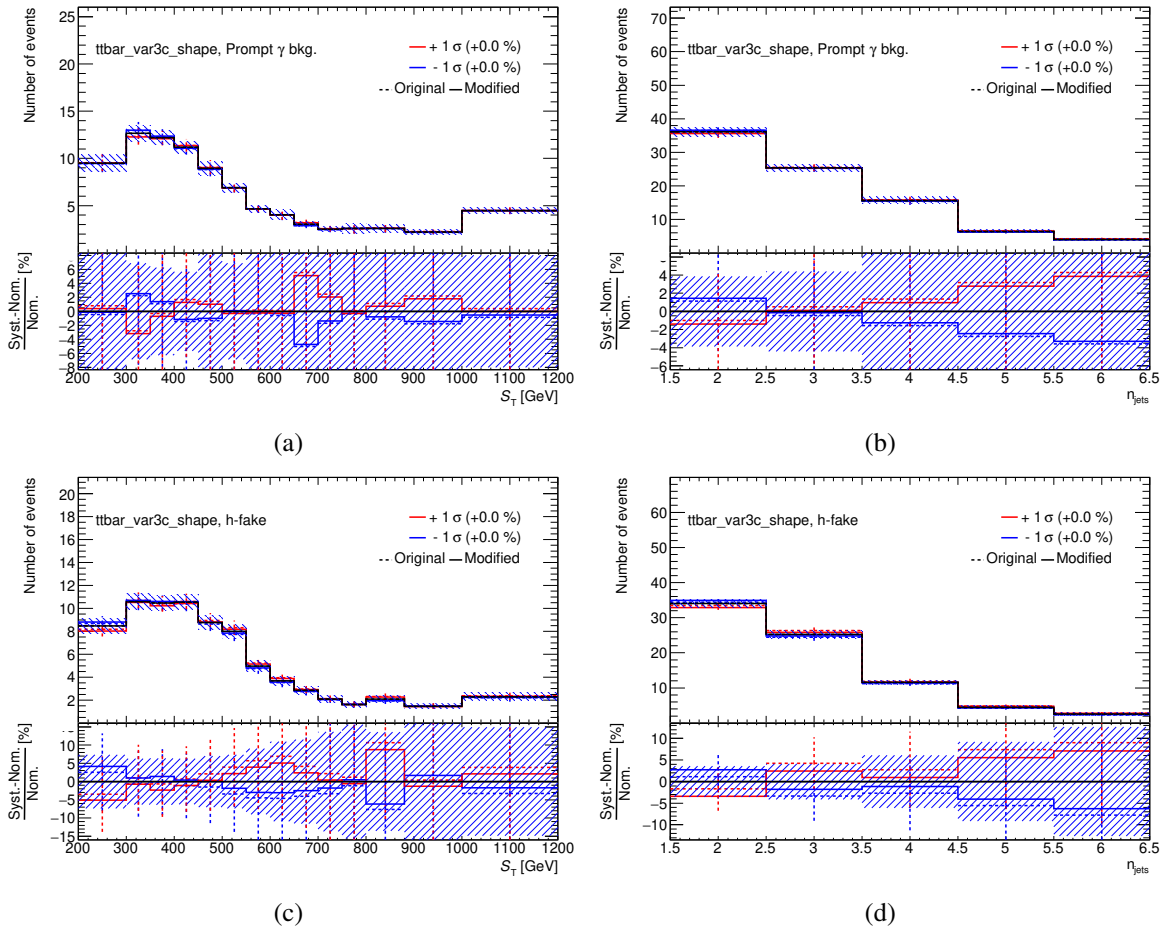


Figure 20: Systematic uncertainties on ISR and FSR in  $t\bar{t}$  ( $t\bar{t}$  var3c). The dotted points show the systematic variations with respect to the nominal distribution in black. The red and blue lines represent the resulting up/down variations after their normalisation components are dropped. Shown are the variations for (a) + (b) the prompt  $\gamma$  category, and (c) + (d) h-fake photons, both for the total transverse energy of the event  $S_T$  on the left-hand side, and the jet multiplicity on the right-hand side.

Not reviewed, for internal circulation only

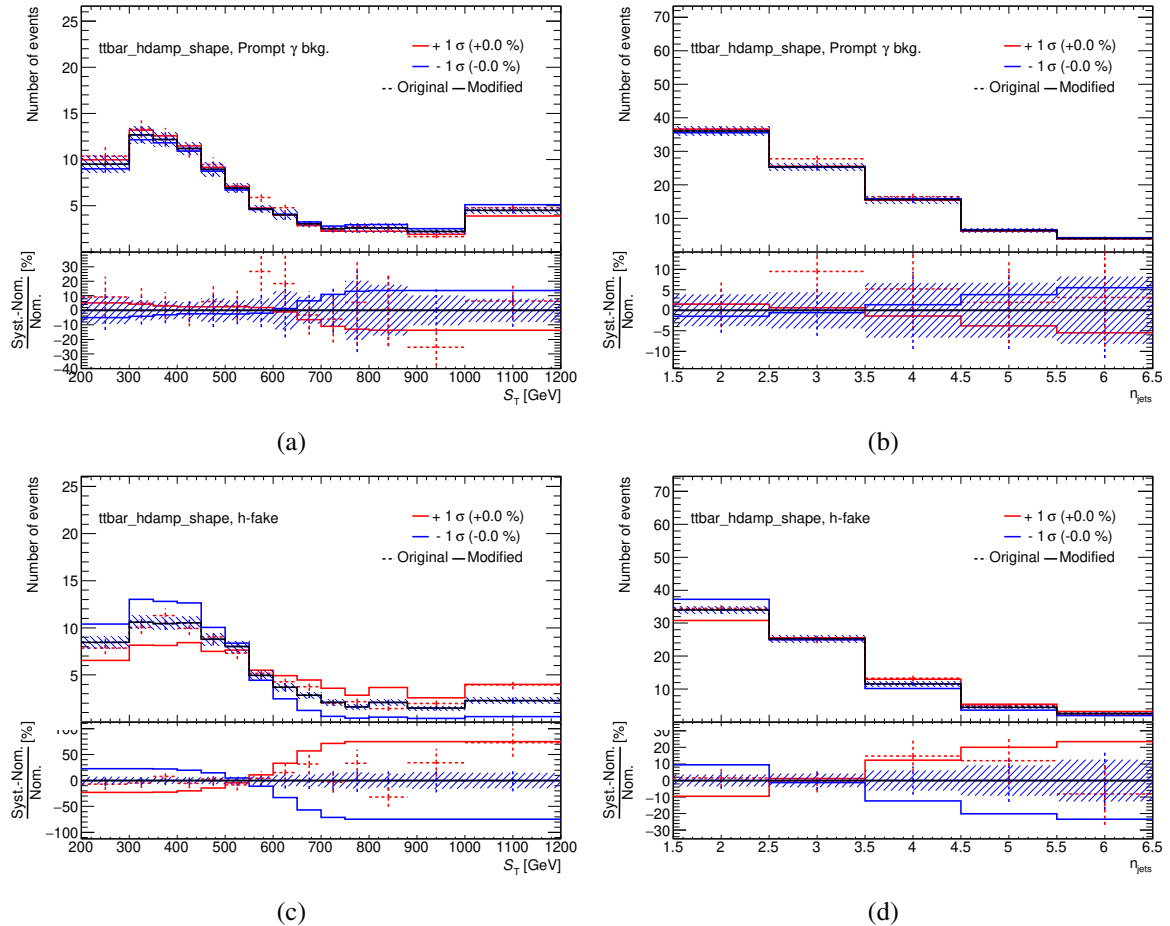


Figure 21: Systematic uncertainties on the choice of the  $hdamp$  parameter for  $t\bar{t}$  ( $t\bar{t}$   $hdamp$ ). The dotted points show the systematic variations with respect to the nominal distribution in black. The red and blue lines represent the resulting up/down variations after symmetrisation and smoothing including pre-smoothing. Note that only the shape is considered for  $t\bar{t}$  variations, and that the shape effect is amplified by a factor 3. Shown are the variations for (a) + (b) the prompt  $\gamma$  category, and (c) + (d) h-fake photons, both for the total transverse energy of the event  $S_T$  on the left-hand side, and the jet multiplicity on the right-hand side.

## 6.2 Experimental Uncertainties

Experimental uncertainties common to signal and background processes and their treatment are summarised in this section. These include reconstruction and identification efficiency uncertainties for the reconstructed physics objects in the analysis, including leptons, photons, jets and  $E_T^{\text{miss}}$ , but also uncertainties on the scales and resolutions of momenta and energies. In addition, uncertainties on flavour-tagging of jets, the jet vertex fraction, the integrated luminosity value and the pile-up simulation are considered.

### Lepton uncertainties

Lepton *efficiency* refers to the reconstruction and identification efficiencies, isolation efficiency as well as the trigger efficiency. For Monte-Carlo samples, these efficiencies are corrected by applying scale factors, calculated as the ratio between the efficiencies measured in data and those in simulation using the tag-and-probe method in  $Z \rightarrow ee$  and  $J/\Psi \rightarrow ee$  decays for electrons, as well as  $Z \rightarrow \mu\mu$  decays for muons. These scale factors, which vary with  $E_T^{\text{miss}}$  and  $\eta$ , are varied up and down by one standard deviation to study the impact of lepton efficiency uncertainties on the analysis result [56, 69].

The measured lepton energy/momenta is calibrated using Monte-Carlo-based techniques. Correction factors, derived from the study of dileptonic decays of the  $Z$  boson, are applied to correct possible detector mis-modelling in the calibration. These correction factors, are varied up and down by one standard deviation to study the lepton energy (momentum) scale uncertainty. As an example, these systematic variations of the identification correction factors are shown in Figure 22 for electrons. For electrons, the energy scale and resolution are calculated in conjunction with those of photons and are called  $e/\gamma$  scale and resolution.

### Photon uncertainties

The scale factor for the photon ID efficiency is derived from three measurements: the radiative  $Z$  boson method using a sample enriched in events with radiative  $Z$  boson decays, the electron extrapolation

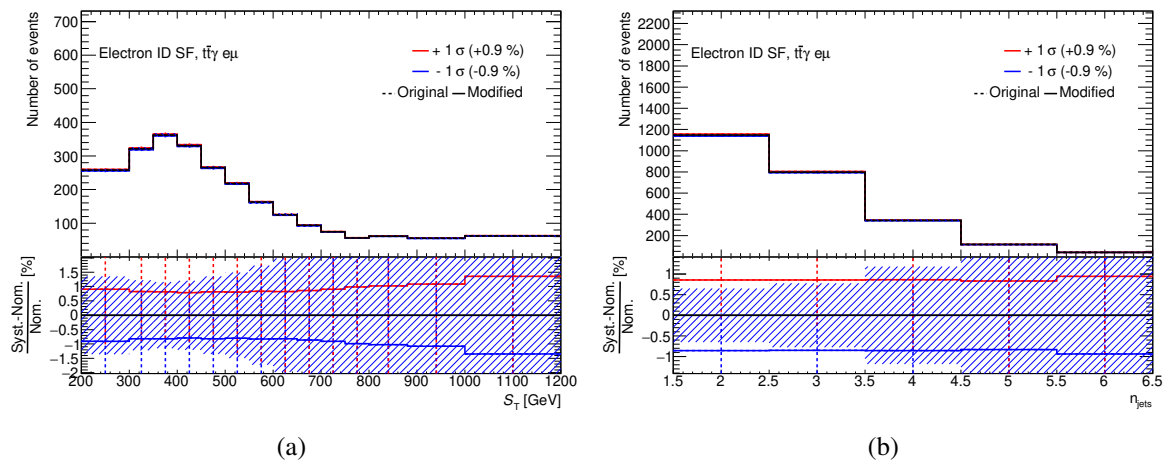


Figure 22: Systematic variations of the electron identification scale factor for the  $t\bar{t}\gamma$  signal. Shown are the variations for (a) the total transverse energy of the event  $S_T$ , and (b) the jet multiplicity.

technique using a sample enriched in  $Z \rightarrow ee$  events where the similarity between electrons and photons in the detector is exploited, and the matrix method using a sample enriched with isolated, high- $pT$  photons and exploiting that the narrow-strip variables are only weakly correlated to the isolation. The scale factor is computed as the ratio of the efficiency measured in data and that determined in simulation. The sets of scale factors of all measurements are combined into one single set that is applied to simulation to correct for deviations between efficiencies measured in data and found in simulation. The scale factors for photon isolation were measured in Ref. [70]. These scale factors are varied up and down by one standard deviation to study their impact on the analysis. As an example, Figure 23 shows the systematic variations of the photon identification scale factor.

The photon energy calibration and the study of its scale and resolution uncertainties are calculated together with the electrons as  $e/\gamma$  scale and resolution, the first of which are shown in Figure 24.

Not reviewed, for internal circulation only

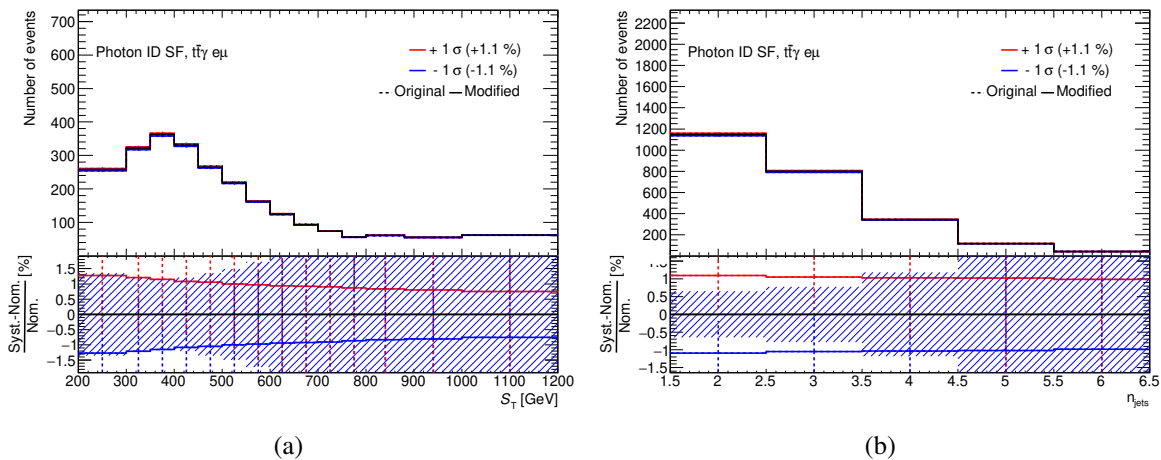


Figure 23: Systematic variations of the photon identification scale factor for the  $t\bar{t}\gamma$  signal. Shown are the variations for (a) the total transverse energy of the event  $S_T$ , and (b) the jet multiplicity.

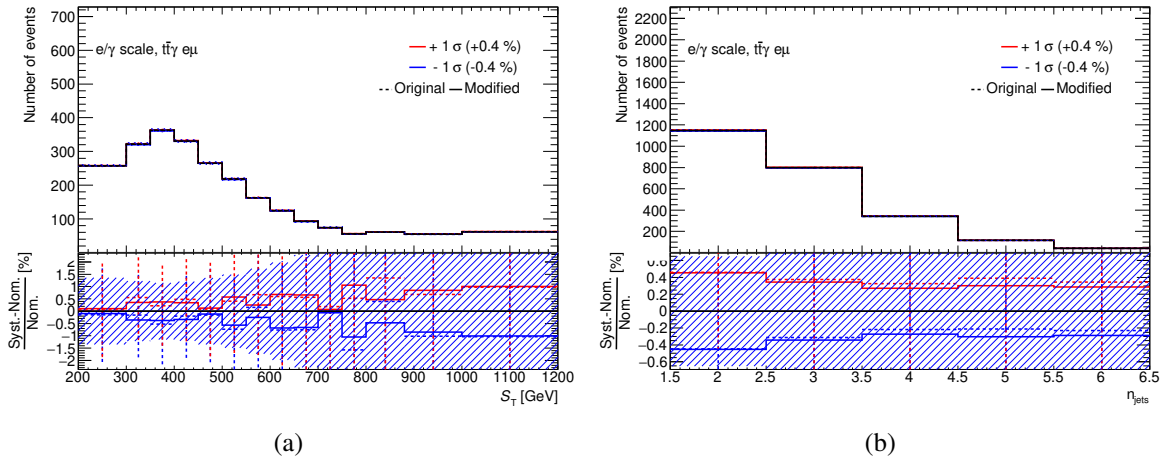


Figure 24: Systematic variations of the  $e/\gamma$  scale for the  $t\bar{t}\gamma$  signal. Shown are the variations for (a) the total transverse energy of the event  $S_T$ , and (b) the jet multiplicity.

## 1027 Jet uncertainties

1028 The jet energy calibration, called jet energy scale (JES), used in this analysis follows the *category reduction*  
 1029 *scheme* with a total of 30 nuisance parameters [61, 71]. The calibration is done in several steps, combining  
 1030 Monte-Carlo simulation and *in situ* measurements, to correct for topo-cluster energy, pile-up effects, etc.  
 1031 Its uncertainty is split into several independent categories: modelling and statistical uncertainties on the  
 1032 extrapolation of the jet calibration from the central region, jet flavour composition, high- $p_T$  jet behaviour,  
 1033  $b$ -jet energy scale uncertainties, uncertainties due to pile-up, uncertainties on *in situ* jet energy corrections,  
 1034 etc. In one category, there are usually more than one physical source of the uncertainty. To study the JES  
 1035 uncertainty, each source is varied up and down independently by its corresponding uncertainty. Figure 25  
 1036 shows the variations of one of the nuisance parameters of the category reduction scheme, the pile-up *rho*  
 1037 *topology*.

1038 The jet energy resolution (JER) is measured using the balance between jets and well measured objects like  
 1039 photons or Z bosons, and it is found to be in agreement between data and MC. There are a total of seven  
 1040 effective nuisance parameters associated to JER in the category reduction scheme, and a single source of  
 1041 uncertainty for the agreement between data and Monte Carlo, all of which are varied by one sigma to study  
 1042 their impact on the analysis.

1043 The systematic uncertainty associated to the jet vertex tagging (JVT) is obtained by varying up and down  
 1044 the JVT cut using the *JetVertexTaggerTool* [62]. The systematic variations of the JVT nuisance parameter  
 1045 are shown in Figure 26.

## 1046 $b$ -tagging uncertainties

1047 Jets coming from a  $b$ -quarks have their own topological features, and  $b$ -tagging allows to distinguish  
 1048 them from light-flavour jets. With *pseudo-continuous*  $b$ -tagging, each jet can be assigned to a different  
 1049 working point, and the  $b$ -tagging uncertainties on this jet are derived for this specific working point. They  
 1050 are accounted for by varying the calibration scale factors for  $b$ -,  $c$ -, and light-flavour jets up and down by

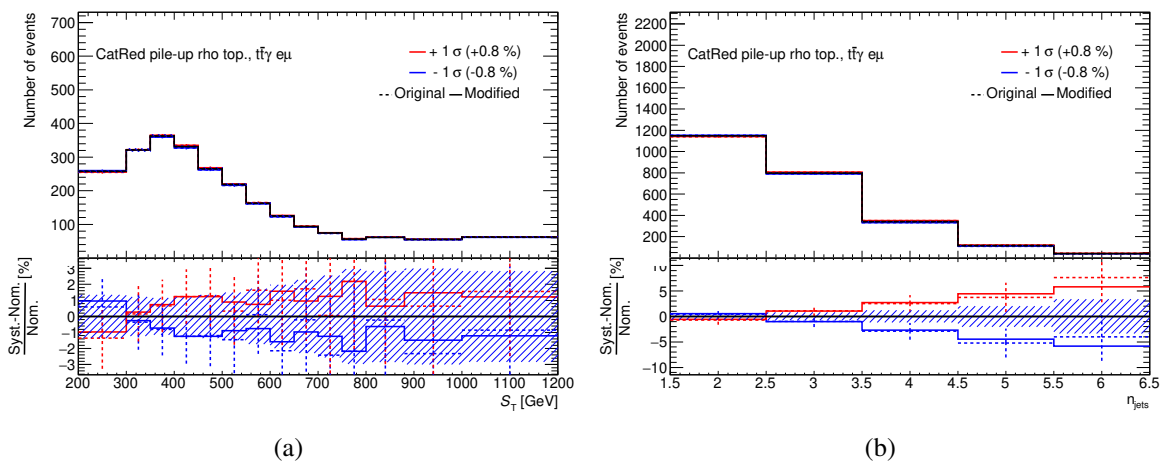


Figure 25: Systematic variations of the pile-up *rho topology* nuisance parameter in the category reduction scheme for jet uncertainties. Shown are the variations on the  $t\bar{t}\gamma$  signal for (a) the total transverse energy of the event  $S_T$ , and (b) the jet multiplicity.

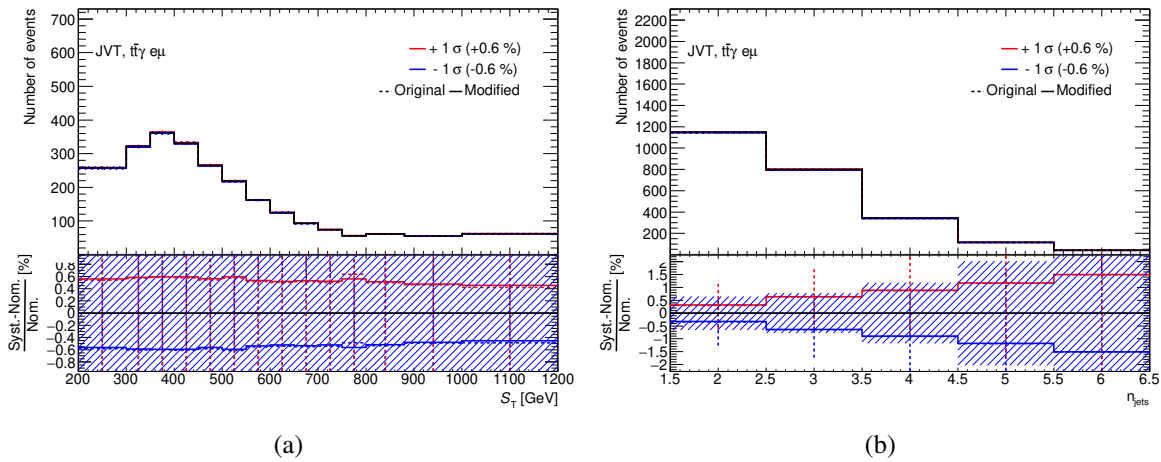


Figure 26: Systematic variations of the nuisance parameter for the jet vertex tagging (JVT) uncertainty. Shown are the variations on the  $t\bar{t}\gamma$  signal for (a) the total transverse energy of the event  $S_T$ , and (b) the jet multiplicity.

their corresponding systematic uncertainties independently. For each jet category, the uncertainties are decomposed into several uncorrelated components using the eigenvector method. For example, there are 45, 20 and 20 eigenvectors for  $b$ -jets,  $c$ -jets and light-flavour jets uncertainties, respectively [72].

#### Missing transverse momentum

The  $E_T^{\text{miss}}$  is reconstructed [65] from the vector sum of several terms corresponding to different types of reconstructed objects. The estimated uncertainties for electrons, muons, photons and jets are propagated into the uncertainty of  $E_T^{\text{miss}}$ . Thus, the only new contribution is the systematic uncertainty of the soft terms  $E_{x,y}^{\text{RefSoftJet}}$  and  $E_{x,y}^{\text{CellOut}}$ .

The systematic uncertainty of the soft-term scale is estimated by comparing the ratio of Monte-Carlo simulation to data. The average deviation of the ratio from unity is taken as a flat uncertainty on the absolute scale. The systematic uncertainty of the soft-term resolution is estimated by evaluating the level of agreement between data and MC in the  $E_x^{\text{miss}}$  and  $E_y^{\text{miss}}$  resolution. Both the scale and resolution of the soft term are varied up and down by one standard deviation to study their impact on the analysis. Resulting variations for scale and resolution parameters are shown in Figure 27.

#### Pile-up uncertainties

Pile-up uncertainties are studied by variation of the pile-up rescaling from the nominal value of 1.09 to 1.0 (up) or 1.18 (down).<sup>11</sup> The effect of the pile-up uncertainties on the  $t\bar{t}\gamma$  signal is shown in Figure 28.

#### Luminosity uncertainties

As quoted in Section 4, the total integrated luminosity has an uncertainty of 1.7%.

<sup>11</sup> More details: <https://twiki.cern.ch/twiki/bin/viewauth/AtlasProtected/ExtendedPileupReweighting>.

Not reviewed, for internal circulation only

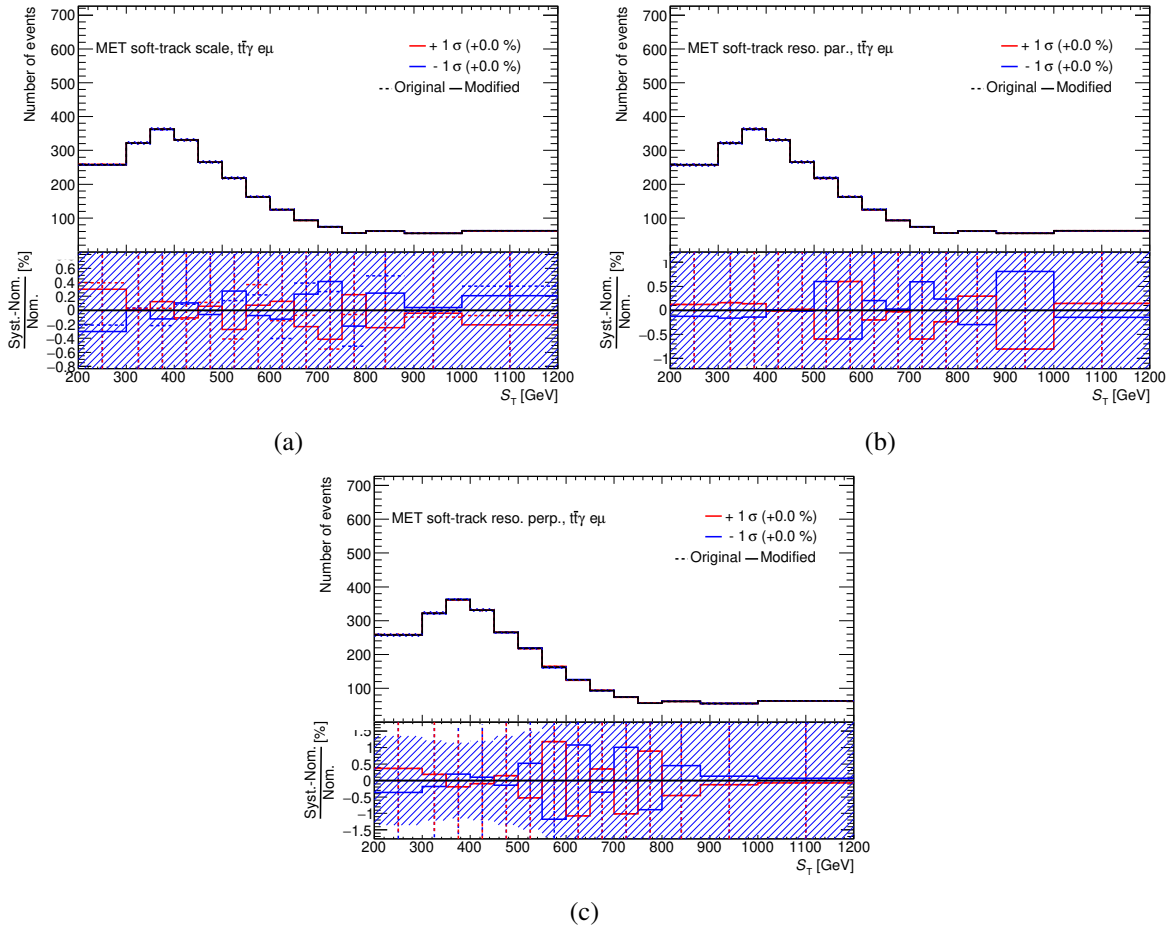


Figure 27: Systematic variations of the nuisance parameters for MET uncertainties. Shown are the variations on the  $t\bar{t}\gamma$  signal for the total transverse energy of the event  $S_T$ .

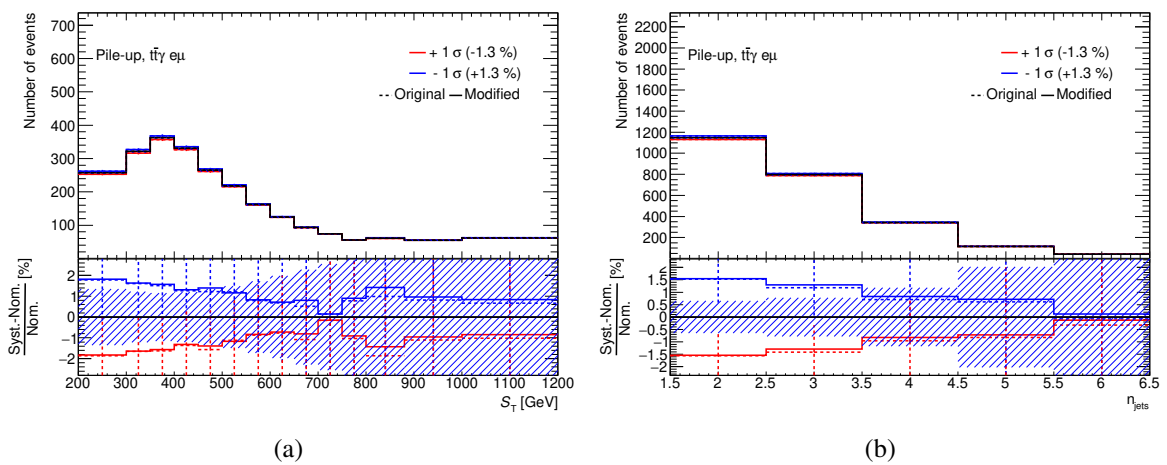


Figure 28: Systematic variations of the pile-up rescaling. Shown are the variations on the  $t\bar{t}\gamma$  signal for (a) the total transverse energy of the event  $S_T$ , and (b) the jet multiplicity.

Table 11: Complete list of systematics considered before pruning is applied.  $N$  indicates that normalisation has been considered as a systematic effect.  $S$  indicates that the shape is considered, with an amplification factor 3 for  $t\bar{t}$  variations.

Systematic	Type	# Components	Notes
$t\bar{t}\gamma \mu_R$ scale	SN	1	acts on $t\bar{t}\gamma e\mu$ and <i>Other</i> $t\bar{t}\gamma$
$t\bar{t}\gamma \mu_F$ scale	SN	1	acts on $t\bar{t}\gamma e\mu$ and <i>Other</i> $t\bar{t}\gamma$
$t\bar{t}\gamma$ PS model	SN	1	acts on $t\bar{t}\gamma e\mu$ and <i>Other</i> $t\bar{t}\gamma$
$t\bar{t}\gamma$ PYTHIA8 var3c	SN	1	acts on $t\bar{t}\gamma e\mu$ and <i>Other</i> $t\bar{t}\gamma$
$t\bar{t}\gamma$ NNPDF variations	SN	1	acts on $t\bar{t}\gamma e\mu$ and <i>Other</i> $t\bar{t}\gamma$
$tW\gamma \mu_R$ scale	SN	1	acts on $tW\gamma e\mu$ and <i>Other</i> $tW\gamma$
$tW\gamma \mu_F$ scale	SN	1	acts on $tW\gamma e\mu$ and <i>Other</i> $tW\gamma$
$tW\gamma$ PS model	SN	1	acts on $tW\gamma e\mu$ and <i>Other</i> $tW\gamma$
$t\bar{t}$ $\mu_R$ scale (shape)	S	1	acts on h-fake and prompt $\gamma$
$t\bar{t}$ $\mu_F$ scale (shape)	S	1	acts on h-fake and prompt $\gamma$
$t\bar{t}$ PS model (shape)	S (3x)	1	acts on h-fake and prompt $\gamma$
$t\bar{t}$ var3c (shape)	S	1	acts on h-fake and prompt $\gamma$
$t\bar{t}$ hdamp (shape)	S (3x)	1	acts on h-fake and prompt $\gamma$
h-fake category	N	1	50% normalisation
e-fake category	N	1	50% normalisation
prompt $\gamma$ category	N	1	50% normalisation
Luminosity	N	1	
Pile-up	SN	1	
Electrons (trigger, reco, ID, isolation)	SN	4	
$e/\gamma$ (resolution, scale)	SN	3	
Muons (trigger, reco, ID, isolation)	SN	15	
MET (resolution, scale)	SN	3	
Photons (efficiency, isolation)	SN	2	
Jet energy scale (JES)	SN	29	
Jet energy resolution (JER)	SN	8	
Jet vertex tagger (JVT)	SN	1	
$b$ -tagging: $b$ -tagging eff.	SN	45	
$b$ -tagging: $c$ -tagging eff.	SN	20	
$b$ -tagging: light-tagging eff.	SN	20	

## 1070 7 Pre-fit distributions and Asimov tests

1071 With all systematic uncertainties introduced in Section 6, the data/MC control plots shown in Figures 4  
 1072 to 6 were reproduced with all systematics applied. Before the actual fit is performed, the Hessian matrix of  
 1073 nuisance parameters is diagonal, because all parameters are assumed to be uncorrelated. The predicted  
 1074 event yields for signal and background categories with all systematic uncertainties included are listed in  
 1075 Table 12. The resulting pre-fit distributions are shown in Figures 29 to 31. The strongly enlarged shaded  
 1076 error bands now cover almost all discrepancies observed between data and prediction. Good agreement is  
 1077 seen for primary kinematic variables, such as  $p_T$ ,  $\eta$  and  $\phi$  for electrons, muons and jets. Small discrepancies  
 1078 are observed for combined variables, such as angular differences  $\Delta\phi$  or distances  $\Delta R$ , in particular in the  
 1079 distributions for the angle difference between the two leptons  $\Delta\phi(\ell, \ell)$  and the minimal distance in the  $\eta$ - $\phi$   
 1080 plane between photon and lepton  $\Delta R_{\min}(\gamma, \ell)$ . Figure 32 shows the five observables used in the differential  
 1081 cross-section measurement; the shown binning is the same as that used in the unfolded distributions in  
 1082 Figures 54 and 56.

1083 Before the actual fit to measure the inclusive cross-section is performed on data, the stability of the fit  
 1084 procedure, the behaviour of the systematic uncertainties and the expected sensitivity of the measurement  
 1085 are evaluated using an *Asimov* dataset. This pseudo dataset is created based on the predicted number of  
 1086 events in Monte Carlo and, hence, constitutes a ‘perfect’ dataset with no statistical fluctuations with respect  
 1087 to the prediction. To mimic the fit on actual data, the Asimov fit is performed on the  $S_T$  variable as well,  
 1088 and the same pruning, smoothing and symmetrisation steps are applied to the systematics.

1089 The remaining systematic nuisance parameters after pruning are shown in Figure 33. The different colours  
 1090 indicate which aspects of the systematic variation are kept and/or dropped: green for both normalisation and  
 1091 shape kept, yellow for normalisation only (shape dropped), orange for shape only (normalisation dropped),  
 1092 and red for dropped entirely. In particular, many of the  $b$ -tagging eigenvariations seem to have little effect  
 1093 on the  $t\bar{t}\gamma$  signal strength and are therefore dropped during pruning. The pruning diagram also points out,  
 1094 for which of the event categories the systematics are kept and/or dropped through the different columns.

1095 The fit on the Asimov dataset also evaluates correlations between nuisance parameters. Since the created  
 1096 pseudo dataset is ‘perfect’, none of the nuisance parameters will be pulled away from its nominal value, but  
 1097 evaluating correlations possibly leads to *constraining* some of them. This can be evaluated by looking  
 1098 at the pull plot in Figure 34. The plot shows all remaining systematic nuisance parameters after pruning.

Table 12: Event yields in the  $e\mu$  signal region. As opposed to Table 5 in Section 4, the quoted uncertainties include all systematic uncertainties introduced in Section 6. Note that the combinations of all  $t\bar{t}\gamma$  and  $tW\gamma$  categories are scaled to match the event yields in data in each column (within uncertainties).

	2015/16	2017	2018	full dataset
$t\bar{t}\gamma e\mu$	$643 \pm 30$	$760 \pm 40$	$989 \pm 50$	$2391 \pm 130$
$tW\gamma e\mu$	$43 \pm 4$	$50 \pm 5$	$63 \pm 3$	$156 \pm 15$
Other $t\bar{t}\gamma$	$71 \pm 8$	$82 \pm 5$	$108 \pm 9$	$260 \pm 17$
Other $tW\gamma$	$5 \pm 1$	$6 \pm 1$	$8 \pm 1$	$19 \pm 2$
h-fake	$23 \pm 12$	$23 \pm 12$	$31 \pm 16$	$78 \pm 40$
e-fake	$6 \pm 3$	$7 \pm 4$	$10 \pm 5$	$23 \pm 12$
Prompt $\gamma$ bkg.	$19 \pm 10$	$30 \pm 15$	$38 \pm 19$	$87 \pm 40$
Total	$809 \pm 40$	$958 \pm 50$	$1247 \pm 70$	$3014 \pm 160$
Data	809	958	1247	3014

Not reviewed, for internal circulation only

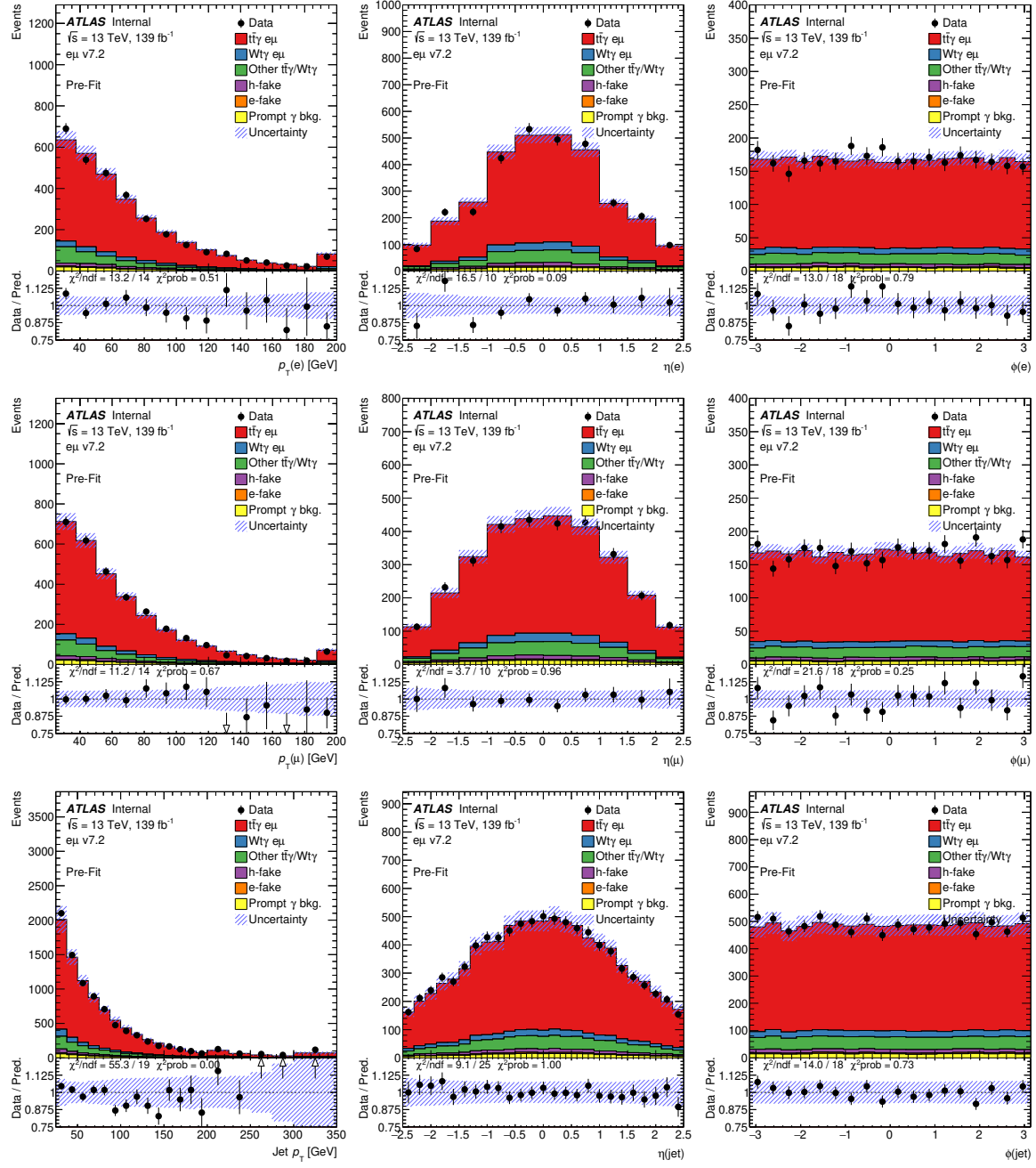


Figure 29: Data/MC pre-fit control plots of the  $e\mu$  signal region, with full statistical and systematic uncertainties, as described in Section 6. The shown variables are: transverse momentum, pseudo-rapidity and  $\phi$  of the electron, and transverse momentum, pseudo-rapidity and  $\phi$  of the muon, and transverse momenta, pseudo-rapidities and  $\phi$  of all jets in the event.

Not reviewed, for internal circulation only

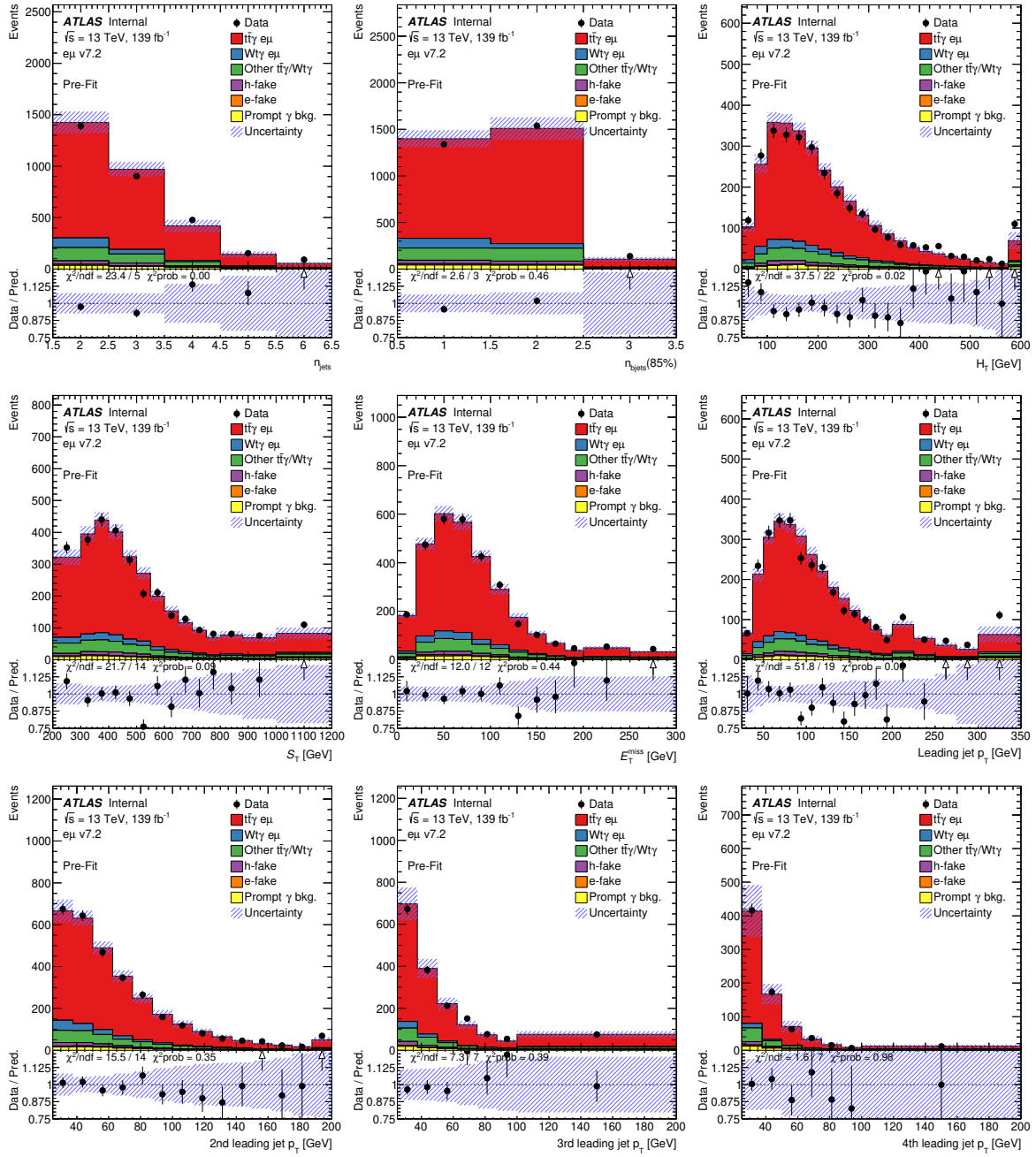


Figure 30: Data/MC pre-fit control plots of the  $e\mu$  signal region, with full statistical and systematic uncertainties, as described in Section 6. The shown variables are: jet multiplicity,  $b$ -jet multiplicity, total hadronic transverse energy, total transverse energy (includes electrons, muons, jets, photons and  $E_T^{\text{miss}}$ ),  $E_T^{\text{miss}}$ , and the transverse momenta of the four leading jets when ordered in transverse momenta.

Not reviewed, for internal circulation only

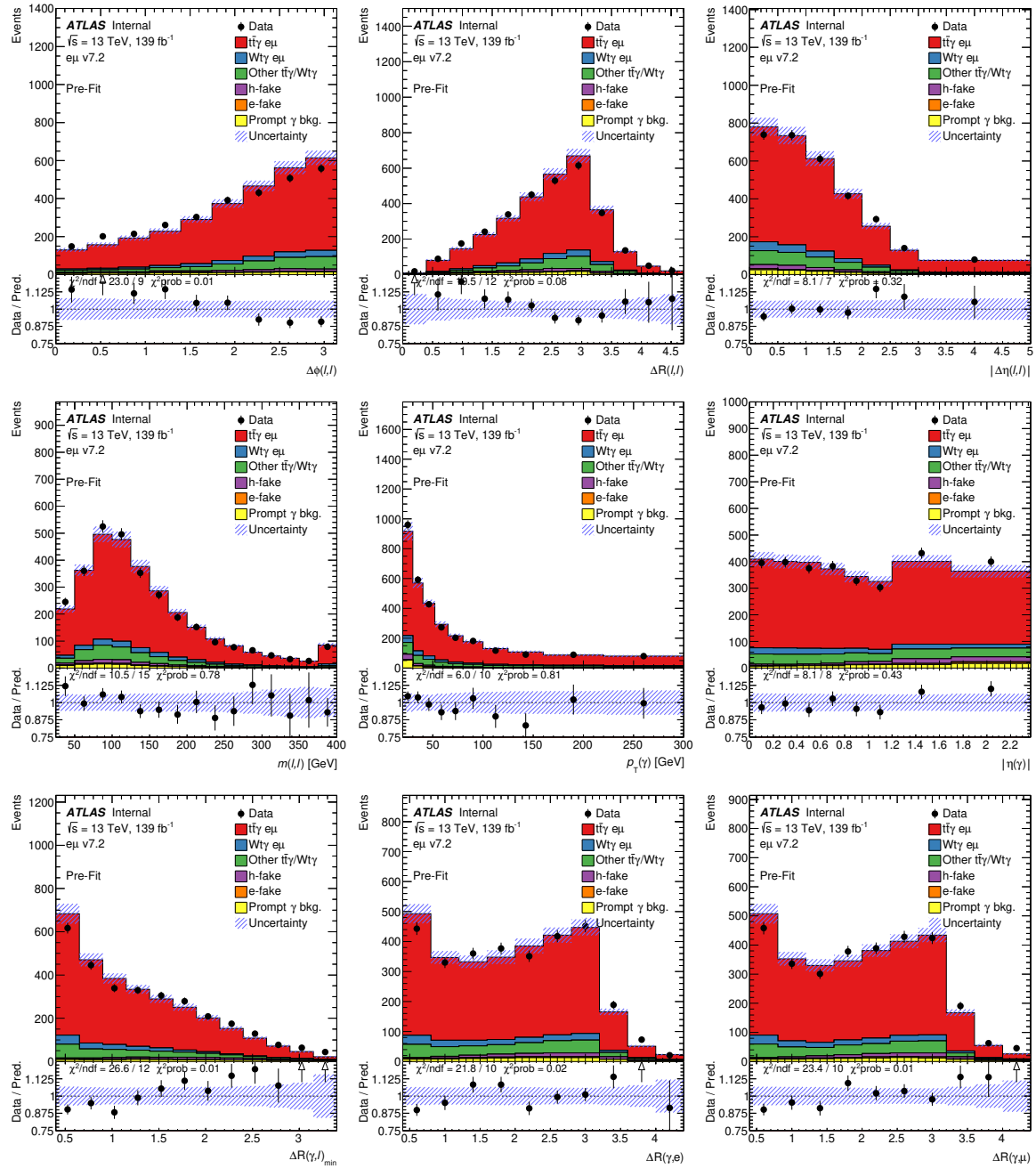


Figure 31: Data/MC pre-fit control plots of the  $e\mu$  signal region, with full statistical and systematic uncertainties, as described in Section 6. The shown variables are:  $\Delta\phi$ ,  $\Delta R$ ,  $|\Delta\eta|$  and invariant mass of the electron-muon pair, transverse momentum and pseudo-rapidity of the photon,  $\Delta R$  between the photon and the closest lepton,  $\Delta R$  between photon and electron, and  $\Delta R$  between photon and muon.

Not reviewed, for internal circulation only

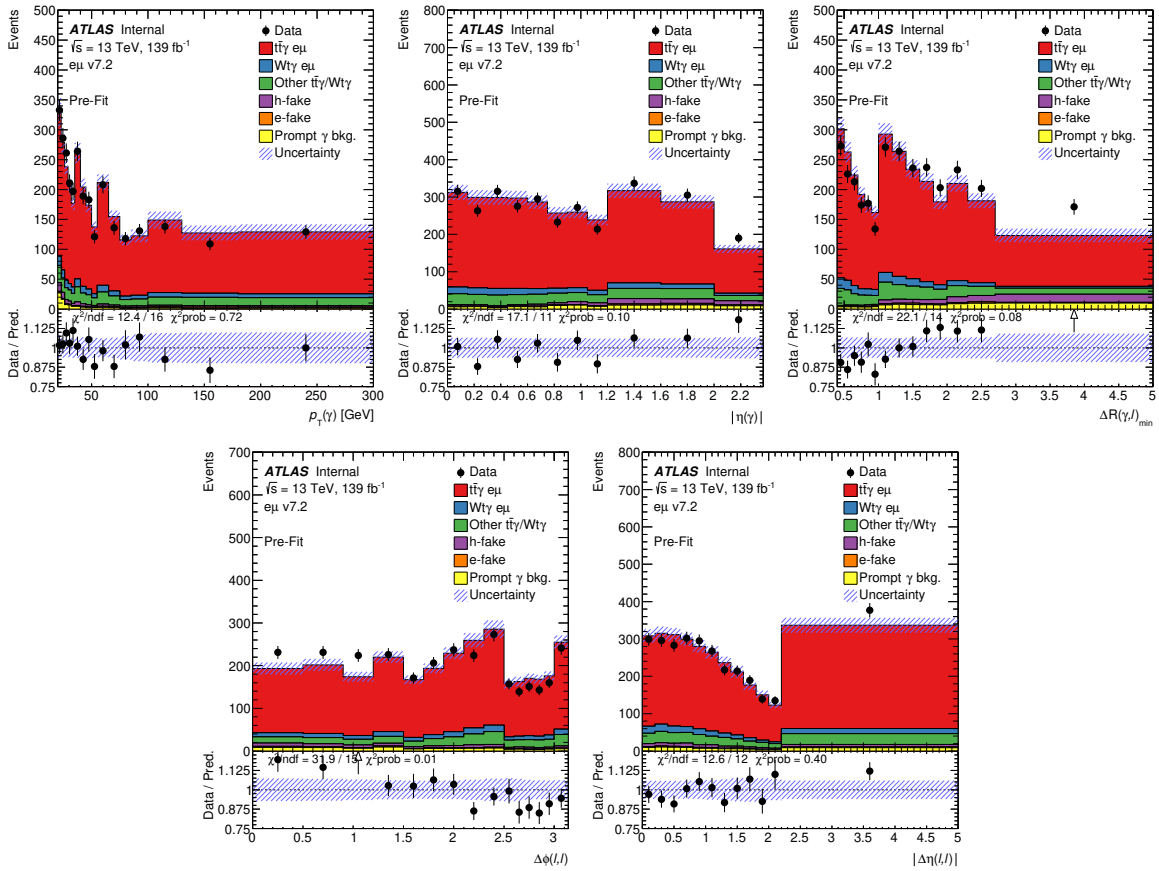


Figure 32: Data/MC pre-fit control plots of the  $e\mu$  signal region, with full statistical and systematic uncertainties, as described in Section 6. The shown variables are the observables used for the differential cross-section measurement: photon  $p_T$  and  $|\eta|$ ,  $\Delta R_{\min}(\gamma, \ell)$ ,  $\Delta\phi(\ell, \ell)$  and  $|\Delta\eta(\ell, \ell)|$ . The binning is the same as that used in the unfolded distributions in Figures 54 and 56.

1099 Some of the parameters show constraints: the  $t\bar{t}\gamma$  *var3c* modelling variation is constrained to 70%, the  $t\bar{t}\gamma$   
 1100 PS model variation is constrained to 71%. This means that – given the number of expected events in each  
 1101 bin in the fitted distribution – the a-priori systematic was estimated to be too large, or could be constrained  
 1102 through (anti-)correlation with other systematics. In addition, the limitations of the individual bin statistics,  
 1103 usually called *gammas*, are shown in Figure 35. They are an indicator whether the significance of the fit  
 1104 result is limited by the bin statistics, and whether the binning should be re-adjusted.

1105 The impact of individual nuisance parameters on the fit result can be evaluated in a nuisance parameter  
 1106 *ranking*, as shown in Figure 36 for the Asimov fit. The rank of a nuisance parameter is evaluated by running  
 1107 the fit with the value of the individual parameter fixed to its nominal value and its  $\pm 1\sigma$  variation value.  
 1108 The resulting value is then compared against the nominal fit, which is an indicator how much changing that  
 1109 nuisance parameter affects the result.

1110 The two highest ranked uncertainties in the Asimov fit are the uncertainties on the normalisation of  
 1111 the prompt  $\gamma$  and h-fake background categories. Among the highest ten, signal modelling variations  
 1112 are included, such as the  $t\bar{t}\gamma$  PS model, the  $tW\gamma$  PS model and the  $t\bar{t}\gamma$  PDF variations. From the  
 1113 experimental side, the photon efficiency isolation and photon identification simulation-to-data scale factors

Not reviewed, for internal circulation only

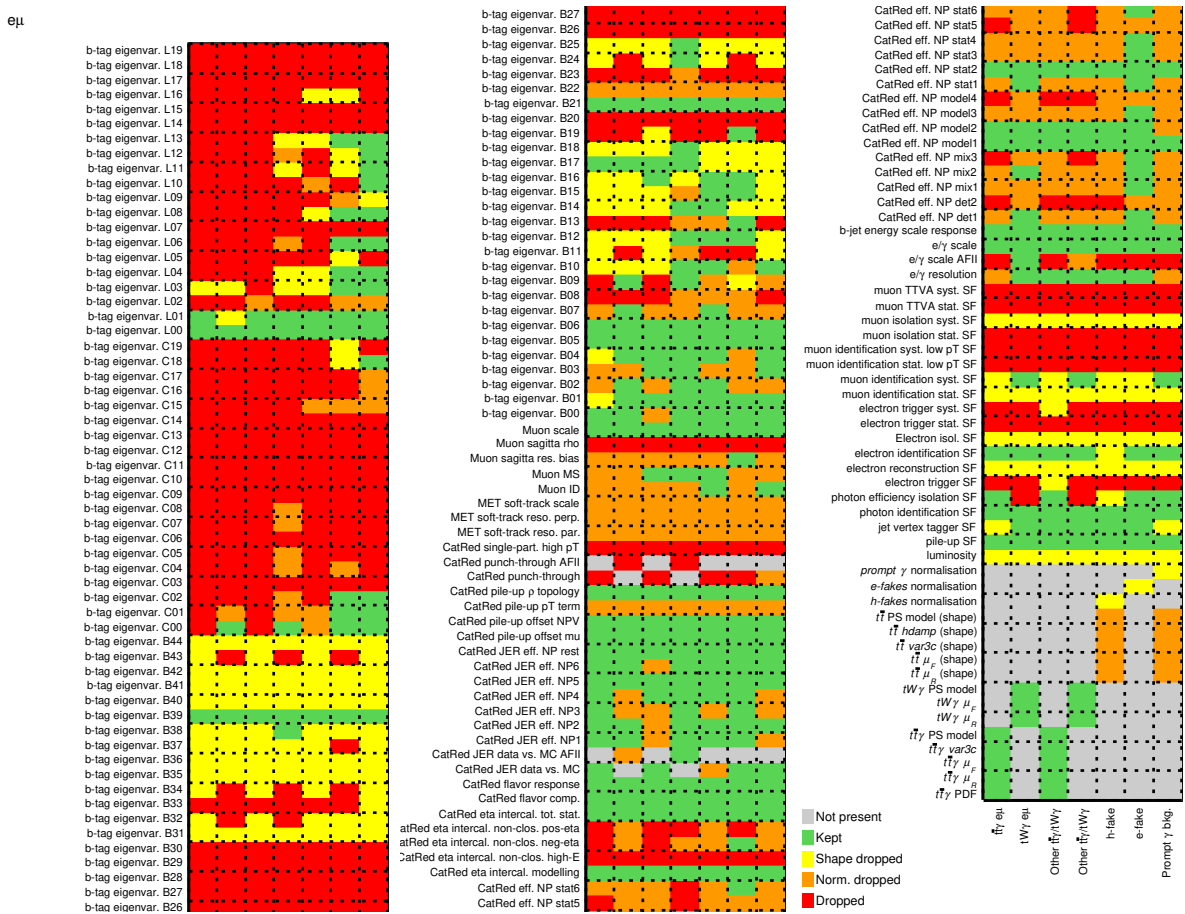


Figure 33: Systematics before and after pruning when performing the Asimov fit. The different columns indicate whether a systematic was pruned for the different event categories. The colour code is: green for both normalisation and shape kept, yellow for normalisation only (shape dropped), orange for shape only (normalisation dropped), and red for dropped entirely.

are ranked highly. Others include the luminosity and pile-up reweighting uncertainty, both of which are expected, because varying any of the two parameters directly affects the measured rate of signal events. For uncertainties with 10% or higher correlation to others the correlation matrix is shown in Figure 37. Particularly high correlations with the signal strength, the parameter of interest, are observed for the aforementioned normalisation uncertainties of the prompt  $\gamma$  and h-fake background categories, the luminosity and pile-up uncertainties, as well as the uncertainties associated to photons. This is expected as all of these uncertainties directly affect the rate of the signal and therefore its signal strength.

The fit on the Asimov dataset also gives values for the measured signal strength including total uncertainty on the result. By construction, the expected value in the Asimov scenario is 1.0, but the performed Asimov fit on  $S_T$  gives an estimate of the total uncertainty to be  $1.0^{+5.9\%}_{-5.6\%}$ . Note that this is just the estimated uncertainty on the signal strength, and that the fiducial cross-section measurement also considers the addition  $tW\gamma$  parton-matching uncertainty on the correction factor  $C$ , as described in Section 5.2.

The variable  $S_T$  was chosen following a series of benchmark fits, performed with multiple variables on Asimov datasets. These tests also included a single-bin distribution ('cut-and-count analysis'). The fit benchmarks are summarised in Appendix G. Compared to other variables,  $S_T$  shows the least constraints of

Not reviewed, for internal circulation only

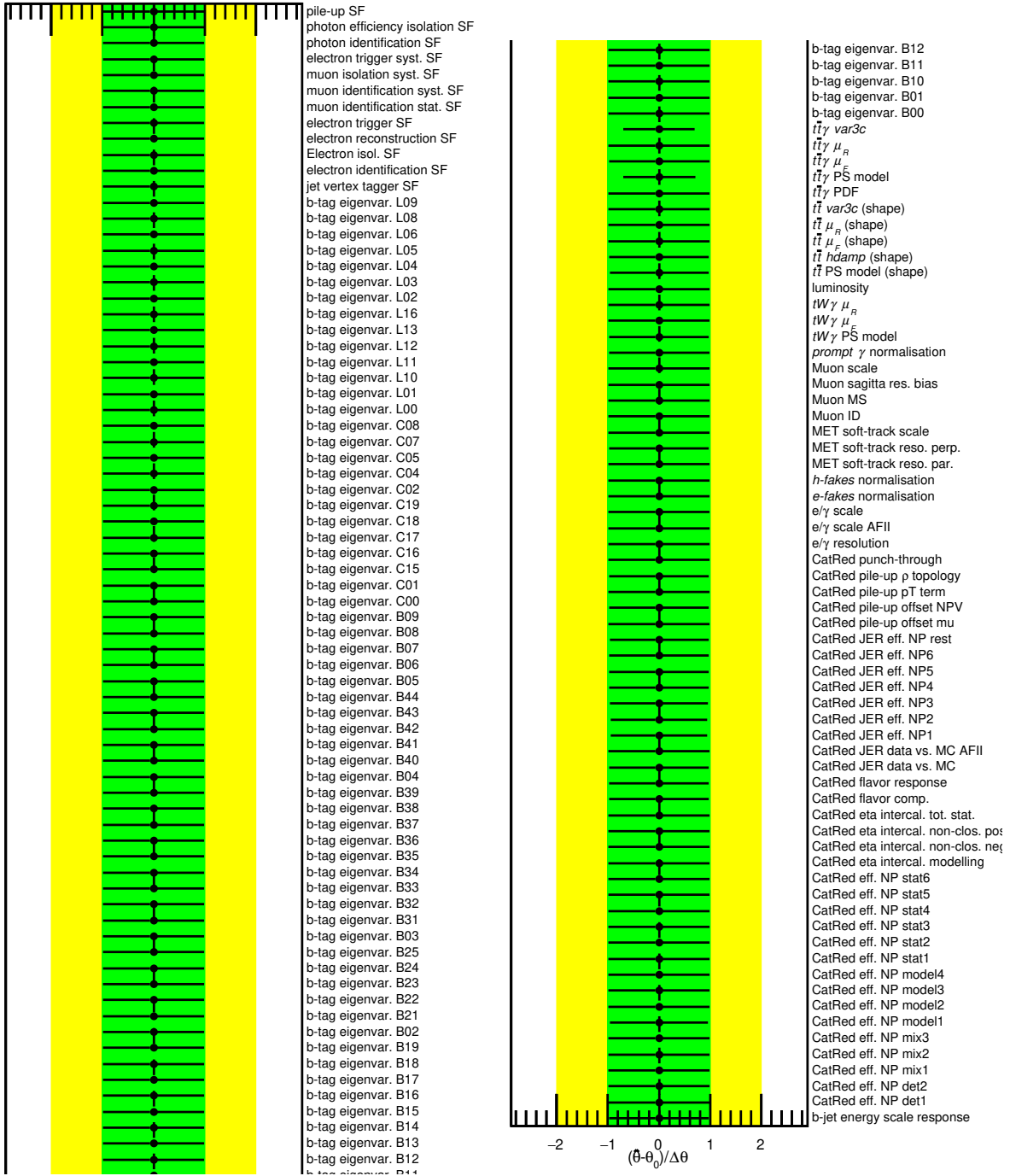


Figure 34: Pull distributions of all remaining nuisance parameters after pruning for the Asimov fit. While none of the parameters is expected to actually be *pulled* in an Asimov scenario, some of the parameters show constraints.

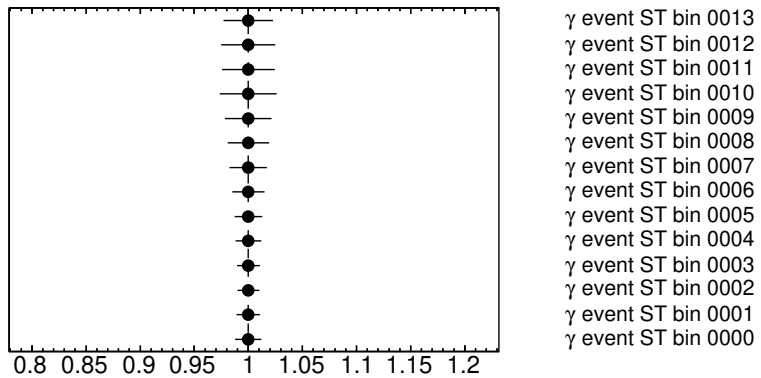


Figure 35: Gammas, that is, limitations of the individual bin statistics of the fitted distribution in the Asimov fit. Very large uncertainties on individual bins could mean that the binning should be re-adjusted.

1129 systematic uncertainties, with the smallest predicted total uncertainty on the signal strength. The appendix  
 1130 also gives a table with the predicted uncertainties on the signal strength for different fit variables. A  
 1131 comparison of the predicted shapes for  $t\bar{t}\gamma e\mu$  signal and all backgrounds (excluding *Other  $t\bar{t}\gamma$* ) is also  
 1132 shown in Figure 38. The comparison reveals small expected differences in the shape between signal and  
 1133 background.

Not reviewed, for internal circulation only

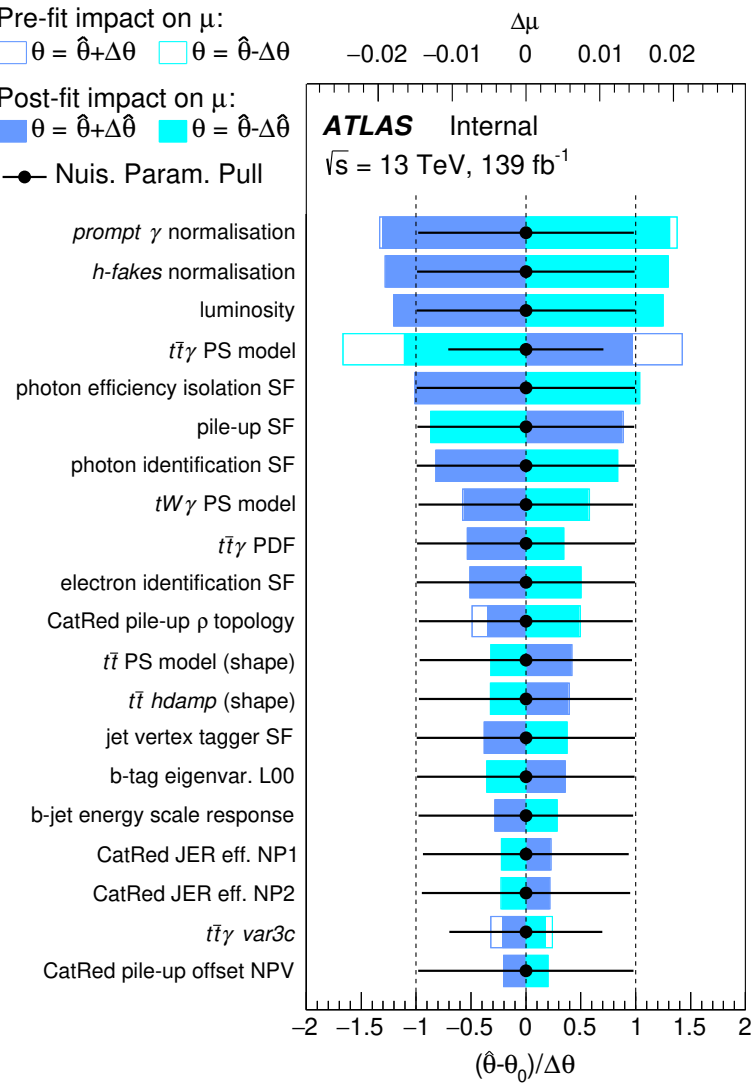


Figure 36: Ranking of systematics in the Asimov fit scenario. The blue and turquoise bands indicate the post-fit impact on the measured signal strength in the fit, whereas the outlined blue and turquoise rectangles show the pre-fit impact. The difference between the two reflects the constraint of the nuisance parameter due to correlations in the fit. The impact is overlaid with the nuisance parameter pulls, as shown in Figure 34 already.

Not reviewed, for internal circulation only

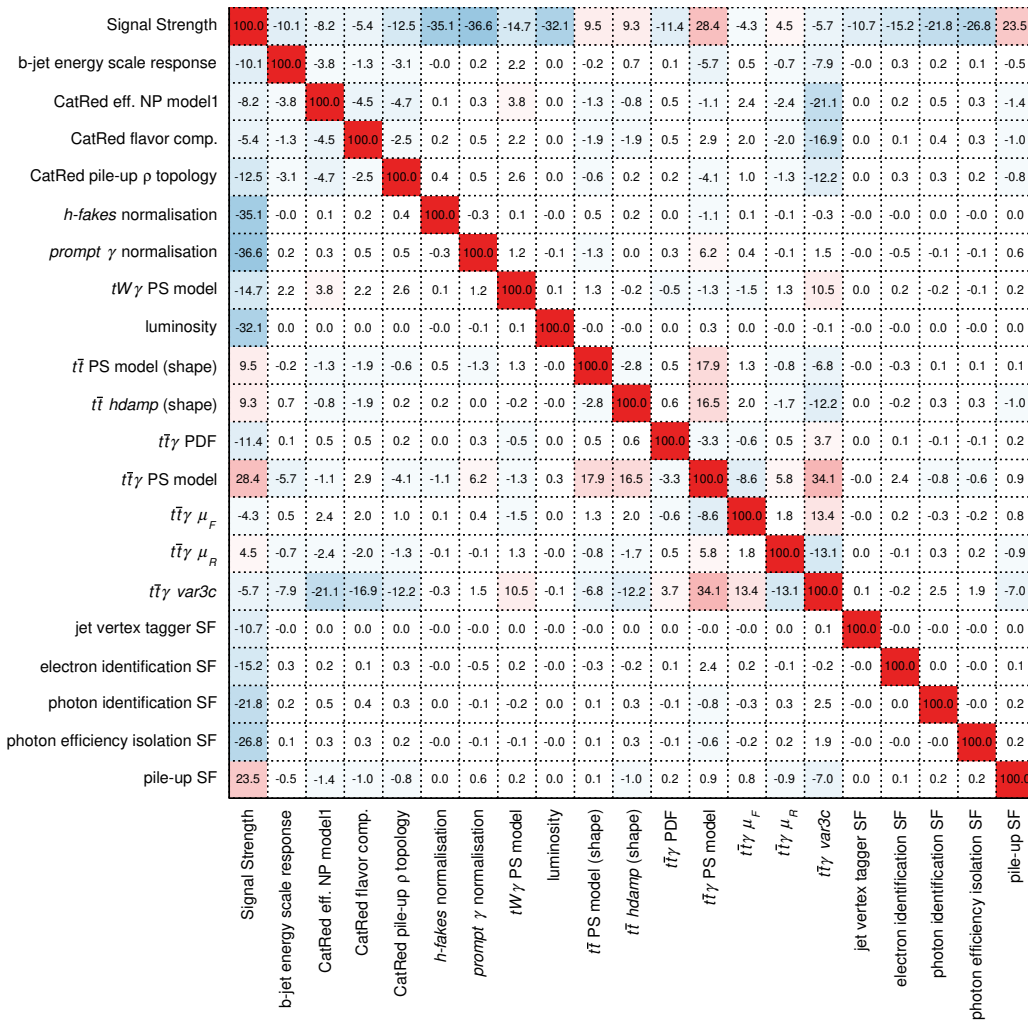


Figure 37: Correlation matrix for those nuisance parameters that have 10% or higher correlations to other uncertainties in the Asimov fit.

Not reviewed, for internal circulation only

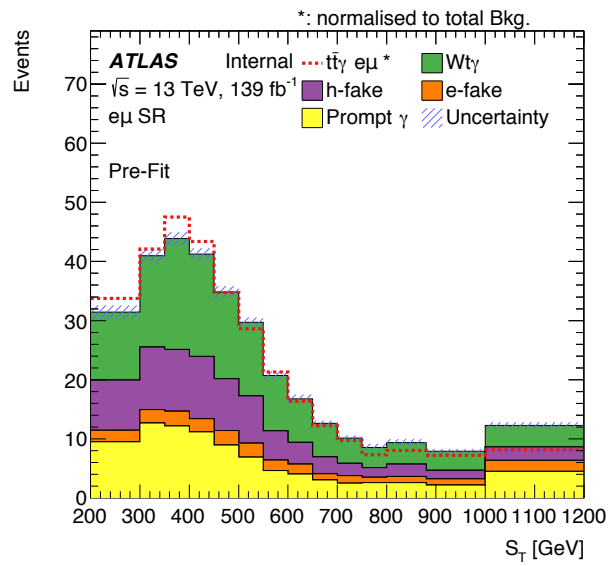


Figure 38: Comparison of the expected shapes for  $t\bar{t}\gamma e\mu$  signal and all backgrounds. The *Other  $t\bar{t}\gamma$*  category is not displayed.

## 1134 8 Unfolding studies

1135 In this section, checks for the unfolding procedure are shown. The criteria for choosing the binning is  
 1136 shown in Section 8.1. The description of pseudo-data, which is used for checking the behaviour of the  
 1137 unfolding machinery, is introduced in Section 8.2. The choice of the number of iterations for the unfolding  
 1138 procedure is discussed in Section 8.3. Closure and pull tests are performed in Section 8.4 and in Section 8.5,  
 1139 respectively. At the end of this chapter, results of stress tests are shown in Section 8.6.

1140 **8.1 Binning optimisation**

1141 A new binning scheme is tested, for all the variables. There is a number of factors that might affect the  
 1142 decision of choosing a bin width. For this analysis, two factors are chosen: the resolution of the kinematic  
 1143 observable (to be unfolded) and the statistical uncertainty per bin. For the statistical uncertainty, it is  
 1144 required to be less than 10% across all bins (this ensures the number of events across all bins will be  
 1145 roughly equal). Thus, the criterion for the binning choice is as follows: the bin width has to be larger  
 1146 than twice the observable's resolution and the statistical uncertainty has to be less than 10% across all  
 1147 bins. The resolution of photon  $p_T$ , precision on the mean of (reconstructed photon  $p_T$  – truth photon  
 1148  $p_T$ ), comparison of bin width to the resolution and the expected statistical uncertainty of the resulting  
 1149 bin width can be seen in Figure 39. The same for photon  $\eta$ ,  $\Delta R_{\min}(\gamma, \ell)$ ,  $\Delta\phi(\ell, \ell)$ , and  $|\Delta\eta(\ell, \ell)|$  can be  
 1150 found in Figures 40 to 43. This optimised binning is checked for closure in Section 8.4 and for stability in  
 1151 Section 8.5. It is worth mentioning that the final binning used is slightly different from the one shown here  
 1152 in order to lower statistical uncertainties for a few bins.

1153 **8.2 Pseudo-data**

1154 To perform checks on the unfolding method (pull, closure, etc.), the measured spectrum is replaced by  
 1155 pseudo-data. Pseudo-data is generated using the  $t\bar{t}\gamma$  MC events which are randomly sampled into two  
 1156 samples, *testing* and *training*, in a way that the testing sample has the equivalent statistical power as the  
 1157 expected signal. The training sample is used to build the unfolding inputs (including the migration matrix)  
 1158 and the testing sample is the pseudo-data to be unfolded.

1159 The following Sections 8.4 and 8.5 use these pseudo-data for further checks.

Not reviewed, for internal circulation only

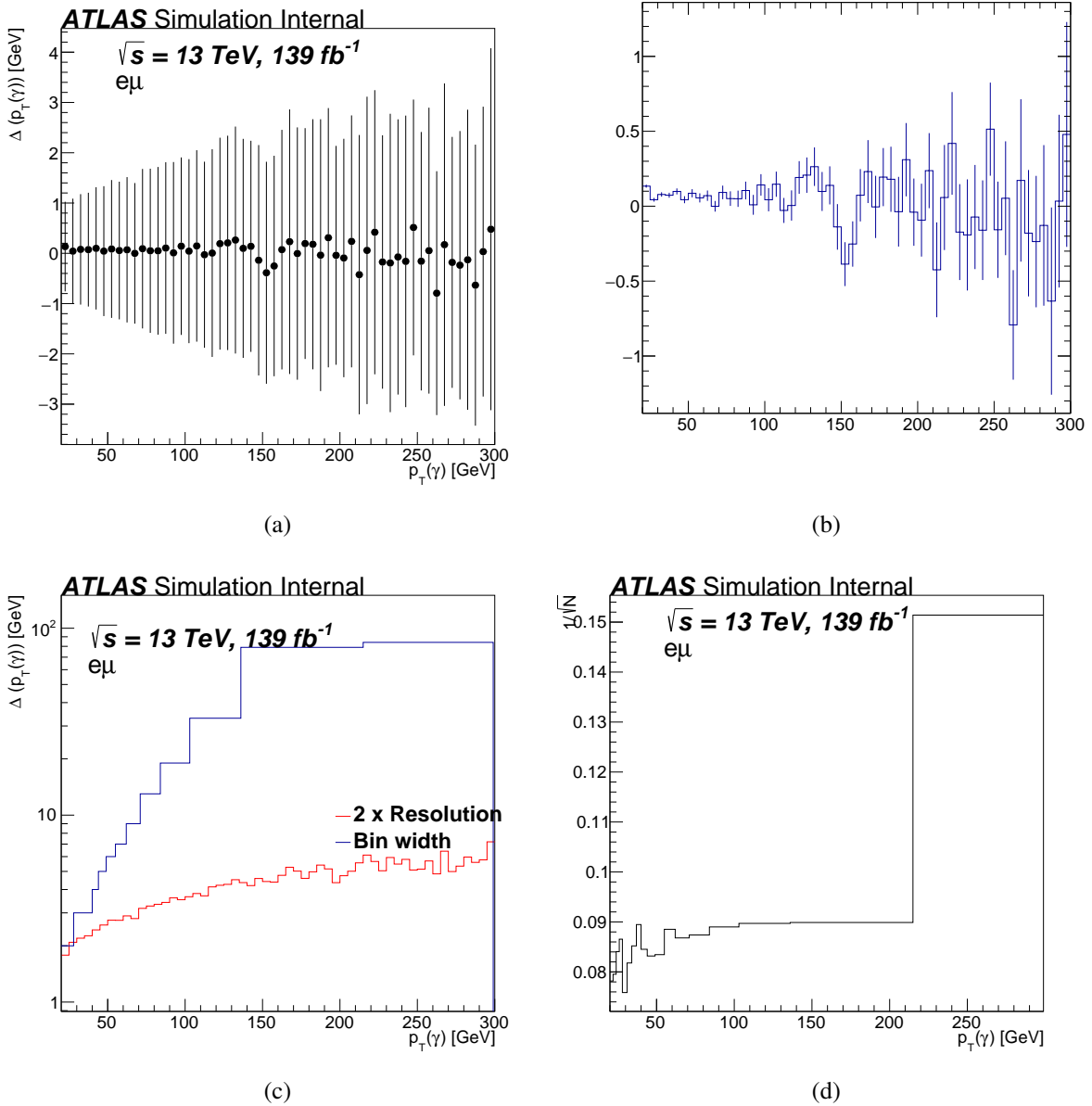


Figure 39: (a) Resolution of the photon  $p_T$  observable is represented by the error bars. The y-axis is the mean of (reconstructed photon  $p_T$  – truth photon  $p_T$ ) in GeV and the error bars represent one standard deviation around that mean. (b) Precision on the mean where the y-axis is the mean of (reconstructed photon  $p_T$  – truth photon  $p_T$ ) in GeV and the error bars represent the error on the mean. (c) The bin width in blue is compared to the resolution multiplied by 2 in red. (d) The expected statistical uncertainty of the resulting bin width.

Not reviewed, for internal circulation only

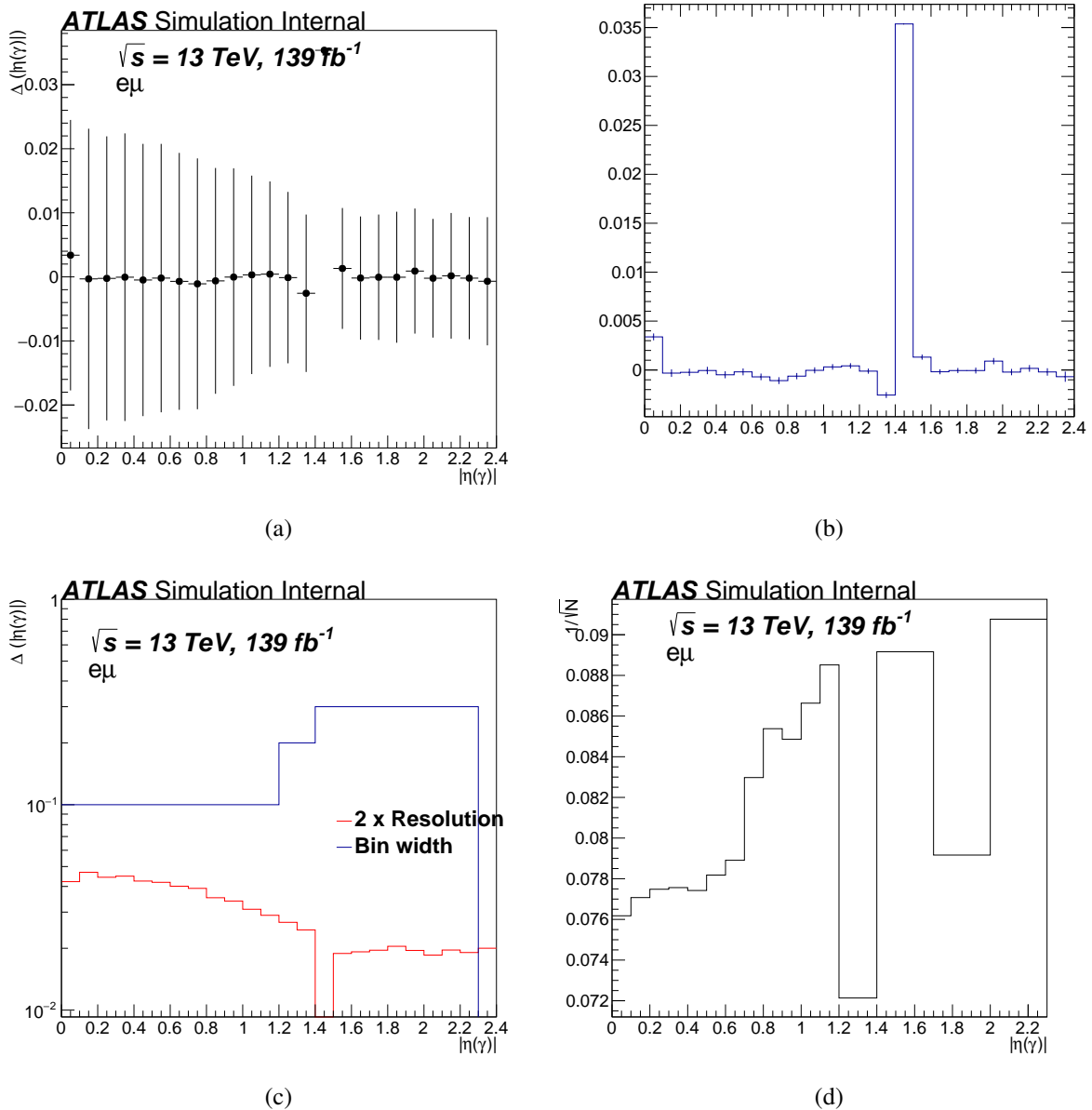


Figure 40: (a) Resolution of the photon  $\eta$  observable is represented by the error bars. The y-axis is the mean of (reconstructed photon  $\eta$  – truth photon  $\eta$ ) and the error bars represent one standard deviation around that mean. (b) Precision on the mean where the y-axis is the mean of (reconstructed photon  $\eta$  – truth photon  $\eta$ ) in GeV and the error bars represent the error on the mean. (c) The bin width in blue is compared to the resolution multiplied by 2 in red. (d) The expected statistical unvertainty of the resulting bin width.

Not reviewed, for internal circulation only

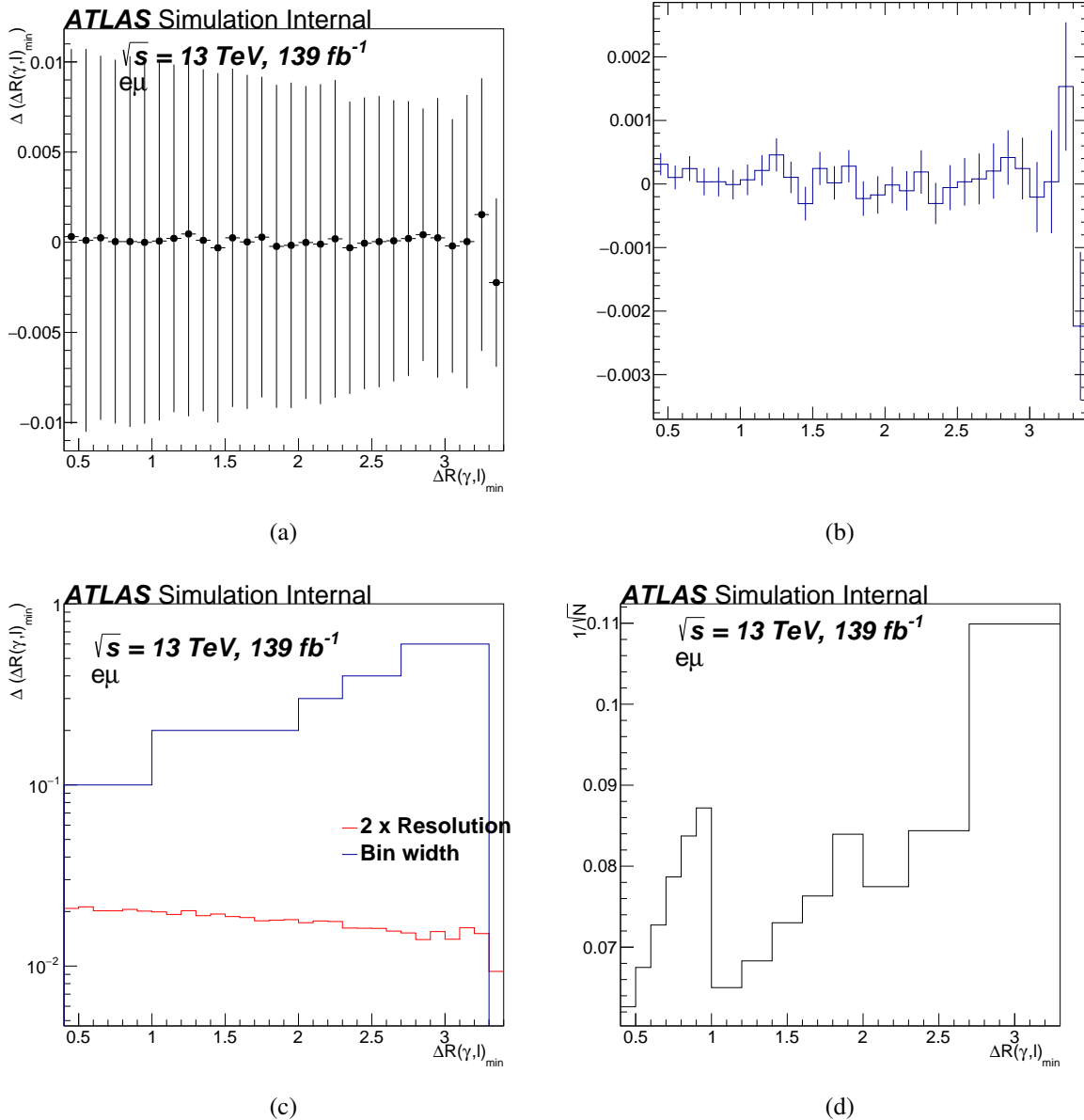


Figure 41: (a) Resolution of the  $\Delta R_{\min}(\gamma, \ell)$  observable is represented by the error bars. The y-axis is the mean of (reconstructed  $\Delta R_{\min}(\gamma, \ell)$  – truth  $\Delta R_{\min}(\gamma, \ell)$ ) in GeV and the error bars represent one standard deviation around that mean. (b) Precision on the mean where the y-axis is the mean of (reconstructed  $\Delta R_{\min}(\gamma, \ell)$  – truth  $\Delta R_{\min}(\gamma, \ell)$ ) in GeV and the error bars represent the error on the mean. (c) The bin width in blue is compared to the resolution multiplied by 2 in red. (d) The expected statistical uncertainty of the resulting bin width.

Not reviewed, for internal circulation only

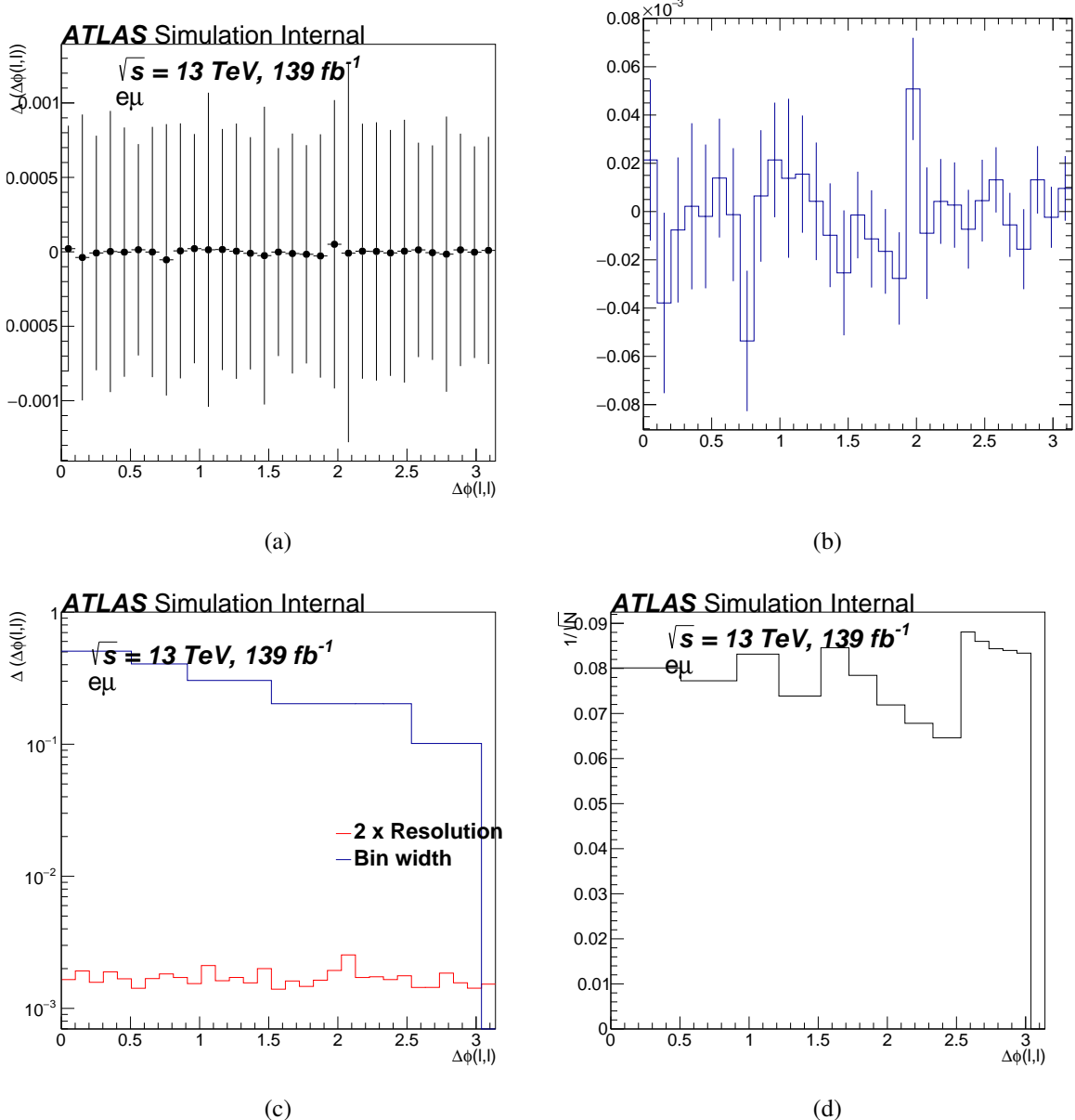


Figure 42: (a) Resolution of the  $\Delta\phi(\ell, \ell)$  observable is represented by the error bars. The y-axis is the mean of (reconstructed  $\Delta\phi(\ell, \ell)$  – truth  $\Delta\phi(\ell, \ell)$ ) and the error bars represent one standard deviation around that mean. (b) Precision on the mean where the y-axis is the mean of (reconstructed  $\Delta\phi(\ell, \ell)$  – truth  $\Delta\phi(\ell, \ell)$ ) in GeV and the error bars represent the error on the mean. (c) The bin width in blue is compared to the resolution multiplied by 2 in red. (d) The expected statistical unvertainty of the resulting bin width.

Not reviewed, for internal circulation only

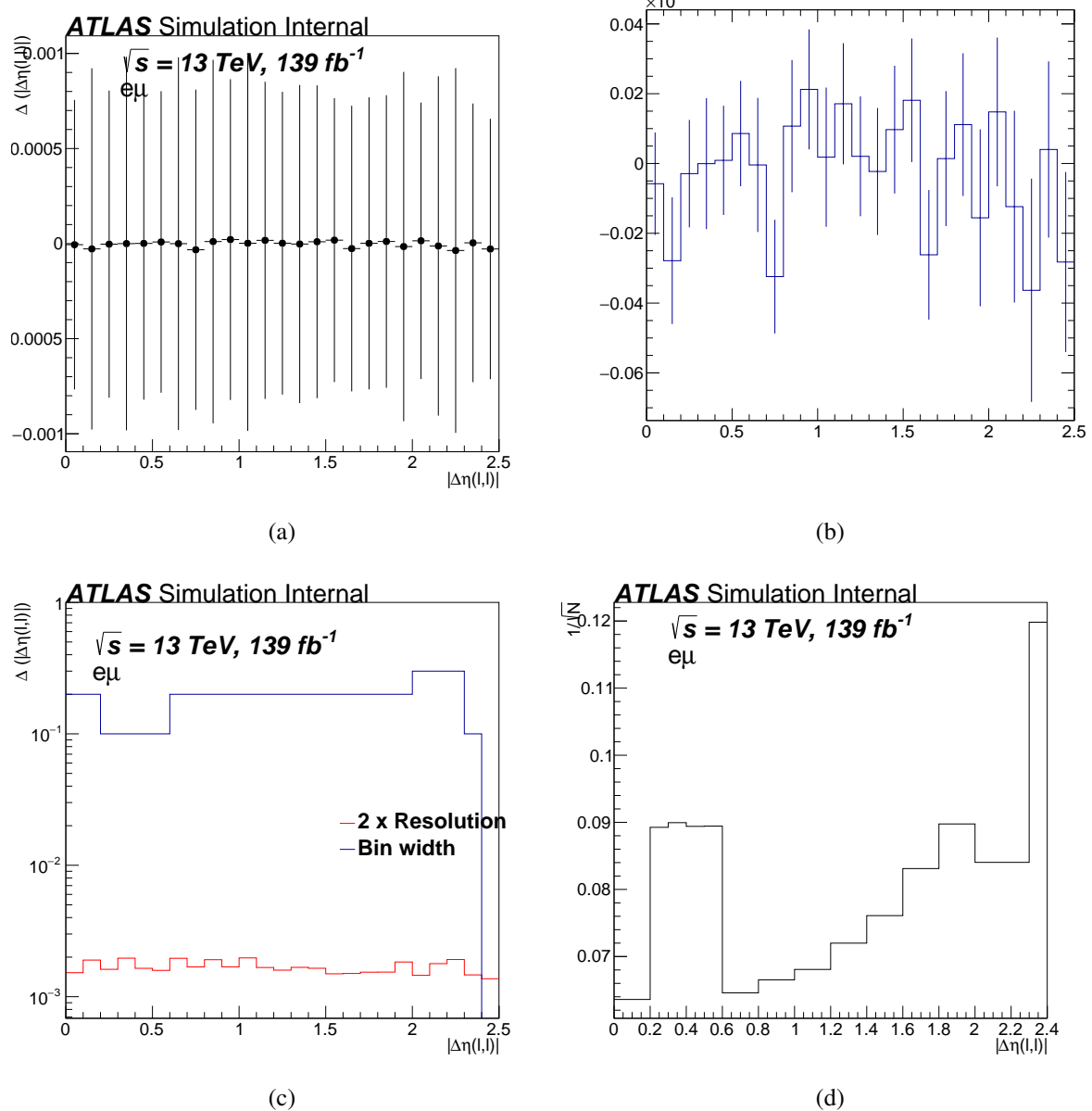


Figure 43: (a) Resolution of the  $|\Delta\eta(\ell, \ell)|$  observable is represented by the error bars. The y-axis is the mean of (reconstructed  $|\Delta\eta(\ell, \ell)|$  – truth  $|\Delta\eta(\ell, \ell)|$ ) and the error bars represent one standard deviation around that mean. (b) Precision on the mean where the y-axis is the mean of (reconstructed  $|\Delta\eta(\ell, \ell)|$  – truth  $|\Delta\eta(\ell, \ell)|$ ) in GeV and the error bars represent the error on the mean. (c) The bin width in red is compared to the resolution multiplied by 2 in red. (d) The expected statistical unvertainty of the resulting bin width.

### 1160 8.3 Number of iterations

1161 The IBS method is an iterative process which means that we need to find the number of iterations at  
 1162 which we stop the iteration procedure. The number of iterations, which is a regularisation parameter,  
 1163 is determined by making a  $\chi^2$  test between unfolded pseudo-data (at reconstructed-level) and the truth  
 1164 distribution. The procedure for the  $\chi^2$  test is the following: 1000 pesudo-experiments are generated for the  
 1165 response matrix using a Poisson distribution. Then pseudo-data (reconstruction-level of the testing sample)  
 1166 is unfolded using the varied response matrix from the training sample. Afterwards the  $\chi^2$  test between  
 1167 unfolded pseudo-data and the truth distibution (from the testing sample) is made. The mean of the  $\chi^2/NDF$   
 1168 for all the variables can be seen in Figure 44. As can be seen from the figure, the mean is very close to 1  
 1169 for most variables, for most of the number of iterations. A number of iterations equal to two is chosen for  
 1170 the unfolding, to have as small statistical fluctuations as possible. This number is used in unfolding when  
 1171 performing all the tests as well as the differential cross-section results.

Not reviewed, for internal circulation only

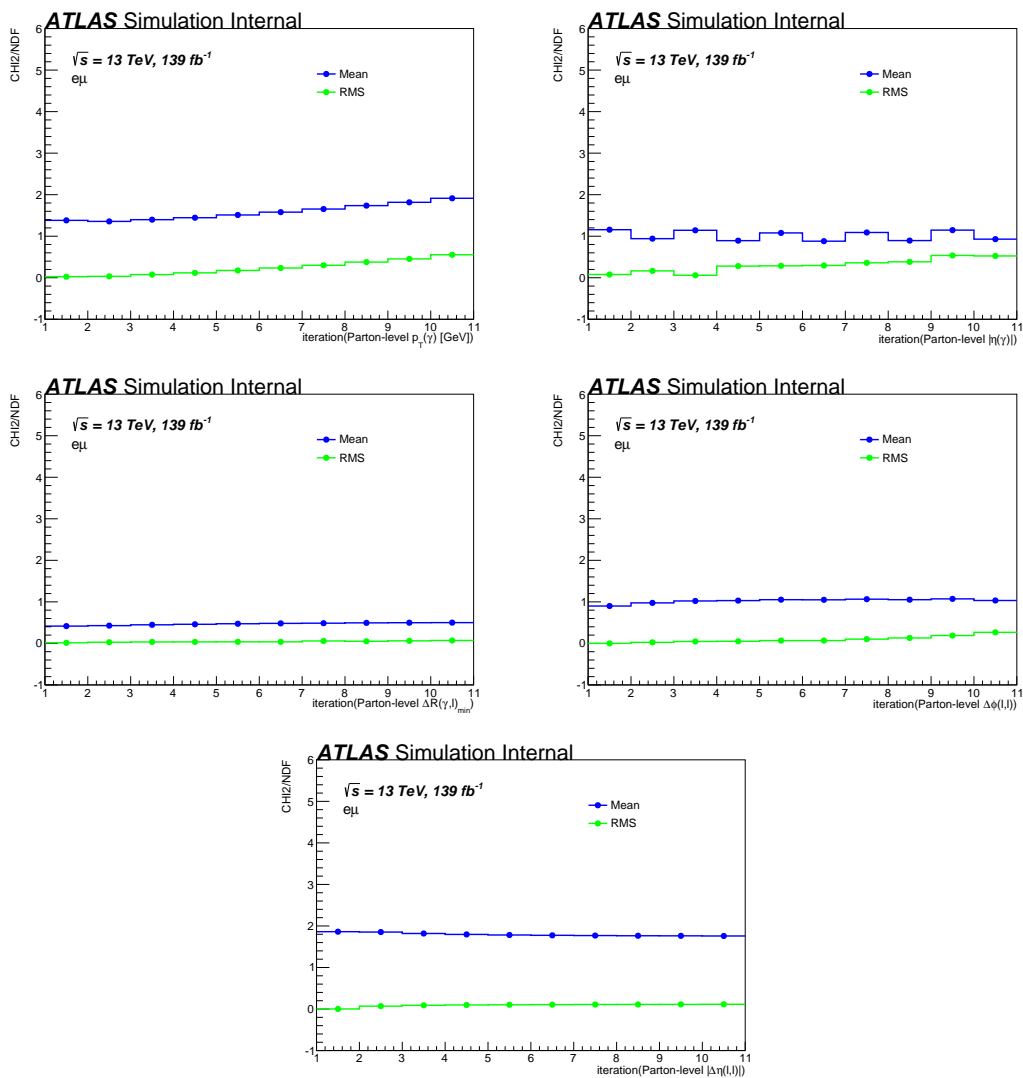


Figure 44:  $\chi^2$  test with mean in blue and RMS in green for photon  $p_T$ , photon  $\eta$ ,  $\Delta R_{\min}(\gamma, \ell)$ ,  $\Delta\phi(\ell, \ell)$  and  $|\Delta\eta(\ell, \ell)|$ .

## 1172 8.4 Closure test

1173 The closure test is performed to check if the unfolding procedure can recover the truth spectrum.  
 1174 To do that, pseudo-data distributions of the testing sample at the reconstruction-level, which has the  
 1175 same statistical power as the expected signal, are unfolded using the migration matrix from the training  
 1176 sample. The result of the closure of pseudo-data can be seen in Figure 45. A  $\chi^2$  values between unfolded  
 1177 pseudo-data and truth distributions is shown in Table 13.

Not reviewed, for internal circulation only

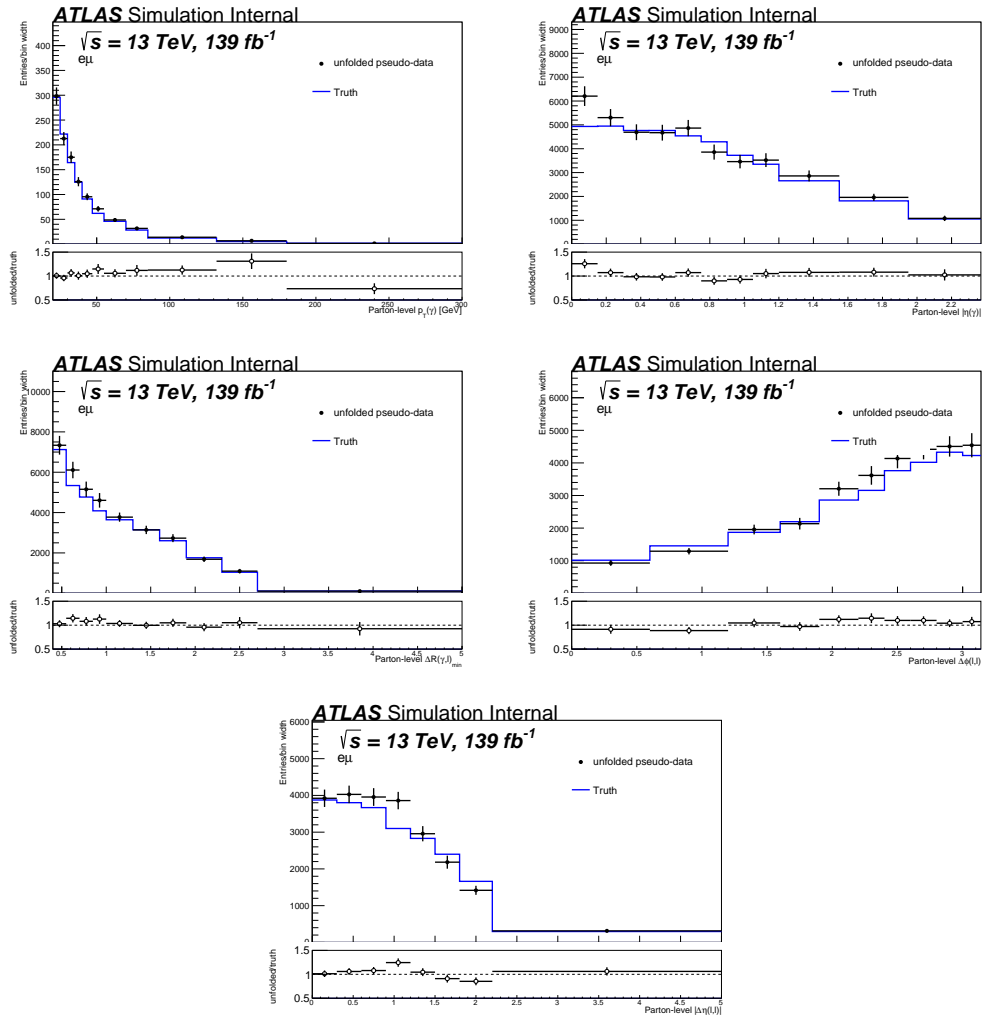


Figure 45: Overlay of unfolded pseudo-data and truth distributions after 2 iterations as a function of the photon  $p_T$ , photon  $\eta$  and  $\Delta R_{\min}(\gamma, \ell)$ ,  $\Delta\phi(\ell, \ell)$  and  $|\Delta\eta(\ell, \ell)|$ . The pseudo-data has the same statistical power as the expected signal is unfolded using the machinery built from the training sample.

Table 13:  $\chi^2/\text{NDF}$  values between unfolded pseudo-data and truth distributions.

Variable	$p_T(\gamma)$	$ \eta(\gamma) $	$\Delta R_{\min}(\gamma, \ell)$	$ \Delta\eta(\ell, \ell) $	$\Delta\phi(\ell, \ell)$
$\chi^2/\text{NDF}$	1.3	1.2	0.5	2.0	1.0

## 1178 8.5 Pull test

1179 Pull tests are preformed to check the stability of the binning choice. The same pseudo-data described in  
 1180 Section 8.2 is used where 1000 pseudo-experiments are generated from the testing sample at reconstruction-  
 1181 level using a Poisson distribution, and then being unfolded. Afterwards, the pulls are calculated per bin  
 1182 as:

$$\text{Pull} = \frac{(\text{truth} - \text{unfold})}{\sigma_{\text{unfold}}}, \quad (9)$$

1183 and then are fitted by a Gaussian function. The pull is expected to have a mean value of zero which  
 1184 indicates no bias, and width of one which means the statistical uncertainty is estimated correctly. Figure 46  
 1185 shows the behavior of the pull (after 2 iterations) where it is observed that there is no bias in the bin choice  
 1186 and the width is consistent with one.

Not reviewed, for internal circulation only

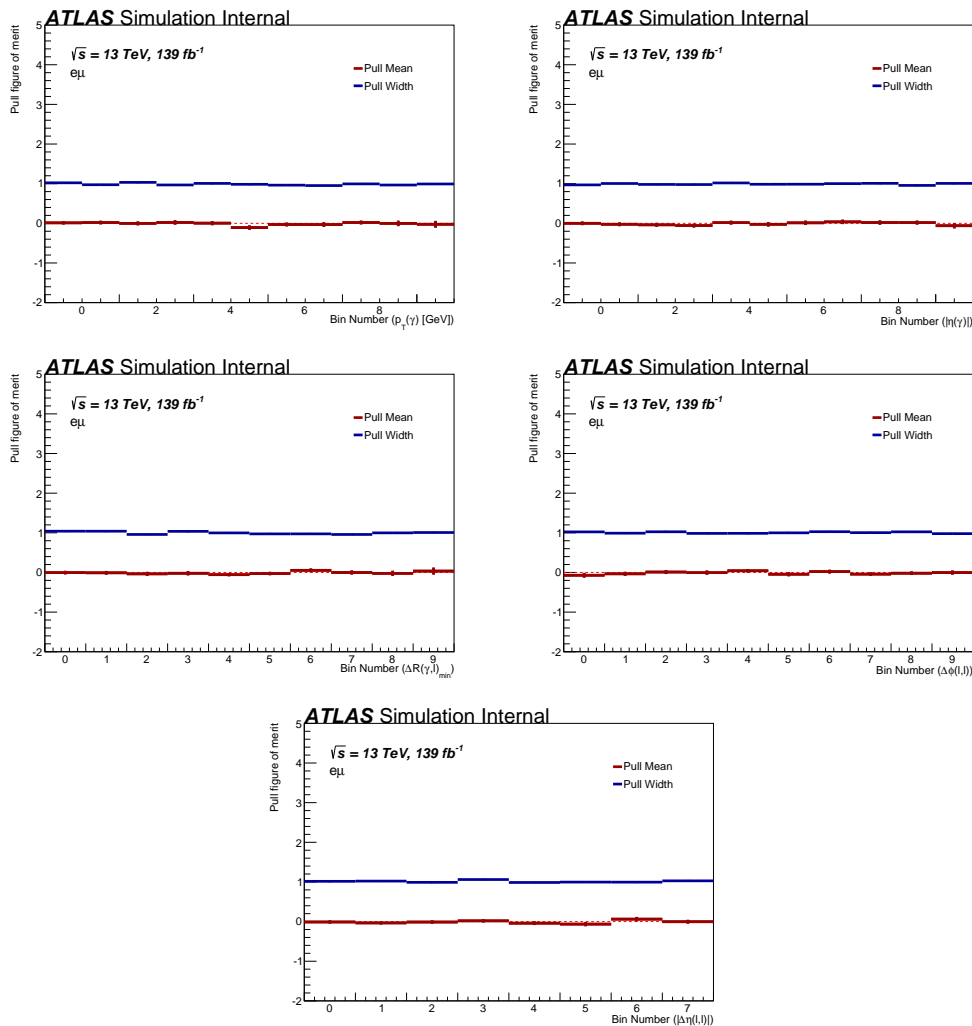


Figure 46: Pull test for photon  $p_T$ , photon  $\eta$ ,  $\Delta R_{\min}(\gamma, \ell)$ ,  $\Delta\phi(\ell, \ell)$ , and  $|\Delta\eta(\ell, \ell)|$ .

## 1187 8.6 Stress test

1188 The stress test is performed in order to verify that the unfolding procedure is not biased to any specific  
 1189 shape of the particle level distribution. The truth-level and reconstruction-level distributions obtained  
 1190 from the testing sample are weighted, and then the weighted reconstructed distribution is unfolded using  
 1191 the nominal inputs from the training sample, and the unfolded results are compared to the corresponding  
 1192 truth-level distribution. There are two weights considered to smear distributions. The first is to have a  
 1193 linear skewness of the shape. Such weight is defined as the following, in case of the photon  $p_T$ :

$$\text{weight} = 1 + \frac{100 - i}{300} = 1 + X, \quad (10)$$

Not reviewed, for internal circulation only

<sup>1194</sup> and the case of the photon  $|\eta|$ :

$$\text{weight} = 1 + \frac{1.2 - i}{2.37} = 1 + X, \quad (11)$$

<sup>1195</sup> and for the  $\Delta R_{\min}(\gamma, \ell)$  by:

$$\text{weight} = 1 + \frac{1.8 - i}{6} = 1 + X, \quad (12)$$

<sup>1196</sup> and for the  $\Delta\phi(\ell, \ell)$  by:

$$\text{weight} = 1 + \frac{1.75 - i}{3.14} = 1 + X, \quad (13)$$

<sup>1197</sup> and for the  $|\Delta\eta(\ell, \ell)|$  by:

$$\text{weight} = 1 + \frac{1.2 - i}{2.5} = 1 + X, \quad (14)$$

<sup>1198</sup> where  $i$  is the bin centre.

<sup>1199</sup> The second weight is chosen by taking the difference at reconstruction-level between data and MC as the  
<sup>1200</sup> following:

$$\text{weight} = 1 + \frac{\text{data}_i - \text{MC}_i}{\text{data}_i} = 1 + Y, \quad (15)$$

<sup>1201</sup> The results of the test can be seen in Figure 47 where no bias of the unfolding procedure towards the  
<sup>1202</sup> nominal shape of the truth-level distribution is seen.

Not reviewed, for internal circulation only

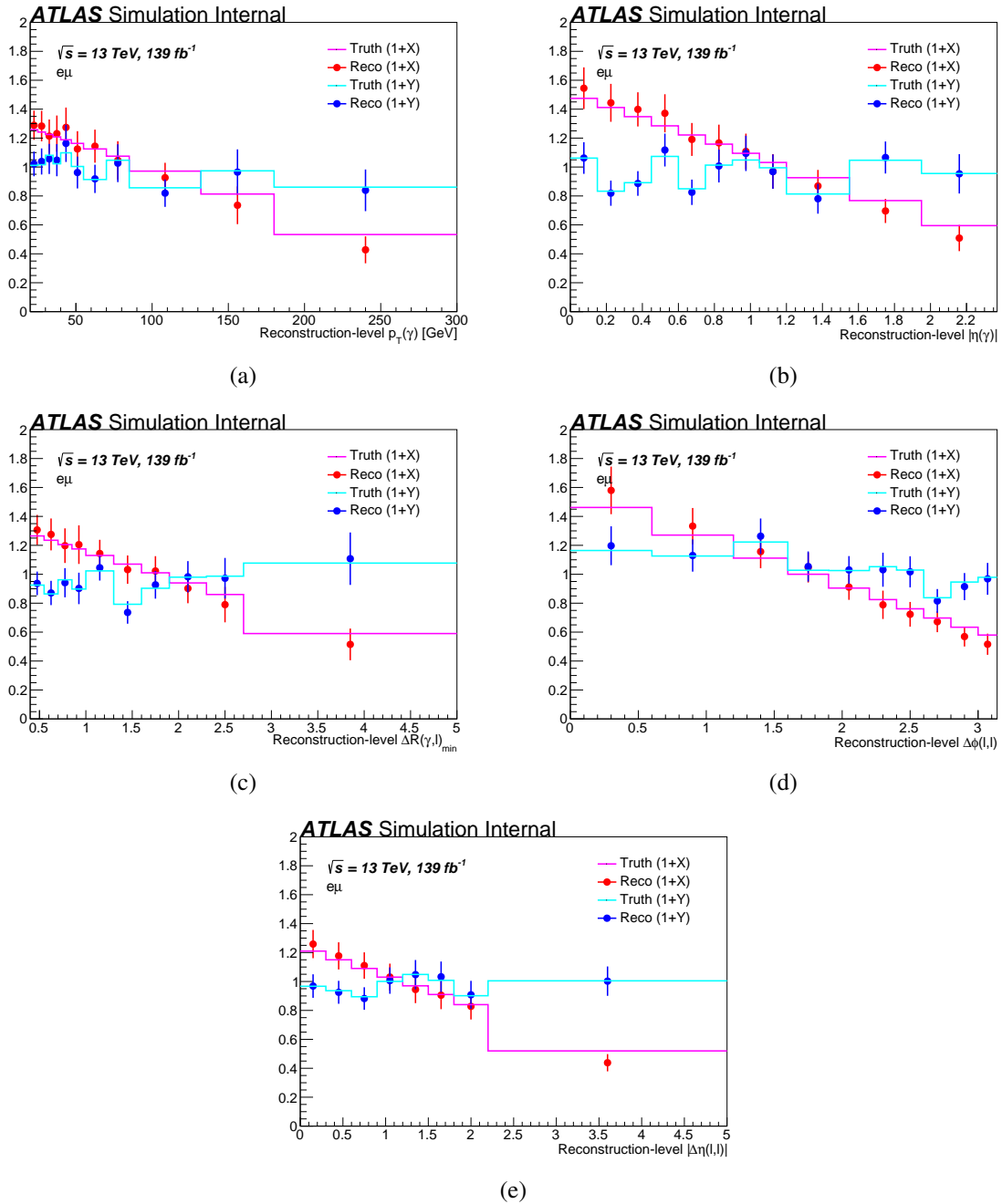


Figure 47: Stress test for photon  $p_T$ , photon  $|\eta|$  and  $\Delta R_{\min}(\gamma, \ell)$ ,  $|\Delta\eta(\ell, \ell)|$  and  $\Delta\phi(\ell, \ell)$ . Both the dots and lines are ratios made with respect to the nominal truth-level. The dots are the ratio of the unfolded reweighted reconstruction-level to the nominal truth-level distribution, while the solid lines are the ratio of the reweighted truth-level distributions to the nominal one. X is defined in Equations (10) to (14), while Y in Equation (15).

1203 **9 Results**

1204 **9.1 Inclusive fiducial cross-section**

1205 Following the same fit procedure already done on the Asimov dataset in Section 7, a fit was performed to  
 1206 ATLAS data. In contrast to the Asimov fit, the nuisance parameters of the systematic uncertainties can now  
 1207 be pulled to compensate for discrepancies between data and simulation. The initial fit setup, identical to  
 1208 that used for the Asimov dataset in Section 7, revealed that the fit is particularly sensitive to two modelling  
 1209 variations of the  $t\bar{t}\gamma$  signal: the  $t\bar{t}\gamma$  PYTHIA8 *var3c* and the  $t\bar{t}\gamma$  PS model variations. The Asimov fit already  
 1210 showed strong constraints of the nuisance parameters of those two variations, but the fit to data also pulled  
 1211 them far away from their central value. Their template distributions with respect to the total MC prediction  
 1212 and to data are shown in Figure 48. To have a better handle on their behaviour, and to understand whether  
 1213 the shape of their templates or their overall rate uncertainty triggers the pulls and constraints, it was decided  
 1214 to decorrelate rate and shape for both modelling variations for the final results presented in this section.  
 1215 That is, their rate differences with respect to the nominal prediction are removed from the templates, and  
 1216 they are added to the fit through separate nuisance parameters instead. For reference, the fit results with  
 1217 correlated rate and shape components are summarised in Appendix I.

1218 The pull distributions for the gamma parameters associated to each bin of the  $S_T$  are shown in Figure 49.  
 1219 None of them shows strong pulls away from the predicted nominal value. The pulls of the nuisance  
 1220 parameters can be found in Figure 50. For pulls shorter than the green  $\pm 1\sigma$  interval, the corresponding  
 1221 nuisance parameter is constrained during the fit. For values pulled away from the nominal, the fit favours  
 1222 the up or the down variation of the systematic. Nuisance parameters pulled by more than  $\pm 0.30$  and those  
 1223 constrained to less than 90% are listed in Table 14. A combination of strong pull and large constraint is  
 1224 only observed for the  $t\bar{t}\gamma$  *var3c* and PS model (shape only) modelling variations. Compared to the scenario  
 1225 presented in Appendix I, where rate and shape enter the same nuisance parameter for these two variations,  
 1226 the constraints are relaxed by about 5% each. In addition, the pull of the  $t\bar{t}\gamma$  *var3c* (shape only) nuisance  
 1227 parameter is looser in the decorrelated scenario. The pull for the  $t\bar{t}\gamma$  PS model variation remains similar in  
 1228 both correlated and decorrelated scenarios. It can be explained with Figure 48, where the down variation

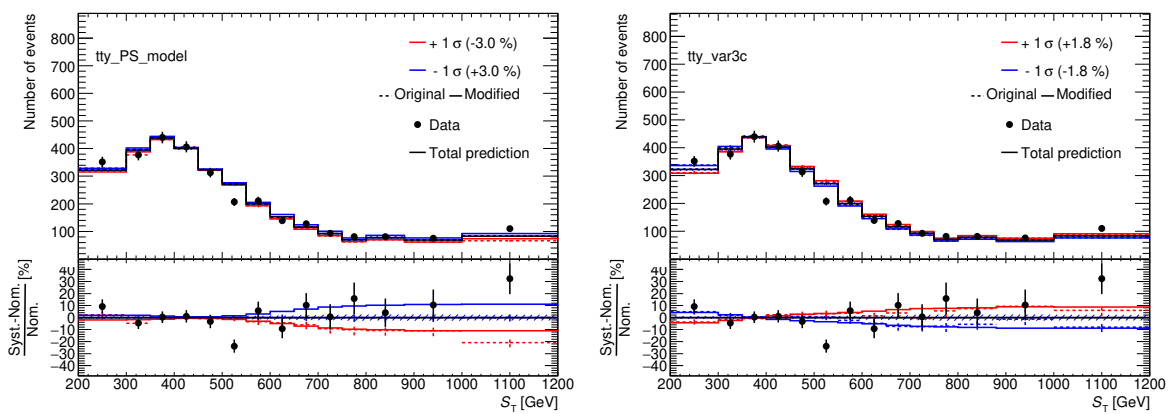


Figure 48: Systematic variations and their total impact on the MC prediction in comparison with data for (1) the  $t\bar{t}\gamma$  PS model uncertainty (alternative showering with HERWIG7) and (2) the  $t\bar{t}\gamma$  PYTHIA8 *var3c* tune variations. Due to strong pulls and constraints on the respective nuisance parameters, these two modelling variations enter the fit decorrelated in rate and shape.

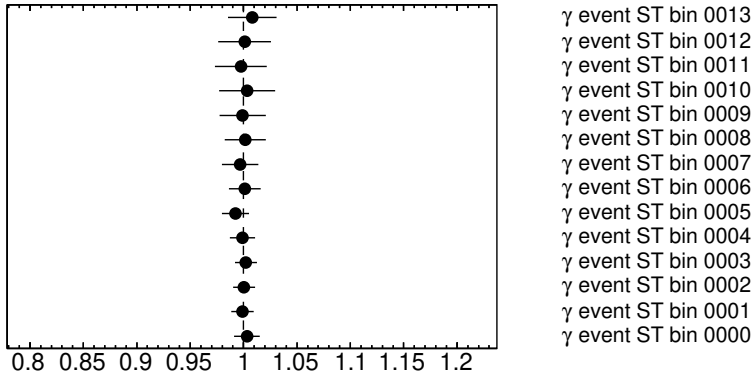


Figure 49: Gammas, that is, limitations of the individual bin statistics of the fitted distribution in the Asimov fit. Very large uncertainties on individual bins could mean that the binning should be re-adjusted. Strong pulls suggest the simulation to over/underpredict the data in certain bins.

Table 14: Strongly pulled and constrained nuisance parameters. Pulls are observed for a total of three modelling variations (top) and various experimental uncertainties (bottom), mostly related to the jet energy scale/resolution. Large constraints are only observed for the  $t\bar{t}\gamma$  PYTHIA8 *var3c* and the  $t\bar{t}\gamma$  PS model variations. The thresholds are pulls by more than  $\pm 0.30$  and constraints to less than 90%.

Nuisance parameter	pull value $(\hat{\theta} - \theta_0)/\Delta\theta$	constraint $\Delta\hat{\theta}/\Delta\theta [\%]$
$t\bar{t}\gamma$ <i>var3c</i> (shape only)	-0.39	70.6
$t\bar{t}\gamma$ PS model (shape only)	-1.43	71.0
$t\bar{t}$ PS model (shape only)	0.33	—
b-jet energy scale response	-0.39	—
CatRed eff. NP model1	-0.50	—
CatRed JER eff. NP1	0.43	—
CatRed JER eff. NP2	0.45	—
CatRed JER eff. NP3	0.68	—
CatRed JER eff. NP6	0.48	—
CatRed JER eff. NP rest	0.51	—
MET soft-track reso. par.	0.53	—
MET soft-track reso. perp.	0.58	—

Not reviewed, for internal circulation only

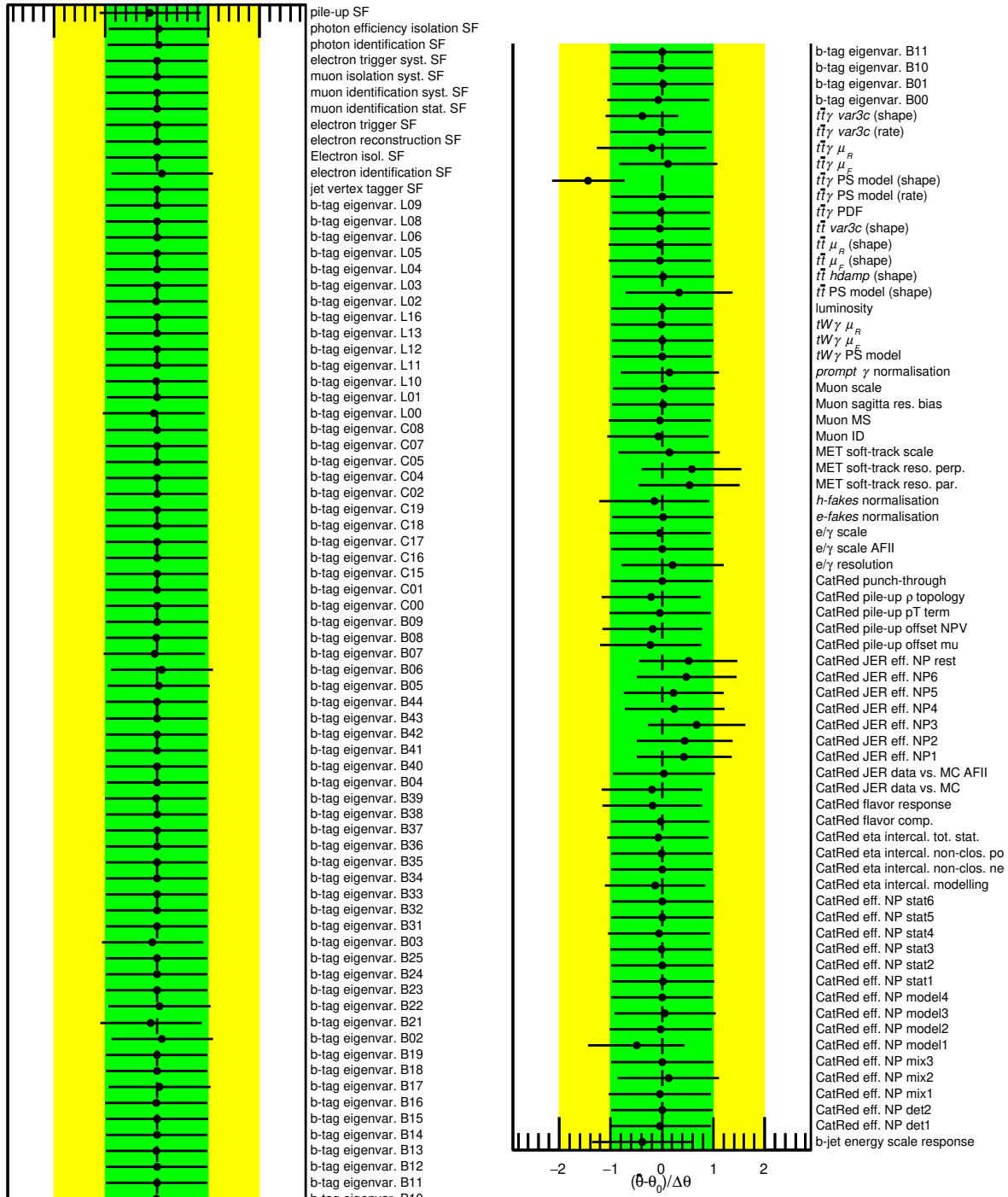


Figure 50: Pull distributions of all remaining nuisance parameters after pruning for the fit on data. If the error bar is shorter than the  $\pm 1\sigma$  interval, the corresponding nuisance parameter is constrained during the fit. If the mean value of the parameter is not zero, the fit favours the up or the down variation of the systematic. Pulls away from the nominal value are observed for some of the modelling uncertainties.

1229 goes in the same direction as the data points, and therefore is favoured by the fit. This applies to both the  
 1230 shape-only component in the results presented here and the correlated rate/shape nuisance parameter used  
 1231 in the appendix.

1232 The ranking of systematic uncertainties for the fit to data is shown in Figure 51, the results of which are  
 1233 very similar to the ranking performed to the Asimov dataset shown in Figure 36. The plot shows the 20  
 1234 highest ranked uncertainties, none of which show strong pulls or constraints. The critical shape-only  
 1235 modelling variations,  $t\bar{t}\gamma$  PYTHIA8 *var3c* and  $t\bar{t}\gamma$  PS model, are ranked far below the thresholds to enter the  
 1236 plot. However, their rate components, which are not pulled and unconstrained due to the removed shape  
 1237 component, are the highest ranked uncertainties for the final results. When correlating rate and shape, as  
 1238 presented in Appendix I, the two rate components are combined with shape information, and their impact  
 1239 on the parameter of interest is limited by the constraint that the shape invokes on the nuisance parameter.  
 1240 Apart from these two modelling variations, the highest ranked nuisance parameters are identical to those  
 1241 observed in the Asimov fit scenario: the normalisation of the background categories, photon efficiency  
 1242 isolation and identification scale factors, pile-up and luminosity.

1243 For nuisance parameters with 10% or higher correlation to others the correlation matrix is shown in Figure 52.  
 1244 Nuisance parameters with very high (positive or negative) correlation to the signal strength, such as the  $t\bar{t}\gamma$   
 1245 PS model (rate only) and the  $t\bar{t}\gamma$  PYTHIA8 *var3c* (rate only) modelling variations, are also the highest ranked  
 1246 uncertainties of the fit result. Other notably large values are observed between: (1) the h-fake background  
 1247 normalisation and the  $t\bar{t}$  PS model (shape) nuisance parameters, because they both act on the same event  
 1248 categories; (2) the  $t\bar{t}\gamma$  PS model (shape only) and the  $t\bar{t}\gamma$  *var3c* (shape only) nuisance parameters, which  
 1249 show similar shape differences to the nominal prediction, as shown in Figure 48.

1250 Pre-fit and post-fit yields for all categories are listed in Table 15. As done before, the pre-fit values of the  
 1251 signal categories are scaled to match the total predicted event yields to the number of events observed  
 1252 in data. Comparing pre-fit and post-fit values, the fit only has little impact on the central values of all  
 1253 categories – the largest effect are strong reductions of the uncertainties associated with the signal categories  
 1254 and the total prediction. The reduction is obtained both through constraining the impact of individual  
 1255 nuisance parameters, but also through correlations between them calculated during the fit.

Not reviewed, for internal circulation only

Table 15: Pre-fit and post-fit yields for all MC categories, including all uncertainties as described in Section 6. The pre-fit values of the signal categories are scaled to match the total predicted event yields to the number of events observed in data.

	Pre-fit	Post-fit
$t\bar{t}\gamma e\mu$	$2391 \pm 130$	$2390 \pm 70$
$tW\gamma e\mu$	$156 \pm 15$	$155 \pm 15$
Other $t\bar{t}\gamma/tW\gamma$	$280 \pm 17$	$280 \pm 9$
h-fake	$78 \pm 40$	$70 \pm 40$
e-fake	$23 \pm 12$	$23 \pm 11$
Prompt $\gamma$	$87 \pm 40$	$90 \pm 40$
Total	$3014 \pm 160$	$3010 \pm 60$
Data	3014	3014

Not reviewed, for internal circulation only

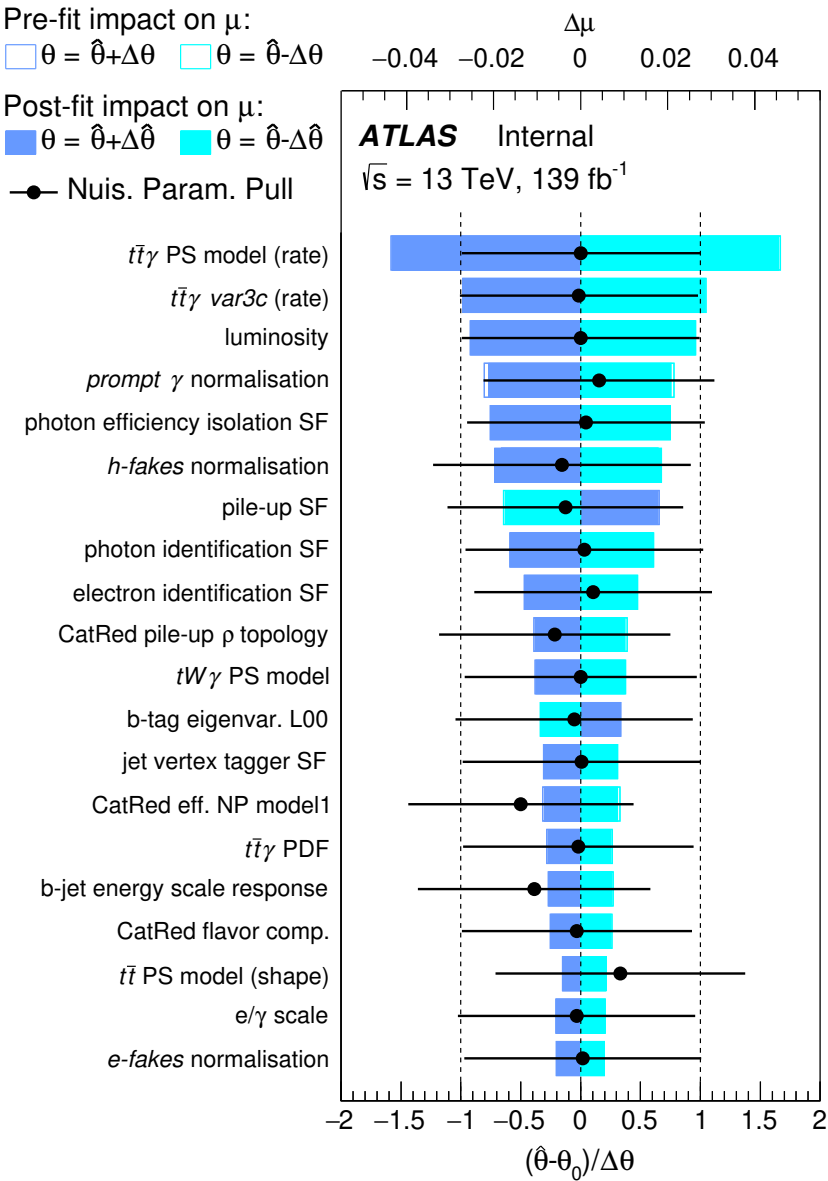


Figure 51: Ranking of systematics for the fit on data. The blue and turquoise bands indicate the post-fit impact on the measured signal strength in the fit, whereas the outlined blue and turquoise rectangles show the pre-fit impact. The difference between the two reflects the constraint of the nuisance parameter due to correlations in the fit. The impact is overlaid with the nuisance parameter pulls, as shown in Figure 50 already.



The resulting signal strength, defined as measured over predicted number of events, is found to be:

$$\mu = \frac{N_{\text{reco}}^{\text{meas.}}}{N_{\text{reco}}^{\text{pred.}}} = 1.422^{+0.028}_{-0.027} (\text{stat.})^{+0.085}_{-0.078} (\text{syst.}) = 1.422^{+0.089}_{-0.083},$$

corresponding to a relative uncertainty of  $^{+6.2\%}_{-5.8\%}$ . It should be noted, that the predicted cross-section from MC is only calculated at leading order in QCD and no k-factor is applied, hence the large discrepancy with a value of 1.0. The dependence on this signal strength can be avoided for measuring the inclusive fiducial cross-section if the ratio of the  $e\mu$  categories and the other decay channels is considered (i.e.  $t\bar{t}\gamma e\mu + tW\gamma e\mu$  over all  $t\bar{t}\gamma + tW\gamma$ ). Using the correction factor  $C = 0.4622$ , as introduced in Section 5, the fiducial cross-section for  $t\bar{t}\gamma$  production in the  $e\mu$  channel is measured to be

$$\sigma_{\text{fid}}(t\bar{t}\gamma \rightarrow e\mu) = \frac{N_{\text{reco}}^{\text{data}} - N_{\text{reco}}^{\text{bkg}}}{\mathcal{L}} \cdot \frac{N_{\text{reco}}^{e\mu \text{ signal}}}{N_{\text{reco}}^{\text{all signal}}} \cdot \frac{1}{C_{e\mu}} = 39.6^{+0.8}_{-0.8} (\text{stat.})^{+2.6}_{-2.2} (\text{syst.}) \text{ fb} = 39.6^{+2.7}_{-2.3} \text{ fb},$$

where the  $tW\gamma$  parton matching uncertainty, evaluated as a relative uncertainty on  $C$  with  $-2.75\%$ , was flipped and added to the systematic uncertainties in quadrature. The total relative uncertainty on the fiducial cross-section amounts to  $^{+6.8\%}_{-5.8\%}$ . Note that the signal strength does not consider the  $tW\gamma$  parton matching uncertainty, hence the difference in the relative uncertainties. A breakdown of the groups of systematic uncertainties and their impact is listed in Table 16. The  $tW\gamma$  parton matching uncertainty is listed separately since it is not included in the fit directly. As expected from the ranking shown in Figure 51, the largest impact comes from the nuisance parameters associated with signal modelling. The post-fit distribution of  $S_T$  is shown in Figure 53.

Table 16: Groups of systematic uncertainties and their relative impact on the result.

Group	Uncertainty
Signal modelling	3.8%
Background modelling	2.1%
Photons	1.9%
Luminosity	1.8%
Jets	1.6%
Pile-up	1.3%
Leptons	1.1%
Flavour-tagging	1.1%
MC statistics	0.4%
$E_T^{\text{miss}}$	0.2%
Total systematic impact	5.7%
$\oplus tW\gamma$ parton matching	-2.75%

Not reviewed, for internal circulation only

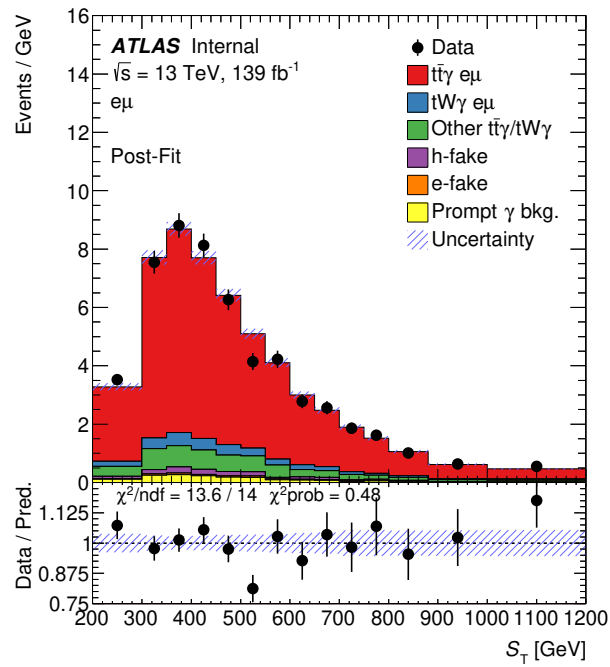


Figure 53: Post-fit distribution of  $S_T$ , the sum of all transverse momenta, the variable which was used in the fit.

## 1264 9.2 Differential cross-section

1265 The normalised measured differential cross-sections are shown in Figure 54, while the absolute measured  
 1266 differential cross-sections are shown in Figure 56. The measured distributions are obtained from data after  
 1267 subtracting the pref-fit background distributions. The last bin of the distributions does not include the  
 1268 overflow bin or in other words the differential cross-sections are measured in the range shown. In practise,  
 1269 this only affects the photon  $p_T$  distribution, for which few data events have larger  $p_T$  (permil contribution).  
 1270 The unfolded results are compared to the NLO theory prediction where the unfolding machinery is built  
 1271 using the combined signal  $t\bar{t}\gamma + tW\gamma$  MC to unfold (data-Bkg). The decomposed uncertainties of the  
 1272 unfolded distributions for the normalised and absolute differential cross-sections are illustrated in Figure 55  
 1273 and Figure 57, respectively. The numerical values of the normalised differential cross-sections results  
 1274 are summarised in Tables 17 to 21, while the absolute are shown in Tables 22 to 26. The last line in  
 1275 the absolute cross-section tables corresponds to the inclusive cross-section. The results agree with the  
 1276 inclusive cross-section (and among themselves) within  $\sim 1\%$ .

1277 To quantify the agreement between the theory and the unfolded distributions,  $\chi^2$ 's and their corresponding  
 1278  $p$ -values are calculated using the total covariance matrix. The formula for  $\chi^2$  is:

$$\chi^2 = (\sigma_{j,\text{unfold}}^{\text{diff,norm}} - \sigma_{j,\text{pred}}^{\text{diff,norm}}) \cdot C_{jk}^{-1} \cdot (\sigma_{k,\text{unfold}}^{\text{diff,norm}} - \sigma_{k,\text{pred}}^{\text{diff,norm}}) \quad (16)$$

1279 where  $C^{-1}$  is the inverse of the covariance matrix, and  $(\sigma_{j,\text{unfold}}^{\text{diff,norm}} - \sigma_{j,\text{pred}}^{\text{diff,norm}})$  is the difference between the  
 1280 unfolded and predicted distributions. For the normalized distribution, the last bin is not included in the  
 1281 above formula to take into account the fact that there is one additional redundant degree of freedom. The  
 1282  $\chi^2$  tests for the normalised cross-sections compared with a number of MC predictions as well as the theory  
 1283 NLO prediction are summarised in Table 27 while for absolute cross-sections they are shown in Table 28.

1284 The correlation matrices for the normalised cross-sections are shown in Tables 29 to 33, while for the  
 1285 absolute cross-sections they are shown in Tables 34 to 38.

Not reviewed, for internal circulation only

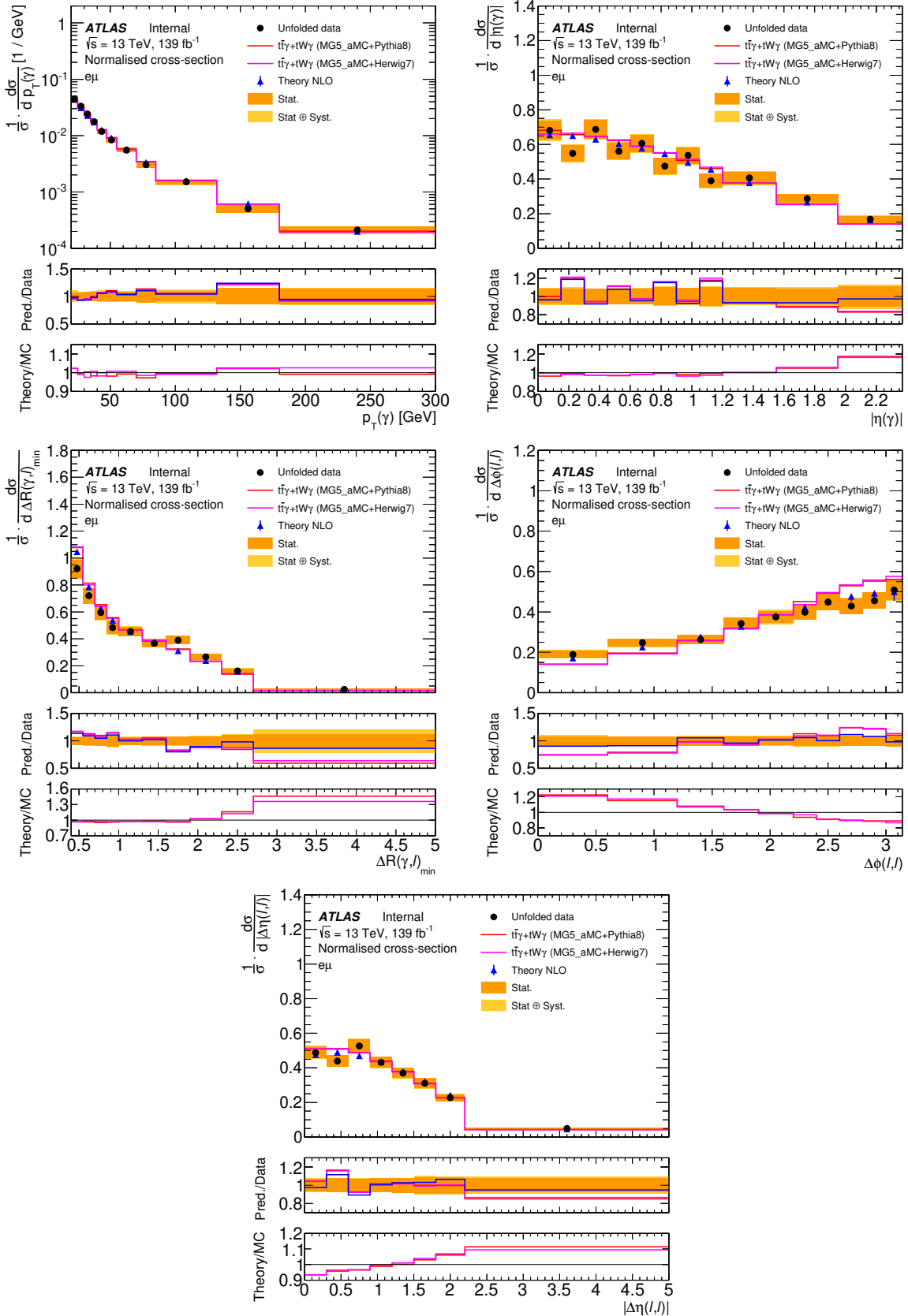


Figure 54: The normalized differential cross-section for the photon  $p_T$ , photon  $|\eta|$ ,  $\Delta R_{\min}(\gamma, \ell)$ ,  $\Delta\phi(\ell, \ell)$  and  $|\Delta\eta(\ell, \ell)|$ . The unfolded distribution to the parton-level (dots) is compared to the parton-level distributions of  $t\bar{t}\gamma + tW\gamma$  (MADGRAPH5\_aMC@NLO +PYTHIA8) (red),  $t\bar{t}\gamma + tW\gamma$  (MADGRAPH5\_aMC@NLO +HERWIG7) (Magenta) and theory NLO prediction (blue).

Not reviewed, for internal circulation only

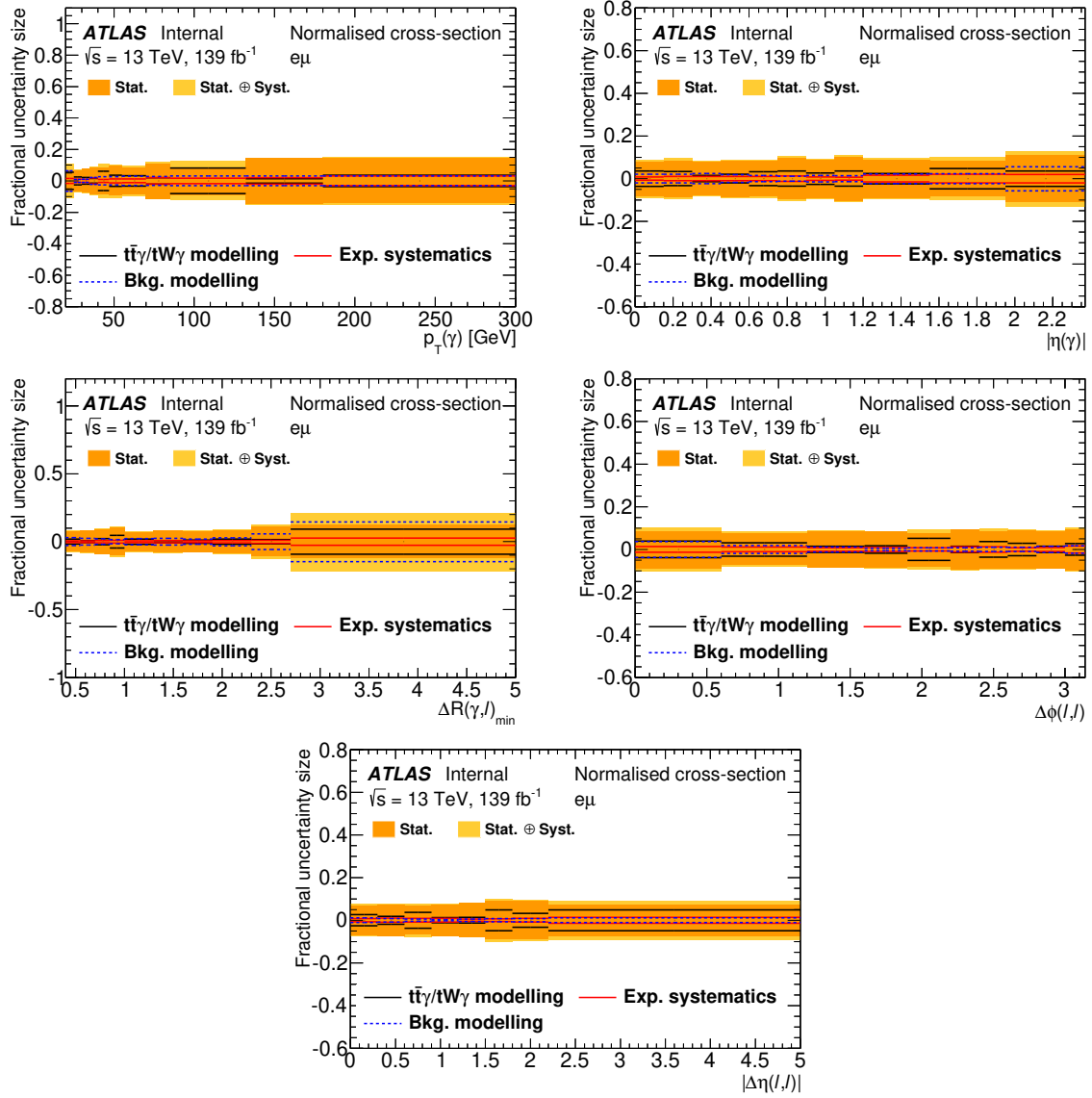


Figure 55: The decomposed systematic uncertainties for the normalised differential cross-sections as a function of photon  $p_T$ , photon  $|\eta|$ ,  $\Delta R_{\min}(\gamma, \ell)$ ,  $\Delta\phi(\ell, \ell)$  and  $|\Delta\eta(\ell, \ell)|$ .

Not reviewed, for internal circulation only

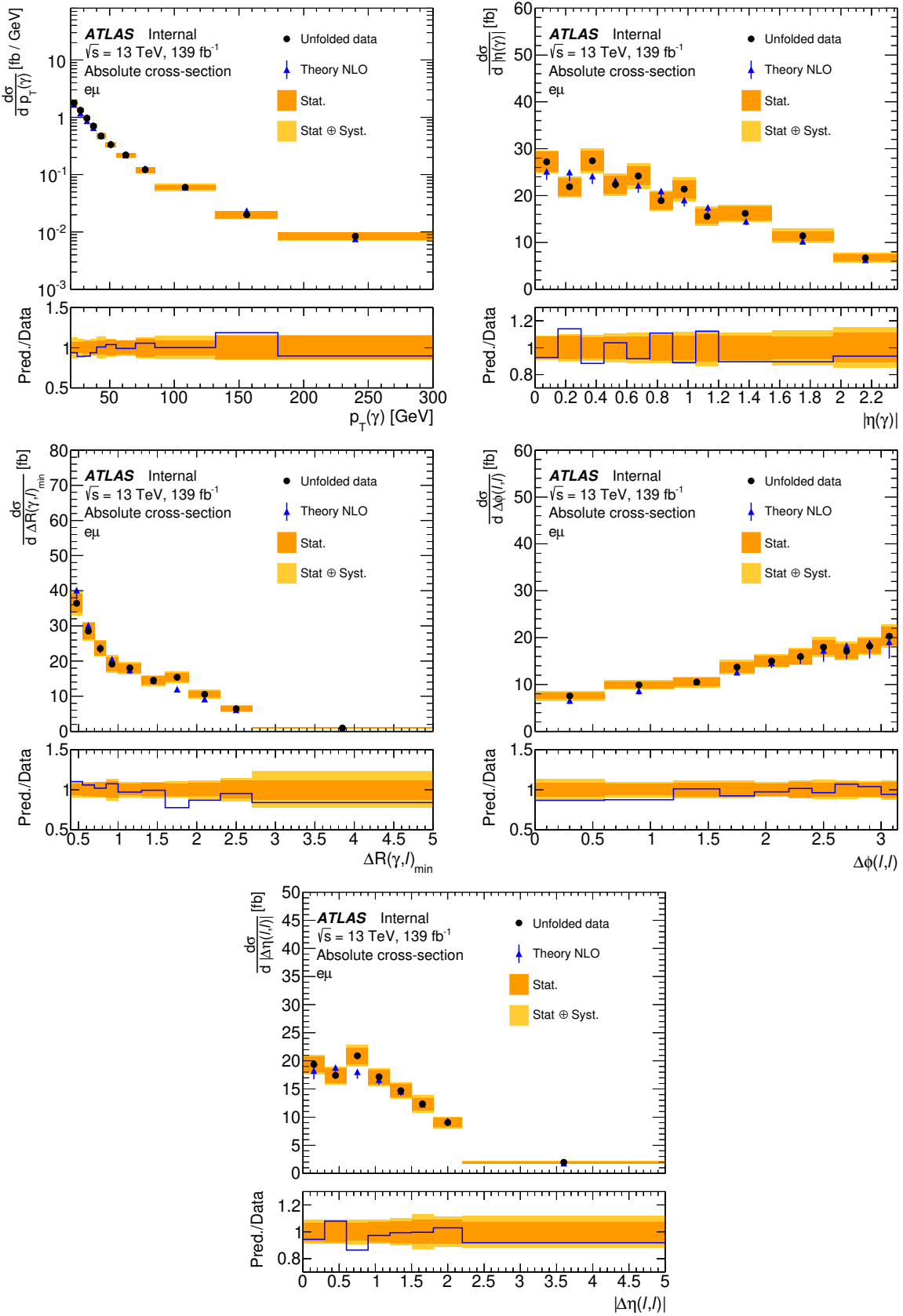


Figure 56: The absolute differential cross-section for the photon  $p_T$ , photon  $|\eta|$ ,  $\Delta R_{\min}(\gamma, \ell)$ ,  $\Delta\phi(\ell, \ell)$  and  $|\Delta\eta(\ell, \ell)|$ . The unfolded distribution to the parton-level (dots) is compared to the NLO theory prediction (blue).

Not reviewed, for internal circulation only

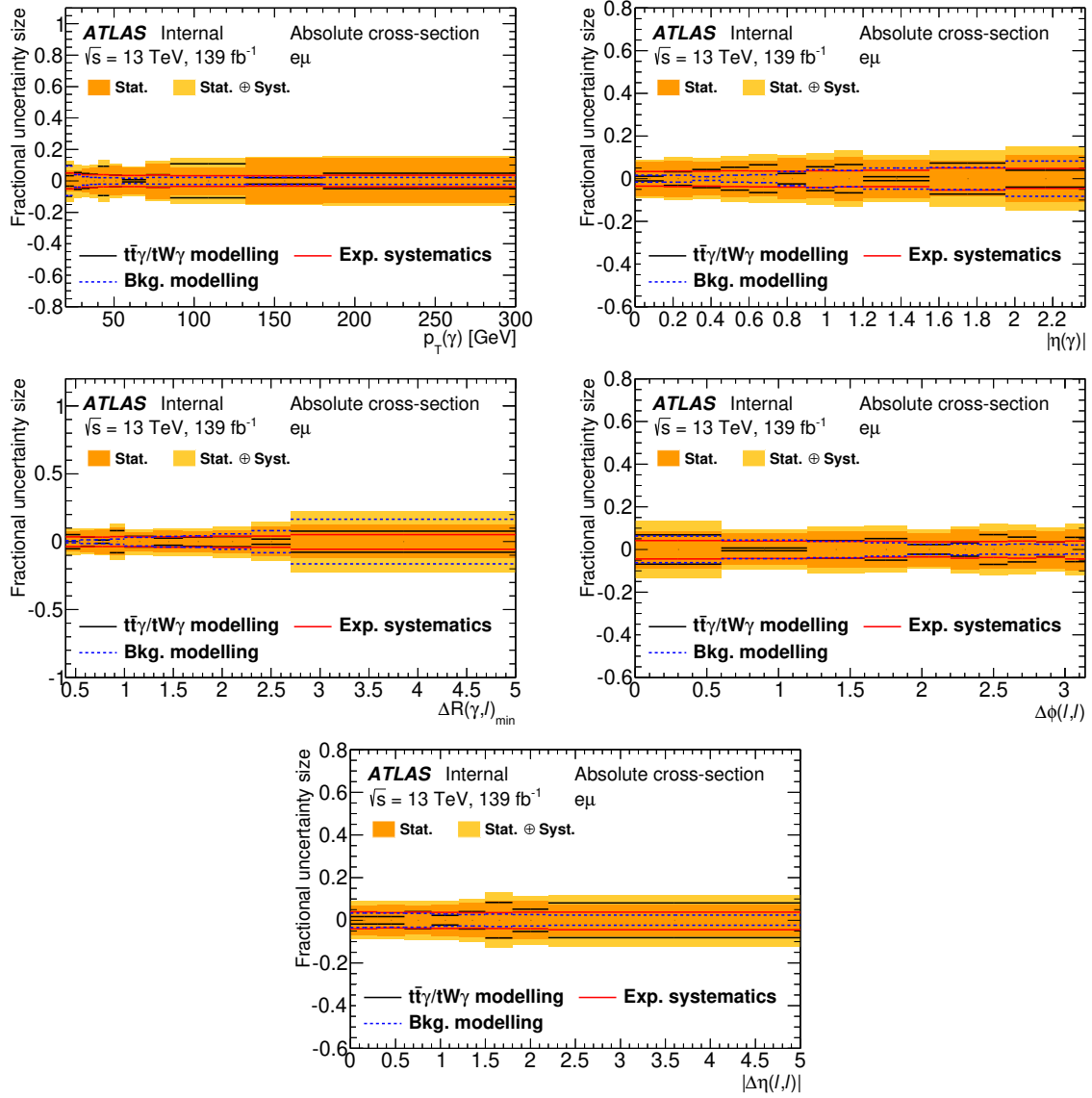


Figure 57: The decomposed systematic uncertainties for the absolute differential cross-sections as a function of the photon  $p_T$ , photon  $|\eta|$ ,  $\Delta R_{\min}(\gamma, \ell)$ ,  $\Delta\phi(\ell, \ell)$  and  $|\Delta\eta(\ell, \ell)|$ .

Table 17: The normalised differential cross-section in  $p_T(\gamma)$  bins, obtained using the iterative Bayesian method. The first and second associated uncertainties are the statistical and the systematic uncertainty, respectively.

$p_T(\gamma)$ [Gev]	normalised cross-section
20 – 25	$0.0447 \pm 0.0029 \pm 0.0039$
25 – 30	$0.0333 \pm 0.0022 \pm 0.0009$
30 – 35	$0.0243 \pm 0.0018 \pm 0.0006$
35 – 40	$0.0177 \pm 0.0015 \pm 0.0006$
40 – 47	$0.0119 \pm 0.0010 \pm 0.0008$
47 – 55	$0.0084 \pm 0.0008 \pm 0.0004$
55 – 70	$0.0055 \pm 0.0005 \pm 0.0003$
70 – 85	$0.0031 \pm 0.0003 \pm 0.0001$
85 – 132	$0.0015 \pm 0.0001 \pm 0.0001$
132 – 180	$0.0005 \pm 0.0001 \pm 0.0000$
180 – 300	$0.0002 \pm 0.0000 \pm 0.0000$

Table 18: The normalised differential cross-section in  $|\eta|(\gamma)$  bins, obtained using the iterative Bayesian method. The first and second associated uncertainties are the statistical and the systematic uncertainty, respectively.

$ \eta (\gamma)$	normalised cross-section
0.00 – 0.15	$0.68 \pm 0.05 \pm 0.03$
0.15 – 0.30	$0.55 \pm 0.05 \pm 0.02$
0.30 – 0.45	$0.69 \pm 0.05 \pm 0.02$
0.45 – 0.60	$0.56 \pm 0.05 \pm 0.02$
0.60 – 0.75	$0.61 \pm 0.05 \pm 0.02$
0.75 – 0.90	$0.47 \pm 0.05 \pm 0.02$
0.90 – 1.05	$0.54 \pm 0.05 \pm 0.02$
1.05 – 1.20	$0.39 \pm 0.04 \pm 0.02$
1.20 – 1.55	$0.41 \pm 0.04 \pm 0.02$
1.55 – 1.95	$0.29 \pm 0.02 \pm 0.02$
1.95 – 2.37	$0.17 \pm 0.02 \pm 0.01$

Table 19: The normalised differential cross-section in  $\Delta R_{\min}(\gamma, \ell)$  bins, obtained using the iterative Bayesian method. The first and second associated uncertainties are the statistical and the systematic uncertainty, respectively.

$\Delta R_{\min}(\gamma, \ell)$	normalised cross-section
0.40 – 0.55	$0.921 \pm 0.066 \pm 0.032$
0.55 – 0.70	$0.720 \pm 0.057 \pm 0.019$
0.70 – 0.85	$0.596 \pm 0.053 \pm 0.019$
0.85 – 1.00	$0.484 \pm 0.048 \pm 0.024$
1.00 – 1.30	$0.455 \pm 0.032 \pm 0.014$
1.30 – 1.60	$0.367 \pm 0.029 \pm 0.010$
1.60 – 1.90	$0.390 \pm 0.030 \pm 0.009$
1.90 – 2.30	$0.267 \pm 0.022 \pm 0.009$
2.30 – 2.70	$0.162 \pm 0.018 \pm 0.010$
2.70 – 5.00	$0.025 \pm 0.003 \pm 0.004$

Table 20: The normalised differential cross-section in  $|\Delta\eta(\ell, \ell)|$  bins, obtained using the iterative Bayesian method. The first and second associated uncertainties are the statistical and the systematic uncertainty, respectively.

$ \Delta\eta(\ell, \ell) $	normalised cross-section
0.0 – 0.3	$0.49 \pm 0.03 \pm 0.01$
0.3 – 0.6	$0.44 \pm 0.03 \pm 0.01$
0.6 – 0.9	$0.53 \pm 0.04 \pm 0.02$
0.9 – 1.2	$0.43 \pm 0.03 \pm 0.01$
1.2 – 1.5	$0.37 \pm 0.03 \pm 0.01$
1.5 – 1.8	$0.31 \pm 0.03 \pm 0.02$
1.8 – 2.2	$0.23 \pm 0.02 \pm 0.01$
2.2 – 5.0	$0.05 \pm 0.00 \pm 0.00$

Table 21: The normalised differential cross-section in  $\Delta\phi(\ell, \ell)$  bins, obtained using the iterative Bayesian method. The first and second associated uncertainties are the statistical and the systematic uncertainty, respectively.

$\Delta\phi(\ell, \ell)$	normalised cross-section
0.00 – 0.60	$0.19 \pm 0.02 \pm 0.01$
0.60 – 1.20	$0.25 \pm 0.02 \pm 0.01$
1.20 – 1.60	$0.26 \pm 0.02 \pm 0.01$
1.60 – 1.90	$0.34 \pm 0.03 \pm 0.01$
1.90 – 2.20	$0.38 \pm 0.03 \pm 0.02$
2.20 – 2.40	$0.40 \pm 0.04 \pm 0.01$
2.40 – 2.60	$0.45 \pm 0.04 \pm 0.02$
2.60 – 2.80	$0.43 \pm 0.04 \pm 0.01$
2.80 – 3.00	$0.46 \pm 0.04 \pm 0.01$
3.00 – 3.14	$0.51 \pm 0.05 \pm 0.02$

Table 22: The absolute differential cross-section in  $p_T(\gamma)$  bins, obtained using the iterative Bayesian method. The first and second associated uncertainties are the statistical and the systematic uncertainty, respectively.

$p_T(\gamma)$ [Gev]	absolute cross-section [fb]
20 – 25	$1.782 \pm 0.116 \pm 0.200$
25 – 30	$1.328 \pm 0.089 \pm 0.106$
30 – 35	$0.966 \pm 0.072 \pm 0.066$
35 – 40	$0.705 \pm 0.058 \pm 0.043$
40 – 47	$0.474 \pm 0.040 \pm 0.049$
47 – 55	$0.333 \pm 0.031 \pm 0.018$
55 – 70	$0.221 \pm 0.019 \pm 0.009$
70 – 85	$0.122 \pm 0.014 \pm 0.007$
85 – 132	$0.060 \pm 0.005 \pm 0.007$
132 – 180	$0.020 \pm 0.003 \pm 0.001$
180 – 300	$0.009 \pm 0.001 \pm 0.001$
Sum(cross-section per bin x bin width)	$39.8 \pm 4.7$

Table 23: The absolute differential cross-section in  $|\eta|(\gamma)$  bins, obtained using the iterative Bayesian method. The first and second associated uncertainties are the statistical and the systematic uncertainty, respectively.

$ \eta (\gamma)$	absolute cross-section [fb]
0.00 – 0.15	$27.21 \pm 2.17 \pm 1.06$
0.15 – 0.30	$21.90 \pm 1.88 \pm 1.11$
0.30 – 0.45	$27.40 \pm 2.12 \pm 1.52$
0.45 – 0.60	$22.36 \pm 1.89 \pm 1.50$
0.60 – 0.75	$24.18 \pm 1.98 \pm 1.85$
0.75 – 0.90	$18.93 \pm 1.83 \pm 1.02$
0.90 – 1.05	$21.40 \pm 1.90 \pm 1.69$
1.05 – 1.20	$15.58 \pm 1.60 \pm 1.32$
1.20 – 1.55	$16.21 \pm 1.44 \pm 1.04$
1.55 – 1.95	$11.44 \pm 0.94 \pm 1.17$
1.95 – 2.37	$06.70 \pm 0.73 \pm 0.69$
Sum(cross-section per bin x bin width)	$39.9 \pm 4.5$

Table 24: The absolute differential cross-section in  $\Delta R_{\min}(\gamma, \ell)$  bins, obtained using the iterative Bayesian method. The first and second associated uncertainties are the statistical and the systematic uncertainty, respectively.

$\Delta R_{\min}(\gamma, \ell)$	absolute cross-section [fb]
0.40 – 0.55	$36.45 \pm 2.61 \pm 2.33$
0.55 – 0.70	$28.50 \pm 2.26 \pm 1.45$
0.70 – 0.85	$23.58 \pm 2.08 \pm 0.91$
0.85 – 1.00	$19.15 \pm 1.89 \pm 1.76$
1.00 – 1.30	$18.02 \pm 1.28 \pm 1.12$
1.30 – 1.60	$14.52 \pm 1.15 \pm 0.88$
1.60 – 1.90	$15.42 \pm 1.20 \pm 1.02$
1.90 – 2.30	$10.55 \pm 0.88 \pm 0.84$
2.30 – 2.70	$06.42 \pm 0.70 \pm 0.60$
2.70 – 5.00	$00.98 \pm 0.12 \pm 0.19$
Sum(cross-section per bin x bin width)	$39.6 \pm 4.4$

Table 25: The absolute differential cross-section in  $|\Delta\eta(\ell, \ell)|$  bins, obtained using the iterative Bayesian method. The first and second associated uncertainties are the statistical and the systematic uncertainty, respectively.

$ \Delta\eta(\ell, \ell) $	absolute cross-section [fb]
0.0 – 0.3	$19.38 \pm 1.35 \pm 1.05$
0.3 – 0.6	$17.44 \pm 1.27 \pm 0.90$
0.6 – 0.9	$20.91 \pm 1.39 \pm 1.35$
0.9 – 1.2	$17.15 \pm 1.27 \pm 0.90$
1.2 – 1.5	$14.68 \pm 1.16 \pm 0.88$
1.5 – 1.8	$12.34 \pm 1.09 \pm 1.17$
1.8 – 2.2	$09.05 \pm 0.80 \pm 0.63$
2.2 – 5.0	$01.97 \pm 0.15 \pm 0.18$
Sum(cross-section per bin x bin width)	$39.7 \pm 4.0$

Table 26: The absolute differential cross-section in  $\Delta\phi(\ell, \ell)$  bins, obtained using the iterative Bayesian method. The first and second associated uncertainties are the statistical and the systematic uncertainty, respectively.

$\Delta\phi(\ell, \ell)$	absolute cross-section [fb]
0.00 – 0.60	$07.58 \pm 0.66 \pm 0.77$
0.60 – 1.20	$09.89 \pm 0.72 \pm 0.58$
1.20 – 1.60	$10.49 \pm 0.90 \pm 0.71$
1.60 – 1.90	$13.69 \pm 1.16 \pm 0.96$
1.90 – 2.20	$15.02 \pm 1.17 \pm 0.72$
2.20 – 2.40	$15.96 \pm 1.50 \pm 0.88$
2.40 – 2.60	$17.97 \pm 1.57 \pm 1.47$
2.60 – 2.80	$17.13 \pm 1.51 \pm 1.27$
2.80 – 3.00	$18.20 \pm 1.56 \pm 1.00$
3.00 – 3.14	$20.32 \pm 1.96 \pm 1.47$
Sum(cross-section per bin x bin width)	$40.0 \pm 4.4$

Table 27:  $\chi^2$  values between the normalised unfolded cross-section and various predictions from the MC simulation as well as between normalised unfolded cross-section and theoretical NLO prediction in the  $e\mu$  channel.

Predictions	$p_T(\gamma)$		$ \eta (\gamma)$		$\Delta R_{\min}(\gamma, \ell)$		$ \Delta\eta(\ell, \ell) $		$\Delta\phi(\ell, \ell)$	
	$\chi^2/\text{NDF}$	$p\text{-value}$	$\chi^2/\text{NDF}$	$p\text{-value}$	$\chi^2/\text{NDF}$	$p\text{-value}$	$\chi^2/\text{NDF}$	$p\text{-value}$	$\chi^2/\text{NDF}$	$p\text{-value}$
$t\bar{t}\gamma + tW\gamma$ (MADGRAPH5_aMC@NLO +PYTHIA8)	6.3/10	0.79	16.4/10	0.09	20.1/9	0.02	6.5/7	0.48	30.8/9	<0.01
$t\bar{t}\gamma + tW\gamma$ (MADGRAPH5_aMC@NLO +HERWIG7)	5.3/10	0.87	18.3/10	0.05	18.9/9	0.03	6.8/7	0.45	31.6/9	<0.01
Theory NLO	6.0/10	0.82	14.6/10	0.15	13.5/9	0.14	5.6/7	0.59	5.8/9	0.76

Table 28:  $\chi^2$  values between the absolute unfolded cross-section and theoretical NLO prediction in the  $e\mu$  channel.

Predictions	$p_T(\gamma)$		$ \eta (\gamma)$		$\Delta R_{\min}(\gamma, \ell)$		$ \Delta\eta(\ell, \ell) $		$\Delta\phi(\ell, \ell)$	
	$\chi^2/\text{NDF}$	$p\text{-value}$	$\chi^2/\text{NDF}$	$p\text{-value}$	$\chi^2/\text{NDF}$	$p\text{-value}$	$\chi^2/\text{NDF}$	$p\text{-value}$	$\chi^2/\text{NDF}$	$p\text{-value}$
Theory NLO	6.1/11	0.87	13.9/11	0.24	11.7/10	0.31	6.2/8	0.62	5.8/10	0.83



Table 33: Full correlation matrix for the normalised  $\Delta\phi(\ell, \ell)$  observable in the  $e\mu$  channel, accounting for the statistical and systematic uncertainties.

Bin	0.0 - 0.6	0.6 - 1.2	1.2 - 1.6	1.6 - 1.9	1.9 - 2.2	2.2 - 2.4	2.4 - 2.6	2.6 - 2.8	2.8 - 3.0	3.0 - 3.14
0.0 - 0.6	<b>1.00</b>	0.00	-0.02	-0.03	-0.05	-0.04	-0.05	-0.04	-0.04	-0.03
0.6 - 1.2	0.00	<b>1.00</b>	-0.03	-0.04	-0.05	-0.04	-0.04	-0.04	-0.04	-0.03
1.2 - 1.6	-0.02	-0.03	<b>1.00</b>	-0.04	-0.05	-0.04	-0.05	-0.05	-0.05	-0.04
1.6 - 1.9	-0.03	-0.04	-0.04	<b>1.00</b>	-0.04	-0.04	-0.04	-0.04	-0.04	-0.03
1.9 - 2.2	-0.05	-0.05	-0.05	-0.04	<b>1.00</b>	-0.03	-0.03	-0.04	-0.04	-0.02
2.2 - 2.4	-0.04	-0.04	-0.04	-0.04	-0.03	<b>1.00</b>	-0.03	-0.03	-0.03	-0.02
2.4 - 2.6	-0.05	-0.04	-0.05	-0.04	-0.03	-0.03	<b>1.00</b>	-0.03	-0.03	-0.02
2.6 - 2.8	-0.04	-0.04	-0.05	-0.04	-0.04	-0.03	-0.03	<b>1.00</b>	-0.03	-0.02
2.8 - 3.0	-0.04	-0.04	-0.05	-0.04	-0.04	-0.03	-0.03	-0.03	<b>1.00</b>	-0.02
3.0 - 3.14	-0.03	-0.03	-0.04	-0.03	-0.02	-0.02	-0.02	-0.02	-0.02	<b>1.00</b>



Not reviewed, for internal circulation only

Table 37: Full correlation matrix for the absolute  $|\Delta\eta(\ell, \ell)|$  observable in the  $e\mu$  channel, accounting for the statistical and systematic uncertainties.

Bin	0.0 - 0.3	0.3 - 0.6	0.6 - 0.9	0.9 - 1.2	1.2 - 1.5	1.5 - 1.8	1.8 - 2.2	2.2 - 5.0
0.0 - 0.3	<b>1.00</b>	0.20	0.21	0.19	0.17	0.16	0.16	0.16
0.3 - 0.6	0.20	<b>1.00</b>	0.20	0.18	0.16	0.15	0.15	0.15
0.6 - 0.9	0.21	0.20	<b>1.00</b>	0.19	0.17	0.15	0.16	0.16
0.9 - 1.2	0.19	0.18	0.19	<b>1.00</b>	0.16	0.14	0.15	0.15
1.2 - 1.5	0.17	0.16	0.17	0.16	<b>1.00</b>	0.13	0.13	0.14
1.5 - 1.8	0.16	0.15	0.15	0.14	0.13	<b>1.00</b>	0.12	0.13
1.8 - 2.2	0.16	0.15	0.16	0.15	0.13	0.12	<b>1.00</b>	0.13
2.2 - 5.0	0.16	0.15	0.16	0.15	0.14	0.13	0.13	<b>1.00</b>

Table 38: Full correlation matrix for the absolute  $\Delta\phi(\ell, \ell)$  observable in the  $e\mu$  channel, accounting for the statistical and systematic uncertainties.

Bin	0.0 - 0.6	0.6 - 1.2	1.2 - 1.6	1.6 - 1.9	1.9 - 2.2	2.2 - 2.4	2.4 - 2.6	2.6 - 2.8	2.8 - 3.0	3.0 - 3.14
0.0 - 0.6	<b>1.00</b>	0.21	0.17	0.15	0.14	0.13	0.12	0.14	0.14	0.13
0.6 - 1.2	0.21	<b>1.00</b>	0.19	0.16	0.17	0.15	0.15	0.16	0.15	0.15
1.2 - 1.6	0.17	0.19	<b>1.00</b>	0.15	0.15	0.14	0.13	0.15	0.13	0.12
1.6 - 1.9	0.15	0.16	0.15	<b>1.00</b>	0.13	0.12	0.11	0.12	0.12	0.11
1.9 - 2.2	0.14	0.17	0.15	0.13	<b>1.00</b>	0.12	0.12	0.13	0.12	0.11
2.2 - 2.4	0.13	0.15	0.14	0.12	0.12	<b>1.00</b>	0.11	0.13	0.11	0.11
2.4 - 2.6	0.12	0.15	0.13	0.11	0.12	0.11	<b>1.00</b>	0.12	0.10	0.10
2.6 - 2.8	0.14	0.16	0.15	0.12	0.13	0.13	0.12	<b>1.00</b>	0.12	0.12
2.8 - 3.0	0.14	0.15	0.13	0.12	0.12	0.11	0.10	0.12	<b>1.00</b>	0.11
3.0 - 3.14	0.13	0.15	0.12	0.11	0.11	0.11	0.10	0.12	0.11	<b>1.00</b>

---

**1286 10 Conclusion**

1287 An inclusive and differential measurement of the  $t\bar{t}\gamma$  production cross-section has been performed. The  
1288 cross-section is measured in a fiducial phase space region based on kinematic cuts on photon,  $b$ -jet and  
1289 charged lepton momenta in the final state with one electron and one muon. For the estimation of efficiencies  
1290 and acceptance corrections, a LO Monte Carlo simulation of the  $2 \rightarrow 7$  process is used. The simulation  
1291 includes initial- and final state radiation of the photon from all involved partons in the matrix element.  
1292 Only resonant top-quark production is taken into account in the simulation. Possible off-shell contribution  
1293 leading to the same final state is included in the simulation of the  $tW\gamma$  process.

1294 The results are compared to the prediction from the LO Monte Carlo simulation and the latest NLO theory  
1295 prediction for the  $pp \rightarrow bWbW\gamma$  process from Ref. [1] which includes the off-shell contribution.

Not reviewed, for internal circulation only

1296 **References**

- [1] G. Bevilacqua, H. B. Hartanto, M. Kraus, T. Weber and M. Worek, *Hard photons in hadroproduction of top quarks with realistic final states*, JHEP **10** (2018) 158, arXiv: [1803.09916 \[hep-ph\]](#) (cit. on pp. 5, 12, 16, 24, 25, 30, 104).
- [2] U. Husemann, *Top-Quark Physics: Status and Prospects*, Prog. Part. Nucl. Phys. **95** (2017) 48, arXiv: [1704.01356 \[hep-ex\]](#) (cit. on p. 11).
- [3] U. Baur, A. Juste, L. H. Orr and D. Rainwater, *Probing electroweak top quark couplings at hadron colliders*, Phys. Rev. **D71** (2005) 054013, arXiv: [hep-ph/0412021 \[hep-ph\]](#) (cit. on p. 11).
- [4] A. O. Bouzas and F. Larios, *Electromagnetic dipole moments of the top quark*, Phys. Rev. **D87** (2013) 074015, arXiv: [1212.6575 \[hep-ph\]](#) (cit. on p. 11).
- [5] R. Röntsch and M. Schulze, *Probing top-Z dipole moments at the LHC and ILC*, JHEP **08** (2015) 044, arXiv: [1501.05939 \[hep-ph\]](#) (cit. on p. 11).
- [6] M. Schulze and Y. Soreq, *Pinning down electroweak dipole operators of the top quark*, Eur. Phys. J. **C76** (2016) 466, arXiv: [1603.08911 \[hep-ph\]](#) (cit. on p. 11).
- [7] O. Bessidskaia Bylund, F. Maltoni, I. Tsinikos, E. Vryonidou and C. Zhang, *Probing top quark neutral couplings in the Standard Model Effective Field Theory at NLO in QCD*, JHEP **05** (2016) 052, arXiv: [1601.08193 \[hep-ph\]](#) (cit. on p. 11).
- [8] P.-F. Duan, Y. Zhang, Y. Wang, M. Song and G. Li, *Electroweak corrections to top quark pair production in association with a hard photon at hadron colliders*, Phys. Lett. **B766** (2017) 102, arXiv: [1612.00248 \[hep-ph\]](#) (cit. on p. 11).
- [9] CDF Collaboration (Aaltonen, T. et al.), *Evidence for  $t\bar{t}\gamma$  production and measurement of  $\sigma_{t\bar{t}\gamma}/\sigma_{t\bar{t}}$* , Phys. Rev. **D84** (2011) 031104, arXiv: [1106.3970 \[hep-ex\]](#) (cit. on p. 11).
- [10] ATLAS Collaboration, *Measurement of the inclusive  $t\bar{t}\gamma$  cross section at  $\sqrt{s} = 7$  TeV with the ATLAS detector*, ATLAS-CONF-2011-153, 2011, URL: <https://cds.cern.ch/record/1398197> (cit. on p. 11).
- [11] ATLAS Collaboration, *Observation of top-quark pair production in association with a photon and measurement of the  $t\bar{t}\gamma$  production cross section in  $pp$  collisions at  $\sqrt{s} = 7$  TeV using the ATLAS detector*, Phys. Rev. D **91** (2015) 072007, arXiv: [1502.00586 \[hep-ex\]](#) (cit. on p. 11).
- [12] *Measurement of the inclusive top-quark pair + photon production cross section in the muon + jets channel in  $pp$  collisions at 8 TeV*, tech. rep. CMS-PAS-TOP-13-011, CERN, 2014, URL: <https://cds.cern.ch/record/1644573> (cit. on p. 11).
- [13] CMS Collaboration, *Measurement of the semileptonic  $t\bar{t} + \gamma$  production cross section in  $pp$  collisions at  $\sqrt{s} = 8$  TeV*, JHEP **10** (2017) 006, arXiv: [1706.08128 \[hep-ex\]](#) (cit. on p. 11).
- [14] ATLAS Collaboration, *Measurement of the  $t\bar{t}\gamma$  production cross section in proton–proton collisions at  $\sqrt{s} = 8$  TeV with the ATLAS detector*, JHEP **11** (2017) 086, arXiv: [1706.03046 \[hep-ex\]](#) (cit. on p. 11).
- [15] ATLAS Collaboration, *Measurements of inclusive and differential fiducial cross-sections of  $t\bar{t}\gamma$  production in leptonic final states at  $\sqrt{s} = 13$  TeV in ATLAS*, Eur. Phys. J. C **79** (2019) 382, arXiv: [1812.01697 \[hep-ex\]](#) (cit. on pp. 11, 21, 40).

- [16] K. Melnikov, M. Schulze and A. Scharf, *QCD corrections to top quark pair production in association with a photon at hadron colliders*, Phys. Rev. **D83** (2011) 074013, arXiv: [1102.1967 \[hep-ph\]](#) (cit. on p. 11).
- [17] ATLAS Collaboration, *The ATLAS Experiment at the CERN Large Hadron Collider*, JINST **3** (2008) S08003 (cit. on p. 14).
- [18] ATLAS Collaboration, *ATLAS Insertable B-Layer Technical Design Report*, ATLAS-TDR-19, 2010, URL: <https://cds.cern.ch/record/1291633> (cit. on p. 14), Addendum: ATLAS-TDR-19-ADD-1, 2012, URL: <https://cds.cern.ch/record/1451888>.
- [19] B. Abbott et al., *Production and integration of the ATLAS Insertable B-Layer*, JINST **13** (2018) T05008, arXiv: [1803.00844 \[physics.ins-det\]](#) (cit. on p. 14).
- [20] ATLAS Collaboration, *Performance of the ATLAS trigger system in 2015*, Eur. Phys. J. C **77** (2017) 317, arXiv: [1611.09661 \[hep-ex\]](#) (cit. on p. 14).
- [21] ATLAS Collaboration, *The ATLAS Simulation Infrastructure*, Eur. Phys. J. C **70** (2010) 823, arXiv: [1005.4568 \[physics.ins-det\]](#) (cit. on p. 15).
- [22] S. Agostinelli et al., *GEANT4 – a simulation toolkit*, Nucl. Instrum. Meth. A **506** (2003) 250 (cit. on p. 15).
- [23] T. Sjöstrand, S. Mrenna and P. Skands, *PYTHIA 6.4 physics and manual*, JHEP **05** (2006) 026, arXiv: [hep-ph/0603175](#) (cit. on p. 15).
- [24] T. Sjöstrand et al., *An introduction to PYTHIA 8.2*, Comput. Phys. Commun. **191** (2015) 159, arXiv: [1410.3012 \[hep-ph\]](#) (cit. on p. 15).
- [25] ATLAS Collaboration, *Summary of ATLAS Pythia 8 tunes*, ATL-PHYS-PUB-2012-003, 2012, URL: <https://cds.cern.ch/record/1474107> (cit. on p. 15).
- [26] A. D. Martin, W. J. Stirling, R. S. Thorne and G. Watt, *Parton distributions for the LHC*, Eur. Phys. J. C **63** (2009) 189, arXiv: [0901.0002 \[hep-ph\]](#) (cit. on p. 15).
- [27] J. Alwall et al., *The automated computation of tree-level and next-to-leading order differential cross sections, and their matching to parton shower simulations*, JHEP **07** (2014) 079, arXiv: [1405.0301 \[hep-ph\]](#) (cit. on p. 15).
- [28] R. D. Ball et al., *Parton distributions with LHC data*, Nucl. Phys. B **867** (2013) 244, arXiv: [1207.1303 \[hep-ph\]](#) (cit. on p. 15).
- [29] ATLAS Collaboration, *ATLAS Pythia 8 tunes to 7 TeV data*, ATL-PHYS-PUB-2014-021, 2014, URL: <https://cds.cern.ch/record/1966419> (cit. on p. 15).
- [30] D. J. Lange, *The EvtGen particle decay simulation package*, Nucl. Instrum. Meth. A **462** (2001) 152 (cit. on p. 15).
- [31] T. Gleisberg et al., *Event generation with SHERPA 1.1*, JHEP **02** (2009) 007, arXiv: [0811.4622 \[hep-ph\]](#) (cit. on p. 16).
- [32] S. Höche, F. Krauss, S. Schumann and F. Siegert, *QCD matrix elements and truncated showers*, JHEP **05** (2009) 053, arXiv: [0903.1219 \[hep-ph\]](#) (cit. on p. 16).
- [33] T. Gleisberg and S. Höche, *Comix, a new matrix element generator*, JHEP **12** (2008) 039, arXiv: [0808.3674 \[hep-ph\]](#) (cit. on p. 16).
- [34] S. Schumann and F. Krauss, *A parton shower algorithm based on Catani–Seymour dipole factorisation*, JHEP **03** (2008) 038, arXiv: [0709.1027 \[hep-ph\]](#) (cit. on p. 16).

- [35] S. Höche, F. Krauss, M. Schönher and F. Siegert, *A critical appraisal of NLO+PS matching methods*, JHEP **09** (2012) 049, arXiv: [1111.1220 \[hep-ph\]](#) (cit. on p. 16).
- [36] S. Catani, F. Krauss, B. R. Webber and R. Kuhn, *QCD matrix elements + parton showers*, JHEP **11** (2001) 063, arXiv: [hep-ph/0109231 \[hep-ph\]](#) (cit. on p. 16).
- [37] S. Höche, F. Krauss, M. Schönher and F. Siegert, *QCD matrix elements + parton showers. The NLO case*, JHEP **04** (2013) 027, arXiv: [1207.5030 \[hep-ph\]](#) (cit. on p. 16).
- [38] F. Caccioli, P. Maierhöfer and S. Pozzorini, *Scattering Amplitudes with Open Loops*, Phys. Rev. Lett. **108** (2012) 111601, arXiv: [1111.5206 \[hep-ph\]](#) (cit. on p. 16).
- [39] A. Denner, S. Dittmaier and L. Hofer, *COLLIER: A fortran-based complex one-loop library in extended regularizations*, Comput. Phys. Commun. **212** (2017) 220, arXiv: [1604.06792 \[hep-ph\]](#) (cit. on p. 16).
- [40] P. Nason, *A new method for combining NLO QCD with shower Monte Carlo algorithms*, JHEP **11** (2004) 040, arXiv: [hep-ph/0409146](#) (cit. on p. 17).
- [41] S. Frixione, P. Nason and C. Oleari, *Matching NLO QCD computations with parton shower simulations: the POWHEG method*, JHEP **11** (2007) 070, arXiv: [0709.2092 \[hep-ph\]](#) (cit. on p. 17).
- [42] S. Alioli, P. Nason, C. Oleari and E. Re, *A general framework for implementing NLO calculations in shower Monte Carlo programs: the POWHEG BOX*, JHEP **06** (2010) 043, arXiv: [1002.2581 \[hep-ph\]](#) (cit. on p. 17).
- [43] R. D. Ball et al., *Parton distributions for the LHC Run II*, JHEP **04** (2015) 040, arXiv: [1410.8849 \[hep-ph\]](#) (cit. on p. 17).
- [44] M. Czakon and A. Mitov, *Top++: A program for the calculation of the top-pair cross-section at hadron colliders*, Comput. Phys. Commun. **185** (2014) 2930, arXiv: [1112.5675 \[hep-ph\]](#) (cit. on p. 17).
- [45] N. Kidonakis, *Next-to-next-to-leading logarithm resummation for s-channel single top quark production*, Phys. Rev. **D81** (2010) 054028, arXiv: [1001.5034 \[hep-ph\]](#) (cit. on p. 17).
- [46] N. Kidonakis, *Two-loop soft anomalous dimensions for single top quark associated production with a W- or H-*, Phys. Rev. **D82** (2010) 054018, arXiv: [1005.4451 \[hep-ph\]](#) (cit. on p. 17).
- [47] N. Kidonakis, *Next-to-next-to-leading-order collinear and soft gluon corrections for t-channel single top quark production*, Phys. Rev. **D83** (2011) 091503, arXiv: [1103.2792 \[hep-ph\]](#) (cit. on p. 17).
- [48] ATLAS Collaboration, *Measurement of  $W^\pm$  and Z Boson Production Cross Sections in pp Collisions at  $\sqrt{s} = 13$  TeV with the ATLAS Detector*, ATLAS-CONF-2015-039, 2015, URL: <https://cds.cern.ch/record/2045487> (cit. on p. 17).
- [49] J. M. Campbell and R. K. Ellis, *Update on vector boson pair production at hadron colliders*, Phys. Rev. D **60** (1999) 113006, arXiv: [hep-ph/9905386](#) (cit. on p. 17).
- [50] D. de Florian et al., *Handbook of LHC Higgs cross sections: 4. Deciphering the nature of the Higgs sector*, (2016), arXiv: [1610.07922 \[hep-ph\]](#) (cit. on p. 17).
- [51] ATLAS Collaboration, *Luminosity determination in pp collisions at  $\sqrt{s} = 13$  TeV using the ATLAS detector at the LHC*, ATLAS-CONF-2019-021, 2019, URL: <https://cds.cern.ch/record/2677054> (cit. on p. 21).
- [52] G. Avoni et al., *The new LUCID-2 detector for luminosity measurement and monitoring in ATLAS*, JINST **13** (2018) P07017 (cit. on p. 21).

- [53] ATLAS Collaboration, *Measurements of top-quark pair differential cross-sections in the  $e\mu$  channel in  $pp$  collisions at  $\sqrt{s} = 13$  TeV using the ATLAS detector*, *Eur. Phys. J. C* **77** (2017) 292, arXiv: [1612.05220 \[hep-ex\]](https://arxiv.org/abs/1612.05220) (cit. on p. 21).
- [54] ATLAS Collaboration, *Electron reconstruction and identification in the ATLAS experiment using the 2015 and 2016 LHC proton–proton collision data at  $\sqrt{s} = 13$  TeV*, *Eur. Phys. J. C* **79** (2019) 639, arXiv: [1902.04655 \[physics.ins-det\]](https://arxiv.org/abs/1902.04655) (cit. on p. 21).
- [55] ATLAS Collaboration, *Electron and photon energy calibration with the ATLAS detector using 2015–2016 LHC proton–proton collision data*, *JINST* **14** (2019) P03017, arXiv: [1812.03848 \[hep-ex\]](https://arxiv.org/abs/1812.03848) (cit. on pp. 21, 22).
- [56] ATLAS Collaboration, *Muon reconstruction performance of the ATLAS detector in proton–proton collision data at  $\sqrt{s} = 13$  TeV*, *Eur. Phys. J. C* **76** (2016) 292, arXiv: [1603.05598 \[hep-ex\]](https://arxiv.org/abs/1603.05598) (cit. on pp. 22, 54).
- [57] ATLAS Collaboration, *Measurement of the photon identification efficiencies with the ATLAS detector using LHC Run 2 data collected in 2015 and 2016*, *Eur. Phys. J. C* **79** (2019) 205, arXiv: [1810.05087 \[hep-ex\]](https://arxiv.org/abs/1810.05087) (cit. on pp. 22, 122).
- [58] M. Cacciari, G. P. Salam and G. Soyez, *The anti- $k_t$  jet clustering algorithm*, *JHEP* **04** (2008) 063, arXiv: [0802.1189 \[hep-ph\]](https://arxiv.org/abs/0802.1189) (cit. on p. 22).
- [59] M. Cacciari, G. P. Salam and G. Soyez, *FastJet user manual*, *Eur. Phys. J. C* **72** (2012) 1896, arXiv: [1111.6097 \[hep-ph\]](https://arxiv.org/abs/1111.6097) (cit. on p. 22).
- [60] ATLAS Collaboration, *Properties of jets and inputs to jet reconstruction and calibration with the ATLAS detector using proton–proton collisions at  $\sqrt{s} = 13$  TeV*, ATL-PHYS-PUB-2015-036, 2015, URL: <https://cds.cern.ch/record/2044564> (cit. on p. 22).
- [61] ATLAS Collaboration, *Jet energy scale measurements and their systematic uncertainties in proton–proton collisions at  $\sqrt{s} = 13$  TeV with the ATLAS detector*, *Phys. Rev. D* **96** (2017) 072002, arXiv: [1703.09665 \[hep-ex\]](https://arxiv.org/abs/1703.09665) (cit. on pp. 22, 56).
- [62] ATLAS Collaboration, *Tagging and suppression of pileup jets with the ATLAS detector*, ATLAS-CONF-2014-018, 2014, URL: <https://cds.cern.ch/record/1700870> (cit. on pp. 22, 56).
- [63] ATLAS Collaboration, *Optimisation and performance studies of the ATLAS b-tagging algorithms for the 2017-18 LHC run*, ATL-PHYS-PUB-2017-013, 2017, URL: <https://cds.cern.ch/record/2273281> (cit. on p. 22).
- [64] ATLAS Collaboration, *Measurements of b-jet tagging efficiency with the ATLAS detector using  $t\bar{t}$  events at  $\sqrt{s} = 13$  TeV*, *JHEP* **08** (2018) 089, arXiv: [1805.01845 \[hep-ex\]](https://arxiv.org/abs/1805.01845) (cit. on p. 22).
- [65] ATLAS Collaboration,  *$E_T^{\text{miss}}$  performance in the ATLAS detector using 2015–2016 LHC pp collisions*, ATLAS-CONF-2018-023, 2018, URL: <https://cds.cern.ch/record/2625233> (cit. on pp. 22, 57).
- [66] ATLAS Collaboration, *Measurement of the  $t\bar{t}\gamma$  production cross-section in  $pp$  collision at  $\sqrt{s} = 13$  TeV with the ATLAS detector*, tech. rep. ATL-COM-PHYS-2017-673, CERN, 2017, URL: <https://cds.cern.ch/record/2266485> (cit. on p. 24).
- [67] V. Blobel, ‘An Unfolding method for high-energy physics experiments’, *Advanced Statistical Techniques in Particle Physics. Proceedings, Conference, Durham, UK, March 18-22, 2002*, 2002 258, arXiv: [hep-ex/0208022 \[hep-ex\]](https://arxiv.org/abs/hep-ex/0208022), URL: <http://www.ippp.dur.ac.uk/Workshops/02/statistics/proceedings/blobel2.pdf> (cit. on p. 32).

- [68] G. D'Agostini, *A Multidimensional unfolding method based on Bayes' theorem*, Nucl. Instrum. Meth. **A362** (1995) 487 (cit. on p. 37).
- [69] ATLAS Collaboration, *Electron efficiency measurements with the ATLAS detector using the 2015 LHC proton–proton collision data*, ATLAS-CONF-2016-024, 2016, URL: <https://cds.cern.ch/record/2157687> (cit. on p. 54).
- [70] ATLAS Collaboration, *Photon identification in 2015 ATLAS data*, ATL-PHYS-PUB-2016-014, 2016, URL: <https://cds.cern.ch/record/2203125> (cit. on p. 55).
- [71] ATLAS Collaboration, *Jet energy measurement and its systematic uncertainty in proton–proton collisions at  $\sqrt{s} = 7\text{ TeV}$  with the ATLAS detector*, Eur. Phys. J. C **75** (2015) 17, arXiv: [1406.0076 \[hep-ex\]](https://arxiv.org/abs/1406.0076) (cit. on p. 56).
- [72] ATLAS Collaboration, *Optimisation of the ATLAS b-tagging performance for the 2016 LHC Run*, ATL-PHYS-PUB-2016-012, 2016, URL: <https://cds.cern.ch/record/2160731> (cit. on p. 57).

Not reviewed, for internal circulation only

## 1473 A $Wt+PS$ versus $tW\gamma$

1474 The  $tW\gamma$  background, which interferes at next-to-leading order in QCD with the  $t\bar{t}\gamma$  signal, was studied  
 1475 in more detail to find the optimal solution to simulate it. In earlier versions of the note, the  $tW\gamma$   
 1476 contributions were estimated by using inclusive  $Wt$  samples, where the photons are entirely generated  
 1477 by the interfaced parton shower ( $Wt+PS$ ). Comparisons between  $Wt+PS$  and dedicated  $tW\gamma$  samples are  
 1478 shown in Appendix A.1. At the same time,  $t\bar{t}+PS$  samples are compared against the dedicated  $t\bar{t}\gamma$  sample  
 1479 as well. In the results, the dedicated  $tW\gamma$  sample, described in Section 3, is used. However, at the time of  
 1480 these comparison studies, the  $tW\gamma$  sample only included photons from radiative production. Therefore,  
 1481 reweighting techniques were applied to account for the missing contributions from radiative decays. The  
 1482 reweighting is detailed in Appendix A.2.

### 1483 A.1 Summary of the comparison studies

1484 This section compares two  $Wt+PS$  samples: the nominal  $Wt$  simulation with POWHEG and PYTHIA8, as  
 1485 described in Section 3, and a simulation with HERWIG7 as alternative parton shower. This is compared  
 1486 against the  $tW\gamma$  sample as introduced in the same section. As the  $tW\gamma$  sample assumes stable top and  $W$   
 1487 boson, it only accounts for photons from radiative production. A reweighting to combined production  
 1488 and decay mode, as a function of the photon transverse momentum, is applied to  $tW\gamma$ , further detailed  
 1489 in the following Appendix A.2. The top rows of Figures 58 and 59 show the distributions of  $Wt$  with  
 1490 PYTHIA8,  $Wt$  with HERWIG7, and the reweighted  $tW\gamma$  for different observables. The bottom rows compare  
 1491 the nominal  $t\bar{t}+PS$  sample, simulated with POWHEG and PYTHIA8, as described in Section 3, the alternative  
 1492 showering of  $t\bar{t}$  with HERWIG7, and the dedicated  $t\bar{t}\gamma$  sample for the same observables.

1493 Multiple conclusions were drawn from the studies: (1) the rate of photon radiation in PYTHIA8 agrees  
 1494 relatively well with that observed in dedicated samples, where the photon radiation is included in the  
 1495 matrix element. On the other hand, the rate of photon radiation is underestimated in HERWIG7, seen  
 1496 for both  $Wt+PS$  and  $t\bar{t}+PS$  samples, with 39% and 36% lower rates compared to the dedicated samples,  
 1497 respectively. (2) Estimating the  $tW\gamma$  contributions with the nominal inclusive samples, and using the  
 1498 alternative HERWIG7 sample as a systematic variation introduces large uncertainties. Given the shapes and  
 1499 rates from the dedicated  $t\bar{t}\gamma$  and  $tW\gamma$  samples, these uncertainties seem to be an overestimation. (3) Even  
 1500 the nominal inclusive samples with photons from PYTHIA8 do not simulate the photon kinematics correctly,  
 1501 in particular the photon transverse momentum.

1502 Following these conclusions, the decision was taken to *not* estimate the  $tW\gamma$  contributions from inclusive  
 1503 samples, because the photon kinematics are simulated imprecisely, and the alternative showering with  
 1504 HERWIG7 does not agree with the dedicated samples. The latter is consistently observed for  $t\bar{t}+PS$  and  $t\bar{t}\gamma$ ,  
 1505 too. Despite the necessary reweighting of the  $tW\gamma$  production-only sample, this simulation provides the  
 1506 more accurate prediction for  $tW\gamma$  contributions to the analysis.

### 1507 A.2 Reweighting studies of $tW\gamma$ production mode

1508 The production of top quark and  $W$  boson in association with a photon includes several processes where  
 1509 the photon is (1) coming from  $Wt$  production (*production mode*), or (2) from the radiation of either of the  
 1510 top quark or  $W$  boson or their decay products (*decay mode*). At the time of the comparison studies, only  
 1511 the production-mode simulation, as detailed in Section 3, was available. MC samples for the decay mode

Not reviewed, for internal circulation only

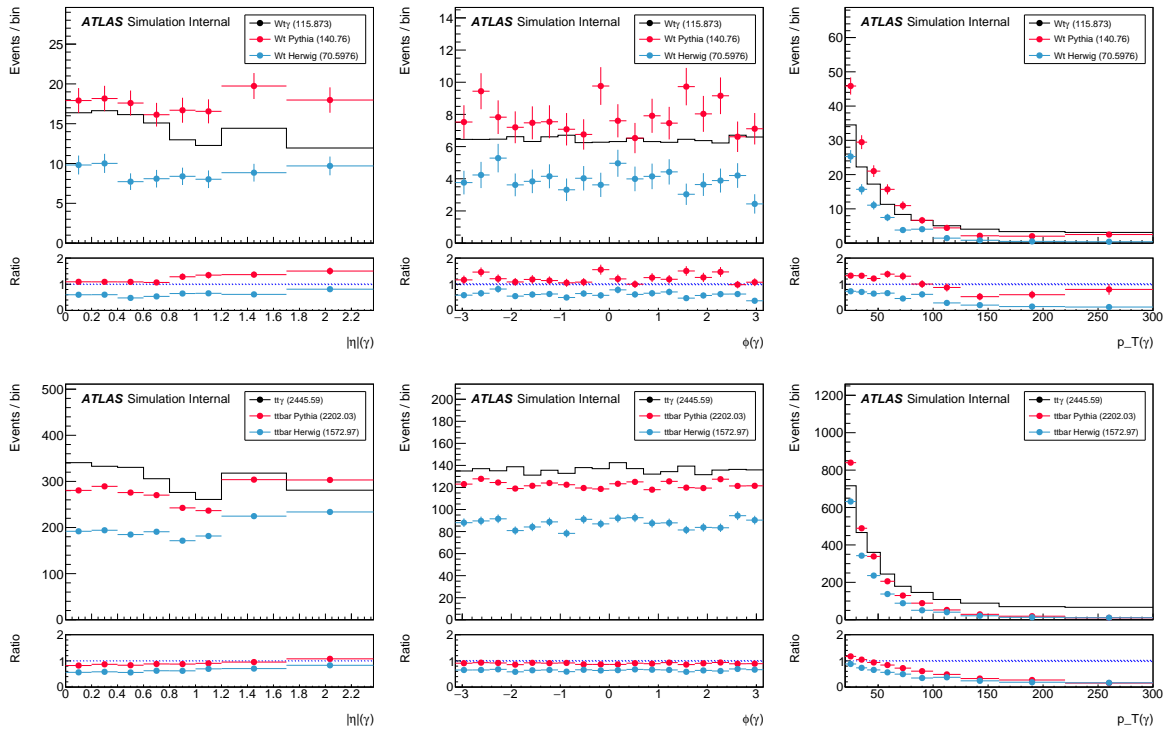


Figure 58: Comparison of  $Wt+PS$  and  $tW\gamma$  samples, as well as  $t\bar{t}+PS$  and  $t\bar{t}\gamma$  samples for the following observables:  $|\eta|(\gamma)$ ,  $\phi(\gamma)$  and  $p_T(\gamma)$ . The default  $e\mu$  signal region event-selection cuts are applied, as detailed in Section 4. The  $tW\gamma$  sample is already reweighted according to the procedure described in Appendix A.2.

generated with **MADGRAPH5\_aMC@NLO** at LO and showered with PYTHIA8 and A14 NNPDF2.3LO tune were under production. Because of this, a reweighting technique is used to scale the available production mode samples to the sum of the two modes, which has a 15% uncertainty due to scale and PDF variations on the fiducial cross-section.

A rivet analysis with truth (EVNT) MC samples (as listed in Appendix C) for both the processes are done following an event selection similar to Section 4. The  $p_T^\gamma$  distribution of the truth events passing the selection are shown for both the processes in Figure 60(a) along with the ratio of the sum of the two processes and the production mode.

A fit of an exponential function is done on this ratio histogram and a nicely fitted function is achieved. The functional form with parameters is given by:

$$R(p_T^\gamma) = 1.10316 + \exp(-2.81183 \cdot 10^{-5} \cdot p_T^\gamma [GeV] + 1.32037)$$

The resulting fitted function is drawn on top of the ratio histogram in Figure 60(b).

Subsequently, the fitted function is used to apply an event-by-event weight on truth level. A comparison is done of the  $tW\gamma$  production-mode MC distributions with the same sample reweighted (to match the sum of production and decay mode process) as shown in Figure 61. The comparison also includes the truth sum of production and decay mode processes. Closure of the two are also shown as a ratio in Figure 61. This reweighting, parameterised in truth photon  $p_T$ , is used to reweight the  $tW\gamma$  simulation in the comparison studies detailed in the previous section.

Not reviewed, for internal circulation only

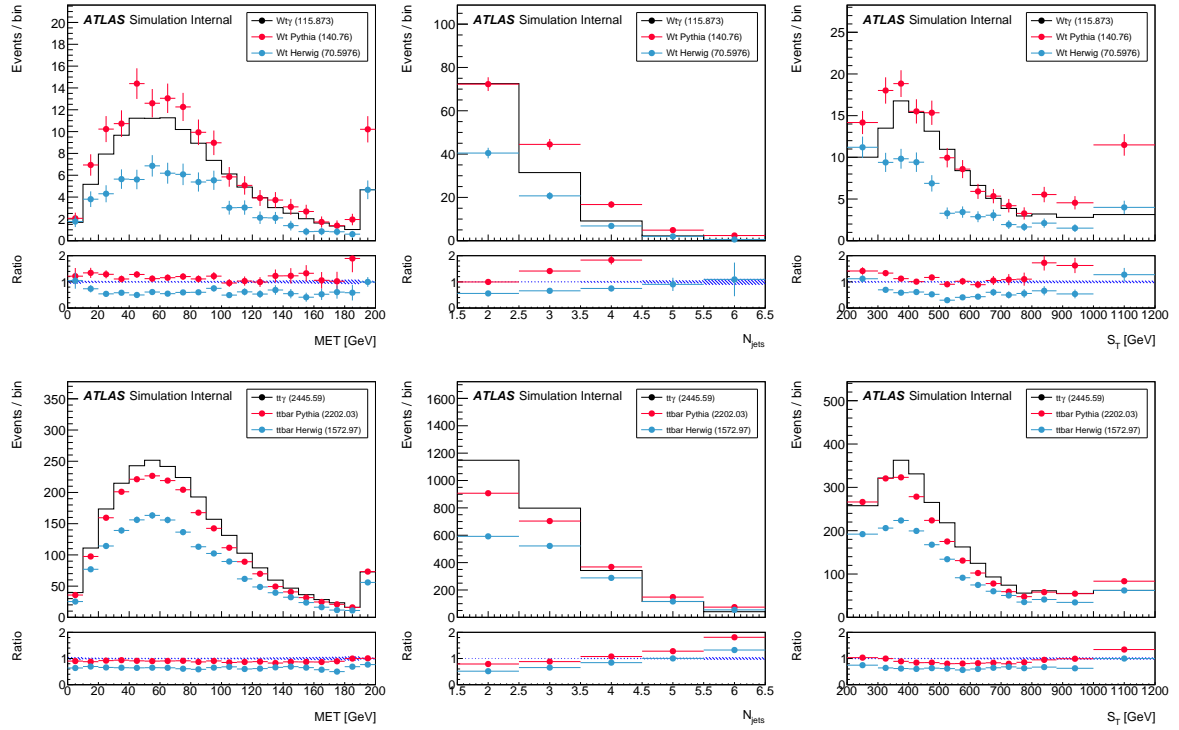


Figure 59: Comparison of  $Wt$ +PS and  $tW\gamma$  samples, as well as  $t\bar{t}$ +PS and  $t\bar{t}\gamma$  samples for the following observables: missing transverse energy  $E_{\text{T}}^{\text{miss}}$ , jet multiplicity  $N_{\text{jets}}$ , and sum over all transverse momenta  $S_{\text{T}}$  of the event. The default  $e\mu$  signal region event-selection cuts are applied, as detailed in Section 4. The  $tW\gamma$  sample is already reweighted according to the procedure described in Appendix A.2.

Not reviewed, for internal circulation only

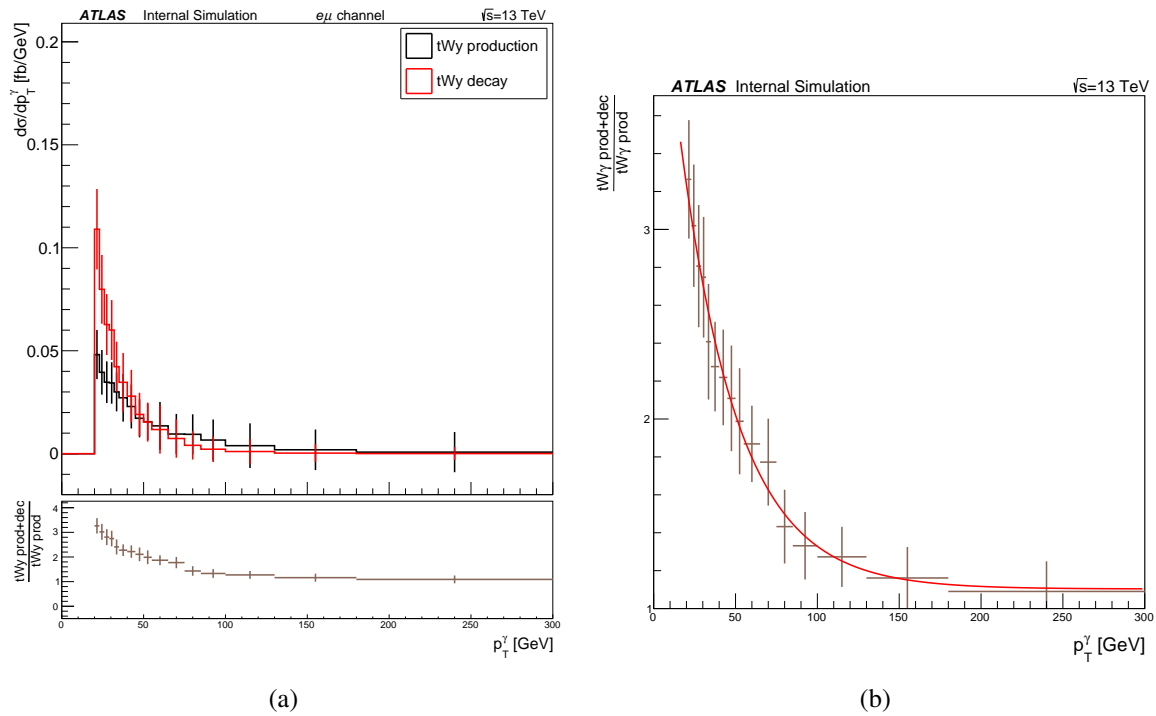


Figure 60: (a) The truth comparison of the  $tW\gamma$  production and decay mode processes and the ratio of the sum of  $tW\gamma$  production+decay mode processes over the production mode process for the transverse momentum of the photon (b) The fit result for this ratio.

Not reviewed, for internal circulation only

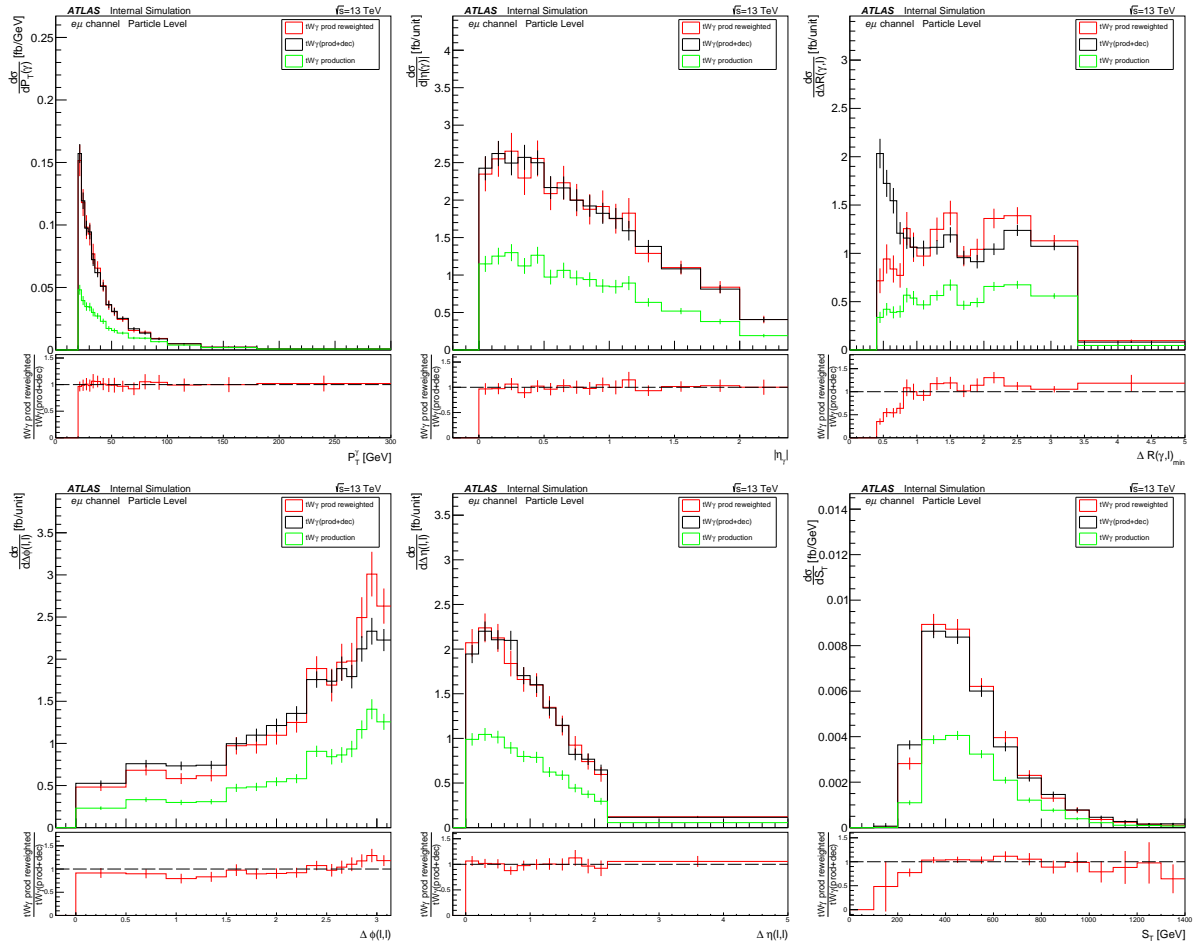


Figure 61: Truth comparison of the reweighted  $tW\gamma$  production mode with the sum of production and decay mode for the photon transverse momentum  $p_T^\gamma$ , the photon eta  $|\eta_\gamma|$ , the distance between photon and closest lepton  $\Delta R_{\min}(\gamma, \ell)$ , the angular difference in  $\phi$  between the two leptons  $\Delta\phi(\ell, \ell)$ , the difference in  $\eta$  between the two leptons  $|\Delta\eta(\ell, \ell)|$ , and the sum over all transverse momenta  $S_T$  of the event. Closure of the two are shown as a ratio.

## 1527 B $tW\gamma$ contribution to fiducial region

1528 The  $tW\gamma$  process is simulated with 5 flavor scheme at leading order in QCD, which means the spectator  
 1529 b-quark, to be distinguished from the other b-quark from the top quark decay, will not appear as final state  
 1530 parton from the hard process. As a result, it is not possible to estimate its contribution to the fiducial region  
 1531 defined in Section 5, since two b-quarks are needed to tag the two b-jets.

1532 However, the spectator b-quark can be found at parton shower stage from initial state radiation associated  
 1533 with the incoming b-quark, together with which a gluon to  $b\bar{b}$  splitting pattern can be identified. By  
 1534 extending the b-quark definition for parton jet b-tagging to include this spectator b-quark added by parton  
 1535 shower, the second b-jet can be found, thus the  $tW\gamma$  contribution to the fiducial region can be estimated.

1536 The resulting b-jet  $p_T$  spectra are shown in Figure 62 for Pythia8 and Herwig7. No attempt is made to  
 1537 distinguish the b-jet tagged by the b-quark from top decay or the spectator b-quark from parton shower.  
 1538 No event selection is applied. The  $p_T$  spectrum of the b-quark from the hard process, after its first QCD  
 1539 radiation of  $\Delta R$  larger than 0.4, is also shown for comparison (this special definition of the b-quark is to  
 1540 mimic the b-jet formed from jet clustering algorithm, since radiation with  $\Delta R$  larger than 0.4 will escape  
 1541 from the jet cone). The negative bin means there is no b-quark or b-jet found. It is 50% of the integral of the  
 1542 histogram for the b-quark case, which is expected as the spectator b-quark doesn't exist in the hard process.  
 1543 But the fraction of this negative bin is largely reduced for the b-jet spectrum, thanks to the spectator b-quark  
 1544 found in the parton shower. It is also seen that the spectator b-quark can not always be found in the parton  
 1545 shower. We can treat these cases as having super soft spectator b-quarks that will fail the b-jet  $p_T$  selection  
 1546 anyway.

1547 The resulting contribution of  $tW\gamma$  to the fiducial region is estimated to be 0.44 fb and 0.41 fb for Pythia8  
 1548 and Herwig7, respectively. Besides, the sample used here only includes the radiative production  $tW\gamma$   
 1549 processes. To take into account the contribution from radiative decay  $tW\gamma$  processes, the contribution  
 1550 should be further scaled up by a factor around 2.

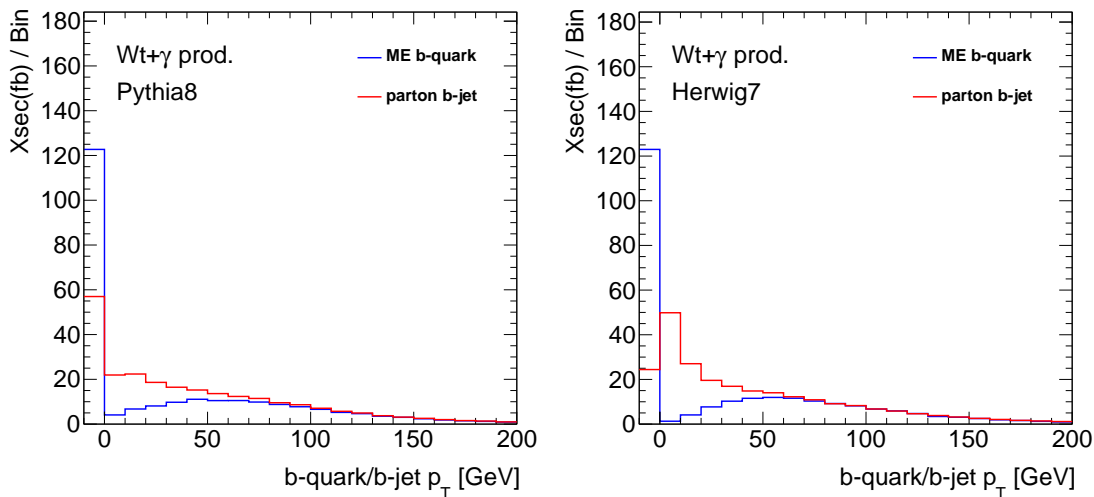


Figure 62: The  $p_T$  spectra of the (red) b-jet formed from partons and the (blue) b-quark from the hard process, after its first QCD radiation of  $\Delta R$  larger than 0.4, for the  $tW\gamma$  process simulated with (left) Pythia8 and (right) Herwig7 parton shower.

## 1551 C Lists of Monte-Carlo samples

1552 The  $t\bar{t}\gamma$  analysis uses various types of Monte-Carlo samples, some of which use dedicated matrix-element  
 1553 generation including a photon, others include photons through the showering algorithm. The following tables  
 1554 give an overview of the samples: Table 39 for all samples that include top quarks, Tables 40 and 41 for  $Z\gamma$   
 1555 and  $W\gamma$  simulations, respectively, Tables 42 and 43 for  $Z + \text{jets}$  and  $W + \text{jets}$  simulations, respectively,  
 1556 Table 44 for  $VV$  production, and Table 45 for  $t\bar{t}V$  production.

1557 The tables only show the AMI tags for the samples of the  $mc16a$  subcampaign. Unless specified otherwise,  
 1558 the samples have identical tags for the other subcampaigns, with the reconstructions tags substituted with  
 1559 r10201 and r10724 for  $mc16d$  and  $mc16e$ , respectively.

Table 39: Monte-Carlo samples with top quarks used for the  $t\bar{t}\gamma$  analysis. Some of them contain filters for exactly one lepton (' $\ell+\text{jets}$ '), at least one lepton ('inclusive') or two leptons ('dilepton'). The stated cross-sections include  $k$ -factors provided by the Physics Modelling Group and possible generator filter efficiencies.

Process	DSID	Generator	Tune	AMI tags	Xsec [pb]
$t\bar{t}\gamma$ (LO 2 → 7)	410389	MG5 + PYTHIA8	A14 NNPDF2.3LO	e6155_s3126_r9364_p3832	5.36
$t\bar{t}\gamma$ (LO 2 → 7, AFII)	410389	MG5 + PYTHIA8	A14 NNPDF2.3LO	e6155_a875_r9364_p3832	5.36
$t\bar{t}\gamma$ ( $\text{var3c up}$ )	410404	MG5 + PYTHIA8	A14 NNPDF2.3LO	e6350_a875_r9364_p3832	5.36
$t\bar{t}\gamma$ ( $\text{var3c down}$ )	410405	MG5 + PYTHIA8	A14 NNPDF2.3LO	e6350_a875_r9364_p3832	5.36
$t\bar{t}\gamma$ (shower variation)	410395	MG5 + HERWIG7	A14 NNPDF2.3LO	e6416_a875_r9364_p3832	5.36
$tW\gamma$ (LO 2 → 3, $\gamma$ from prod.)	412120	MG5 + PYTHIA8	A14 NNPDF2.3LO	e7476_a875_r9364_p3832	0.25
$tW\gamma$ (shower variation, $\gamma$ from prod.)	412122	MG5 + HERWIG7	A14 NNPDF2.3LO	e7575_a875_r9364_p3832	0.25
$tW\gamma$ (LO 2 → 3, $\gamma$ from decay)	412006	MG5 + PYTHIA8	A14 NNPDF2.3LO	e7698_a875_r9364_p3832	0.29
$t\bar{t}$ (inclusive)	410470	POWHEG + PYTHIA8	A14 NNPDF2.3LO	e6337_s3126_r9364_p3832	452.34
$t\bar{t}$ (inclusive, AFII)	410470	POWHEG + PYTHIA8	A14 NNPDF2.3LO	e6337_a875_r9364_p3832	452.34
$t\bar{t}$ ( $\ell+\text{jets}$ , hdamp variation)	410480	POWHEG + PYTHIA8	A14 NNPDF2.3LO	e6454_a875_r9364_p3832	320.01
$t\bar{t}$ ( $\ell+\text{jets}$ , ME variation)	410464	aMC@NLO + PYTHIA8	A14 NNPDF2.3LO	e6762_a875_r9364_p3832	366.27
$t\bar{t}$ ( $\ell+\text{jets}$ , shower variation)	410557	POWHEG + HERWIG7	MMHT2014	e6366_a875_r9364_p3832	320.19
$t\bar{t}$ (dilepton)	410472	POWHEG + PYTHIA8	A14 NNPDF2.3LO	e6337_s3126_r9364_p3832	87.71
$t\bar{t}$ (dilepton, AFII)	410472	POWHEG + PYTHIA8	A14 NNPDF2.3LO	e6348_a875_r9364_p3832	87.71
$t\bar{t}$ (dilepton, hdamp variation)	410482	POWHEG + PYTHIA8	A14 NNPDF2.3LO	e6454_a875_r9364_p3832	76.96
$t\bar{t}$ (dilepton, ME variation)	410465	aMC@NLO + PYTHIA8	A14 NNPDF2.3LO	e6762_a875_r9364_p3832	89.13
$t\bar{t}$ (dilepton, shower variation)	410558	POWHEG + HERWIG7	MMHT2014	e6366_a875_r9364_p3832	77.01
Wt (inclusive, $t$ , DR)	410646	POWHEG + PYTHIA8	A14 NNPDF2.3LO	e6615_s3126_r9364_p3832	35.86
Wt (inclusive, $\bar{t}$ , DR)	410647	POWHEG + PYTHIA8	A14 NNPDF2.3LO	e6615_s3126_r9364_p3832	35.85
Wt (inclusive, $t$ , DR, AFII)	410646	POWHEG + PYTHIA8	A14 NNPDF2.3LO	e6552_a875_r9364_p3832	35.86
Wt (inclusive, $\bar{t}$ , DR, AFII)	410647	POWHEG + PYTHIA8	A14 NNPDF2.3LO	e6552_a875_r9364_p3832	35.85
Wt (inclusive, $t$ , DS)	410654	POWHEG + PYTHIA8	A14 NNPDF2.3LO	e6552_s3126_r9364_p3832	35.72
Wt (inclusive, $\bar{t}$ , DS)	410655	POWHEG + PYTHIA8	A14 NNPDF2.3LO	e6552_s3126_r9364_p3832	35.74
Wt (inclusive, ME variation)	412002	aMC@NLO + PYTHIA8	A14 NNPDF2.3LO	e6817_a875_r9364_p3832	71.70
Wt (inclusive, $t$ , shower variation)	411036	POWHEG + HERWIG7	MMHT2014	e6702_a875_r9364_p3832	35.85
Wt (inclusive, $\bar{t}$ , shower variation)	411037	POWHEG + HERWIG7	MMHT2014	e6702_a875_r9364_p3832	35.85
Wt (dilepton, $t$ , DR)	410648	POWHEG + PYTHIA8	A14 NNPDF2.3LO	e6615_s3126_r9364_p3832	3.78
Wt (dilepton, $\bar{t}$ , DR)	410649	POWHEG + PYTHIA8	A14 NNPDF2.3LO	e6615_s3126_r9364_p3832	3.78
Wt (dilepton, $t$ , DR, AFII)	410648	POWHEG + PYTHIA8	A14 NNPDF2.3LO	e6615_a875_r9364_p3832	3.78
Wt (dilepton, $\bar{t}$ , DR, AFII)	410649	POWHEG + PYTHIA8	A14 NNPDF2.3LO	e6615_a875_r9364_p3832	3.78
Wt (dilepton, $t$ , DS)	410656	POWHEG + PYTHIA8	A14 NNPDF2.3LO	e6615_s3126_r9364_p3832	3.78
Wt (dilepton, $\bar{t}$ , DS)	410657	POWHEG + PYTHIA8	A14 NNPDF2.3LO	e6615_s3126_r9364_p3832	3.77
Wt (dilepton, ME variation)	412003	aMC@NLO + PYTHIA8	A14 NNPDF2.3LO	e6817_a875_r9364_p3832	7.55
Wt (dilepton, $t$ , shower variation)	411038	POWHEG + HERWIG7	MMHT2014	e6702_a875_r9364_p3832	3.78
Wt (dilepton, $\bar{t}$ , shower variation)	411039	POWHEG + HERWIG7	MMHT2014	e6702_a875_r9364_p3832	3.78
s-channel, top	410644	POWHEG + PYTHIA8	A14 NNPDF2.3LO	e6527_s3126_r9364_p3832	2.06
s-channel, anti-top	410645	POWHEG + PYTHIA8	A14 NNPDF2.3LO	e6527_s3126_r9364_p3832	1.29
t-channel, top	410658	POWHEG + PYTHIA8	A14 NNPDF2.3LO	e6671_s3126_r9364_p3832	44.15
t-channel, anti-top	410659	POWHEG + PYTHIA8	A14 NNPDF2.3LO	e6671_s3126_r9364_p3832	26.28

Table 40: Monte-Carlo samples for  $Z\gamma$  production used for the  $t\bar{t}\gamma$  analysis. The samples are split in slices of photon transverse momenta. The stated cross-sections include  $k$ -factors provided by the Physics Modelling Group and possible generator filter efficiencies.

Process	DSID	Generator	Tune	AMI tags	Xsec [pb]
$e\gamma, p_T(\gamma) \in [7, 15] \text{ GeV}$	366140	SHERPA 2.2.4 (LO)	NNPDF3.0NNLO	e7006_s3126_r9364_p3830	46.29
$e\gamma, p_T(\gamma) \in [15, 35] \text{ GeV}$	366141	SHERPA 2.2.4 (LO)	NNPDF3.0NNLO	e7006_s3126_r9364_p3830	29.28
$e\gamma, p_T(\gamma) \in [35, 70] \text{ GeV}$	366142	SHERPA 2.2.4 (LO)	NNPDF3.0NNLO	e7006_s3126_r9364_p3830	5.16
$e\gamma, p_T(\gamma) \in [70, 140] \text{ GeV}$	366143	SHERPA 2.2.4 (LO)	NNPDF3.0NNLO	e7006_s3126_r9364_p3830	0.40
$e\gamma, p_T(\gamma) \geq 140 \text{ GeV}$	366144	SHERPA 2.2.4 (LO)	NNPDF3.0NNLO	e7006_s3126_r9364_p3830	0.05
$\mu\gamma, p_T(\gamma) \in [7, 15] \text{ GeV}$	366145	SHERPA 2.2.4 (LO)	NNPDF3.0NNLO	e7006_s3126_r9364_p3830	46.28
$\mu\gamma, p_T(\gamma) \in [15, 35] \text{ GeV}$	366146	SHERPA 2.2.4 (LO)	NNPDF3.0NNLO	e7006_s3126_r9364_p3830	29.28
$\mu\gamma, p_T(\gamma) \in [35, 70] \text{ GeV}$	366147	SHERPA 2.2.4 (LO)	NNPDF3.0NNLO	e7006_s3126_r9364_p3830	5.16
$\mu\gamma, p_T(\gamma) \in [70, 140] \text{ GeV}$	366148	SHERPA 2.2.4 (LO)	NNPDF3.0NNLO	e7006_s3126_r9364_p3830	0.40
$\mu\gamma, p_T(\gamma) \geq 140 \text{ GeV}$	366149	SHERPA 2.2.4 (LO)	NNPDF3.0NNLO	e7006_s3126_r9364_p3830	0.05
$\tau\gamma, p_T(\gamma) \in [7, 15] \text{ GeV}$	366150	SHERPA 2.2.4 (LO)	NNPDF3.0NNLO	e7029_s3126_r9364_p3830	46.25
$\tau\gamma, p_T(\gamma) \in [15, 35] \text{ GeV}$	366151	SHERPA 2.2.4 (LO)	NNPDF3.0NNLO	e7029_s3126_r9364_p3830	29.28
$\tau\gamma, p_T(\gamma) \in [35, 70] \text{ GeV}$	366152	SHERPA 2.2.4 (LO)	NNPDF3.0NNLO	e7029_s3126_r9364_p3830	5.15
$\tau\gamma, p_T(\gamma) \in [70, 140] \text{ GeV}$	366153	SHERPA 2.2.4 (LO)	NNPDF3.0NNLO	e7029_s3126_r9364_p3830	0.40
$\tau\gamma, p_T(\gamma) \geq 140 \text{ GeV}$	366154	SHERPA 2.2.4 (LO)	NNPDF3.0NNLO	e7029_s3126_r9364_p3830	0.05

Table 41: Monte-Carlo samples for  $W\gamma$  production used for the  $t\bar{t}\gamma$  analysis. The samples are split in slices of photon transverse momenta. The stated cross-sections include  $k$ -factors provided by the Physics Modelling Group and possible generator filter efficiencies.

Process	DSID	Generator	Tune	AMI tags	Xsec [pb]
$e\gamma, p_T(\gamma) \in [15, 35] \text{ GeV}$	364522	SHERPA 2.2.2 (NLO)	NNPDF3.0NNLO	e5928_s3126_r9364_p3830	134.38
$e\gamma, p_T(\gamma) \in [35, 70] \text{ GeV}$	364523	SHERPA 2.2.2 (NLO)	NNPDF3.0NNLO	e5928_s3126_r9364_p3830	19.07
$e\gamma, p_T(\gamma) \in [70, 140] \text{ GeV}$	364524	SHERPA 2.2.2 (NLO)	NNPDF3.0NNLO	e5928_s3126_r9364_p3830	1.92
$e\gamma, p_T(\gamma) \geq 140 \text{ GeV}$	364525	SHERPA 2.2.2 (NLO)	NNPDF3.0NNLO	e5928_s3126_r9364_p3830	0.30
$\mu\gamma, p_T(\gamma) \in [15, 35] \text{ GeV}$	364527	SHERPA 2.2.2 (NLO)	NNPDF3.0NNLO	e5928_s3126_r9364_p3830	134.45
$\mu\gamma, p_T(\gamma) \in [35, 70] \text{ GeV}$	364528	SHERPA 2.2.2 (NLO)	NNPDF3.0NNLO	e5928_s3126_r9364_p3830	19.11
$\mu\gamma, p_T(\gamma) \in [70, 140] \text{ GeV}$	364529	SHERPA 2.2.2 (NLO)	NNPDF3.0NNLO	e5928_s3126_r9364_p3830	1.92
$\mu\gamma, p_T(\gamma) \geq 140 \text{ GeV}$	364530	SHERPA 2.2.2 (NLO)	NNPDF3.0NNLO	e5928_s3126_r9364_p3830	0.30
$\tau\gamma, p_T(\gamma) \in [15, 35] \text{ GeV}$	364532	SHERPA 2.2.2 (NLO)	NNPDF3.0NNLO	e5928_s3126_r9364_p3830	134.43
$\tau\gamma, p_T(\gamma) \in [35, 70] \text{ GeV}$	364533	SHERPA 2.2.2 (NLO)	NNPDF3.0NNLO	e5928_s3126_r9364_p3830	19.12
$\tau\gamma, p_T(\gamma) \in [70, 140] \text{ GeV}$	364534	SHERPA 2.2.2 (NLO)	NNPDF3.0NNLO	e5928_s3126_r9364_p3830	1.93
$\tau\gamma, p_T(\gamma) \geq 140 \text{ GeV}$	364535	SHERPA 2.2.2 (NLO)	NNPDF3.0NNLO	e5928_s3126_r9364_p3830	0.30





Table 44: Monte-Carlo samples for  $VV$  production used for the  $t\bar{t}\gamma$  analysis. The stated cross-sections include  $k$ -factors provided by the Physics Modelling Group and possible generator filter efficiencies.

Process	DSID	Generator	Tune	AMI tags	Xsec [pb]
$ZZ \rightarrow \ell\ell\ell\ell$	364250	SHERPA 2.2.2	NNPDF3.0NNLO	e5894_s3126_r9364_p3830	1.25
$ZW \rightarrow \ell\ell\ell\nu$	364253	SHERPA 2.2.2	NNPDF3.0NNLO	e5916_s3126_r9364_p3830	4.58
$WW/ZZ \rightarrow \ell\ell\nu\nu$	364254	SHERPA 2.2.2	NNPDF3.0NNLO	e5916_s3126_r9364_p3830	12.50
$WZ \rightarrow \ell\nu\nu\nu$	364255	SHERPA 2.2.2	NNPDF3.0NNLO	e5916_s3126_r9364_p3830	3.23
$ZZ \rightarrow qqvv$	363355	SHERPA 2.2.1	NNPDF3.0NNLO	e5525_s3126_r9364_p3830	4.31
$ZZ \rightarrow qq\ell\ell$	363356	SHERPA 2.2.1	NNPDF3.0NNLO	e5525_s3126_r9364_p3830	2.20
$WZ \rightarrow qqvv$	363357	SHERPA 2.2.1	NNPDF3.0NNLO	e5525_s3126_r9364_p3830	6.80
$WZ \rightarrow qq\ell\ell$	363358	SHERPA 2.2.1	NNPDF3.0NNLO	e5525_s3126_r9364_p3830	3.43
$WW \rightarrow qq\ell^-\nu$	363359	SHERPA 2.2.1	NNPDF3.0NNLO	e5583_s3126_r9364_p3830	24.71
$WW \rightarrow qq\ell^+\nu$	363360	SHERPA 2.2.1	NNPDF3.0NNLO	e5983_s3126_r9364_p3830	24.72
$WZ \rightarrow \ell\nu qq$	363489	SHERPA 2.2.1	NNPDF3.0NNLO	e5525_s3126_r9364_p3830	11.42

Table 45: Monte-Carlo samples for  $t\bar{t}V$  production used for the  $t\bar{t}\gamma$  analysis. The stated cross-sections include  $k$ -factors provided by the Physics Modelling Group and possible generator filter efficiencies.

Process	DSID	Generator	Tune	AMI tags	Xsec [pb]
$t\bar{t}W$	410155	aMC@NLO + PYTHIA8	A14 NNPDF2.3LO	e5070_s3126_r9364_p3832	0.60
$t\bar{t}VV$	410156	aMC@NLO + PYTHIA8	A14 NNPDF2.3LO	e5070_s3126_r9364_p3832	0.17
$t\bar{t}qq$	410157	aMC@NLO + PYTHIA8	A14 NNPDF2.3LO	e5070_s3126_r9364_p3832	0.59
$t\bar{t}ee$	410218	aMC@NLO + PYTHIA8	A14 NNPDF2.3LO	e5070_s3126_r9364_p3832	0.04
$t\bar{t}\mu\mu$	410219	aMC@NLO + PYTHIA8	A14 NNPDF2.3LO	e5070_s3126_r9364_p3832	0.04
$t\bar{t}\tau\tau$	410220	aMC@NLO + PYTHIA8	A14 NNPDF2.3LO	e5070_s3126_r9364_p3832	0.04

## 1560 D Hadron-fake estimates

1561 The background contribution due to h-fake photons is largely reduced by applying the photon isolation  
 1562 requirement, but still is an important background category. To estimate the contribution by h-fake photons,  
 1563 first a data-driven two-dimensional sidebands method (ABCD method) is used. Then, the ratio of the  
 1564 data-driven estimate to the MC prediction of h-fake photons is considered as the h-fake scale factor, and is  
 1565 used to correct the Monte-Carlo simulation of h-fake photons in the final fit.

1566 The h-fake scale factors are derived and evaluated using the single-lepton channels. The event selection is  
 1567 based on the pre-selection criteria described in Section 4 and is largely similar to that of the  $e\mu$  signal region.  
 1568 Instead of exactly one electron and one muon, exactly one lepton is required which must be trigger-matched.  
 1569 In addition, events with electrons in the final state must fulfil  $m(l, \gamma) \notin [m_Z \pm 5 \text{ GeV}]$  to suppress e-fake  
 1570 photons from leptonically decaying  $Z$  bosons. Furthermore, as opposed to at least two jets in the signal  
 1571 region, events are required to have four or more jets, one of which must be  $b$ -tagged.

1572 The event selection for the single-lepton channels is summarised in Table 46. To derive the h-fake scale  
 1573 factors, four different regions are defined by dividing the photons into four categories, based on their  
 1574 isolation and identification. The different regions are schematically drawn in Appendix D. Region D is used  
 1575 as a control region of the method, while region A, B and C are dominated by h-fake photons. Photons in  
 1576 regions B and C are required to be non-isolated. For this, they must fail the *FixedCutTight* isolation working  
 1577 point, and in addition fulfil  $p_T^{\text{iso}}|_{\Delta R < 0.2} > 3 \text{ GeV}$ . This extra cut, hereafter simply referred to as *isolation*  
 1578 *gap*, is applied to reduce the prompt  $\gamma$  contamination, specially in region C. Photons in regions A and B  
 1579 are required to be identified as *medium-tight*. The medium-tight identification requires the photon to pass  
 1580 all cuts of the *Tight* identification working point, except the cuts on the shower-shape variables  $f_{\text{side}}$ ,  $W_{s_3}$ ,

Table 46: Event selection for the single-lepton channels, used as control regions to derive h-fake scale factors.

Variable	Selection
Photons	$= 1, p_T > 20 \text{ GeV}$
Jets	$\geq 4$ jets, of which $\geq 1$ $b$ -tagged
MET	—
$m(e, \gamma)$	$\notin [m_Z \pm 5 \text{ GeV}]$
$\Delta R(l, \gamma)$	$\geq 1.0$

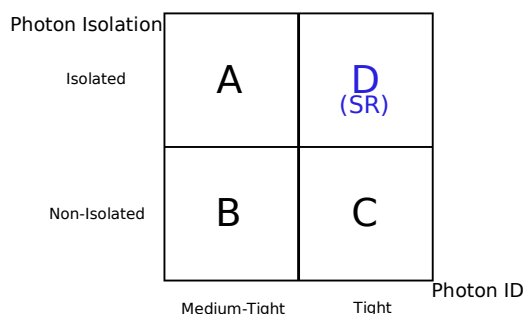


Figure 63: Schematic explanation of the four different regions used in the ABCD method.

1581  $\Delta E$  and  $E_{ratio}$ . At least two of these four cuts are explicitly asked to be failed. These four shower-shape  
 1582 variables contain information from the strip layer, the first layer of the electromagnetic calorimeters. The  
 1583 strip layer is finely granulated in  $\eta$ , with the purpose of suppressing the background photons which typically  
 1584 have a broader shower profile. While these four variables have strong discrimination power between the  
 1585 prompt  $\gamma$  and h-fake photons, their correlation with photon isolation is very small [57].

The choice of the minimum number of failed cuts is based on a compromise between reducing the prompt photon contamination and keeping enough statistics, specifically in region A. Control plots for the region A, B, C and D are shown in Figures 64 to 71. Assuming no correlation between photon isolation and photon identification, the following relation between contributions by h-fake photons in the four region holds:

$$\frac{N_A^{\text{h-fake}}}{N_B^{\text{h-fake}}} = \frac{N_D^{\text{h-fake}}}{N_C^{\text{h-fake}}} \quad (17)$$

Although the isolation and identification criteria are chosen to minimise any such correlation, any deviation from this assumption can be quantified by the following double ratio derived from MC:

$$\theta_{\text{MC}} = \frac{N_{\text{D,MC}}^{\text{h-fake}} / N_{\text{C,MC}}^{\text{h-fake}}}{N_{\text{A,MC}}^{\text{h-fake}} / N_{\text{B,MC}}^{\text{h-fake}}} \quad (18)$$

To estimate the dependence on  $p_T$  and  $|\eta|$ , a two dimensional binning is applied. A comprehensive test of different binning scenarios is performed to determine variable bin widths. The binning in  $|\eta|$  is motivated by the detector geometry with bin edges at  $|\eta| = 0, 0.6, 1.37, 1.52$  and  $2.37$ , excluding the crack region of  $1.37 < |\eta_{\text{clus}}| < 1.52$ . The measured values for  $\theta_{\text{MC}}$  and their uncertainties are shown in Figures 72 and 73 for converted, unconverted and all photons as a function of  $p_T$  and  $|\eta|$ . The initial choice of binning in  $p_T$  is arbitrary. By comparing different choices of binning in  $p_T$  for each bin in  $|\eta|$ , an optimal binning is chosen based on the uncertainties in each bin. Considering the relation in Equation (17) and using  $\theta_{\text{MC}}$  from Equation (18) as a correction factor in order to take any residual correlation between photon isolation and identification into account, the number of h-fake photons  $N_{\text{est.}}^{\text{h-fake}}$  is estimated as:

$$N_{\text{est.}}^{\text{h-fake}} = \frac{N_{\text{A,Data}}^{\text{h-fake}} \times N_{\text{C,Data}}^{\text{h-fake}}}{N_{\text{B,Data}}^{\text{h-fake}}} \times \theta_{\text{MC}}, \quad (19)$$

where  $N_{i,\text{Data}}^{\text{h-fake}}$  with  $i \in [A, B, C]$  is the number of h-fake photons in data in regions A, B and C. Although these three regions are dominated by h-fake photons, as it can be seen from the control plots, there are contaminations from events with prompt  $\gamma$  and e-fake photons. Therefore, the contamination from prompt  $\gamma$  and e-fake photons are subtracted by using Monte-Carlo simulation:

$$N_{i,\text{Data}}^{\text{h-fake}} = N_{i,\text{Data}} - N_{i,\text{MC}}^{\text{prompt-}\gamma} - N_{i,\text{MC}}^{\text{e-fake}}, \quad i \in [A, B, C]. \quad (20)$$

Finally, the h-fake scale factor  $SF^{\text{h-fake}}$  is calculated as:

$$SF^{\text{h-fake}} = \frac{N_{\text{est.}}^{\text{h-fake}}}{N_{\text{MC}}^{\text{h-fake}}}. \quad (21)$$

1586 The  $\theta_{\text{MC}}$  and subsequently the h-fake scale factors  $SF^{\text{h-fake}}$  are measured for bins of  $p_T$  and  $|\eta|$ , separately  
 1587 for converted, unconverted and all photons. The calculation for each bin is performed by using the  $\theta_{\text{MC}}$   
 1588 that is measured for the same kinetic range and conversion type. The resulting values for the h-fake scale

Not reviewed, for internal circulation only

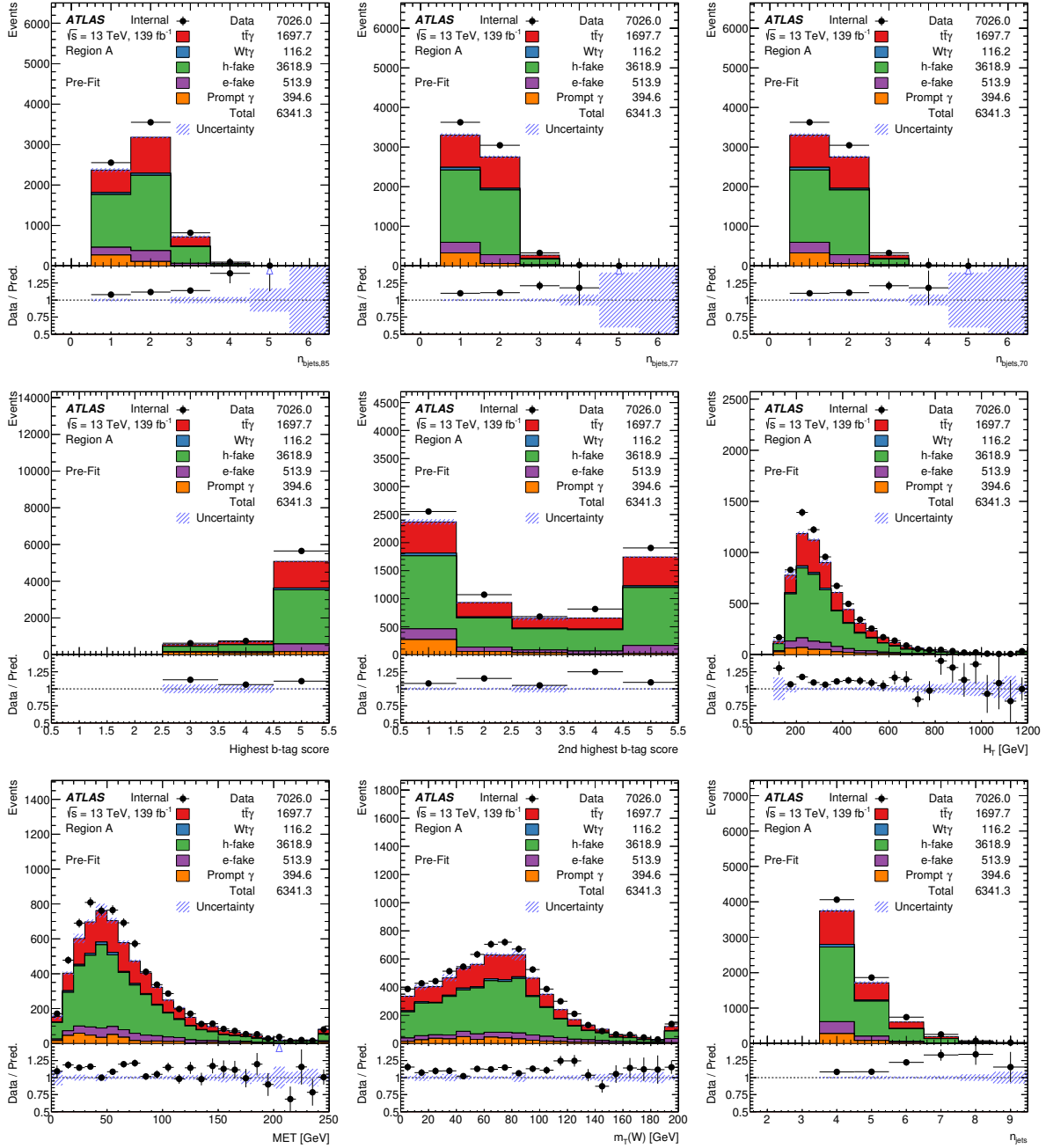


Figure 64: Control plots for region A in the single lepton channels, where photons are identified as medium-tight and isolated. In each plot, the dashed area shows the statistical uncertainty of the total expectation.

Not reviewed, for internal circulation only

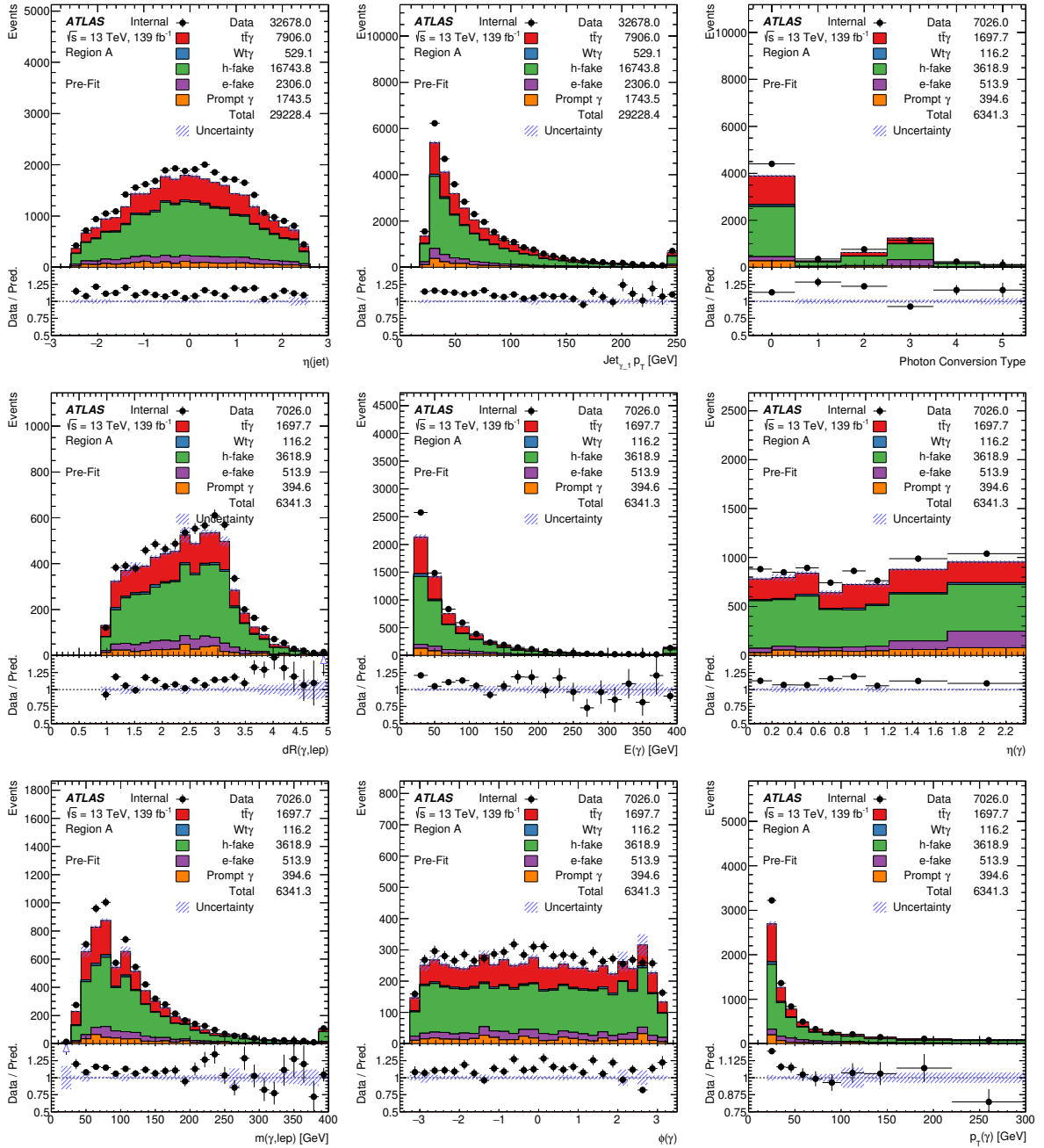


Figure 65: Control plots for region A in the single lepton channels, where photons are identified as medium-tight and isolated. In each plot, the dashed area shows the statistical uncertainty of the total expectation.

Not reviewed, for internal circulation only

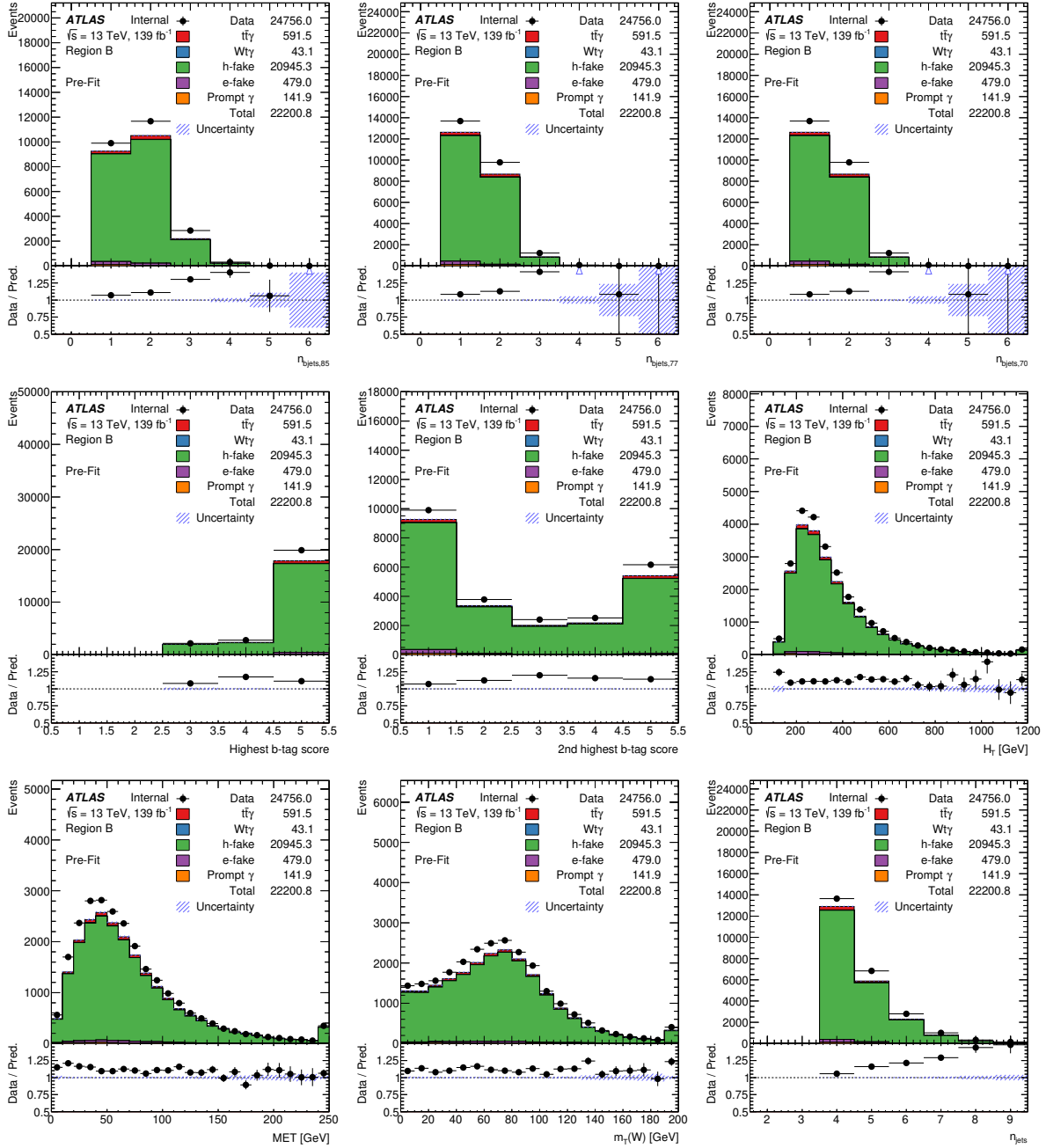


Figure 66: Control plots for region B in the single lepton channels, where photons are identified as medium-tight and non-isolated. In each plot, the dashed area shows the statistical uncertainty of the total expectation.

Not reviewed, for internal circulation only

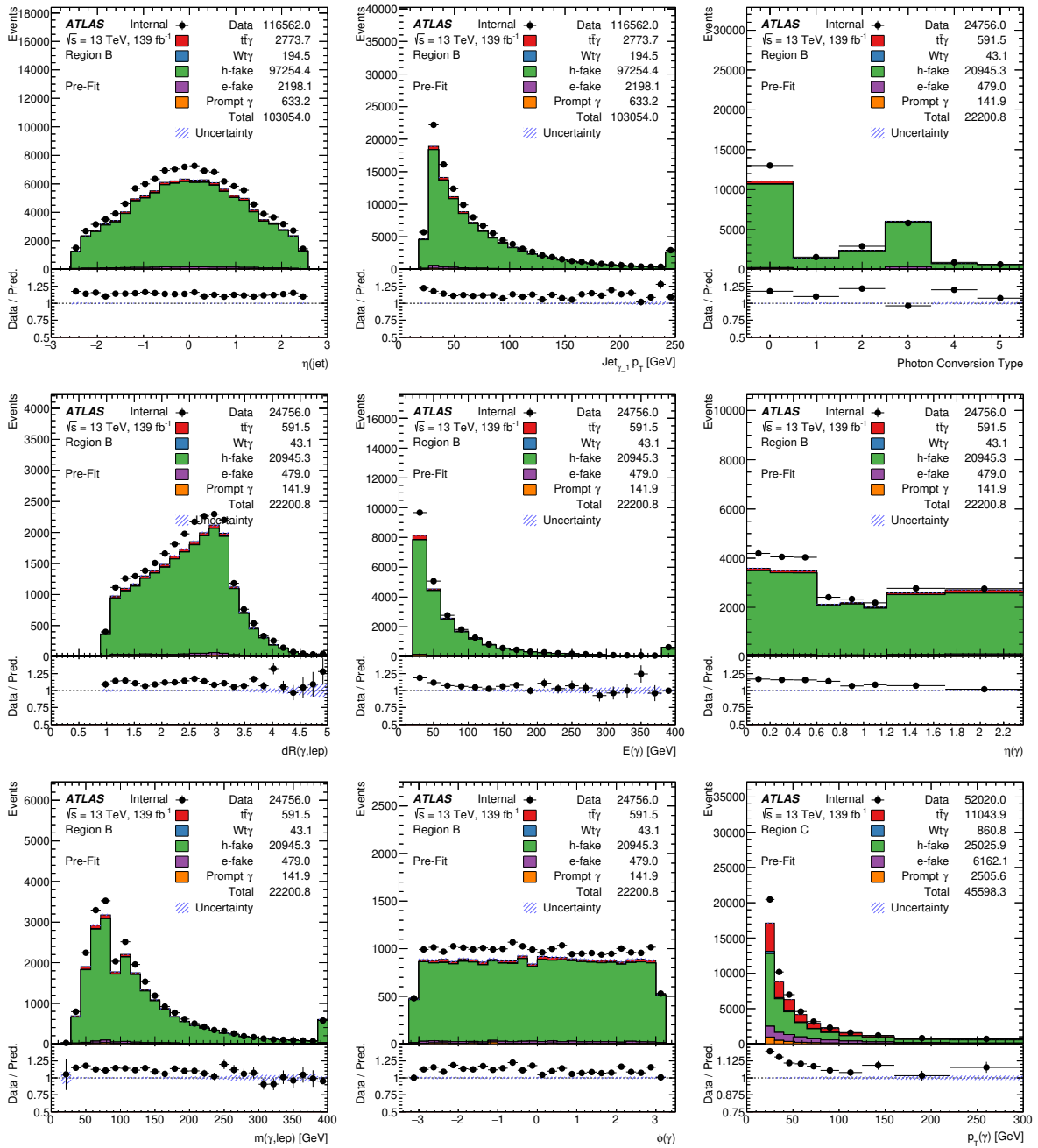


Figure 67: Control plots for region B in the single lepton channels, where photons are identified as medium-tight and non-isolated. In each plot, the dashed area shows the statistical uncertainty of the total expectation.

Not reviewed, for internal circulation only

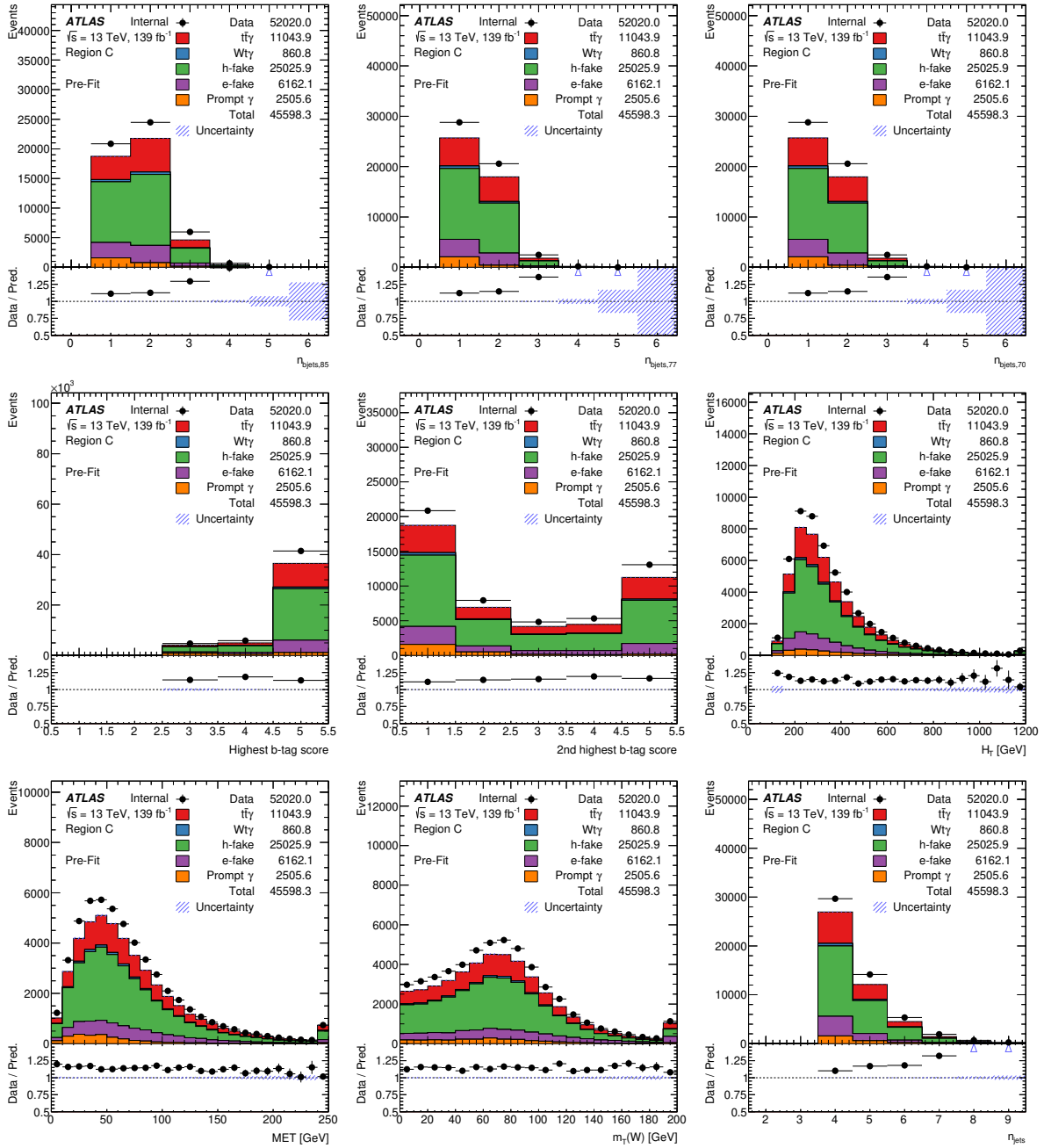


Figure 68: Control plots for region C in the single lepton channels, where photons are identified as tight and non-isolated. In each plot, the dashed area shows the statistical uncertainty of the total expectation.

Not reviewed, for internal circulation only

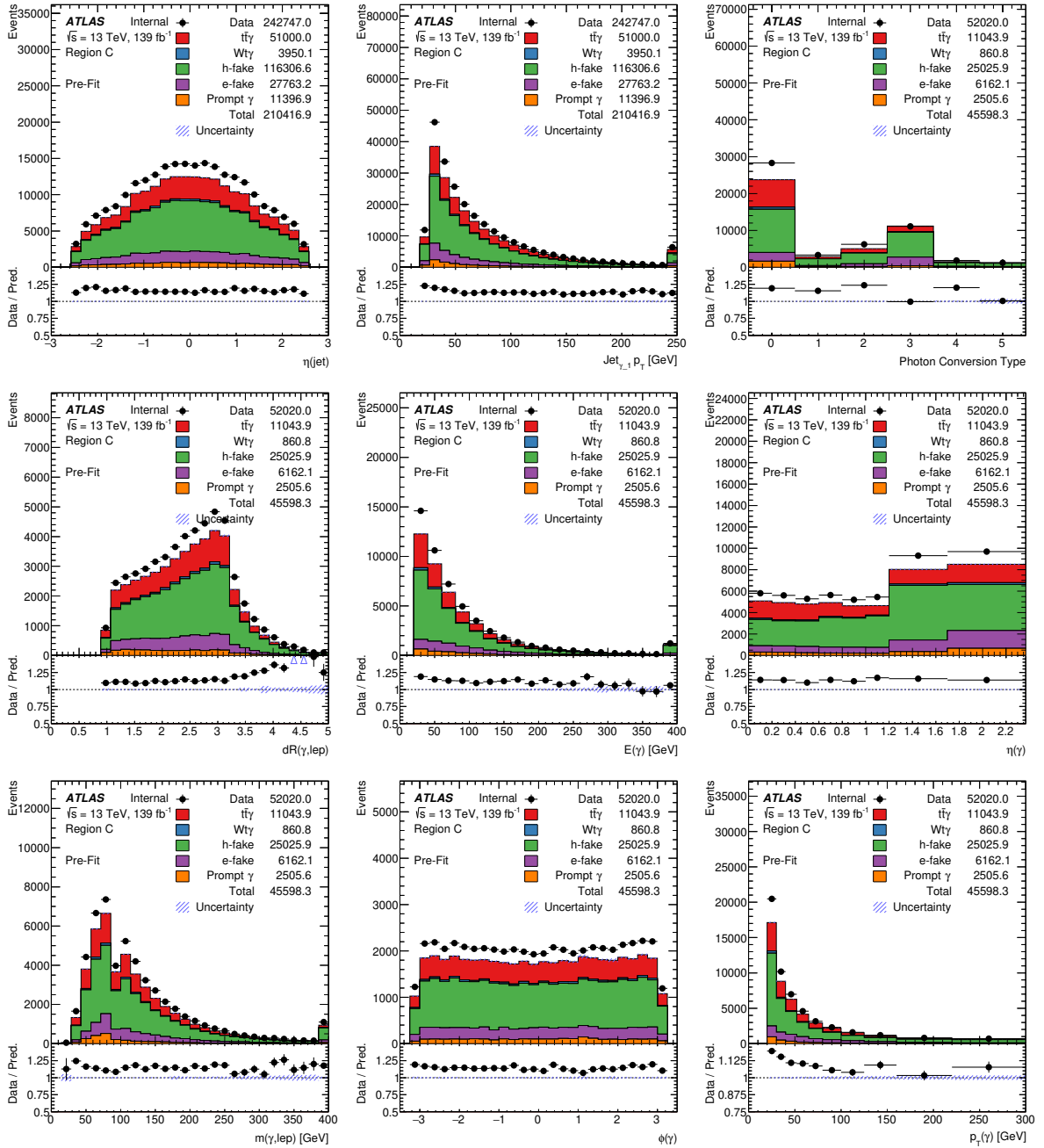


Figure 69: Control plots for region C in the single lepton channels, where photons are identified as tight and non-isolated. In each plot, the dashed area shows the statistical uncertainty of the total expectation.

Not reviewed, for internal circulation only

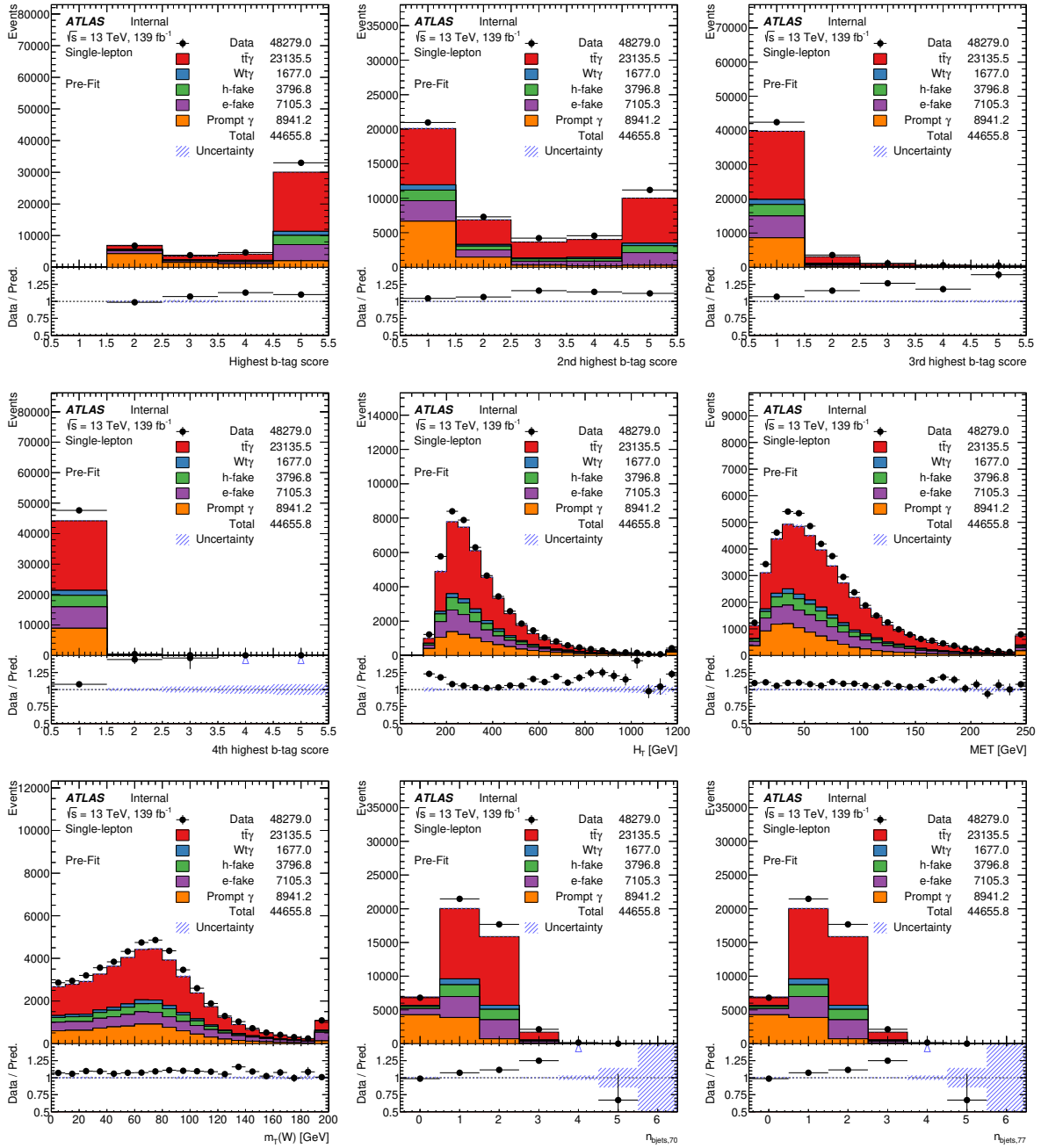


Figure 70: Control plots for region D in the single lepton channels, where photons are identified as tight and isolated. In each plot, the dashed area shows the statistical uncertainty of the total expectation.

Not reviewed, for internal circulation only

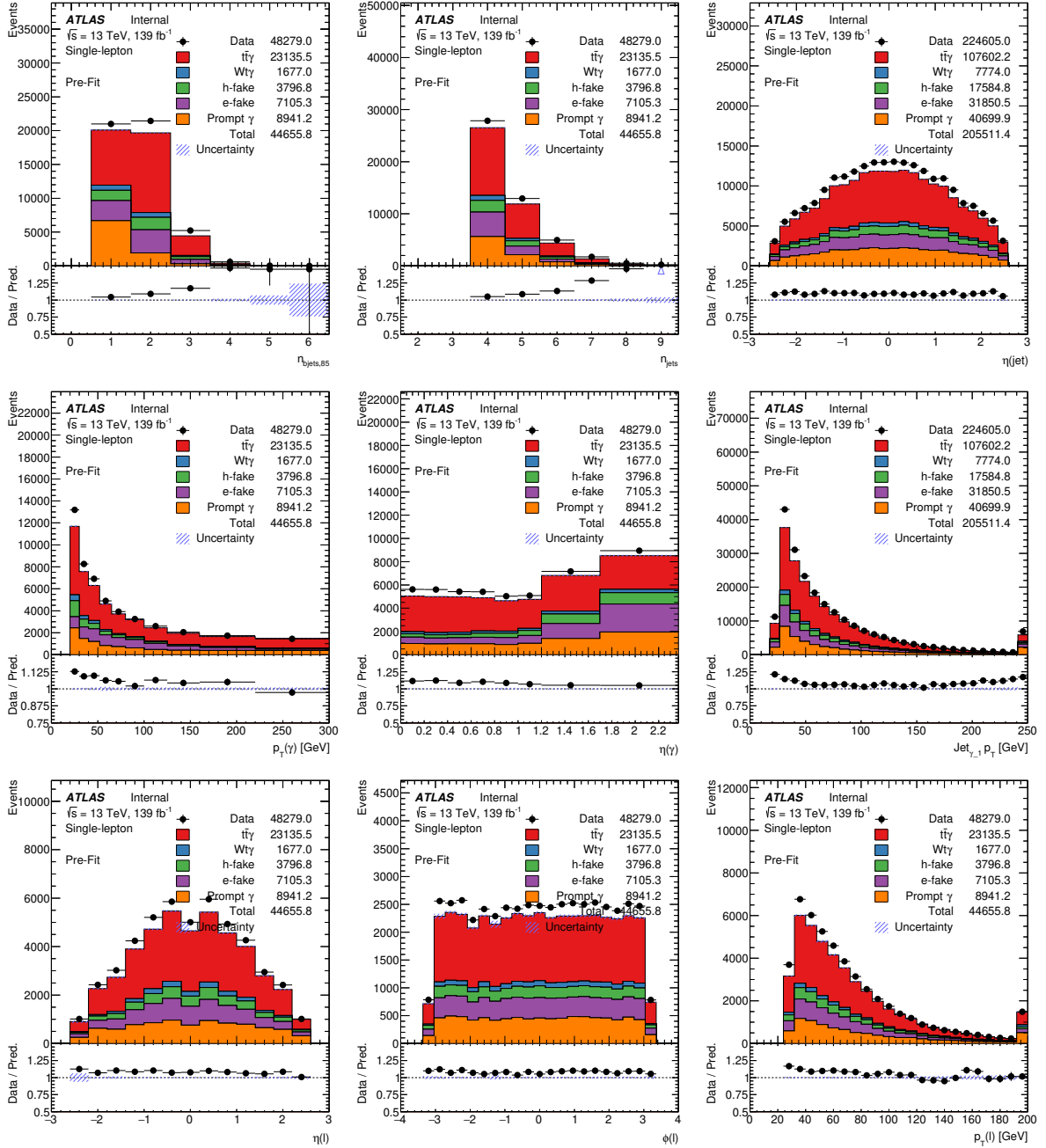


Figure 71: Control plots for region D in the single lepton channels, where photons are identified as tight and isolated. In each plot, the dashed area shows the statistical uncertainty of the total expectation.

Not reviewed, for internal circulation only

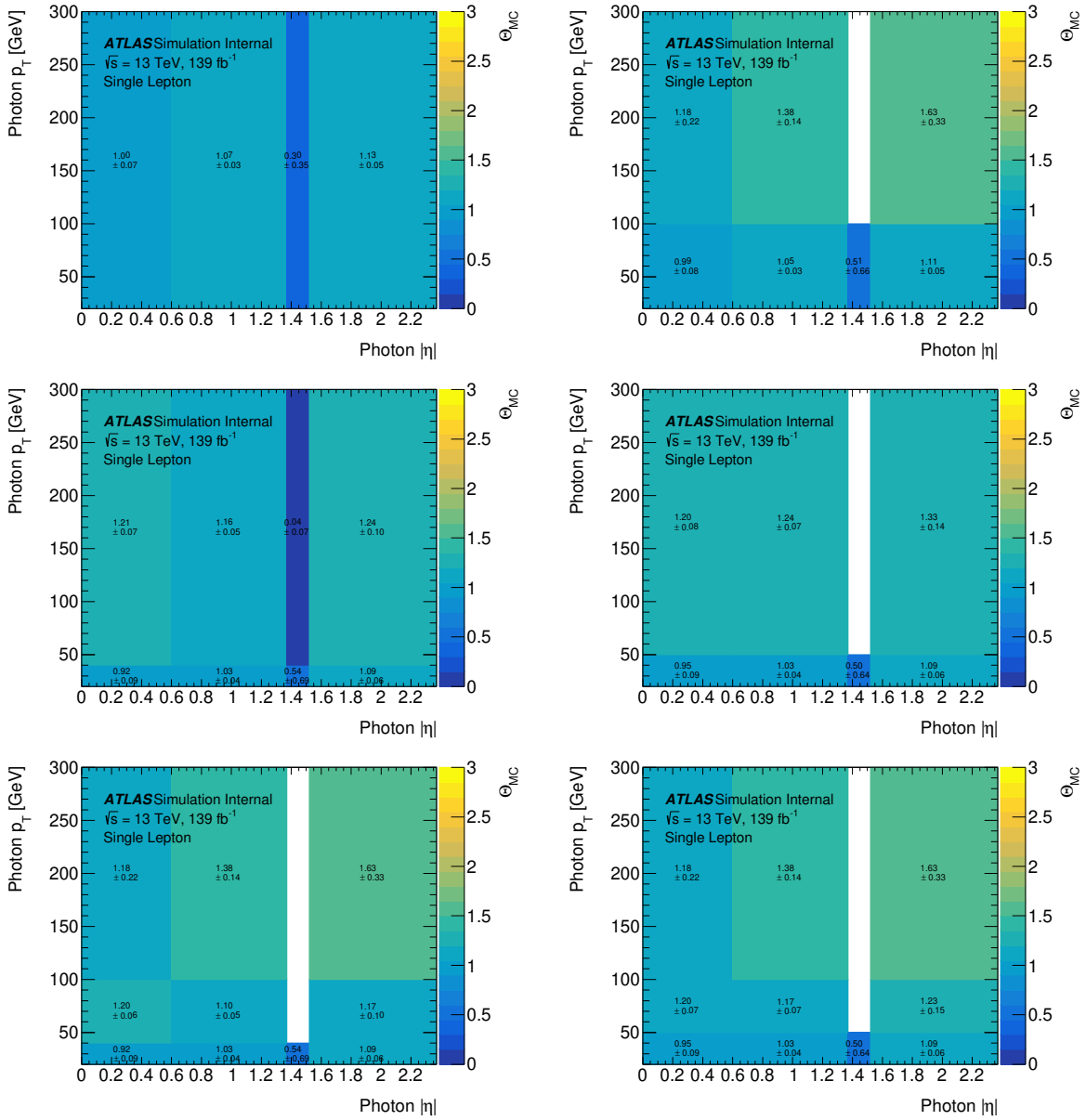


Figure 72: Monte-Carlo-based double ratio  $\theta_{MC}$  measured for converted photons as a function of  $p_T$  and  $|\eta|$ . The  $|\eta|$  bins are motivated and chosen according to the detector geometry, excluding the calorimeter crack region at  $1.37 < |\eta| < 1.52$ . The initial choice of binning in  $p_T$  is arbitrary. By comparing different choices of binning in  $p_T$  for each bin in  $|\eta|$ , an optimal binning is chosen based on the number of events in each bin. Bins in  $p_T$  that agree within uncertainties are subsequently merged together.

Not reviewed, for internal circulation only

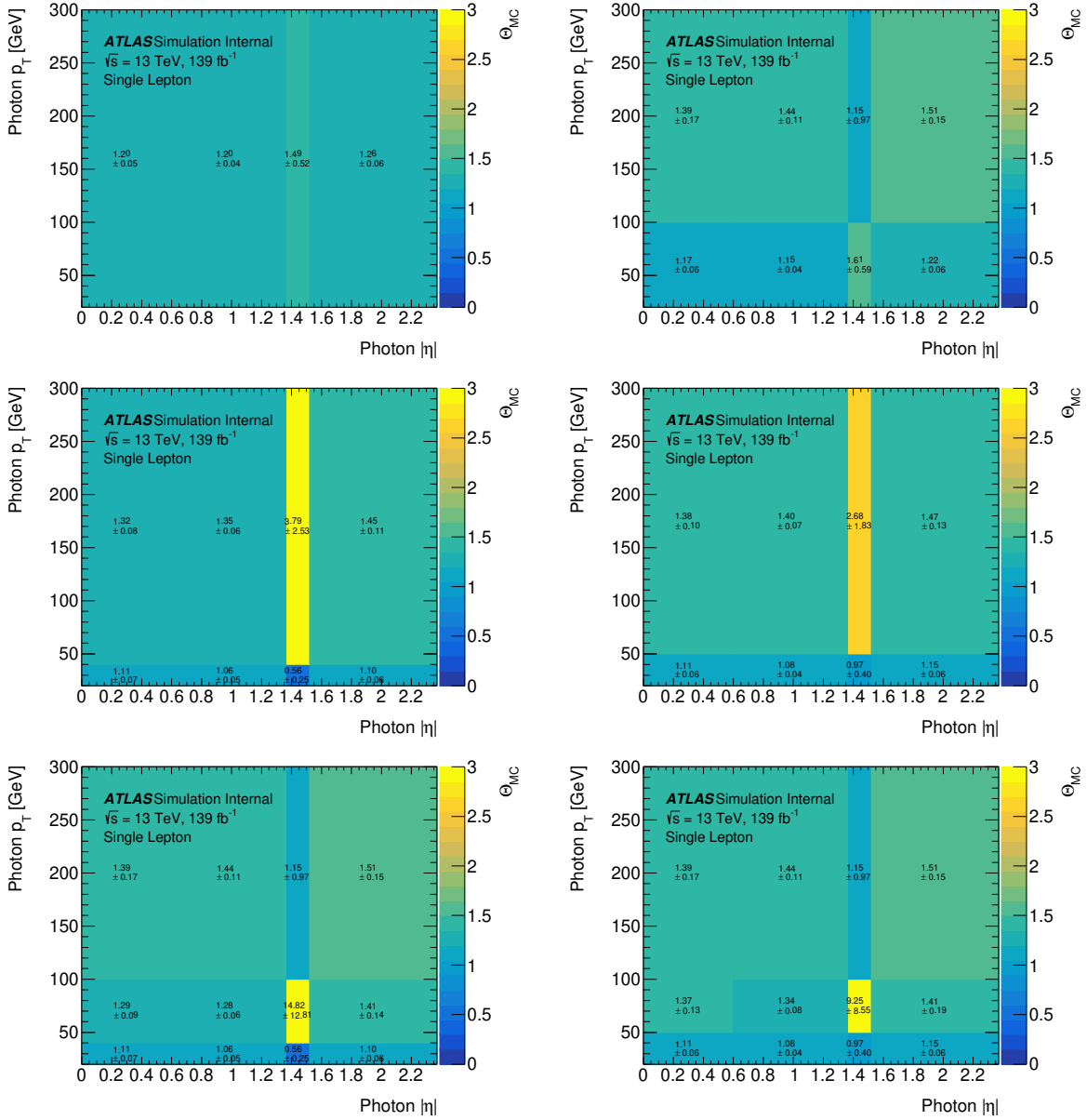


Figure 73: Monte-Carlo-based double ratio  $\theta_{MC}$  measured for unconverted photons as a function of  $p_T$  and  $|\eta|$ . The  $|\eta|$  bins are motivated and chosen according to the detector geometry, excluding the calorimeter crack-region at  $1.37 < |\eta| < 1.52$ . The initial choice of binning in  $p_T$  is arbitrary. By comparing different choices of binning in  $p_T$  for each bin in  $|\eta|$ , an optimal binning is chosen based on number of events in each bin. Bins in  $p_T$  that agree within uncertainties are subsequently merged together.

Not reviewed, for internal circulation only

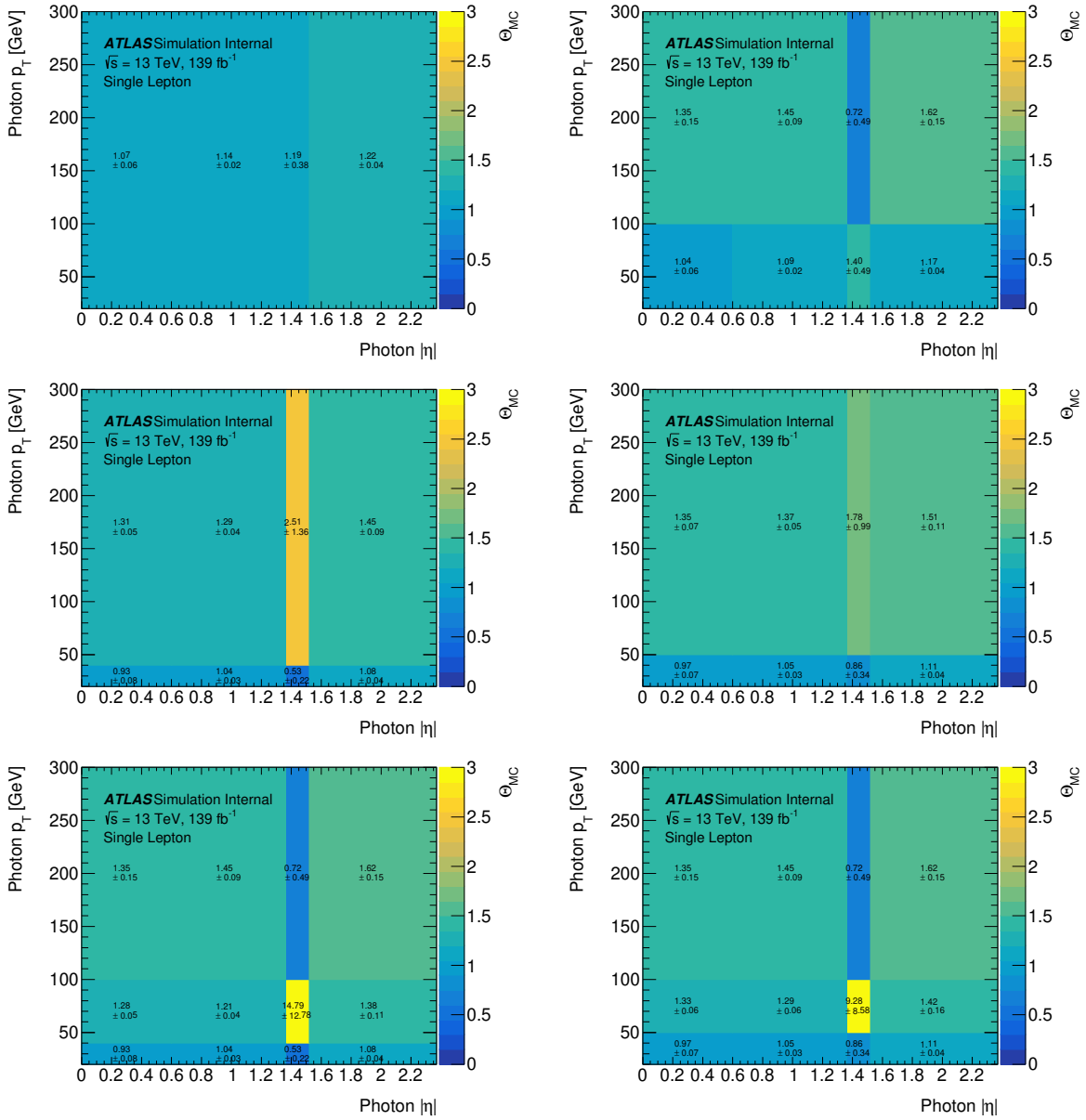


Figure 74: Monte-Carlo-based double ratio  $\theta_{MC}$  measured for all photons as a function of  $p_T$  and  $|\eta|$ . The  $|\eta|$  bins are motivated and chosen according to the detector geometry, excluding the calorimeter crack-region at  $1.37 < |\eta| < 1.52$ . The initial choice of binning in  $p_T$  is arbitrary. By comparing different choices of binning in  $p_T$  for each bin in  $|\eta|$ , an optimal binning is chosen based on number of events in each bin. Bins in  $p_T$  that agree within uncertainties are subsequently merged together.

Not reviewed, for internal circulation only

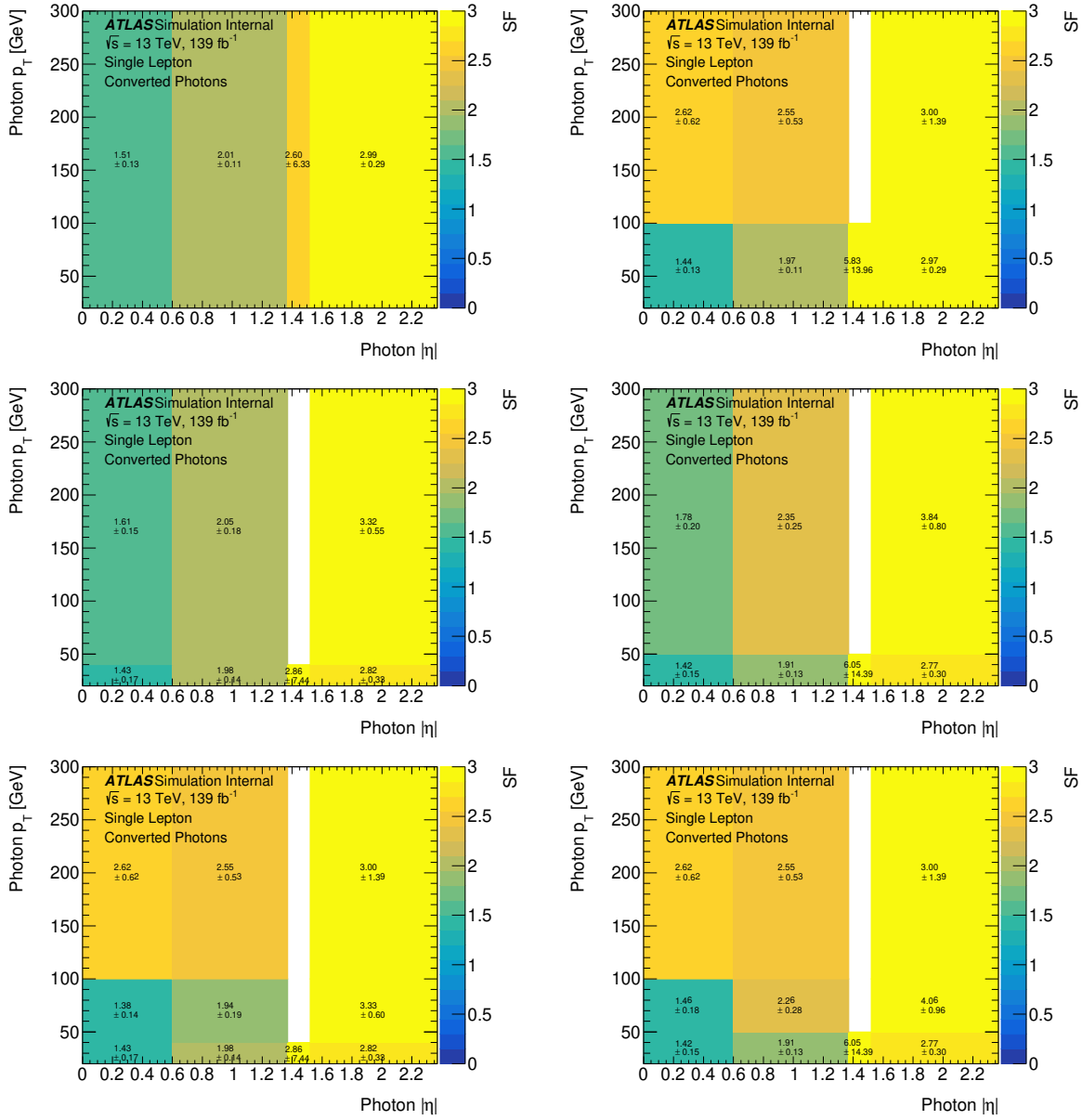


Figure 75: Measured values for  $SF^{h\text{-fake}}$  for converted photons as a function of  $p_T$  and  $|\eta|$ . The  $|\eta|$  bins are motivated and chosen according to the detector geometry, excluding the calorimeter crack-region at  $1.37 < |\eta| < 1.52$ . The initial choice of binning in  $p_T$  is arbitrary. By comparing different choices of binning in  $p_T$  for each bin in  $|\eta|$ , an optimal binning is chosen based on number of events in each bin. Bins in  $p_T$  that agree within uncertainties are subsequently merged together.

Not reviewed, for internal circulation only

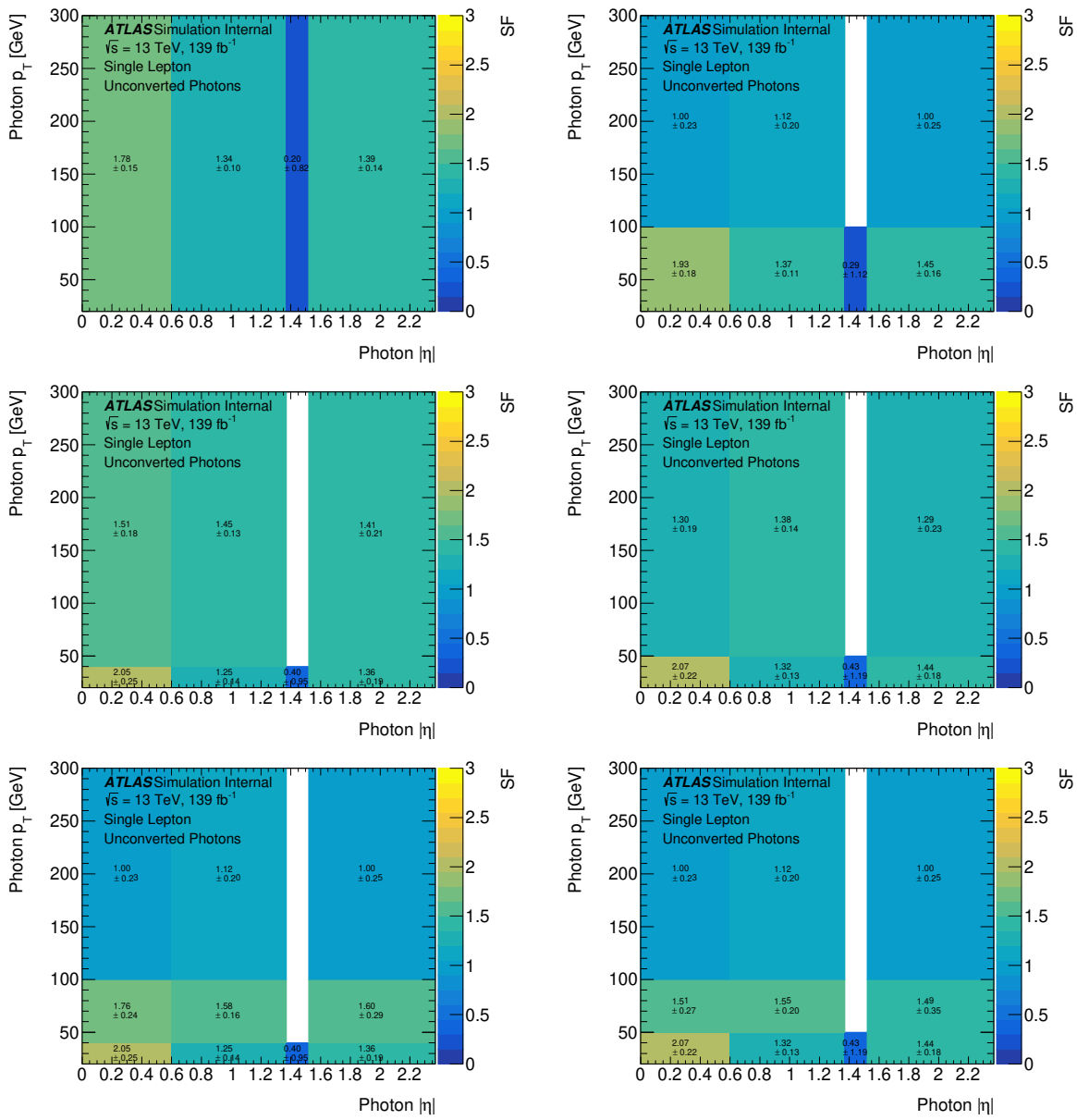


Figure 76: Measured values for  $SF^{h\text{-fake}}$  for unconverted photons as a function of  $p_T$  and  $|\eta|$ . The  $|\eta|$  bins are motivated and chosen according to the detector geometry, excluding the calorimeter crack-region at  $1.37 < |\eta| < 1.52$ . The initial choice of binning in  $p_T$  is arbitrary. By comparing different choices of binning in  $p_T$  for each bin in  $|\eta|$  an optimal binning is chosen based on number of events in each bin. Bins in  $p_T$  that agree within uncertainties are subsequently merged together.

Not reviewed, for internal circulation only

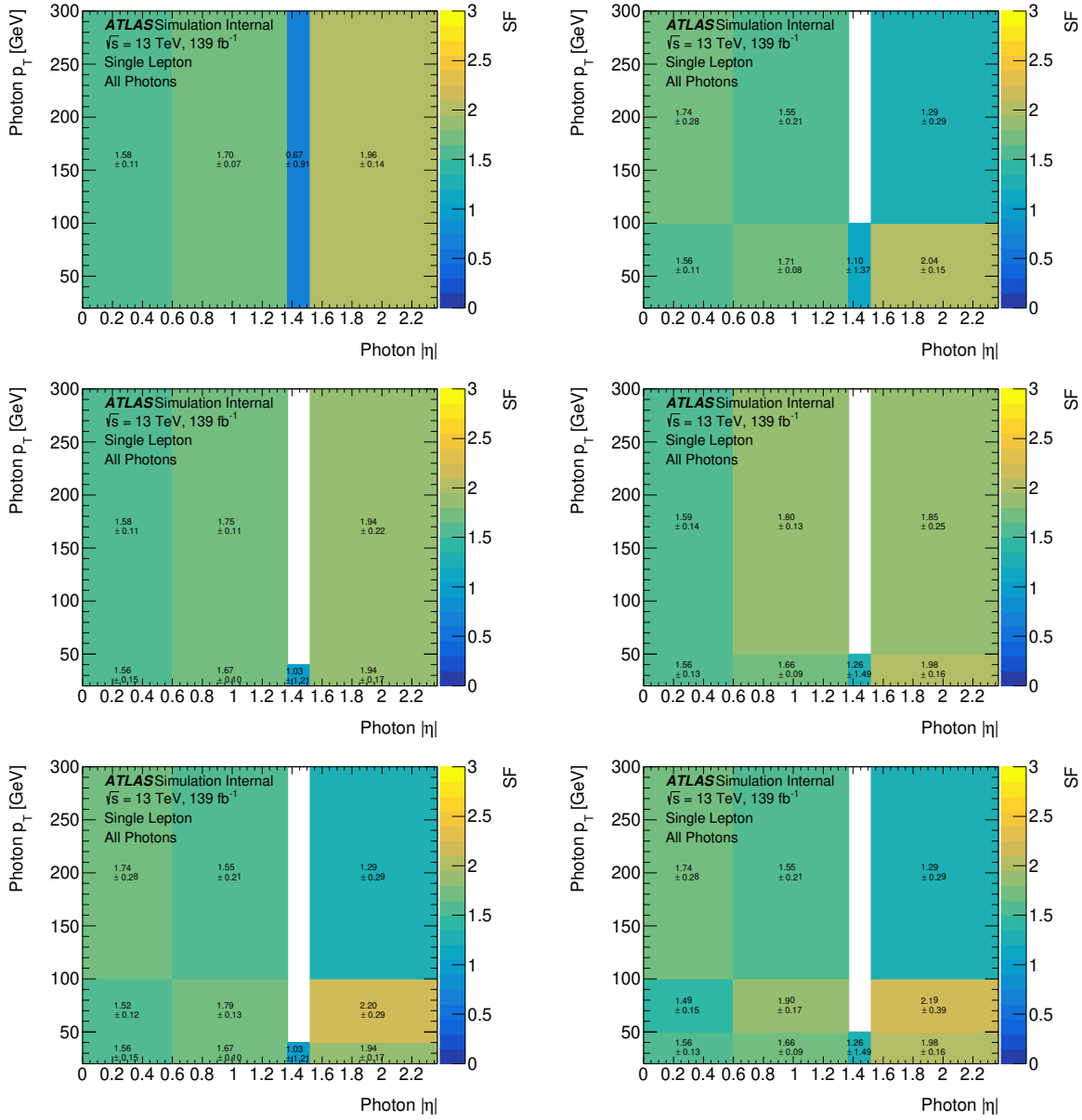


Figure 77: Measured values for  $SF^{h\text{-fake}}$  for all photons as a function of  $p_T$  and  $|\eta|$ . The  $|\eta|$  bins are motivated and chosen according to the detector geometry, excluding the calorimeter crack-region at  $1.37 < |\eta| < 1.52$ . The initial choice of binning in  $p_T$  is arbitrary. By comparing different choices of binning in  $p_T$  for each bin in  $|\eta|$  an optimal binning is chosen based on number of events in each bin. Bins in  $p_T$  that agree within uncertainties are subsequently merged together.

1589 factors are shown in Figures 74 to 76 for converted, unconverted and all photons. Neighbouring kinematic  
1590 bins in  $p_T$  that resulted in h-fake scale factors consistent within statistical uncertainties are merged together.  
1591 This leads to five bins each for the converted and unconverted category.

1592 The measured inclusive and binned  $\theta_{MC}$  are also summarised in Table 47. Any deviation of the measured  
1593  $\theta_{MC}$  from unity indicates a residual correlation between the four regions as described in Equation (17) that  
1594 should be taken into account. The resulting values for  $SF^{h\text{-fake}}$  as a function of  $p_T$  and  $|\eta|$  are shown in  
1595 Table 48.

Not reviewed, for internal circulation only

Table 47: Monte-Carlo-based double ratio  $\theta_{\text{MC}}$ , in three dimensional bins of photon  $p_{\text{T}}\text{-}|\eta|$ -conversion type, in the same binning that is used for the final three dimensional binned h-fake scale factors.

conv. type	$p_{\text{T}}$ bin [GeV]	$ \eta $ bin	$\theta_{\text{MC}}$
converted	$p_{\text{T}} < 40$	$ \eta  < 0.6$	$0.92 \pm 0.09$
	$p_{\text{T}} \geq 40$		$1.21 \pm 0.07$
	$p_{\text{T}} < 50$	$0.6 \geq  \eta  < 1.37$	$1.03 \pm 0.04$
	$p_{\text{T}} \geq 50$		$1.24 \pm 0.07$
	inclusive	$1.52 \geq  \eta  < 2.37$	$1.13 \pm 0.05$
unconverted	inclusive	$ \eta  < 0.6$	$1.20 \pm 0.05$
	$p_{\text{T}} < 100$	$0.6 \geq  \eta  < 1.37$	$1.15 \pm 0.04$
	$p_{\text{T}} \geq 100$		$1.44 \pm 0.11$
	$p_{\text{T}} < 100$	$1.52 \geq  \eta  < 2.37$	$1.22 \pm 0.06$
	$p_{\text{T}} \geq 100$		$1.51 \pm 0.15$

Table 48: Derived values for  $\text{SF}^{\text{h-fake}}$ , in three dimensional bins of photon  $p_{\text{T}}\text{-}|\eta|$ -conversion type, in the same binning that is used for the binned MC-based double ratio  $\theta_{\text{MC}}$  in Table 47.

conv. type	$p_{\text{T}}$ bin [GeV]	$ \eta $ bin	$\text{SF}^{\text{h-fake}}$
converted	$p_{\text{T}} < 40$	$ \eta  < 0.6$	$1.43 \pm 0.17$
	$p_{\text{T}} \geq 40$		$1.61 \pm 0.15$
	$p_{\text{T}} < 50$	$0.6 \geq  \eta  < 1.37$	$1.91 \pm 0.13$
	$p_{\text{T}} \geq 50$		$2.35 \pm 0.25$
	inclusive	$1.52 \geq  \eta  < 2.37$	$2.99 \pm 0.29$
unconverted	inclusive	$ \eta  < 0.6$	$1.78 \pm 0.15$
	$p_{\text{T}} < 100$	$0.6 \geq  \eta  < 1.37$	$1.37 \pm 0.11$
	$p_{\text{T}} \geq 100$		$1.12 \pm 0.20$
	$p_{\text{T}} < 100$	$1.52 \geq  \eta  < 2.37$	$1.45 \pm 0.16$
	$p_{\text{T}} \geq 100$		$1.00 \pm 0.25$

## 1596 E $t\bar{t}\gamma$ -only fit scenario

1597 This appendix summarises an additional measurement, where only the  $t\bar{t}\gamma$  simulation is considered signal.  
 1598 That is, the  $tW\gamma$  as introduced in Section 3 is treated as a background process for this scenario. This  
 1599 additional scenario is tested because the  $tW\gamma$  simulation is generated in the five-flavour scheme without  
 1600 the spectator  $b$ -quark, and acceptance efficiency and migration effects cannot be estimated accurately. The  
 1601  $t\bar{t}\gamma$  simulation provides a more precise evaluation of the acceptance and is therefore tested used as the only  
 1602 signal process in these tests. To allow some freedom to the  $tW\gamma$  simulation, the signal strength of which  
 1603 is measured to be significantly above the Standard Model expectation in Section 9, a 50% uncertainty  
 1604 on the cross-section is assigned. On the other hand, the  $t\bar{t}\gamma/tW\gamma$  fraction uncertainty of 15% is dropped.  
 1605 All systematic uncertainties on the  $tW\gamma$  prediction are now categorised as *background modelling*, that is,  
 1606 signal modelling only comprises uncertainties on the  $t\bar{t}\gamma$  prediction.

1607 Only systematic variations of the  $t\bar{t}\gamma$  prediction are taken into account, that is, scale variations, PS model  
 1608 uncertainty, PYTHIA8 A14 var3c eigentune variations and the NNPDF variations. Using only  $t\bar{t}\gamma$  as the  
 1609 signal requires a recalculation of the reconstruction efficiencies, the outside-migration fractions and the  
 1610 resulting correction factors  $C$  discussed in Section 5. A summary of the calculated values is shown in  
 1611 49, to be compared with Table 7 for the combined  $t\bar{t}\gamma/tW\gamma$  measurement. In comparison, the  $t\bar{t}\gamma$ -only  
 1612 scenario shows almost identical efficiencies, but reduced outside-migration fractions, resulting in a slightly  
 1613 smaller correction factor  $C$ . Dominant uncertainty remains the uncertainty on the  $t\bar{t}\gamma$  PS model.

1614 Following the same procedure as in Section 7, an Asimov fit was performed to estimate the expected  
 1615 uncertainty on the  $t\bar{t}\gamma$  signal strength. The fitted signal strength was found to be  $1.0^{+7.9\%}_{-7.3\%}$  with expected  
 1616 uncertainties about 15% larger than in the combined fit scenario.

Table 49:  $t\bar{t}\gamma$ -only scenario: obtained values for efficiency, outside migration and the correction factor  $C$  for the nominal signal prediction and its systematic variations. These include variations of the renormalisation and factorisation scales  $\mu_R$  and  $\mu_F$ , alternative modelling of the parton shower with HERWIG7, and variations of the PYTHIA eigentune. For the scale variations, relative uncertainties on  $C$  with respect to the nominal full simulation are quoted. For the other three, relative uncertainties with respect to the nominal AFII simulation are given as those Monte Carlo samples use fast simulation.

In addition, uncertainties originating from the choice of the PDF set are evaluated using 100 sampled NNPDF variations. For them, the mean and standard deviation are quoted as well as the resulting relative uncertainty. More details for the evaluation of the NNPDF uncertainties are given in Section 6.

Evaluated model	$\epsilon$	$f_{\text{out}}$	$C$	rel. uncertainty [%]
Nominal FS	0.2972	0.3345	0.4466	–
Nominal AFII	0.2905	0.3358	0.4374	–
$\mu_R \times 2.0$	0.2976	0.3340	0.4468	0.045
$\mu_R \times 0.5$	0.2966	0.3353	0.4462	-0.096
$\mu_F \times 2.0$	0.2970	0.3340	0.4459	-0.155
$\mu_F \times 0.5$	0.2976	0.3349	0.4475	0.194
PS model (HERWIG7)	0.2912	0.3110	0.4226	-3.381
PYTHIA8 var3c up	0.2905	0.3440	0.4428	1.234
PYTHIA8 var3c down	0.2938	0.3273	0.4368	-0.143
NNPDF variations	0.2972(3)	0.3345(9)	0.4466(6)	0.133

Afterwards, a fit was performed on the ATLAS data as done in Section 9. The pull distributions for the gamma bin statistics are shown in Figure 78. The nuisance parameter pulls can be found in Figure 79. These pulls are observed for the same modelling uncertainties as in the combined fit scenario. The ranking of systematic uncertainties for the fit on data is shown in Figure 80. Compared to the ranking of the combined fit scenario in ??, the  $tW\gamma$  cross-section uncertainty of 50% has a large impact on the significance of the result and is the second highest ranked uncertainty. For uncertainties with 10% or higher correlation to others the correlation matrix is shown in Figure 81.

Pre-fit and post-fit yields for all categories are listed in Table 50. The resulting signal strength, defined as measured cross-section over theory prediction is found to be:

$$\mu = \frac{\sigma_{\text{fid}}^{\text{meas.}}}{\sigma_{\text{fid}}^{\text{MC}}} = 1.423^{+0.029}_{-0.029} (\text{stat.})^{+0.093}_{-0.085} (\text{syst.}) = 1.423^{+0.097}_{-0.090},$$

corresponding to a relative uncertainty of  $^{+6.8\%}_{-6.3\%}$ , which is approximately 10% larger than the relative uncertainty in the combined fit scenario. As for the results of the combined fit scenario, no k-factor is applied to the signal simulation, hence the large discrepancy with a value of 1.0.

The dependence on this signal strength can be avoided for measuring the inclusive fiducial cross-section if the ratio of the  $e\mu$  categories and the other decay channels is considered (i.e.  $t\bar{t}\gamma e\mu$  over  $t\bar{t}\gamma e\mu + \text{Other } t\bar{t}\gamma$ ). Using the correction factor  $C$ , the fiducial cross-section for the  $t\bar{t}\gamma$ -only scenario is measured to be:

$$\sigma_{\text{fid}}(t\bar{t}\gamma \rightarrow e\mu) = \frac{N_{\text{reco}}^{\text{data}} - N_{\text{reco}}^{\text{bkg}}}{\mathcal{L}} \cdot \frac{N_{\text{reco}}^{\text{signal}}}{N_{\text{reco}}^{\text{all signal}}} \cdot \frac{1}{C_{e\mu}} = 39.4^{+0.8}_{-0.8} (\text{stat.})^{+2.6}_{-2.3} (\text{syst.}) \text{ fb} = 39.4^{+2.7}_{-2.5} \text{ fb}.$$

which is slightly below, but in agreement with the cross-section calculated in the combined fit scenario. The  $t\bar{t}\gamma$ -only fit scenario shows increased uncertainties, mostly due to the  $tW\gamma$  cross-section uncertainty. A breakdown of the systematic uncertainties and their impact is shown in Table 51. The background-modelling category has significantly higher impact than in the combined fit scenario due to the re-classification of  $tW\gamma$  uncertainties into that category and the added  $tW\gamma$  cross-section uncertainty.

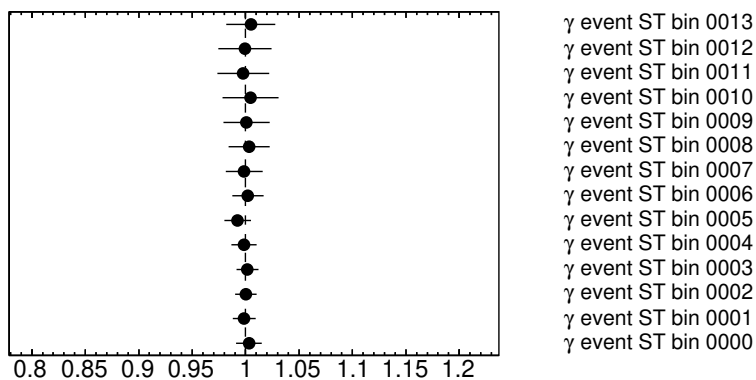


Figure 78: Gammas, that is, limitations of the individual bin statistics of the fitted distribution in the Asimov fit. Very large uncertainties on individual bins could mean that the binning should be re-adjusted.

Not reviewed, for internal circulation only

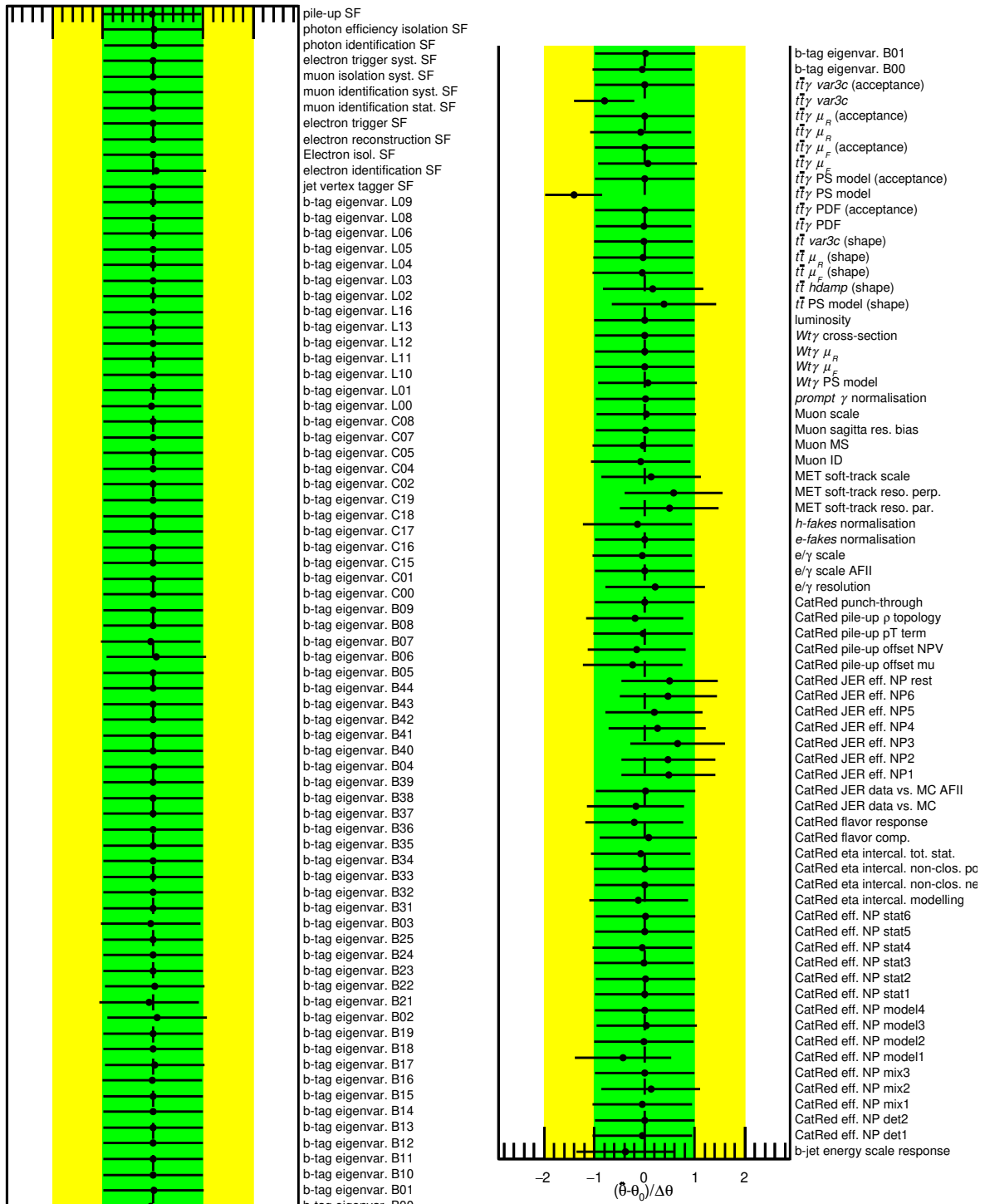


Figure 79: Pull distributions of all remaining nuisance parameters after pruning for the fit on data. If the error bar is shorter than the  $\pm 1\sigma$  interval, the corresponding nuisance parameter is constrained during the fit. If the mean value of the parameter is not zero, the fit favours the up or the down variation of the systematic. Pulls away from the nominal value are observed for some of the modelling uncertainties.

Not reviewed, for internal circulation only

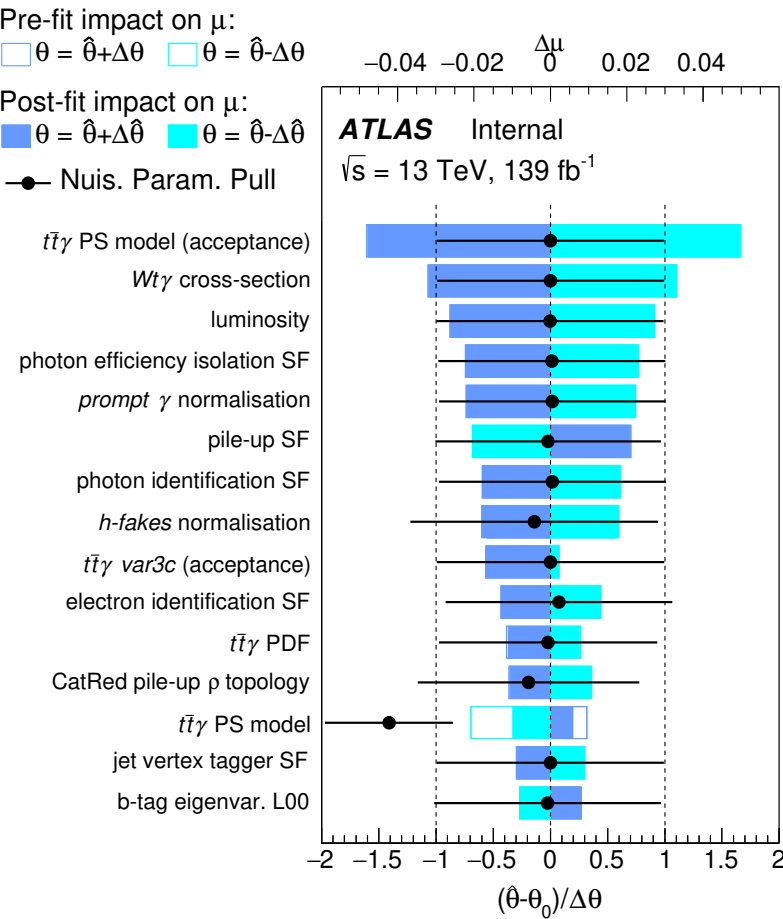


Figure 80: Ranking of systematics for the fit on data. The blue and turquoise bands indicate the post-fit impact on the measured signal strength in the fit, whereas the outlined blue and turquoise rectangles show the pre-fit impact. The difference between the two reflects the constraint of the nuisance parameter due to correlations in the fit. The impact is overlaid with the nuisance parameter pulls, as shown in Figure 79 already.

Table 50: Pre-fit and post-fit yields for all MC categories, including all uncertainties.

	Post-fit
$t\bar{t}\gamma e\mu$	$2440 \pm 100$
$tW\gamma e\mu$	$110 \pm 50$
Other $t\bar{t}\gamma$	$267 \pm 13$
Other $tW\gamma$	$13 \pm 7$
h-fake	$70 \pm 40$
e-fake	$23 \pm 11$
Prompt $\gamma$ bkg.	$90 \pm 40$
Total	$3010 \pm 60$
Data	3014

Not reviewed, for internal circulation only

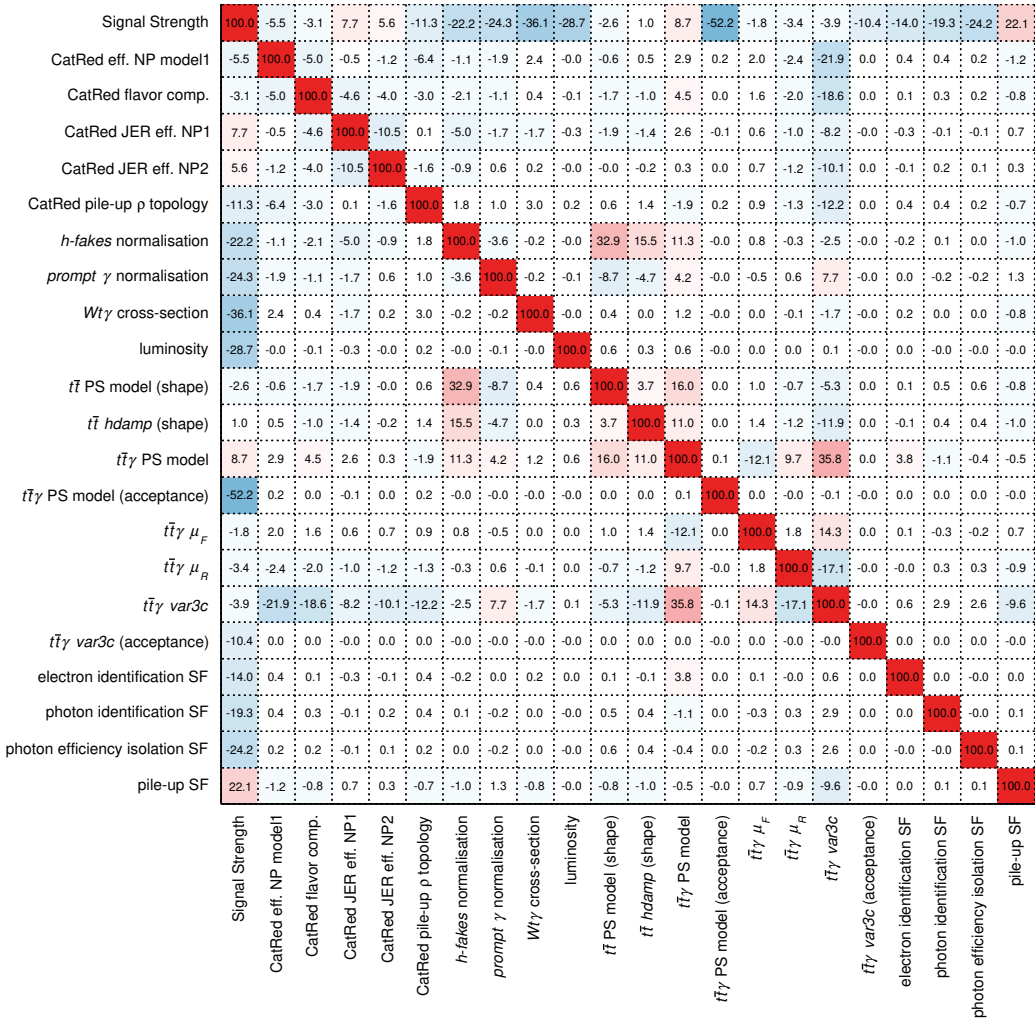


Figure 81: Correlation matrix for those nuisance parameters that have 10% or higher correlations to other uncertainties.

Table 51: Groups of systematic uncertainties and their relative impact on the result.

Group	Uncertainty
Signal modelling	3.6%
Background modelling	3.3%
Photons	2.0%
Luminosity	1.9%
Jets	1.6%
Flavour-tagging	1.1%
MC statistics	0.5%
Others	1.9%
Total syst.	6.2%

## 1632 F $t\bar{t}\gamma$ -only scenario for differential measurement

1633 This appendix summarises the differential measurement where the  $tW\gamma$  is considered as a background,  
 1634 which means only  $t\bar{t}\gamma$  is considered as signal. Regarding systematics, the  $tW\gamma$  systematic variations are  
 1635 still treated the same except one systematic ( $tW\gamma$  parton matching) and all of them, i.e.,  $tW\gamma$  systematics,  
 1636 is included in the Bkg modeling. The  $tW\gamma$  parton matching systematic is considered since the  $tW\gamma$  is  
 1637 generated in the five-flavour scheme where the spectator  $b$ -quark is found only in a fraction of the events,  
 1638 30% and 50% depending on the MC sample. Therefore an uncertainty is assigned to cover for such loss of  
 1639 events. The difference in the treatment is that in the  $t\bar{t}\gamma$ -only scenario, a 50% normalisation uncertainty  
 1640 is assigned to the  $tW\gamma$  rather than the doubling of fiducial parton-level events(done in the combined  
 1641 scenario).

1642 The results for the  $t\bar{t}\gamma$ -only scenarios are as follows. The normalised measured differential cross-sections  
 1643 are shown in Figure 82, while the absolute measured differential cross-sections are shown in Figure 84.  
 1644 The measured distributions are obtained from data after subtracting the pref-fit background distributions.  
 1645 The last bin of the distributions does not include the overflow bin or in other words the differential  
 1646 cross-sections are measured in the range shown. In practise, this only affects the photon  $p_T$  distribution,  
 1647 for which few data events have larger  $p_T$  (permil contribution). The unfolded results are compared to  
 1648 the NLO theory prediction where the unfolding machinery is built using the signal  $t\bar{t}\gamma$  MC to unfold  
 1649 (data-Bkg). The decomposed uncertainties of the unfolded distributions for the normalised and absolute  
 1650 differential cross-sections are illustrated in Figure 83 and Figure 85, respectively. The numerical values of  
 1651 the normalised differential cross-sections results are summarised in Tables 52 to 56, while the absolute are  
 1652 shown in Tables 57 to 61. The last line in the absolute cross-section tables corresponds to the inclusive  
 1653 cross-section. The  $\chi^2$  tests for the normalised cross-sections compared with a number of MC predictions  
 1654 as well as the theory NLO prediction are summarised in Table 62 while for absolute cross-sections they are  
 1655 shown in Table 63.

Not reviewed, for internal circulation only

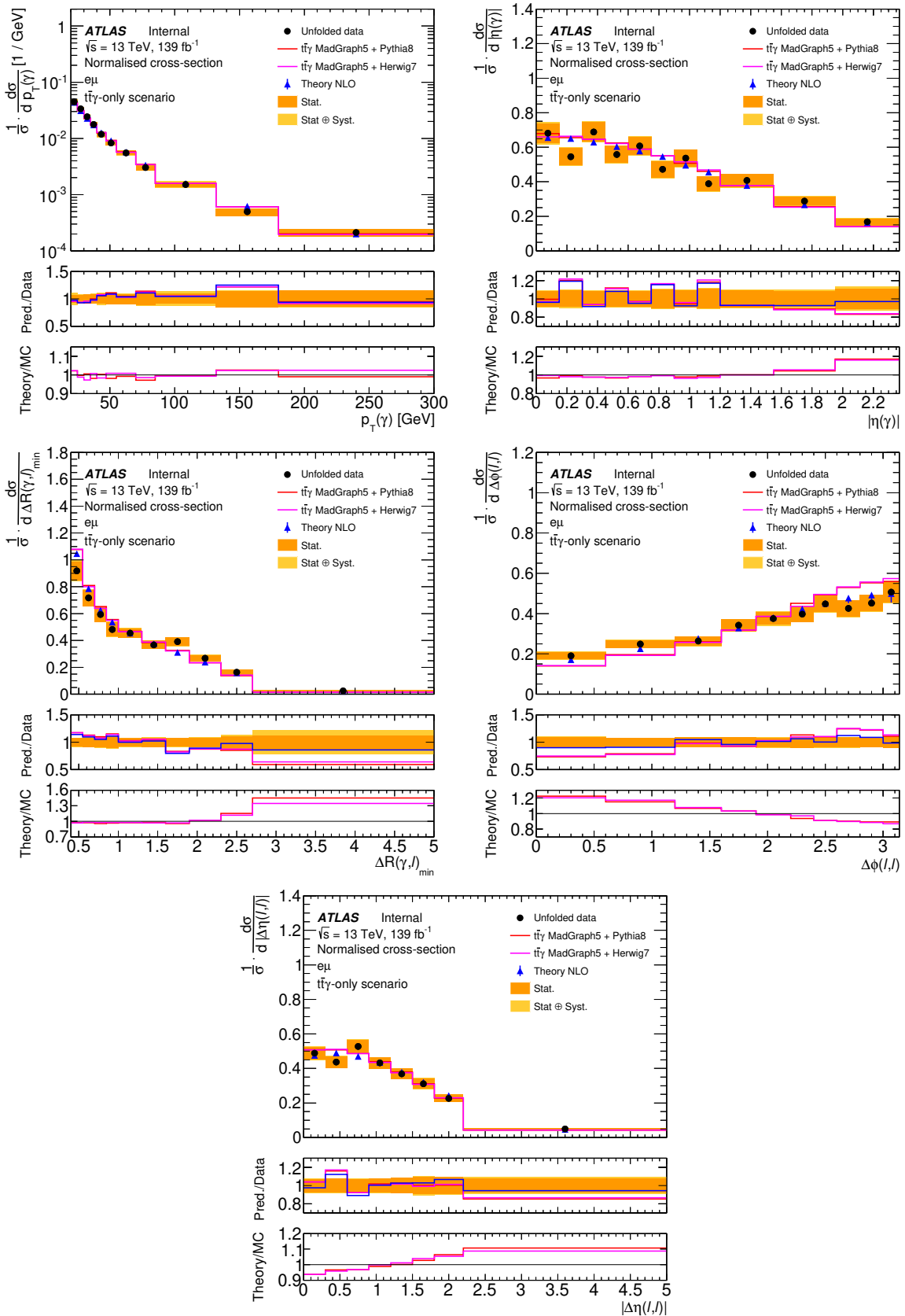


Figure 82: The normalised differential cross-section for the photon  $p_T$ , photon  $|\eta|$ ,  $\Delta R_{\min}(\gamma, \ell)$ ,  $\Delta\phi(\ell, \ell)$  and  $|\Delta\eta(\ell, \ell)|$ . The unfolded distribution to the parton-level (dots) is compared to the parton-level distributions of  $t\bar{t}\gamma$  **MadGraph5\_aMC@NLO +PYTHIA8** (red),  $t\bar{t}\gamma$  **MADGRAPH5\_aMC@NLO +HERWIG7** (Magenta) and theory **NLO** prediction (blue).

Not reviewed, for internal circulation only

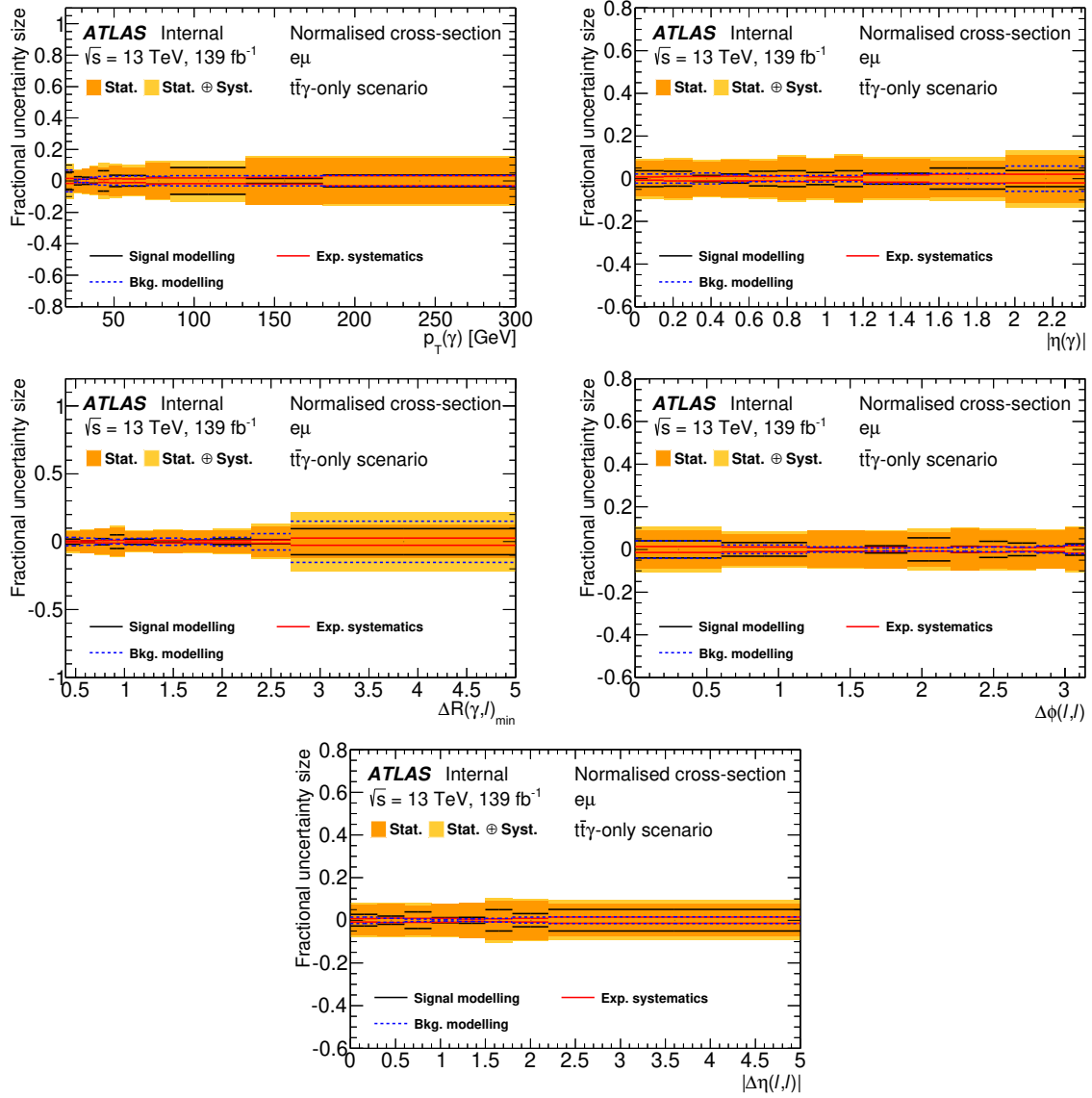


Figure 83: The decomposed systematic uncertainties for the normalised differential cross-sections as a function of photon  $p_T$ , photon  $|\eta|$ ,  $\Delta R_{\min}(\gamma, \ell)$ ,  $\Delta\phi(\ell, \ell)$  and  $|\Delta\eta(\ell, \ell)|$ .

Not reviewed, for internal circulation only

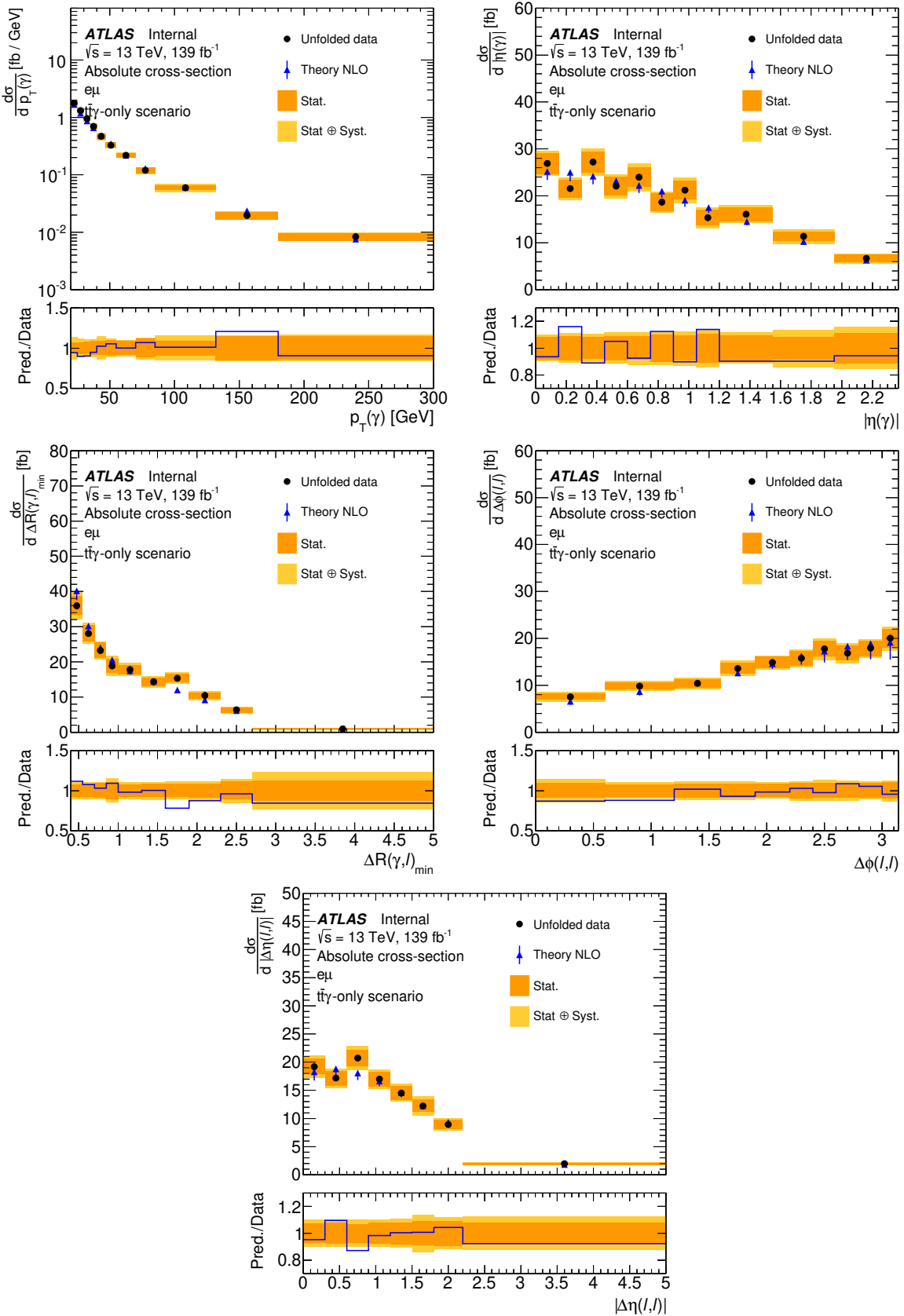


Figure 84: The absolute differential cross-section for the photon  $p_T$ , photon  $|\eta|$ ,  $\Delta R_{\min}(\gamma, \ell)$ ,  $\Delta\phi(\ell, \ell)$  and  $|\Delta\eta(\ell, \ell)|$ . The unfolded distribution to the parton-level (dots) is compared to the NLO theory prediction (blue).

Not reviewed, for internal circulation only

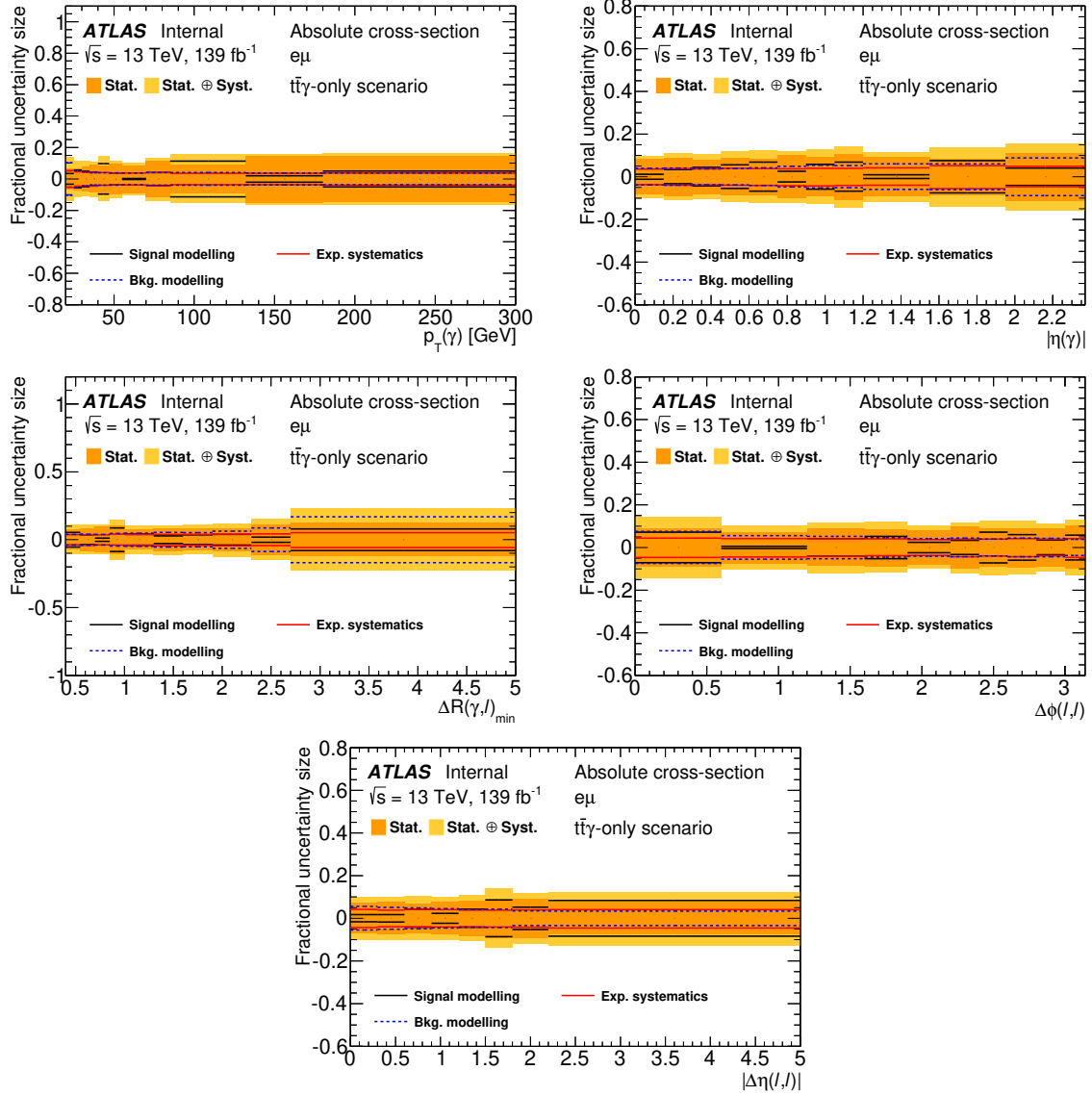


Figure 85: The decomposed systematic uncertainties for the absolute differential cross-sections as a function of the photon  $p_T$ , photon  $|\eta|$ ,  $\Delta R_{\min}(\gamma, \ell)$ ,  $\Delta\phi(\ell, \ell)$  and  $|\Delta\eta(\ell, \ell)|$ .

Table 52: The normalised differential cross-section in  $p_T(\gamma)$  bins, obtained using the iterative Bayesian method. The first and second associated uncertainties are the statistical and the systematic uncertainty, respectively.

$p_T(\gamma)$ [GeV]	normalised cross-section
20.0 - 25.0	$0.0448 \pm 0.003 \pm 0.004$
25.0 - 30.0	$0.0334 \pm 0.0023 \pm 0.001$
30.0 - 35.0	$0.0243 \pm 0.0019 \pm 0.0007$
35.0 - 40.0	$0.0177 \pm 0.0015 \pm 0.0006$
40.0 - 47.0	$0.0119 \pm 0.001 \pm 0.0009$
47.0 - 55.0	$0.0083 \pm 0.0008 \pm 0.0004$
55.0 - 70.0	$0.0055 \pm 0.0005 \pm 0.0003$
70.0 - 85.0	$0.003 \pm 0.0004 \pm 0.0001$
85.0 - 132.0	$0.0015 \pm 0.0001 \pm 0.0001$
132.0 - 180.0	$0.0005 \pm 0.0001 \pm 0.0$
180.0 - 300.0	$0.0002 \pm 0.0 \pm 0.0$

Table 53: The normalised differential cross-section in  $|\eta|(\gamma)$  bins, obtained using the iterative Bayesian method. The first and second associated uncertainties are the statistical and the systematic uncertainty, respectively.

$ \eta (\gamma)$	normalised cross-section
0.0 - 0.15	$0.68 \pm 0.06 \pm 0.03$
0.15 - 0.3	$0.55 \pm 0.05 \pm 0.02$
0.3 - 0.45	$0.69 \pm 0.06 \pm 0.02$
0.45 - 0.6	$0.56 \pm 0.05 \pm 0.02$
0.6 - 0.75	$0.61 \pm 0.05 \pm 0.02$
0.75 - 0.9	$0.47 \pm 0.05 \pm 0.02$
0.9 - 1.05	$0.54 \pm 0.05 \pm 0.02$
1.05 - 1.2	$0.39 \pm 0.04 \pm 0.02$
1.2 - 1.55	$0.41 \pm 0.04 \pm 0.02$
1.55 - 1.95	$0.29 \pm 0.02 \pm 0.02$
1.95 - 2.37	$0.17 \pm 0.02 \pm 0.01$

Table 54: The normalised differential cross-section in  $\Delta R_{\min}(\gamma, \ell)$  bins, obtained using the iterative Bayesian method. The first and second associated uncertainties are the statistical and the systematic uncertainty, respectively.

$\Delta R_{\min}(\gamma, \ell)$	normalised cross-section
0.4 - 0.55	$0.918 \pm 0.068 \pm 0.034$
0.55 - 0.7	$0.717 \pm 0.059 \pm 0.02$
0.7 - 0.85	$0.594 \pm 0.055 \pm 0.02$
0.85 - 1.0	$0.482 \pm 0.05 \pm 0.026$
1.0 - 1.3	$0.455 \pm 0.033 \pm 0.015$
1.3 - 1.6	$0.367 \pm 0.03 \pm 0.011$
1.6 - 1.9	$0.392 \pm 0.031 \pm 0.01$
1.9 - 2.3	$0.268 \pm 0.023 \pm 0.01$
2.3 - 2.7	$0.163 \pm 0.018 \pm 0.01$
2.7 - 5.0	$0.025 \pm 0.003 \pm 0.004$

Table 55: The normalised differential cross-section in  $|\Delta\eta(\ell, \ell)|$  bins, obtained using the iterative Bayesian method. The first and second associated uncertainties are the statistical and the systematic uncertainty, respectively.

$ \Delta\eta(\ell, \ell) $	normalised cross-section
0.0 - 0.3	$0.49 \pm 0.04 \pm 0.02$
0.3 - 0.6	$0.44 \pm 0.03 \pm 0.01$
0.6 - 0.9	$0.53 \pm 0.04 \pm 0.02$
0.9 - 1.2	$0.43 \pm 0.03 \pm 0.01$
1.2 - 1.5	$0.37 \pm 0.03 \pm 0.01$
1.5 - 1.8	$0.31 \pm 0.03 \pm 0.02$
1.8 - 2.2	$0.23 \pm 0.02 \pm 0.01$
2.2 - 5.0	$0.05 \pm 0.0 \pm 0.0$

Not reviewed, for internal circulation only

Table 56: The normalised differential cross-section in  $\Delta\phi(\ell, \ell)$  bins, obtained using the iterative Bayesian method. The first and second associated uncertainties are the statistical and the systematic uncertainty, respectively.

$\Delta\phi(\ell, \ell)$	normalised cross-section
0.0 - 0.6	$0.19 \pm 0.02 \pm 0.01$
0.6 - 1.2	$0.25 \pm 0.02 \pm 0.01$
1.2 - 1.6	$0.26 \pm 0.02 \pm 0.0$
1.6 - 1.9	$0.34 \pm 0.03 \pm 0.01$
1.9 - 2.2	$0.38 \pm 0.03 \pm 0.02$
2.2 - 2.4	$0.4 \pm 0.04 \pm 0.01$
2.4 - 2.6	$0.45 \pm 0.04 \pm 0.02$
2.6 - 2.8	$0.43 \pm 0.04 \pm 0.01$
2.8 - 3.0	$0.45 \pm 0.04 \pm 0.01$
3.0 - 3.14	$0.51 \pm 0.05 \pm 0.02$

Not reviewed, for internal circulation only

Table 57: The absolute differential cross-section in  $p_T(\gamma)$  bins, obtained using the iterative Bayesian method. The first and second associated uncertainties are the statistical and the systematic uncertainty, respectively.

$p_T(\gamma)$ [GeV]	absolute cross-section [fb]
20.0 - 25.0	$1.7684 \pm 0.1188 \pm 0.2159$
25.0 - 30.0	$1.3189 \pm 0.0914 \pm 0.1188$
30.0 - 35.0	$0.9593 \pm 0.0746 \pm 0.076$
35.0 - 40.0	$0.6982 \pm 0.0599 \pm 0.0501$
40.0 - 47.0	$0.4679 \pm 0.0412 \pm 0.0525$
47.0 - 55.0	$0.3289 \pm 0.0321 \pm 0.0219$
55.0 - 70.0	$0.2183 \pm 0.019 \pm 0.0114$
70.0 - 85.0	$0.1202 \pm 0.014 \pm 0.0084$
85.0 - 132.0	$0.0597 \pm 0.0055 \pm 0.0075$
132.0 - 180.0	$0.0196 \pm 0.0029 \pm 0.0011$
180.0 - 300.0	$0.0084 \pm 0.0012 \pm 0.0006$
Sum(cross-section per bin x bin width)	$39.5 \pm 5.0$

Table 58: The absolute differential cross-section in  $|\eta|(\gamma)$  bins, obtained using the iterative Bayesian method. The first and second associated uncertainties are the statistical and the systematic uncertainty, respectively.

$ \eta (\gamma)$	absolute cross-section [fb]
0.0 - 0.15	$26.92 \pm 2.23 \pm 1.46$
0.15 - 0.3	$21.54 \pm 1.93 \pm 1.4$
0.3 - 0.45	$27.22 \pm 2.19 \pm 1.86$
0.45 - 0.6	$22.07 \pm 1.94 \pm 1.72$
0.6 - 0.75	$23.99 \pm 2.04 \pm 2.11$
0.75 - 0.9	$18.68 \pm 1.88 \pm 1.23$
0.9 - 1.05	$21.19 \pm 1.94 \pm 1.86$
1.05 - 1.2	$15.36 \pm 1.64 \pm 1.45$
1.2 - 1.55	$16.09 \pm 1.47 \pm 1.18$
1.55 - 1.95	$11.35 \pm 0.96 \pm 1.25$
1.95 - 2.37	$6.65 \pm 0.74 \pm 0.73$
Sum(cross-section per bin x bin width)	$39.5 \pm 4.8$

Table 59: The absolute differential cross-section in  $\Delta R_{\min}(\gamma, \ell)$  bins, obtained using the iterative Bayesian method. The first and second associated uncertainties are the statistical and the systematic uncertainty, respectively.

$\Delta R_{\min}(\gamma, \ell)$	absolute cross-section [fb]
0.4 - 0.55	$35.944 \pm 2.678 \pm 2.775$
0.55 - 0.7	$28.057 \pm 2.323 \pm 1.874$
0.7 - 0.85	$23.243 \pm 2.136 \pm 1.267$
0.85 - 1.0	$18.876 \pm 1.952 \pm 1.993$
1.0 - 1.3	$17.81 \pm 1.309 \pm 1.307$
1.3 - 1.6	$14.358 \pm 1.182 \pm 1.031$
1.6 - 1.9	$15.337 \pm 1.216 \pm 1.136$
1.9 - 2.3	$10.477 \pm 0.888 \pm 0.897$
2.3 - 2.7	$6.368 \pm 0.71 \pm 0.625$
2.7 - 5.0	$0.976 \pm 0.119 \pm 0.19$
Sum(cross-section per bin x bin width)	$39.2 \pm 4.7$

Table 60: The absolute differential cross-section in  $|\Delta\eta(\ell, \ell)|$  bins, obtained using the iterative Bayesian method. The first and second associated uncertainties are the statistical and the systematic uncertainty, respectively.

$ \Delta\eta(\ell, \ell) $	absolute cross-section [fb]
0.0 - 0.3	$19.2 \pm 1.38 \pm 1.37$
0.3 - 0.6	$17.17 \pm 1.3 \pm 1.14$
0.6 - 0.9	$20.73 \pm 1.42 \pm 1.58$
0.9 - 1.2	$16.99 \pm 1.29 \pm 1.1$
1.2 - 1.5	$14.52 \pm 1.19 \pm 1.02$
1.5 - 1.8	$12.22 \pm 1.11 \pm 1.27$
1.8 - 2.2	$8.93 \pm 0.81 \pm 0.66$
2.2 - 5.0	$1.96 \pm 0.15 \pm 0.19$
Sum(cross-section per bin x bin width)	$39.3 \pm 4.3$

Table 61: The absolute differential cross-section in  $\Delta\phi(\ell, \ell)$  bins, obtained using the iterative Bayesian method. The first and second associated uncertainties are the statistical and the systematic uncertainty, respectively.

$\Delta\phi(\ell, \ell)$	absolute cross-section [fb]
0.0 - 0.6	$7.55 \pm 0.67 \pm 0.85$
0.6 - 1.2	$9.84 \pm 0.73 \pm 0.68$
1.2 - 1.6	$10.43 \pm 0.92 \pm 0.81$
1.6 - 1.9	$13.57 \pm 1.18 \pm 1.09$
1.9 - 2.2	$14.86 \pm 1.19 \pm 0.9$
2.2 - 2.4	$15.76 \pm 1.53 \pm 1.06$
2.4 - 2.6	$17.74 \pm 1.6 \pm 1.61$
2.6 - 2.8	$16.85 \pm 1.55 \pm 1.43$
2.8 - 3.0	$17.91 \pm 1.6 \pm 1.21$
3.0 - 3.14	$20.03 \pm 1.99 \pm 1.62$
Sum(cross-section per bin x bin width)	$39.6 \pm 4.7$

Table 62:  $\chi^2$  values between the normalised unfolded cross-section and various predictions from the MC simulation as well as between normalised unfolded cross-section and theoretical NLO prediction in the  $e\mu$  channel.

Predictions	$p_T(\gamma)$		$ \eta (\gamma)$		$\Delta R_{\min}(\gamma, \ell)$		$ \Delta\eta(\ell, \ell) $		$\Delta\phi(\ell, \ell)$	
	$\chi^2/\text{NDF}$	$p\text{-value}$	$\chi^2/\text{NDF}$	$p\text{-value}$	$\chi^2/\text{NDF}$	$p\text{-value}$	$\chi^2/\text{NDF}$	$p\text{-value}$	$\chi^2/\text{NDF}$	$p\text{-value}$
$t\bar{t}\gamma$ MADGRAPH5_aMC@NLO +PYTHIA8	6.2/10	0.8	15.5/10	0.11	18.3/9	0.03	5.9/7	0.55	28.5/9	<0.01
$t\bar{t}\gamma$ MADGRAPH5_aMC@NLO +HERWIG7	5.1/10	0.88	17.3/10	0.07	17.5/9	0.04	6.3/7	0.51	29.0/9	<0.01
Theory NLO	5.9/10	0.82	14.1/10	0.17	13.2/9	0.15	5.6/7	0.59	5.6/9	0.78

Table 63:  $\chi^2$  values between the absolute unfolded cross-section and theoretical NLO prediction in the  $e\mu$  channel.

Predictions	$p_T(\gamma)$		$ \eta (\gamma)$		$\Delta R_{\min}(\gamma, \ell)$		$ \Delta\eta(\ell, \ell) $		$\Delta\phi(\ell, \ell)$	
	$\chi^2/\text{NDF}$	$p\text{-value}$	$\chi^2/\text{NDF}$	$p\text{-value}$	$\chi^2/\text{NDF}$	$p\text{-value}$	$\chi^2/\text{NDF}$	$p\text{-value}$	$\chi^2/\text{NDF}$	$p\text{-value}$
Theory NLO	6.0/11	0.87	13.5/11	0.26	10.9/10	0.37	5.5/8	0.7	5.0/10	0.89

## 1656 G Fit benchmarks

1657 To choose the optimal variable for the fit of the inclusive measurement, multiple variables were tested in  
 1658 Asimov fit scenarios. Not only the expected sensitivities, as listed in Table 64, are compared, but also  
 1659 the pulls and constraints as well as the systematic ranking were checked. Note that these tests were done  
 1660 with the ntuples v3.1, which is *not* the version used for the results in the main body. The fitted pre-fit  
 1661 distributions of all variables are shown in Figure 86.

1662 One tested variable is the one proposed for the fit: the total transverse momentum  $S_T$  of the event (which  
 1663 includes all hadronic and leptonic transverse momenta, as well as photons and  $E_T^{\text{miss}}$ ). The  $S_T$  distribution  
 1664 is modelled well over the entire spectrum, as seen in the pre-fit distribution. The pull distributions for the  
 1665 Asimov fit scenario are found in Figure 87, the ranking of the nuisance parameters is shown in Figure 88.  
 1666 The expected total uncertainty on the signal strength is found to be  $\pm 5\%$  in this benchmark test.

1667 As a primary benchmark, a single-bin fit was performed on an Asimov dataset. The resulting pull  
 1668 distributions are shown in Figure 89. The nuisance parameter ranking is listed in Figure 90. As seen  
 1669 in the first, none of the nuisance parameters can be constrained, as opposed to the pull distributions for  
 1670  $S_T$ . As a consequence, the nuisance parameters are directly ranked by their normalisation impact on the  
 1671 single-bin distribution. The expected total uncertainty on the signal strength is found to be  $\pm 7\%$ , which is  
 1672 significantly lower than the expected result for  $S_T$ .

1673 A second benchmark fit is performed on the relatively simple distribution of the jet multiplicity (with the  
 1674 bins as presented in the pre-fit plots). The nuisance parameter pull distributions are shown in Figure 91, the  
 1675 ranking can be found in Figure 92. Compared to the Asimov fit results on  $S_T$ , the fit on the jet multiplicity  
 1676 only constrains very few nuisance parameters. The ranking shows very similar importance of nuisance  
 1677 parameters as the single-bin fit scenario. The expected total uncertainty on the signal strength for the jet  
 1678 multiplicity is calculated to be  $\pm 6\%$ .

1679 As a last benchmark, an Asimov fit was performed on the transverse momentum of the leading jet. The  
 1680 nuisance parameter pull distributions are shown in Figure 93, the ranking can be found in Figure 94. The  
 1681 overall behaviour of nuisance parameters is very similar to that of the fit on  $S_T$ . Some of the ranks are  
 1682 swapped, e.g. the  $tW\gamma$  shower and matrix-element variations. The expected total uncertainty on the fit  
 1683 result was also calculated to be  $\pm 5\%$ .

Table 64: Expected total uncertainty on the  $t\bar{t}\gamma$  signal strength for Asimov fit scenarios on different variables.

Variable	Expected sensitivity
$S_T$ (proposed)	0.05
Leading jet $p_T$	0.05
$H_T$	0.06
$n_{\text{jets}}$	0.06
$p_T(\gamma)$	0.06
single bin	0.07

Not reviewed, for internal circulation only

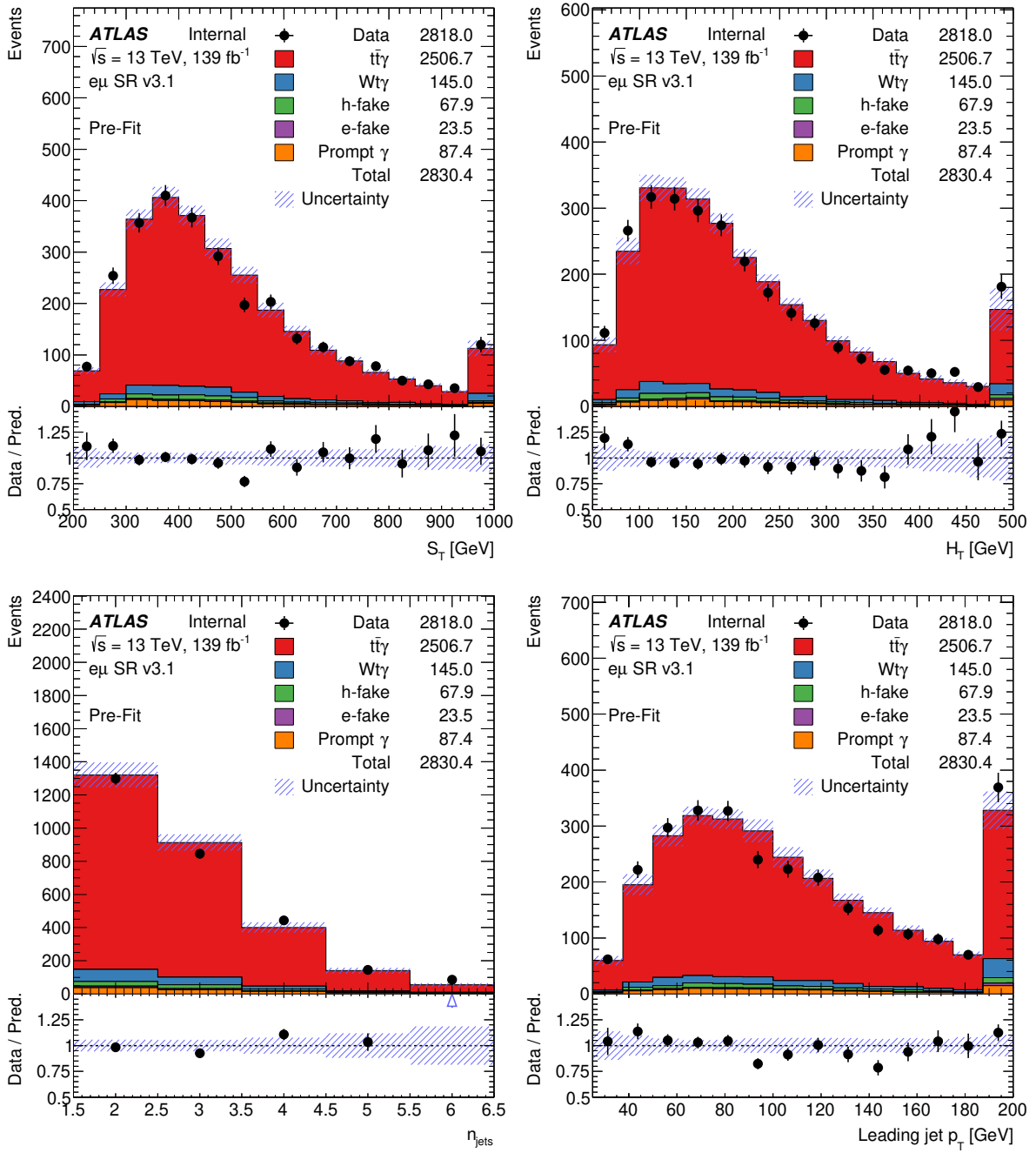


Figure 86: Data/MC pre-fit control plots of the variables used for the fit benchmarks. The displayed uncertainties include both statistical and systematic uncertainties, as present in the ntuples v3.1.

Not reviewed, for internal circulation only

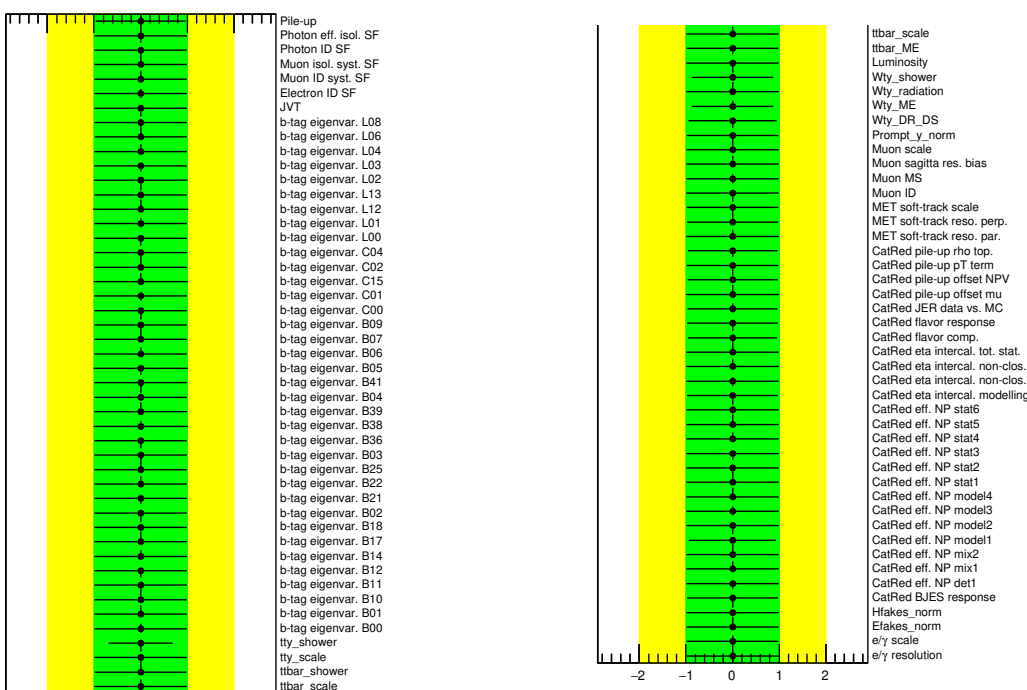


Figure 87: Pull distributions of all remaining nuisance parameters after pruning for the Asimov fit on  $S_T$ .

Not reviewed, for internal circulation only

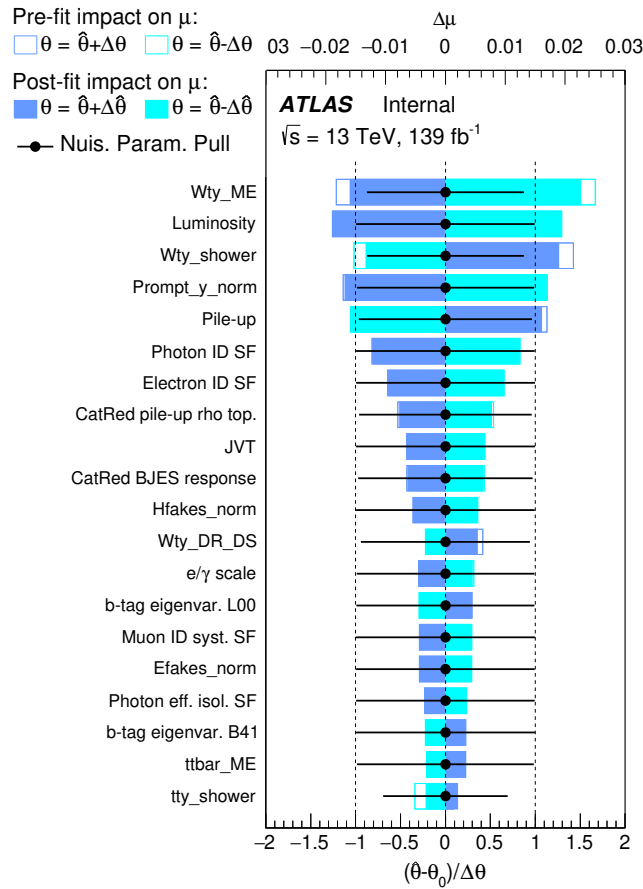


Figure 88: Ranking of systematics in the Asimov fit scenario on  $S_T$ . The blue and turquoise bands indicate the post-fit impact on the measured signal strength in the fit, whereas the outlined blue and turquoise rectangles show the pre-fit impact. The difference between the two reflects the constraint of the nuisance parameter due to correlations in the fit. The impact is overlaid with the nuisance parameter pulls, as shown in Figure 87 already.

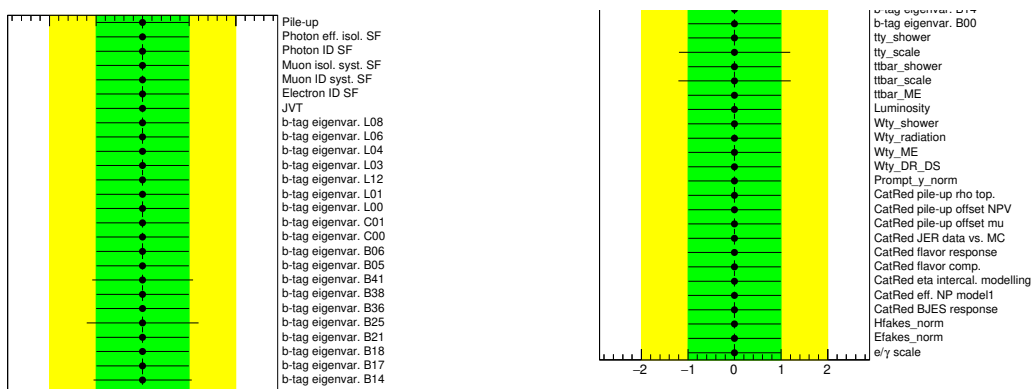


Figure 89: Pull distributions of all remaining nuisance parameters after pruning for the Asimov fit on a single bin.

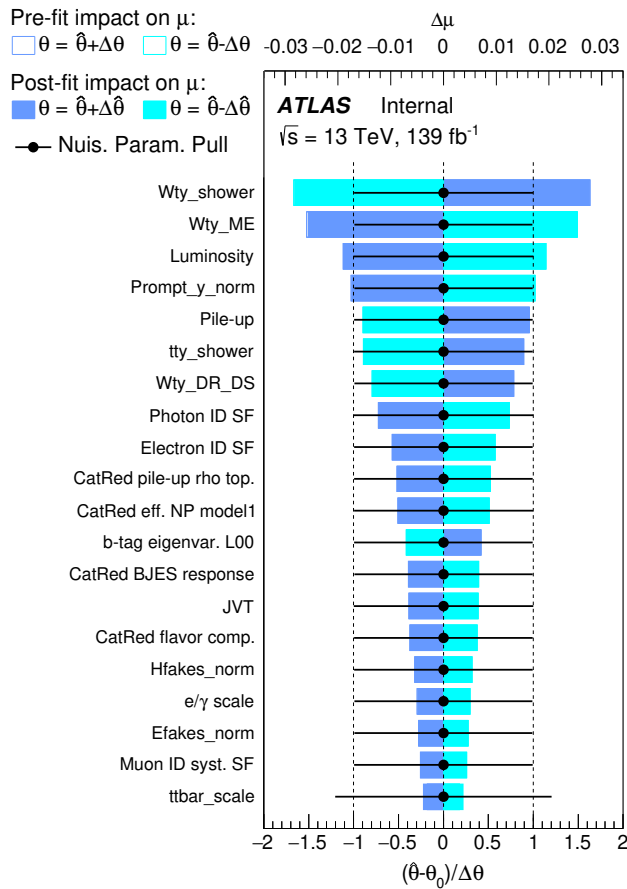


Figure 90: Ranking of systematics in the Asimov fit scenario on a single bin. The blue and turquoise bands indicate the post-fit impact on the measured signal strength in the fit, whereas the outlined blue and turquoise rectangles show the pre-fit impact. The difference between the two reflects the constraint of the nuisance parameter due to correlations in the fit. The impact is overlaid with the nuisance parameter pulls, as shown in Figure 89 already.

Not reviewed, for internal circulation only

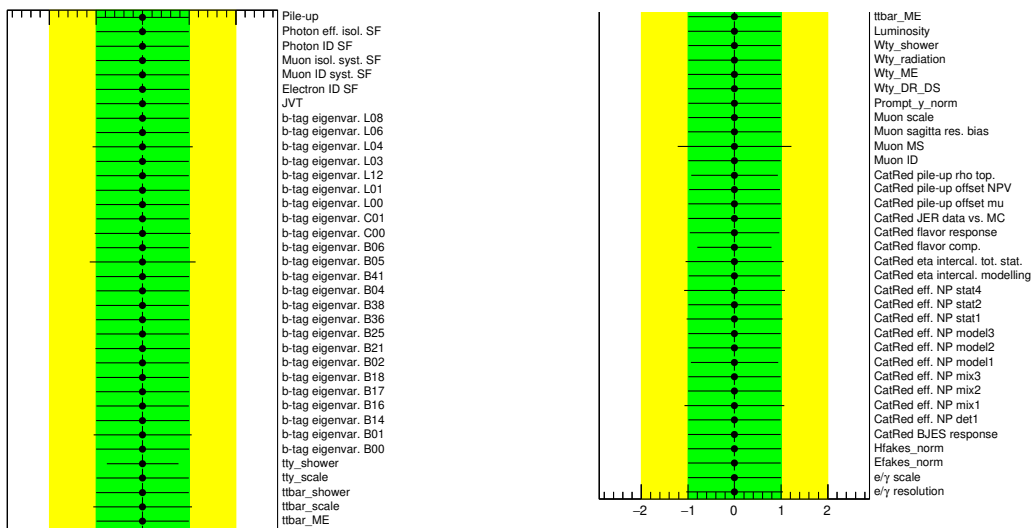


Figure 91: Pull distributions of all remaining nuisance parameters after pruning for the Asimov fit on the jet multiplicity.

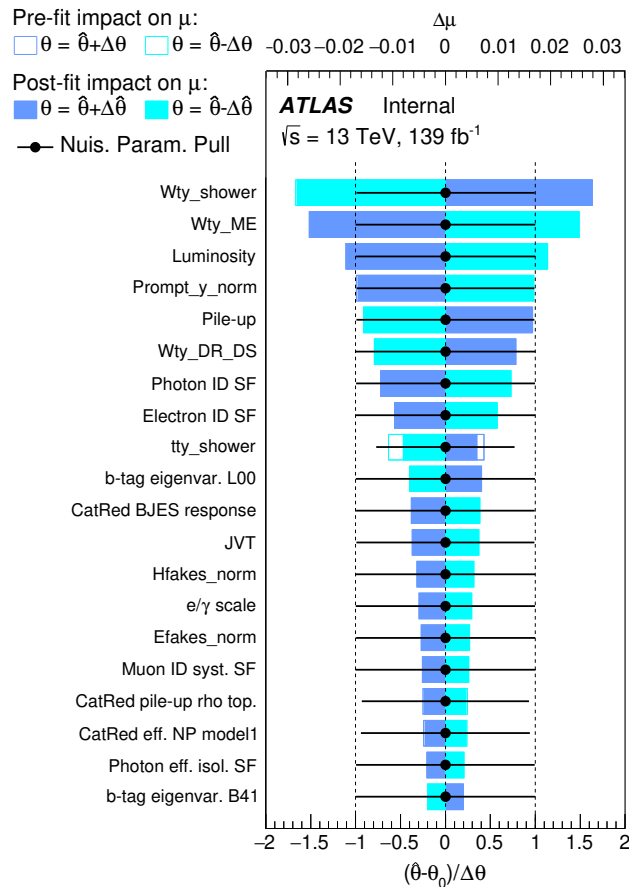


Figure 92: Ranking of systematics in the Asimov fit scenario on the jet multiplicity. The blue and turquoise bands indicate the post-fit impact on the measured signal strength in the fit, whereas the outlined blue and turquoise rectangles show the pre-fit impact. The difference between the two reflects the constraint of the nuisance parameter due to correlations in the fit. The impact is overlaid with the nuisance parameter pulls, as shown in Figure 91 already.

Not reviewed, for internal circulation only

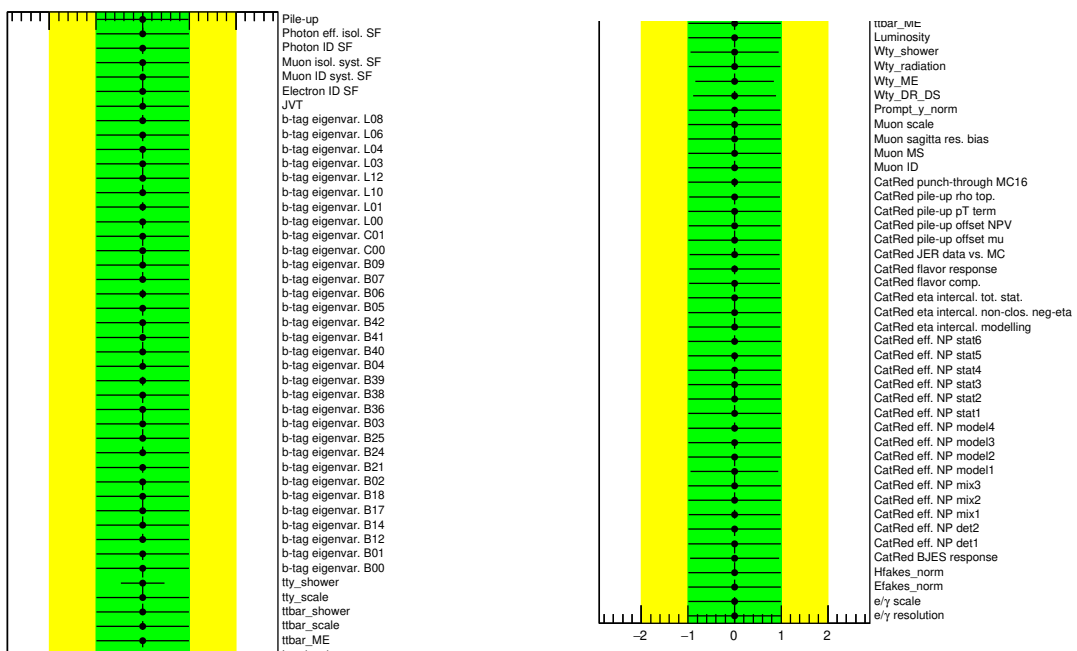


Figure 93: Pull distributions of all remaining nuisance parameters after pruning for the Asimov fit on the leading jet  $p_T$ .

Not reviewed, for internal circulation only

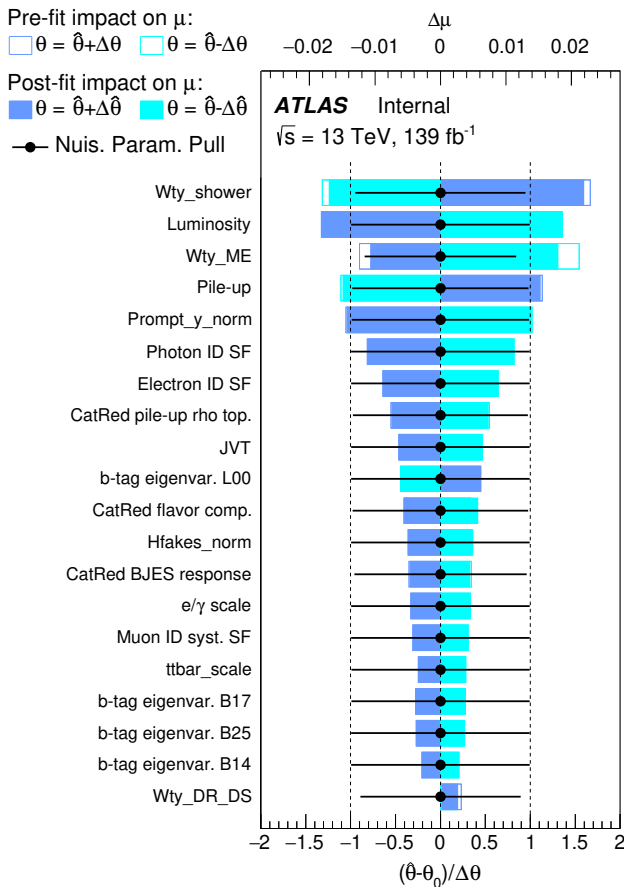


Figure 94: Ranking of systematics in the Asimov fit scenario on the leading jet  $p_T$ . The blue and turquoise bands indicate the post-fit impact on the measured signal strength in the fit, whereas the outlined blue and turquoise rectangles show the pre-fit impact. The difference between the two reflects the constraint of the nuisance parameter due to correlations in the fit. The impact is overlaid with the nuisance parameter pulls, as shown in Figure 93 already.

## 1684 H Pruning optimisation

1685 To test the impact of pruning systematic variations before the fit, different pruning scenarios were tested.  
 1686 These tests were performed with ntuples v5.0 and the systematics available at that point of time.

1687 The idea of pruning is to minimise the number of nuisance parameters in the fit, which both increases speed  
 1688 and improves the overall fit stability. On the other hand, the final result must not be affected by the removal  
 1689 of parameters. To check the impact of pruning, different thresholds were chosen, an Asimov fit scenario  
 1690 was performed, and the expected uncertainty on the  $t\bar{t}\gamma$  signal strength was evaluated. As a benchmark, the  
 1691 fit was first performed *without* pruning of systematics. Then, different thresholds for the normalisation and  
 1692 shape components were tested. The thresholds were chosen in such a way that the number of nuisance  
 1693 parameters was reduced to approximately 1/2, to 1/4 and to 1/5.

1694 The chosen pruning thresholds for normalisation were 0.2%, 0.5% and 1.0%, resulting in approximately  
 1695 41%, 26%, and 15% of the original number of nuisance parameters, respectively. The chosen pruning  
 1696 thresholds for shape were 0.05%, 0.10% and 0.20%, resulting in approximately 41%, 27%, and 19% of  
 1697 the original number of nuisance parameters, respectively. The resulting expected uncertainties of the  $t\bar{t}\gamma$   
 1698 signal strength are summarised in Table 65.

1699 None of the pruning thresholds *significantly* impact the predicted uncertainty on the result – none of them  
 1700 would alter the precision of the result after applying rounding to the significant digits. However, to remain  
 1701 conservative, also because these tests were only performed on an Asimov dataset, the pruning threshold  
 1702 combination of 0.05% for normalisation and 0.2% for shape was chosen for the measurement. Each of  
 1703 these drop more than 50% of the nuisance parameters, while only altering the expected uncertainty on the  
 1704 signal strength by 0.01%, which is a tolerable change for simplifying the fit significantly.

1705 For comparison, a pruning plot for the scenario with *no* pruning is shown in Figure 95. Plots for the three  
 1706 different normalisation pruning thresholds are shown in Figures 96 to 98. Plots for the three different shape  
 1707 pruning thresholds are shown in Figures 99 to 101.

Table 65: Expected uncertainty of the  $t\bar{t}\gamma$  signal strength in percent for different pruning thresholds. The pruning thresholds for shape and normalisation components were varied separately, and the fit was then performed on an Asimov dataset for each combination of thresholds. Three thresholds were chosen for both shape and normalisation, which approximately keep 1/2, 1/4 and 1/5 of the nuisance parameters, respectively. The threshold combination marked with an (\*) is chosen for the measurement.

shape \ norm	–	0.05% (1/2)	0.10% (1/4)	0.20% (1/5)
–	6.27	6.27	6.26	6.23
0.2% (1/2)	6.26	6.26*	6.25	6.22
0.5% (1/4)	6.24	6.23	6.22	6.19
1.0% (1/5)	6.27	6.27	6.25	6.22

Not reviewed, for internal circulation only

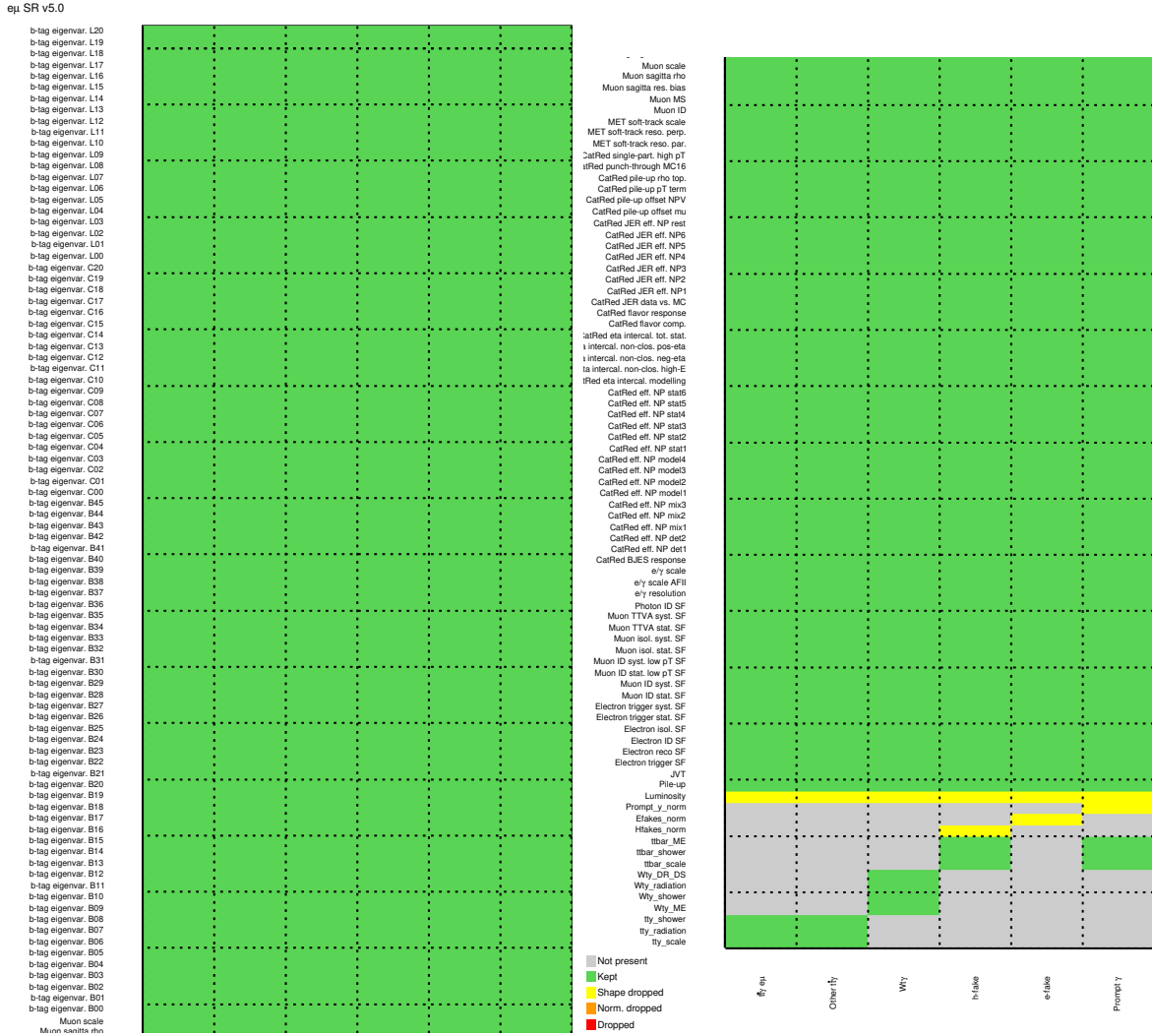


Figure 95: Pruning plot with no normalisation and shape pruning (for comparison only). The resulting expected uncertainty on the  $t\bar{t}\gamma$  signal strength is listed in Table 65. The different columns indicate whether a systematic was pruned for the different event categories. The colour code is: green for both normalisation and shape kept, yellow for normalisation only (shape dropped), orange for shape only (normalisation dropped), and red for dropped entirely.

Not reviewed, for internal circulation only

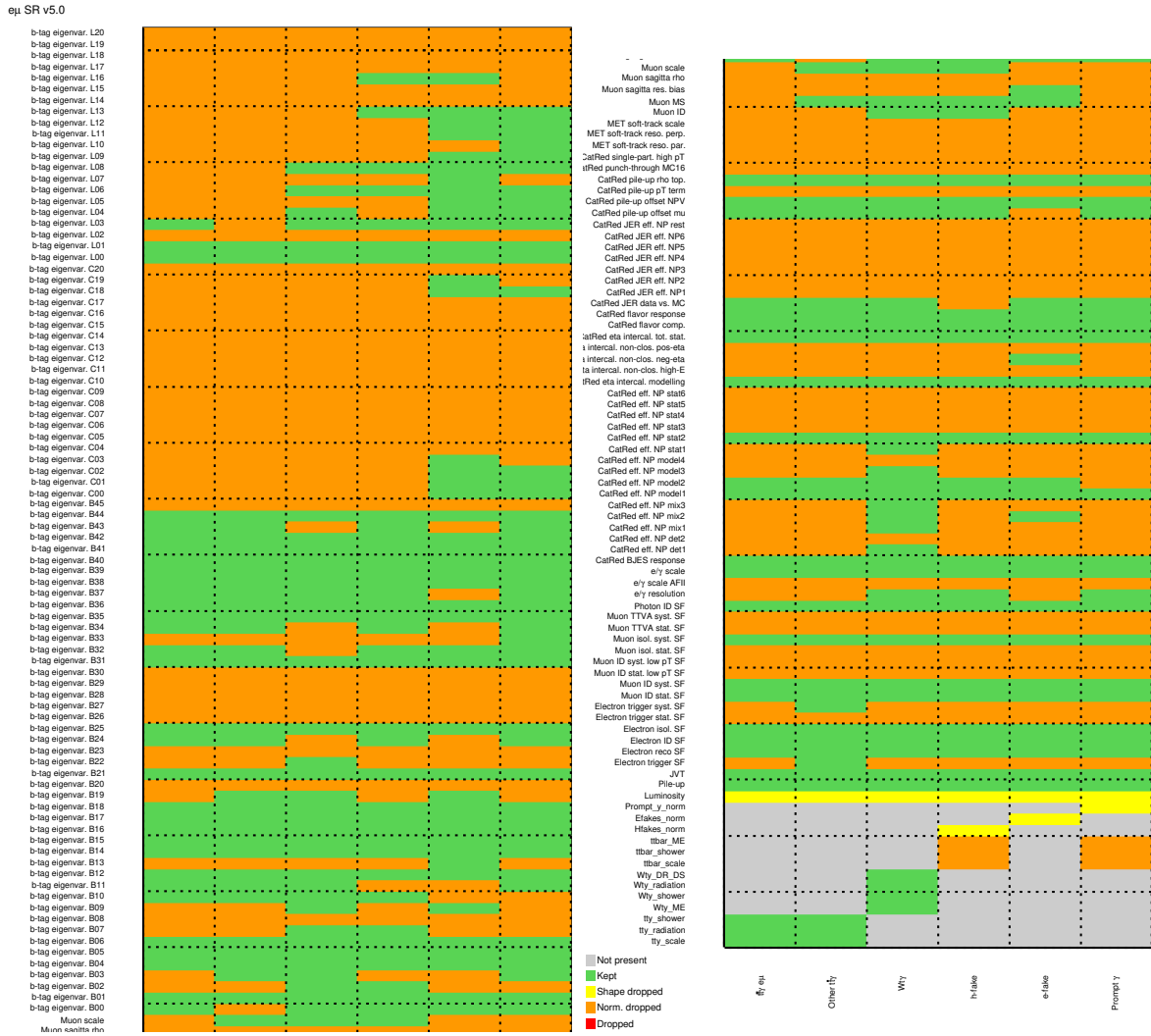


Figure 96: Pruned systematics with a threshold of 0.05% for normalisation pruning, and no shape pruning applied. Approximately 41% of systematics are kept. The resulting expected uncertainty on the  $t\bar{t}\gamma$  signal strength is listed in Table 65. The different columns indicate whether a systematic was pruned for the different event categories. The colour code is: green for both normalisation and shape kept, yellow for normalisation only (shape dropped), orange for shape only (normalisation dropped), and red for dropped entirely.

Not reviewed, for internal circulation only

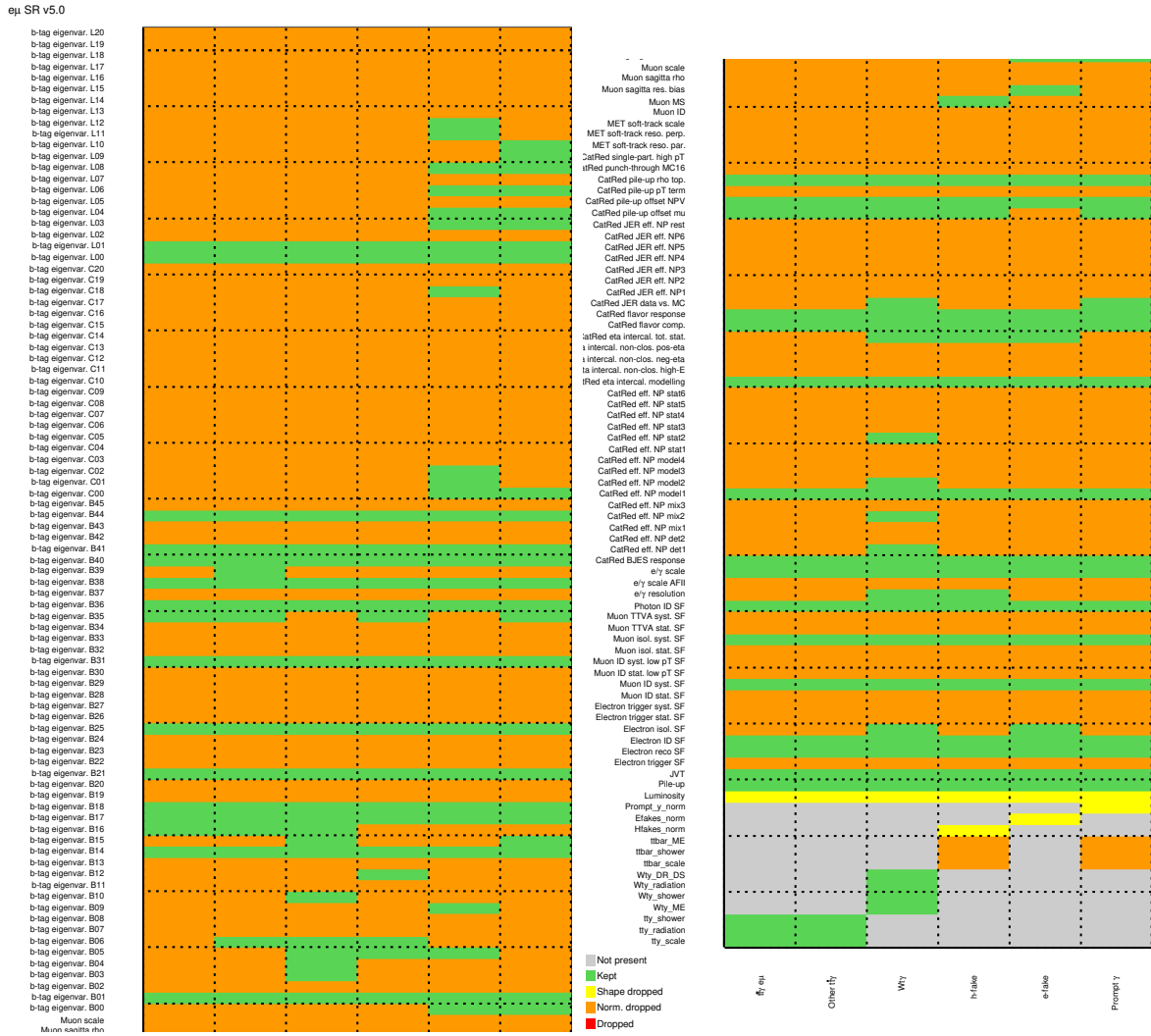
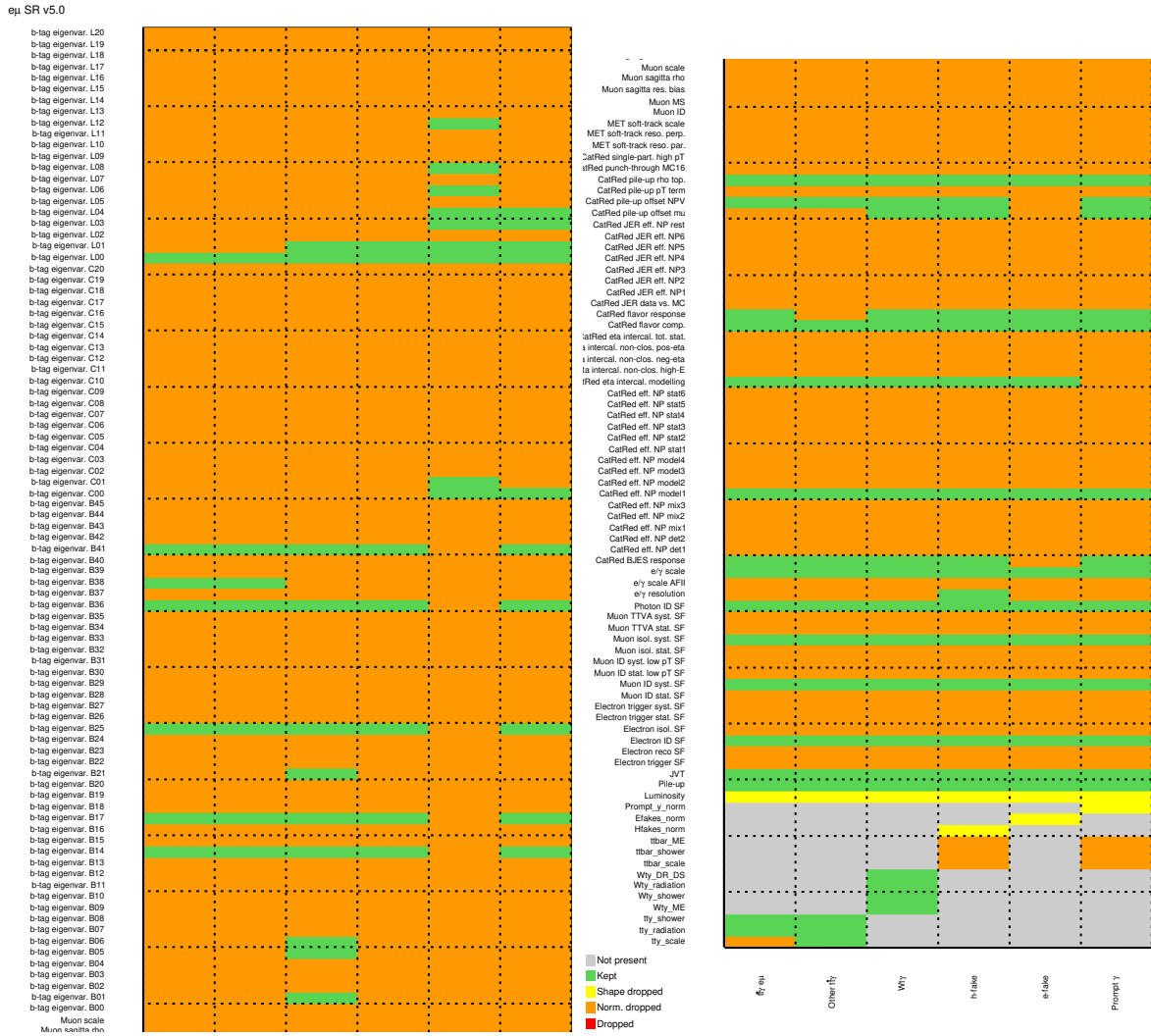


Figure 97: Pruned systematics with a threshold of 0.10% for normalisation pruning, and no shape pruning applied. Approximately 26% of systematics are kept. The resulting expected uncertainty on the  $t\bar{t}\gamma$  signal strength is listed in Table 65. The different columns indicate whether a systematic was pruned for the different event categories. The colour code is: green for both normalisation and shape kept, yellow for normalisation only (shape dropped), orange for shape only (normalisation dropped), and red for dropped entirely.

Not reviewed, for internal circulation only



Not reviewed, for internal circulation only

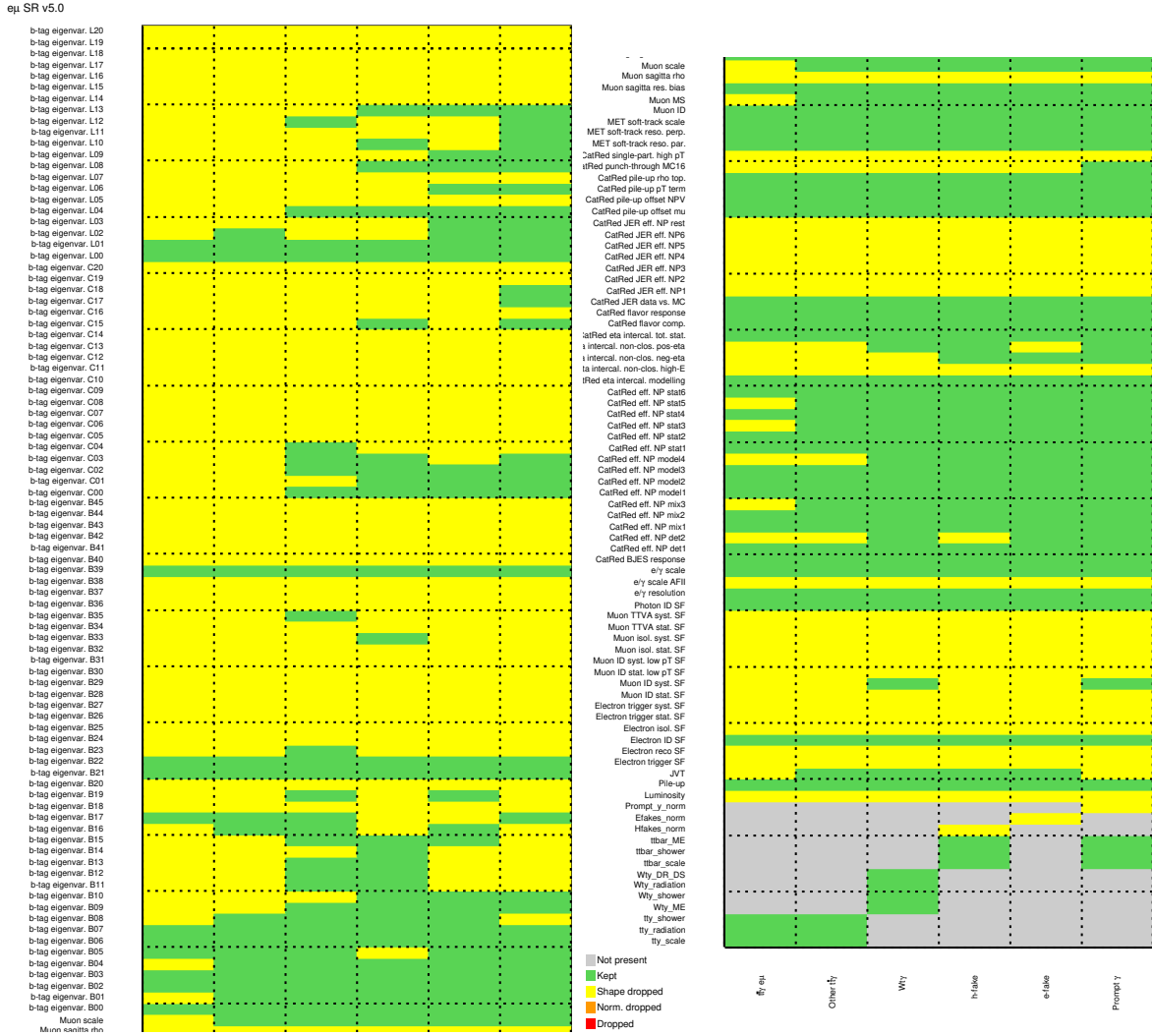
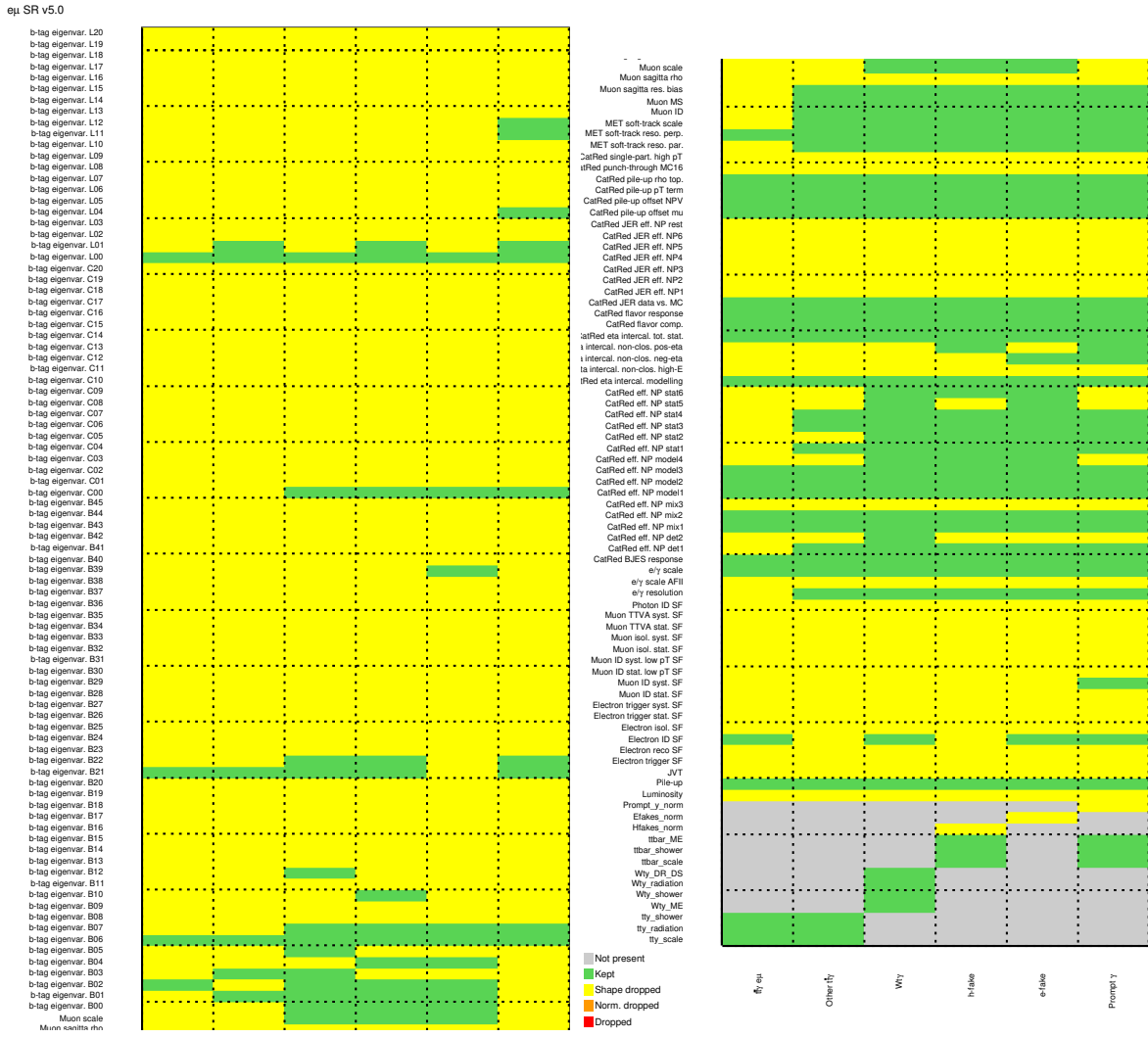


Figure 99: Pruned systematics with a threshold of 0.20% for shape pruning, and no normalisation pruning applied. Approximately 41% of systematics are kept. The resulting expected uncertainty on the  $t\bar{t}\gamma$  signal strength is listed in Table 65. The different columns indicate whether a systematic was pruned for the different event categories. The colour code is: green for both normalisation and shape kept, yellow for normalisation only (shape dropped), orange for shape only (normalisation dropped), and red for dropped entirely.

Not reviewed, for internal circulation only



Not reviewed, for internal circulation only

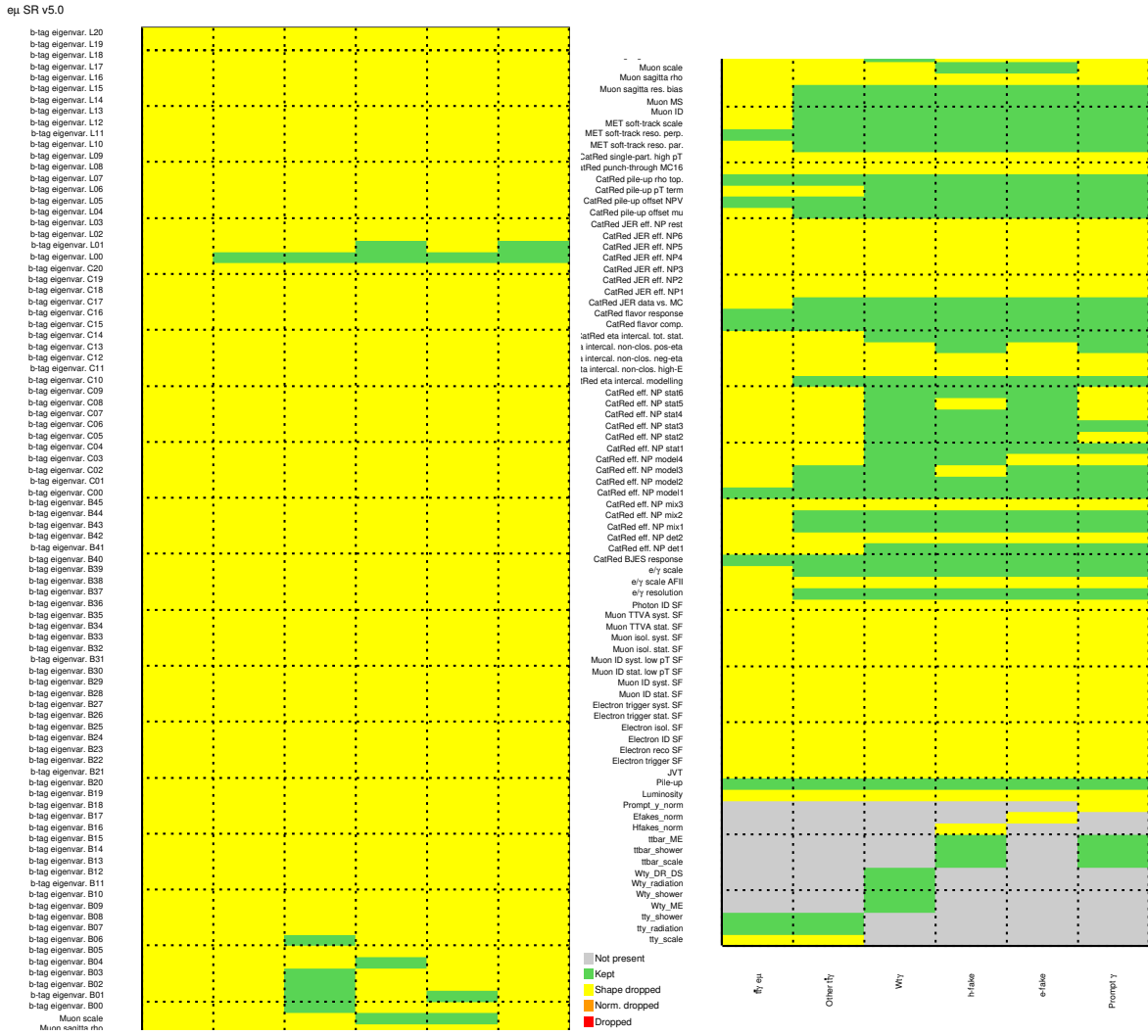


Figure 101: Pruned systematics with a threshold of 1.00% for shape pruning, and no normalisation pruning applied. Approximately 19% of systematics are kept. The resulting expected uncertainty on the  $t\bar{t}\gamma$  signal strength is listed in Table 65. The different columns indicate whether a systematic was pruned for the different event categories. The colour code is: green for both normalisation and shape kept, yellow for normalisation only (shape dropped), orange for shape only (normalisation dropped), and red for dropped entirely.

## I Fit results with correlated rate/shape modelling variations

Not reviewed, for internal circulation only

- 1708 As of INT note v0.13, the final fit results presented in the main body decorrelate rate and shape for two  
 1709 modelling variations:  $t\bar{t}\gamma$  PYTHIA8 *var3c* and  $t\bar{t}\gamma$  PS model. Both of these modelling variations show large  
 1710 pulls and constraints in their shape components. This appendix summarises the results with a fit to data,  
 1711 where rate and shape of these two modelling variations remain correlated. In other terms, everything is  
 1712 identical to the results presented in the main body of INT note v0.13.  
 1713
- 1714 The pulls of the nuisance parameters can be found in Figure 102. For pulls shorter than the green  $\pm 1\sigma$   
 1715 interval, the corresponding nuisance parameter is constrained during the fit. For values pulled away from  
 1716 the nominal, the fit favours the up or the down variation of the systematic. Nuisance parameters pulled by  
 1717 more than  $\pm 0.30$  and those constrained to less than 90% are listed in Table 66. Similarly to what is seen in  
 1718 the main body, a combination of strong pull and large constraint is only observed for the  $t\bar{t}\gamma$  PYTHIA8 *var3c*  
 1719 and  $t\bar{t}\gamma$  PS model variations. Compared to the main results, the constraints are stronger by about 5% each.  
 1720  $t\bar{t}\gamma$  PYTHIA8 *var3c* is pulled stronger, to  $-0.64$  instead of  $-0.39$ .  
 1721
- 1722 The ranking of systematic uncertainties for the fit to data is shown in Figure 103. The plot shows the 20  
 1723 highest ranked uncertainties, which includes the strongly pulled and constrained  $t\bar{t}\gamma$  PS model variation.  
 1724 When compared to the ranking in Figure 51 in the main body, the  $t\bar{t}\gamma$  PS model variation is ranked lower  
 1725 than its decorrelated rate component in the main body. This is due to the constraint imposed by the shape  
 1726 information. The  $t\bar{t}\gamma$  PYTHIA8 *var3c*, the rate component of which is dominant in the results in the main  
 1727 body, is below the ranking threshold in the correlated scenario. Otherwise, the highest ranked uncertainties  
 1728 are similar to those in Figure 51.  
 1729
- 1730 For uncertainties with 10% or higher correlation to others the correlation matrix is shown in Figure 104.  
 1731 Compared to the correlation matrix in Figure 52 in the main body, the correlated rate/shape of the  $t\bar{t}\gamma$  PS

Table 66: Strongly pulled and constrained nuisance parameters. Pulls are observed for a total of three modelling variations (top) and various experimental uncertainties (bottom), mostly related to the jet energy scale/resolution. Large constraints are only observed for the  $t\bar{t}\gamma$  PYTHIA8 *var3c* and the  $t\bar{t}\gamma$  PS model variations. The thresholds are pulls by more than  $\pm 0.30$  and constraints to less than 90%.

Nuisance parameter	pull value $(\hat{\theta} - \theta_0)/\Delta\theta$	constraint $\Delta\hat{\theta}/\Delta\theta [\%]$
$t\bar{t}\gamma$ <i>var3c</i>	-0.64	65.3
$t\bar{t}\gamma$ PS model	-1.49	66.0
$t\bar{t}$ PS model (shape only)	0.38	—
b-jet energy scale response	-0.33	—
CatRed eff. NP model1	-0.35	—
CatRed JER eff. NP1	0.48	—
CatRed JER eff. NP2	0.51	—
CatRed JER eff. NP3	0.73	—
CatRed JER eff. NP6	0.50	—
CatRed JER eff. NP rest	0.55	—
MET soft-track reso. par.	0.51	—
MET soft-track reso. perp.	0.56	—

Not reviewed, for internal circulation only

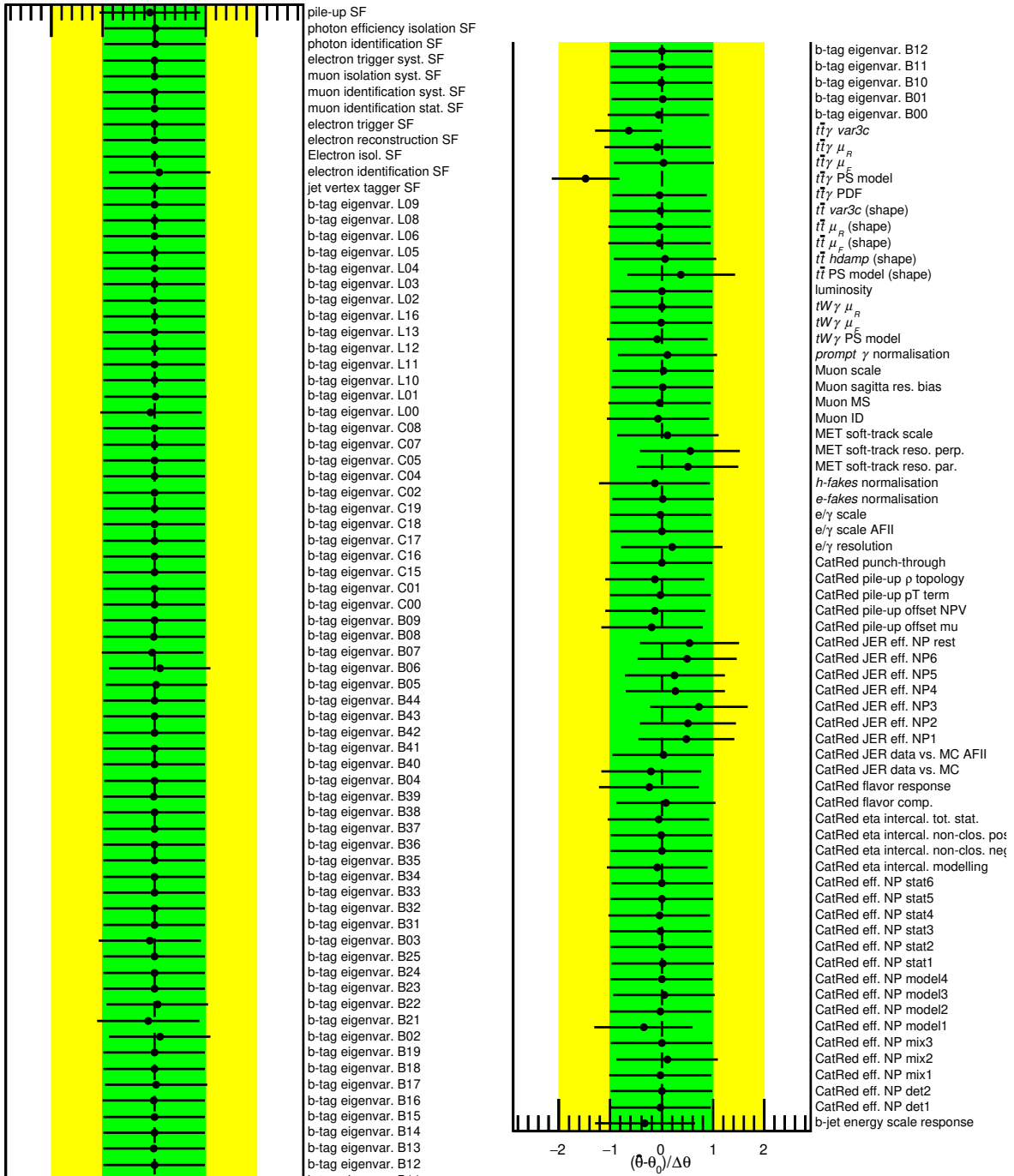


Figure 102: Pull distributions of all remaining nuisance parameters after pruning for the fit to data. If the error bar is shorter than the  $\pm 1\sigma$  interval, the corresponding nuisance parameter is constrained during the fit. If the mean value of the parameter is not zero, the fit favours the up or the down variation of the systematic. Pulls away from the nominal value are observed for some of the modelling uncertainties.

Not reviewed, for internal circulation only

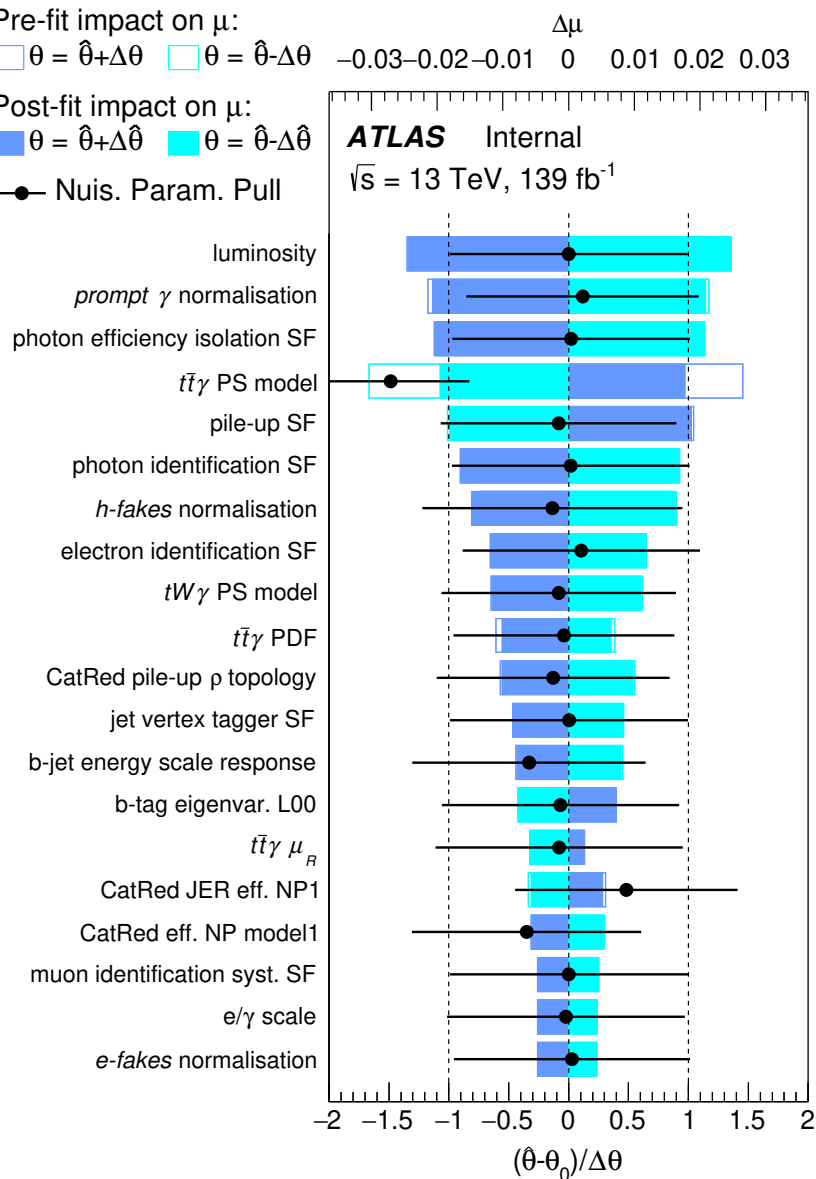


Figure 103: Ranking of systematics for the fit on data.

model variation shows a correlation with the signal strength of 27.1%, compared to -52.1% and -2.6% for the rate and shape components in the decorrelated scenario, respectively. This explains the lower ranking of the  $t\bar{t}\gamma$  PS model variation compared to its rate component, which is the highest ranked uncertainty in the main body. The  $t\bar{t}\gamma$  PYTHIA8 *var3c* variation shows little correlation to the signal strength of -5.3%, compared to -32.7% and 1.5% for the rate and shape components in the decorrelated scenario, respectively. Therefore, this modelling uncertainty does not enter the 20 highest ranked uncertainties in the correlated scenario at all, as shown in Figure 103, whereas its rate component is the second-highest ranked nuisance parameter in Figure 51 in the main body.

The signal strength is fitted to be:

$$\mu = 1.372 {}^{+0.027}_{-0.026} \text{ (stat.)} {}^{+0.065}_{-0.062} \text{ (syst.)} = 1.372 {}^{+0.071}_{-0.067},$$

corresponding to a relative uncertainty of  ${}^{+5.1\%}_{-4.9\%}$ , compared to  ${}^{+6.2\%}_{-5.8\%}$  in the decorrelated scenario in the main body. The fiducial cross-section is measured to be

$$\sigma_{\text{fid}}(t\bar{t}\gamma \rightarrow e\mu) = 39.7 {}^{+0.8}_{-0.8} \text{ (stat.)} {}^{+2.2}_{-1.8} \text{ (syst.) fb} = 39.7 {}^{+2.3}_{-1.9} \text{ fb},$$

corresponding to a relative uncertainty of  ${}^{+5.8\%}_{-4.9\%}$ , compared to  ${}^{+6.8\%}_{-5.8\%}$  in the main body. A breakdown of the systematic uncertainties and their impact in Table 67 reveals that the signal modelling is ranked much lower than in the main body: its impact is calculated to be 1.9%, compared to 3.8% in the decorrelated scenario. The other groups of systematic uncertainties show similar impact in both scenarios and, thus, are not the dominant reason for the differences in the relative uncertainties.

Not reviewed, for internal circulation only

Table 67: Groups of systematic uncertainties and their relative impact on the result.

Group	Uncertainty
Background modelling	2.1%
Signal modelling	1.9%
Photons	1.9%
Luminosity	1.8%
Jets	1.6%
Pile-up	1.4%
Leptons	1.0%
Flavour-tagging	1.0%
MC statistics	0.5%
$E_T^{\text{miss}}$	0.2%
Total systematic impact	4.6%
$\oplus tW\gamma$ parton matching	-2.75%

Not reviewed, for internal circulation only

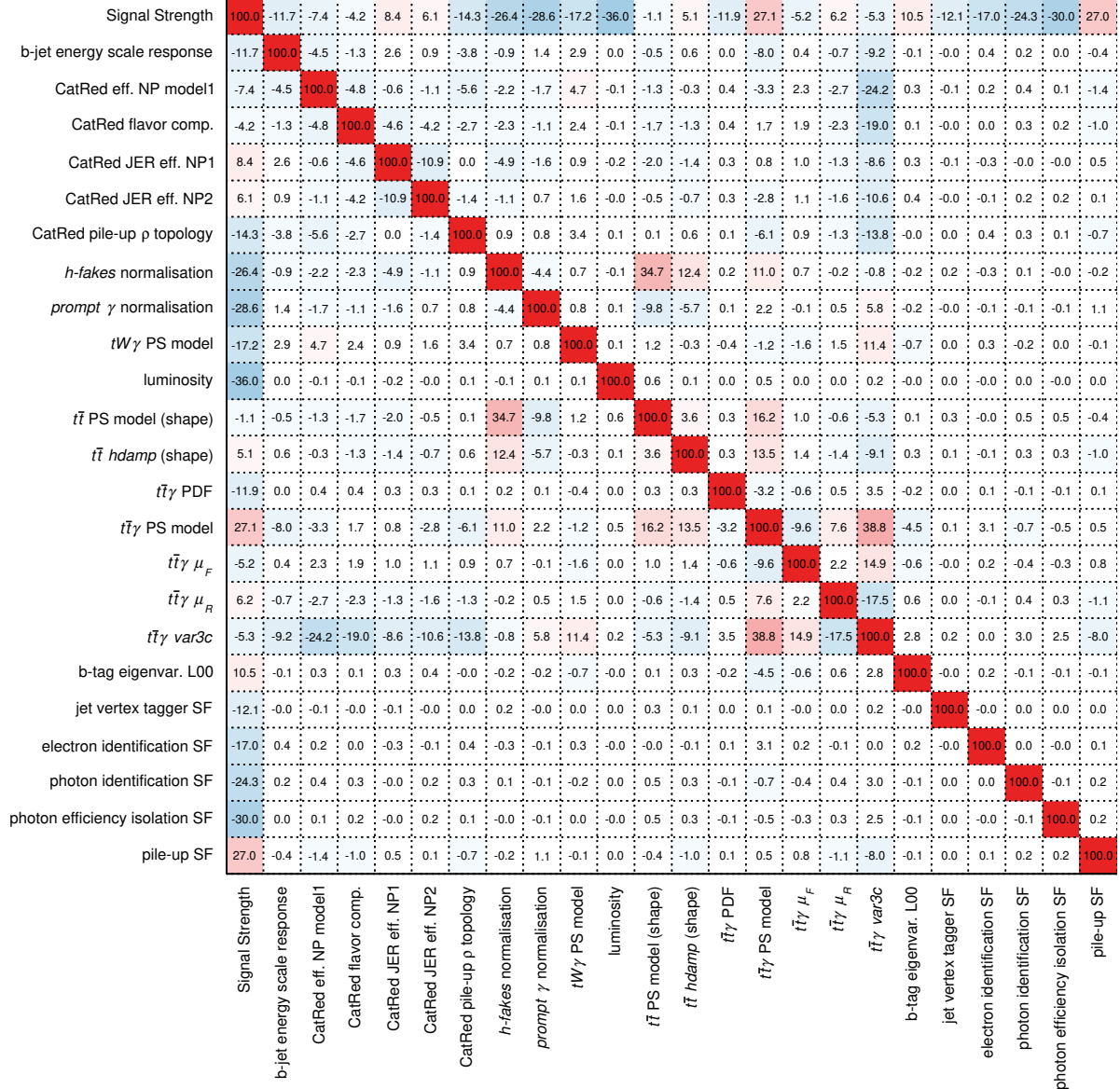


Figure 104: Correlation matrix for those nuisance parameters that have 10% or higher correlations to other uncertainties in the fit.